

**Future Evolution of the Amundsen Sea
Embayment, West Antarctica: Exploring the
Modelled Ice Stream Sensitivity to
Numerical Representation**

Alanna Vanessa Alevropoulos-Borrill

Victoria University of Wellington

A thesis submitted to the Victoria University of Wellington in fulfilment
of the requirements for the degree of

Doctor of Philosophy

2022

”Unless someone like you
cares a whole awful lot,
nothing is going to get better
it’s not” - Seuss, 1971

Abstract

The Amundsen Sea Embayment (ASE) is among the most dynamic catchments in Antarctica. With a recent history of increasing mass loss, and the potential to raise global sea levels by 1.2 m, the evolution of ice streams in the ASE in response to a changing climate must be understood. Sub-ice shelf (IS) basal melting of ASE ice streams is projected to increase in the future in response to climate change, which could initiate unstable retreat in the region. Ice sheet models are used to numerically represent ice flow and simulate future evolution of ice sheets in response to climate. Representation of processes, boundary conditions, model initialisation and the input datasets are at the discretion of model users. However, numerical representation impacts the modelled behaviour of ice streams and can lead to uncertainty in future projections. Understanding the interplay between uncertainty in external forcing and internal ice sheet model configuration is important for constraining future estimates of ASE sea level contribution. This thesis explores the future evolution of ASE ice streams with a focus on the sensitivity of ice streams to IS melting and the role of numerical representation in altering the sensitivity of ice streams to future forcing.

Here, century scale simulations are performed on a regional ASE domain with the high resolution adaptive mesh refinement model, BISICLES. BISICLES captures both shear-dominated flow of grounded ice and longitudinal stress-dominated flow of floating ice, while resolving the grounding line to 250 m, meaning the fast evolving ice streams in the ASE are well represented. Experiments use perturbations of IS melting to force the ice sheet over 200 years. Different representations of subglacial rheology (sliding law), calving front position, geometry product, choice of ice sheet model and parameterization of IS melting are explored for simulations with varying future IS melt rates.

Following a multi-decadal period of elevated IS melting, a sustained reduction in

melting to below present-day rates can limit the total mass loss from the ASE and drive regrowth of ice streams through grounding line advance. Pine Island Glacier (PIG) is more sensitive to the choice of sliding law than to the migration of a calving front, however, sliding law and ice front are most important during application of positive forcing. Thwaites Glacier is less sensitive to the sliding law than PIG, but is more sensitive to the bed geometry product used, particularly in inducing acceleration consistent with observations. Differences in the parameterization of IS melt over the 21st century leads to a doubling in projected mass loss for a single future climate scenario. The results of a model comparison demonstrate the choice of ice flow model is less important than the model initialisation, which amplifies model differences in response to perturbed IS melting. The exploration presented here into the role of numerical representation provides context for the interpretation of existing ASE simulations and also helps clarify which model configuration(s) are best able to reduce sea-level projection uncertainty.

Acknowledgments

This thesis represents a mere fraction of a turbulent but rewarding journey. A journey could not have been embarked upon without the help, support and kindness of others.

I would like to thank my supervisors Nicholas Golledge and Stephen Cornford. Nick has always had faith in me when I didn't have faith in myself. He advocates for others, helping people develop as individuals and researchers. Steph continues to make time for me despite the awkward time difference, his busy schedule and vast research interests. My virtual meetings with Steph are always enjoyable, I leave every conversation more inspired and knowledgeable, even at 6 am. I have cherished being mentored by both Nick and Steph and I am eternally grateful for their unwavering patience and support.

I would like to thank Dan Lowry, Laurine van Haastrecht, Fran Baldacchino, Alex Gossart and Nick for being incredible fieldwork companions. Antarctica is a special place and I am so grateful to have shared those experiences with them. And to Dan and Fran, thank you for supporting me through my meltdowns (pun intended) and ice sheet modelling rambles. My thanks go to the National Modelling Hub Research Fellows for taking me under their wing. To Huw Horgan and Darcy Mandeno, thank you for the patience and support with fieldwork preparation. Thank you to the Antarctic Research Centre, Victoria University of Wellington, Antarctica New Zealand and New Zealand eScience Infrastructure for supporting this research.

To my family, thank you for supporting me from afar and encouraging me to pursue my dreams- I'm sorry I have been gone for so long, but I will be home soon. To my Aotearoa family, Charlotte Pizer, Matthew Tankersley, Sarah Willette, Abbie Bender, Heather Pickard and Reuben Moss; without you, this would not have been possible.

Contents

Figures	x
Acronyms	xiv
Nomenclature	xvi
1 Introduction and Geographical Context	1
1.1 Introduction	1
1.1.1 Aims and Significance	3
1.1.2 Objectives	3
1.1.3 Thesis Structure	4
1.2 Antarctic Glaciology	4
1.2.1 Antarctica	4
1.2.2 Ice Sheet Dynamics	5
1.2.3 Ice Streams	5
1.2.4 Ice Shelves	7
1.2.5 The Grounding Zone	7
1.2.6 Antarctic Mass Balance	8
1.2.7 Marine Ice Sheet Instability	11
1.2.8 Ice Shelf Buttressing	14
1.2.9 Topographic Controls	17
1.3 The Amundsen Sea Embayment (ASE) Ice Streams	18
1.3.1 Pine Island Glacier	19
1.3.2 Thwaites Glacier	20
1.3.3 Pope Smith and Kohler Glaciers	22
1.4 Amundsen Sea Oceanography	23

1.5	Amundsen Sea Sub-Ice Shelf Basal Melting	26
1.6	Future Simulations of the Amundsen Sea Embayment	28
1.6.1	Future Climate	28
1.6.2	Future Ice Evolution	30
1.7	Summary	32
2	The History and Future of Ice Sheet Modelling	34
2.1	Introduction	34
2.2	The Introduction and Development of Ice Sheet Models	35
2.3	The Hierarchy of Ice Sheet Models	38
2.3.1	Stokes Equations	38
2.3.2	Boundary conditions	41
2.3.3	Model Approximations	41
2.3.4	Grid Representation	47
2.4	Model Initialisation Methods	48
2.4.1	Inverse Methods	48
2.4.2	Spin-ups	50
2.5	Representation of Basal Friction	51
2.6	Surface Fluxes	55
2.6.1	Melt Rate Parameterization	56
2.6.2	Parameterization Assessments	59
2.7	Ice Sheet Model Intercomparison Project (ISMIP)	60
2.8	The Future of Ice Sheet Modelling: Coupling	63
2.9	BISICLES	65
2.9.1	Model Initialisation	66
2.9.2	Model Application	67
2.10	Summary	67
3	Re-advancing the grounding lines of marine terminating glaciers in the Amundsen Sea Embayment	69
3.1	Introduction	69
3.2	Methods	71
3.2.1	Regional Model Domain	71
3.2.2	Ensemble Description	72
3.3	Results	76

3.3.1	Sea Level Contribution	76
3.3.2	Grounding Line Positions	79
3.3.3	Individual Drainage Basin Response	81
3.3.4	Specific Simulations: Equivalent Sea Level Contribution	86
3.4	Discussion	89
3.5	Conclusion	94
4	Understanding the modelled response of Pine Island Glacier to varied basal melting	96
4.1	Introduction	96
4.2	Methods	99
4.2.1	Experimental Design	99
4.2.2	Reference Model	99
4.2.3	Alternative Sliding Law	100
4.2.4	Migrated Calving Front	101
4.2.5	Basal Melt Forcing	102
4.3	Results	105
4.3.1	Bedmap2-W-fixed	105
4.3.2	Alternative Model Configurations	111
4.4	Discussion	116
4.4.1	Reference Model	116
4.4.2	Comparison of Configurations	118
4.5	Conclusion	125
5	The Influence of Topography and Thickness Products on Future Simulations of the Amundsen Sea Embayment	128
5.1	Introduction	128
5.2	Method	132
5.2.1	Initialisation	132
5.3	Control Simulations	137
5.3.1	Basal Mass Balance	137
5.3.2	Simulations	137
5.3.3	Results	139
5.4	Perturbed Simulations	145
5.4.1	Simulations	145

5.4.2	Results	146
5.5	Discussion	154
5.5.1	PIG	157
5.5.2	Thwaites Glacier	160
5.5.3	Sliding Law Comparison	164
5.5.4	Limitations and Future Work	165
5.6	Conclusion	166
6	Understanding the contribution of ice flow representation and melt rate parameterizations to uncertainty in future simulations of the Amundsen Sea Embayment	168
6.1	Introduction	168
6.2	Methods	170
6.2.1	Input Datasets	170
6.2.2	BISICLES	171
6.2.3	ISSM	172
6.2.4	Experiments	174
6.3	Description of Melt Rate Inputs	176
6.4	Initialized Models	180
6.5	Results	181
6.5.1	Sea Level Contribution	181
6.5.2	Change in Grounded Area	184
6.5.3	Individual Simulations	187
6.6	Discussion	194
6.7	Conclusion	200
7	Synthesis	202
7.1	The Response of the ASE Ice Streams to Sub-ice Shelf Melting	202
7.2	Uncertainties in Ice Sheet Model Practices	204
7.3	The Stability of the ASE Ice Streams	211
7.4	Future Investigations	213
8	Conclusions	215
8.1	Chapter Summaries	215
8.1.1	Re-growth of the ASE Ice Streams	215

8.1.2	The Sensitivity of PIG to Ice Shelf Melting	215
8.1.3	The Role of Bedrock Topography in Influencing Ice Stream Behaviour	216
8.1.4	Comparing Future Simulations from High Resolution Ice Sheet Models	217
8.2	Key Conclusions	217
	References	220

List of Figures

1.1	Velocity map of the Antarctic Ice Sheet from Rignot et al. (2011) Fig. 1	6
1.2	Schematic of ocean and atmosphere processes within cold and a warm ice shelf cavities from Holland et al. (2020)	10
1.3	Marine ice sheet instability schematic from Church et al. (2013)	12
1.4	Ice shelf buttressing schematic from Gudmundsson et al. (2019)	15
1.5	Velocity map of Amundsen Sea Embayment domain	18
1.6	Bathymetry of the Amundsen Sea Embayment continental shelf from Klages et al. (2015)	25
1.7	Map of Antarctic ice shelf melt rates and offshore potential temperature from Adusumilli et al. (2020)	27
2.1	Schematic of the principal stresses included in each of the ice sheet model approximations; FS: Full Stokes, HO: Higher Order, SSA: Shallow Shelf Approximation and SIA: Shallow Ice Approximation. The right column shows the corresponding velocities. Arrows x , y and z mark the directions of the principal stresses and planes and u , v w show the directional velocity components.	43
2.2	Diagram of ice flow approximations from Nowicki and Seroussi (2018)	46
2.3	Schematic of basal sliding mechanisms and the associated sliding laws. Three bottom panels depict hard bed sliding, sliding with cavitation and soft bed sliding at the ice-bed interface with basal velocity depicted by the red arrows. Beneath each figure is the equation for the respective sliding law, here m is equivalent to the inverse of the m described in the text. Top right panel depicts the simplified relationship between basal velocity, u_b , and basal drag, τ_b , for each of the sliding laws.	52

3.1	Present-day ice shelf melt rates in the Amundsen Sea Embayment from Cornford et al. (2015)	73
3.2	Ensemble of idealised melt rate anomalies	75
3.3	Sea level equivalent over two-hundred years for the ensemble of simulations grouped by magnitude of negative anomaly	77
3.4	Rate of sea level equivalent contribution over two-hundred years from ensemble of simulations grouped by magnitude of negative anomaly	78
3.5	Boxplot of end of simulation sea level contribution	79
3.6	End of simulation grounding line positions for full ensemble of simulations grouped by the magnitude of negative anomaly	80
3.7	Sea level contribution from ensemble of simulations for each Amundsen Sea Embayment drainage basin	82
3.8	Rate of sea level contribution for each Amundsen Sea Embayment drainage basin grouped by the magnitude of negative anomaly	83
3.9	Relationship between cumulative melting and sea level contribution for each Amundsen Sea Embayment drainage basin	85
3.10	Comparison of sub-shelf melt anomaly and sea level contribution for two simulations	87
3.11	Grounding line migration and thickness change for two simulations	89
4.1	Map of Pine Island Glacier velocity averaged over 2007-2009 and Bedmap2 topography map	97
4.2	Change in thickness of Pine Island Glacier with a retreating ice front based on observations	102
4.3	Melt rate forcing ensemble for simulations	104
4.4	Total mass loss and rate of mass loss from ensemble of Pine Island Glacier simulations	106
4.5	End of simulation grounding line position and ice geometry of Pine Island Glacier	108
4.6	Grounding line migration along the trunk of Pine Island Glacier	109
4.7	Grounding line migration of Pine Island Glacier presented every 20 years	110
4.8	Grounding line migration and sea level contribution for alternative model configurations in response to low magnitude melt forcing	111

4.9	Grounding line migration and sea level contribution for alternative model configurations in response to high magnitude melt forcing	112
4.10	Ice geometry evolution over cross-section of Pine Island Glacier for alternative model configurations forced with high magnitude melt anomalies	113
4.11	End of simulation velocity change	115
4.12	Difference in end of simulation gravitational driving stress for Bedmap2-W-fixed high and low melt simulations	117
4.13	a-d) Velocity change at $t = 0$, $t = 20$ and $t = 100$ and e-f) ice geometry evolution over cross-section for models with different sliding laws . . .	120
4.14	Velocity profile along Pine Island Glacier relative to $t = 0$	121
4.15	Velocity and longitudinal strain difference from $t = 12$ to $t = 20$ between simulations with fixed and retreated ice fronts	123
5.1	BedMachine and Bedmap2 bedrock elevation over the Amundsen Sea Embayment	131
5.2	Basal traction and ice rheology over Pine Island Glacier	135
5.3	Basal traction and ice rheology over Thwaites Glacier	136
5.4	Velocity change along Pine Island Glacier transect	139
5.5	Comparison of ice geometry variables for BedMachine and Bedmap2 over Pine Island Glacier	140
5.6	Maps of Pine Island Glacier velocity difference over simulation	142
5.7	Comparison of ice geometry variables for BedMachine and Bedmap2 over Thwaites Glacier	143
5.8	Maps of Thwaites Glacier velocity difference over simulation	145
5.9	Difference in Pine Island Glacier sea level contribution for melt forced simulations	147
5.10	Pine Island Glacier grounding line and grounded area evolution	149
5.11	Thwaites Glacier difference in sea level contribution	151
5.12	Thwaites Glacier grounding line and grounded area evolution	153
5.13	Distributions of initial ice geometry variables over domain	155
5.14	Difference between BedMachine and Bedmap2 bedrock elevation for select areas	156
5.15	Sea level contribution for all simulations performed	157
5.16	Velocity evolution along transect of Pine Island Glacier	158

5.17	Inset of Thwaites Glacier viscosity coefficient parameter difference between BedMachine and Bedmap2 model domains.	161
5.18	Velocity comparison for simulations with and without calving of Thwaites Glacier western ice tongue	162
5.19	Three-dimensional topography of Bedmap2 and BedMachine around the Thwaites Glacier grounding line	163
6.1	Melt rate maps of Amundsen Sea ice shelves produced by models and from observations	177
6.2	Projected 21st century total meltwater production from FESOM and NEMO models with observations for comparison	179
6.3	Maps of projected melt rate anomalies from NEMO and FESOM	180
6.4	Initial velocity difference between BISICLES and ISSM and observations used for initialisation	181
6.5	Twenty-first century sea level equivalent contributions from BISICLES and ISSM simulations	182
6.6	Box-plot of end of century sea level contributions from BISICLES and ISSM simulations	183
6.7	Relationship between cumulative ice shelf melt and sea level contribution for BISICLES and ISSM simulations	184
6.8	End of century grounding line positions for BISICLES and ISSM simulations	186
6.9	Change in grounded area over the twenty-first century for BISICLES and ISSM simulations	187
6.10	Velocity difference between BISICLES-CTRL-W and ISSM-CTRL-W simulations in 2008 and 2100	189
6.11	Thickness change and grounding line migration for CTRL simulations .	191
6.12	Velocity difference between BISICLES-LINEAR-W and ISSM-LINEAR-W simulations in 2008 and 2100	193
6.13	Thickness change and grounding line migration for LINEAR simulations.	194
6.14	Sea level equivalent contribution relative to the control simulations. . .	197
6.15	Relationship between cumulative melting and sea level equivalent . . .	199

Acronyms

ACC Antarctic Circumpolar Current

AIS Antarctic Ice Sheet

AOGCM Atmosphere Ocean General Circulation Model

AOGCM-ISM Coupled Atmosphere-Ocean General Circulation Model with an Interactive Ice Sheet Model

ASE Amundsen Sea Embayment

BISICLES Berkeley Ice Sheet Initiative for Climate at Extreme Scales model

CDW Circumpolar Deep Water

CMIP Coupled Model Intercomparison Project

initMIP Initial State Intercomparison Experiment

IPCC Intergovernmental Panel for Climate Change

ISMIP6 Ice Sheet Model Intercomparison Project for CMIP6

ISSM Ice Sheet System Model

MISI Marine Ice Sheet Instability

MISMIP3D+ Marine Ice Sheet Model Intercomparison Project 3D+

PIG Pine Island Glacier

PSK Pope Smith and Kohler Glaciers

RCP Representative Concentration Pathway

SIA Shallow Ice Approximation

SLE Sea Level Equivalent

SMB Surface Mass Balance

SSA Shallow Shelf Approximation

SSP Shared Socioeconomic Pathway

TG Thwaites Glacier

WAIS West Antarctic Ice Sheet

Nomenclature

Physics Constants

ρ_i	Density of ice	918 kg m ⁻³
ρ_w	Density of freshwater	1000 kg m ⁻³
ρ_{sw}	Density of sea water	1028 kg m ⁻³
g	Gravitational Acceleration	9.81 m s ⁻²
m	Sliding law exponent	3
n	Exponent n Glen's flow law	3

Variables

$\dot{\epsilon}$	Strain Rate Tensor	Pa s ⁻¹
σ	Cauchy stress tensor	Pa
τ_b	Basal Shear Stress	Pa
τ	Deviatoric stress tensor	Pa
u_b	Basal velocity	m yr ⁻¹
u_{obs}	Observed velocity	m yr ⁻¹
u	Velocity	m yr ⁻¹
δT	Temperature Correction	K
$\dot{\epsilon}_e$	Effective strain rate	Pa s ⁻¹
η	Effective viscosity of ice	Pa s ⁻¹
γ_0	Uniform Coefficient	—
μ	Vertically varying effective viscosity	Pa s ⁻¹
ϕ	Ice Rheology Coefficient	—
A	Rate factor in Glen's flow law	Pa ³ yr ⁻¹
C	Basal Traction Coefficient	Sliding Law Dependent
h	Ice Thickness	m
h_T	Threshold Thickness	m
l	Lag Distance	m

M	Mass	kg
M_b	Basal Mass Balance	m yr^{-1}
M_s	Surface Mass Balance	m yr^{-1}
N	Effective Pressure	Pa
r	Bedrock Elevation	m
s	Surface Elevation	m
T	Temperature	K
t	Time	yr
u_0	Threshold Velocity	m yr^{-1}
z_b	Ice Base Elevation	m

Chapter 1

Introduction and Geographical Context

1.1 Introduction

Sea level rise could have devastating global consequences (Oppenheimer and Hinkel, 2019). Reliable estimates of future sea level rise are needed to help support the 390 million people living within 5 m of coastlines (McMichael et al., 2020). At present, the greatest uncertainty in estimates of future sea level rise are associated with the projected mass loss from the Antarctic Ice Sheet (AIS; Seroussi et al., 2020; Lowry et al., 2021). Currently, the West Antarctic Ice Sheet (WAIS) is in disequilibrium, losing mass at a rate equivalent to 4.5 cm of global sea level rise per century (Shepherd et al., 2018). Mass loss from WAIS is expected to increase in the future in response to atmospheric and oceanic warming that is induced by anthropogenic climate change (Seroussi et al., 2020; Lowry et al., 2021; Cornford et al., 2015; Golledge et al., 2015). Evidence suggests WAIS has collapsed in response to past climate warm periods (Lowry et al., 2019; Steig et al., 2015; Dutton et al., 2015) and has the potential to collapse in the future, should climate forced instability mechanisms be triggered (Feldmann and Levermann, 2015; Martin et al., 2019). Complete collapse of WAIS could raise global mean sea level by 4.3 m (Fretwell et al., 2013) and therefore understanding the dynamic evolution of the ice sheet in response to climate is essential to constrain estimates of future sea level rise.

Computer based ice sheet models are tools widely used to estimate the future evo-

lution of glaciers and ice sheets in response to changes in climate by numerically representing ice flow under external forcing (Nowicki and Seroussi, 2018; Pattyn, 2018; Blatter et al., 2010). Global ice sheet model intercomparisons have identified disagreement between the representation of present day ice flow by different models, which creates uncertainty in the projected evolution of the AIS (Seroussi et al., 2020; Cornford et al., 2020; Seroussi et al., 2019). Although ice sheet model capabilities have advanced substantially in the last two decades (Pattyn, 2018), simplistic approximations, parameterizations and tuning procedures exist in models to account for limited observations, poorly understood processes and high computational demands (Blatter et al., 2010; Pattyn, 2018). Research has shown the representation of unknowns in models can amplify the uncertainty in projected ice sheet evolution in response to climate change (Lowry et al., 2021; Schlegel et al., 2018). In better understanding and quantifying the sources of uncertainty within and between models, future projections of sea level contribution from AIS can be constrained.

Estimates of future sea level rise are skewed by the (in)stability of regions of Antarctica that reside on bedrock below sea level (Weertman, 1974; Robel et al., 2019; Edwards et al., 2021), such as the Amundsen Sea Embayment (ASE) in West Antarctica. The ASE sector currently experiences the greatest mass loss of all Antarctic regions (IMBIE, 2018), coinciding with thinning and acceleration of ice streams (Robel and Banwell, 2019; Bamber and Dawson, 2020; Mouginot et al., 2019) and retreat of grounding lines (Scheuchl et al., 2016; Wild et al., 2021). The future of the ASE is dependent on changes in the volume of warm water within the region's ice shelf cavities which drives melting from beneath (Shean et al., 2019; Donat-Magnin et al., 2017; Pritchard et al., 2012; Naughten et al., 2018b). Increased sub-ice shelf melting could trigger unstable retreat (Joughin et al., 2014; Favier et al., 2014) and current research aims to determine both how much mass may be lost from the region, and when this will occur (Scambos et al., 2017). Regional ice sheet modelling investigations that simulate the evolution of the ASE in response to climate perturbations improve the understanding of the behaviour of the region (Nias et al., 2019). Furthermore, with a high sensitivity to numerical representation (Lowry et al., 2021; Nias et al., 2016; Alevropoulos-Borrill et al., 2020; Brondex et al., 2019), exploring the interplay between external forcing and internal model variables can provide additional constraints on the uncertainty in the future contribution of the ASE to global sea level rise.

1.1.1 Aims and Significance

This thesis investigates the role of ice sheet models in improving the understanding of ice stream behaviour in one of Antarctica's most dynamic and vulnerable regions, the ASE. The research considers the modelled stability of the ASE ice streams in response to evolving melt rates beneath floating ice shelves while also accounting for the role of ice sheet model physics, initialisation and configuration in modifying the sensitivity of ice streams to climate forcing.

1.1.2 Objectives

1. To assess the ability of ASE ice stream grounding lines to advance following a period of retreat. To achieve this, an ensemble of simulations with varying sub-ice shelf melt anomalies is performed with an initial positive melt phase (retreat) followed by a negative melt phase (advance). The magnitude of melt reduction and refreezing required to stabilise the ice streams is quantified.

2. To explore the glaciological controls on a single ice stream, Pine Island Glacier, in response to future ocean induced melting. A reduced set of simulations is performed with varying sub-ice shelf basal melt for three different model configurations, with two sliding regimes and calving front positions. The interplay between external ocean forcing and internal model set up is compared and the relative importance of the different configurations on ice dynamics is considered.

3. To compare the modelled response of ASE ice streams to sub-ice shelf melting with a domain initialised with bed topography and ice thickness from Bedmap2 and BedMachine. A series of simulations are performed for the two geometry products, to consider the importance of bed topography and ice thickness in altering the modelled ice stream sensitivity to melting and sliding. These experiments provide continuity between the results of existing studies using the older product, a modified coarser resolution Bedmap2, compared with the product, BedMachine Antarctica version 1.

4. To compare the modelled response of ASE ice streams to future climate change using two state of the art ice sheet models, ISSM and BISICLES. A regional high resolution model comparison is performed using seven basal melt parameterizations and two sliding laws to provide a detailed consideration of the differences in the representation of ice flow of one of the most dynamic and sensitive regions in

Antarctica.

1.1.3 Thesis Structure

The structure of this thesis follows the above objectives. There are two introductory chapters. Here, in Chapter 1, Antarctica and the ASE region is introduced geographically and the processes dictating ice stream behaviour and evolution are discussed. In Chapter 2, ice sheet modelling methods are discussed and the primary ice sheet model used throughout this thesis is described.

This thesis contains four research chapters. Chapter 3 presents an assessment of the sensitivity of the ASE ice streams to increased and reduced sub-ice shelf melting over varying timescales. Chapter 4 focuses on the modelling of Pine Island Glacier, with a detailed consideration of the dynamic response of the ice stream to basal melting with a modified model configuration. Chapter 5 discusses the modelled response of the ASE to alternative ice geometry products to further explore the role of basal sliding and topography in controlling ice dynamics. Chapter 6 presents a comparison of simulations using two different high resolution ice sheet models. The chapter discusses the role of englacial stresses, model initialisation and representation of basal friction in altering the response of the region to sub-ice shelf melting. Chapters 7 and 8 integrate the findings of the four research chapters and compares the key results of the thesis with literature in order to highlight the improvements in the understanding of ice flow in the ASE.

1.2 Antarctic Glaciology

1.2.1 Antarctica

The Antarctic Ice Sheet (AIS) is an interactive and regulatory component of the earth system (Vizcaino, 2014). The AIS controls global sea level through retention of frozen water, and local sea level, through both its gravitational pull of its mass (Leuliette and Nerem, 2016) and vertical movement of the earth beneath it (Whitehouse et al., 2019). The high reflectivity of the ice surface influences global climate (Box et al., 2012) whilst the continental topography directly influences orographic precipitation and winds (Tewari et al., 2021). Melting of ice at the periphery drives global overturning circulation through the stratification of the water column and production of sea ice (Bintanja

et al., 2015a; Mackie et al., 2020; Bronselaer et al., 2018). The ice sheet also plays a primary role in regulation of Southern Ocean ecosystems and global biogeochemical cycles (Vizcaino, 2014).

The AIS consists primarily of grounded ice over the Antarctic Plate, which is separated into the geologic East and West Antarctica overlain by the East and West Antarctic Ice Sheets. The AIS is made up of both grounded and floating ice and the state of the ice sheet is constantly evolving.

1.2.2 Ice Sheet Dynamics

The velocity of the AIS varies spatially, with areas frozen to the bed exhibiting negligible velocity contrasting with the fast flow of ice streams and shelves that have observed velocities reaching up to 6 km yr^{-1} (Mouginot et al., 2017). In response to gravitational forces, the ice sheet experiences large driving stress causing ice to travel in the direction of surface slope, from the interior flowing out to the periphery of the ice sheet (Paterson, 1994). Grounded ice flow is facilitated by three primary mechanisms, internal ice deformation (creep), sliding of ice over a water saturated base and sliding as a result of sediment deformation at the bed (Paterson, 1994). Much of the interior flows predominantly through ice deformation, where ice is mostly frozen to the bed. The fastest flowing ice is found within ice streams, where there is a combination of internal deformation, sliding through basal lubrication and sliding through the deformation of sediment.

1.2.3 Ice Streams

Approximately 80 % of ice discharged from the ice sheet is drained through fast flowing ice streams (Mouginot et al., 2014) with velocities orders of magnitude greater than surrounding ice (fig. 1.1; Rignot et al., 2011). Ice streams predominantly consist of a main trunk fed by smaller tributaries that extend up to 1000km into the interior of the ice sheet (Bamber et al., 2000). Ice streams vary in size, but typically exceed 20 km in width and 150 km length (Stokes and Clark, 1999) and are laterally constrained by both topographic boundaries (topographic ice streams) and shear margins adjacent to slower flowing ice (pure ice streams).

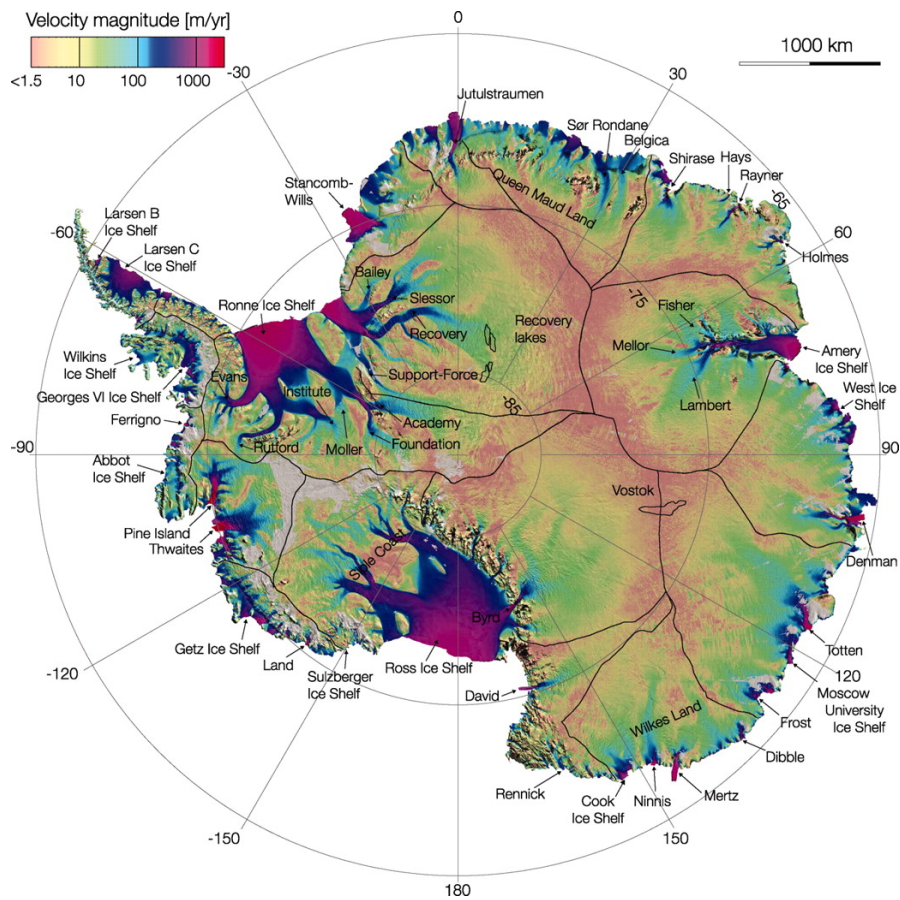


Figure 1.1: Velocity map of the Antarctic Ice Sheet. From Rignot et al. (2011), Figure 1, reprinted with permission from AAAS.

Ice streams are situated in topographic lows, where the thicker ice experiences greater driving stress at the base and subsequent increased deformation controlled by basal and internal shear (Paterson, 1994). Ice stream flow is facilitated by pressure melting at the bed, resulting in a thin film of water that provides lubrication reducing slip and enhancing sliding at the ice base. Furthermore, with a rough bed, melting at the base of the ice can be increased as a result of a pressure and heat build up allowing ice to flow through regelation, a process of creep driven by refreezing on the lee side of a topographic high or obstacle (Benn and Evans, 2014).

Both the rheology of the sediment beneath the ice (till) and the rheology of the ice are additional controls on the velocity of ice, where increased deformation of sediment further promotes elevated basal velocity. Subglacial till deformation occurs when basal shear stress exceeds the yield strength of the till. High water content leads to high pore pressure which makes the sediment more susceptible to deformation. Recent re-

search has suggested that deformable sediments are a pre-requisite for the fast ice flow observed in Antarctic ice streams (Bougamont et al., 2014), highlighting the role of subglacial geology in Antarctic ice dynamics.

1.2.4 Ice Shelves

Antarctic ice shelves cover an area of over 1.6 million square kilometers, surrounding 75 % of the coast of the continent (Rignot et al., 2013a). Ice shelves form where marine based ice streams at the periphery of the continent meet the ocean and thin to the point of floatation, given that ice has a lower density than ocean water. Ice shelves are connected to and fed by fast flowing grounded ice upstream. The point at which ice transitions from grounded to floating is known as the grounding zone. As ice crosses the grounding zone it is discharged into the floating ice shelf and the volume of this ice discharge determines the Antarctic sea level contribution.

1.2.5 The Grounding Zone

The grounding zone defines the upstream boundary of the ice shelf. The grounding line marks the point of hydrostatic floatation, though its position varies within the grounding zone. A grounding zone occurs when the ice surface gradient is low and there is a larger area where ice transitions between near floating and lightly grounded (Benn and Evans, 2014). Furthermore, with tidal flexure, the grounding line can migrate upstream within the grounding zone.

Across the grounding line there is a transition of flow regimes, from basal shear dominated where grounded to ice shelf flow is controlled by membrane stresses, the shear and horizontal normal stresses acting on the horizontal plane (see Chapter 3). This transition occurs gradually over the grounding zone, where increased till saturation of sediment exposed to the ocean during tidal flexure leads to reduced basal friction, more closely representing an ice shelf. Appropriately representing the coupling between the two different stress regimes of the ice stream and ice shelf has been a primary challenge in numerically representing Antarctic ice dynamics (Pattyn, 2018).

While a grounding zone more appropriately describes this transition, for the remainder of this thesis the term grounding line will be used. The Amundsen Sea Embayment ice streams, that are the focus of this thesis, have high surface slopes at the grounding

line and therefore a more defined transition meaning the term grounding line is more appropriate. Furthermore, the ice sheet models used in this thesis represent the grounding line as the grid cell boundary between fully floating and fully grounded grid cells which is more representative of a grounding line.

1.2.6 Antarctic Mass Balance

The mass balance of the ice sheet describes the net difference between accumulation (mass gain) and ablation (mass loss), where an ice sheet in equilibrium has a balance of the two. Changes to the mass balance of the AIS are primarily externally controlled by atmospheric and oceanic processes at the surface and base. At present, the ice sheet is out of balance, with ablation exceeding accumulation (Shepherd et al., 2018), meaning Antarctica is contributing to sea level rise.

From 1992 to 2017 the AIS contributed 7.6 ± 3.9 mm (IMBIE, 2018) to global sea level rise. From 2012 to 2017 the AIS contributed 0.56 mm yr⁻¹ (Bamber et al., 2018; Shepherd et al., 2018; Oppenheimer and Hinkel, 2019) to sea level, which is nearly four times greater than the mean contribution from 1992 to 2001. While East Antarctica is near balance (IMBIE, 2018), the observed mass loss from Antarctica is dominated by increased ice discharge into the ocean through floating ice shelves in West Antarctica (Bamber et al., 2009; Rignot et al., 2019; IMBIE, 2018; Mouginot et al., 2014; Rignot et al., 2014; Scheuchl et al., 2016; Gardner et al., 2018), resulting in increased sub-ice shelf melting and calving.

1.2.6.1 Surface Mass Balance

Surface mass balance (SMB) is the net change in mass at the surface of the ice sheet through the combined effects of accumulation in the form of snowfall balanced with surface melting, wind blown snow erosion and surface runoff. Accumulation occurs predominantly in the form of precipitation as snowfall which offsets Antarctic mass loss by 5.2 mm yr⁻¹ of global sea level equivalent at present (Wessem et al., 2018). SMB over the ice sheet is currently positive, where high rates of accumulation over East Antarctica exceed mass loss through surface melting and erosion. Estimates of SMB gain over the 20th century equate to a reduction in sea level of -7.7 mm \pm 4.0 from East Antarctica and -2.8 mm \pm 1.7 from WAIS (Medley and Thomas, 2019). However, ice core records show a decrease in AIS SMB of -2.7 ± 3.8 Gt yr⁻² mostly through

reduced SMB over East Antarctica (Medley et al., 2018). This trend contrasts with projected changes in SMB by earth system models that indicate an increase in global air temperatures will lead to increased retention of water vapour in the atmosphere leading to increased precipitation (Nowicki et al., 2020; Previdi and Polvani, 2016). Subsequently, in a scenario where global greenhouse emissions continue unabated, AIS SMB is projected to increase by up to 25 % by 2100, offsetting the future mass loss occurring through basal processes (Medley and Thomas, 2019).

At present, surface melt is confined mostly to the Antarctic Peninsula (Scambos et al., 2009; Trusel et al., 2013) and some areas of the Amundsen Sea (Donat-Magnin et al., 2020) and Ross Sea sector (Bell et al., 2017). Over the majority of the continent, rates of snowfall drastically exceed surface melt rates because any surface melt that does occur tends to refreeze within the snowpack (Munneke et al., 2014). In a warmer climate, as is expected in response to present rates of global emissions, surface melt will increase exponentially leading to higher mass loss through runoff and contributing to increased calving through hydrofracturing (Munneke et al., 2014) which can lead to ice shelf collapse (Robel and Banwell, 2019; McGrath et al., 2012). Furthermore, surface lowering through dynamic ice sheet thinning will also contribute to increased surface melting as part of the surface elevation feedback (Cuffey and Paterson, 2010). Given the role of surface melt in potentially destabilising ice shelves, SMB is an important component of ice sheet health (Donat-Magnin et al., 2021).

1.2.6.2 Basal Mass Balance

The basal mass balance of the ice sheet is determined by mass loss (ablation) in the form of ice shelf melting and calving and gain through refreezing or accretion of marine ice beneath ice shelves.

Basal Melting Sub-ice shelf basal melting is a process that scientists are still yet to fully represent at a micro-scale (Malyarenko et al., 2020), although half of Antarctic mass loss occurs through this process (Liu et al., 2015; Rignot et al., 2013a). Sub-ice shelf basal melting occurs in response to thermal forcing where ocean water that has temperature above the local freezing point makes contact with the base of an ice shelf situated in ocean water. Thermodynamic melting is therefore dependent on both the local water and ice temperatures which are influenced by ice shelf depth, the ocean salinity, the material composition and the speed of interacting water masses at the ice-

ocean boundary layer.

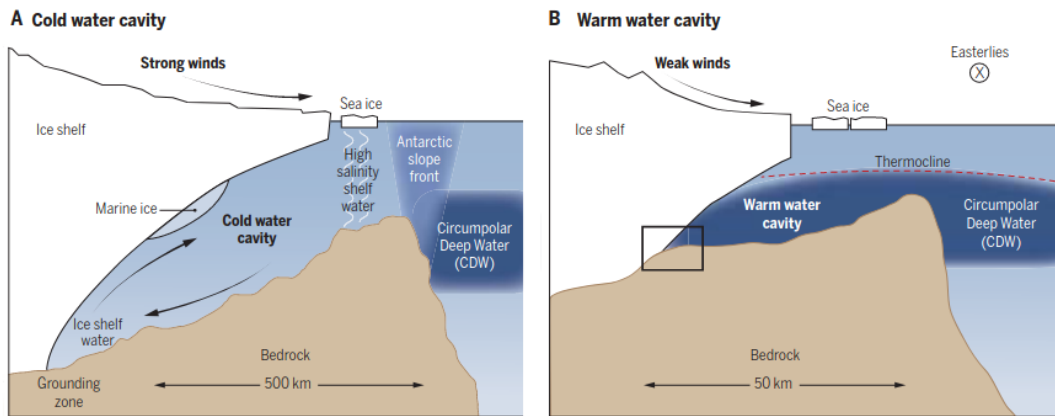


Figure 1.2: Cross-section schematic of processes in A) cold and B) warm-water ice shelf cavities. Differences between the two cavities is the connectivity of the circumpolar deep water (CDW) with the continental shelf and ice shelf. From Holland et al. (2020), Figure 2, reprinted with permission from AAAS.

Ice shelf cavities in Antarctica can be characterised as cold (fig. 1.2A) or warm-water cavities (fig. 1.2B). Cold water cavities include the Filchner-Ronne ice shelves, where Circumpolar Deep Water (CDW) is blocked from the continent by topography and a deepened thermocline which is mostly attributed to a strong Antarctic Slope Front. In such cavities, strong katabatic winds push sea ice away from the continent, permitting the formation high salinity water through brine rejection during sea ice formation. The Antarctic Slope Front and downwelling of cold saline shelf waters blocks warm water from these cavities. Melting in cold-water cavities is therefore driven by the large salinity gradient between the ice and ocean. In contrast, warm water cavities occur where warm CDW is not blocked from the ice shelf due to a shallower thermocline, the presence of deep troughs incising the shelf break leading to melting at depth; as is seen in the ASE. Cold cavities tend to be characterised by low melt rates and accretion of marine ice through refreezing, warm-water cavities experience high melt rates and little accretion. A more detailed description of processes within ASE ice shelf cavities is presented in Section 1.4.

Calving Iceberg calving occurs when englacial stresses exceed the yield strength of ice, leading to mechanical fracture causing masses of ice to detach from a glacier or ice shelf. For a marine terminating ice stream with an ice shelf, the calving front generally marks the lateral extent of an ice shelf, where the ice face meets the ocean. There are

four primary mechanisms responsible for calving (Benn and Evans, 2014) though all involve propagation of rifts or crevasses through the ice. Changes in the velocity gradients of ice drives longitudinal stress gradients which can result in ice stretching, compressing, or shearing, causing crevassing. Calving events occur when crevasses propagate through the depth of the glacier due to large tensile stresses. For ice shelves, fracture propagation can be driven by torque from buoyant forces in addition to undercutting through lateral melting at the ice face. Although mostly controlled by mechanical processes within the ice, iceberg calving can be influenced by both ocean processes through buoyancy and melting (Liu et al., 2015) and atmospheric processes such as hydrofracturing due to surface melting (Munneke et al., 2014).

1.2.7 Marine Ice Sheet Instability

A marine ice sheet is a mass of glacial ice that resides on a bedrock situated below sea level. The Marine Ice Sheet Instability (MISI; fig.1.3) principle states that marine based ice sheets are vulnerable to irreversible collapse when the grounding line rests on retrograde (downward sloping toward the interior) bed. MISI was proposed in the 1970s (Weertman, 1974; Thomas and Bentley, 1978; Thomas, 1979) and first considered analytically in one dimension in 2007 (Schoof, 2007). However, the mechanism continues to remain a focus of research and debate (Sergienko and Wingham, 2021; Pegler, 2018a,b).

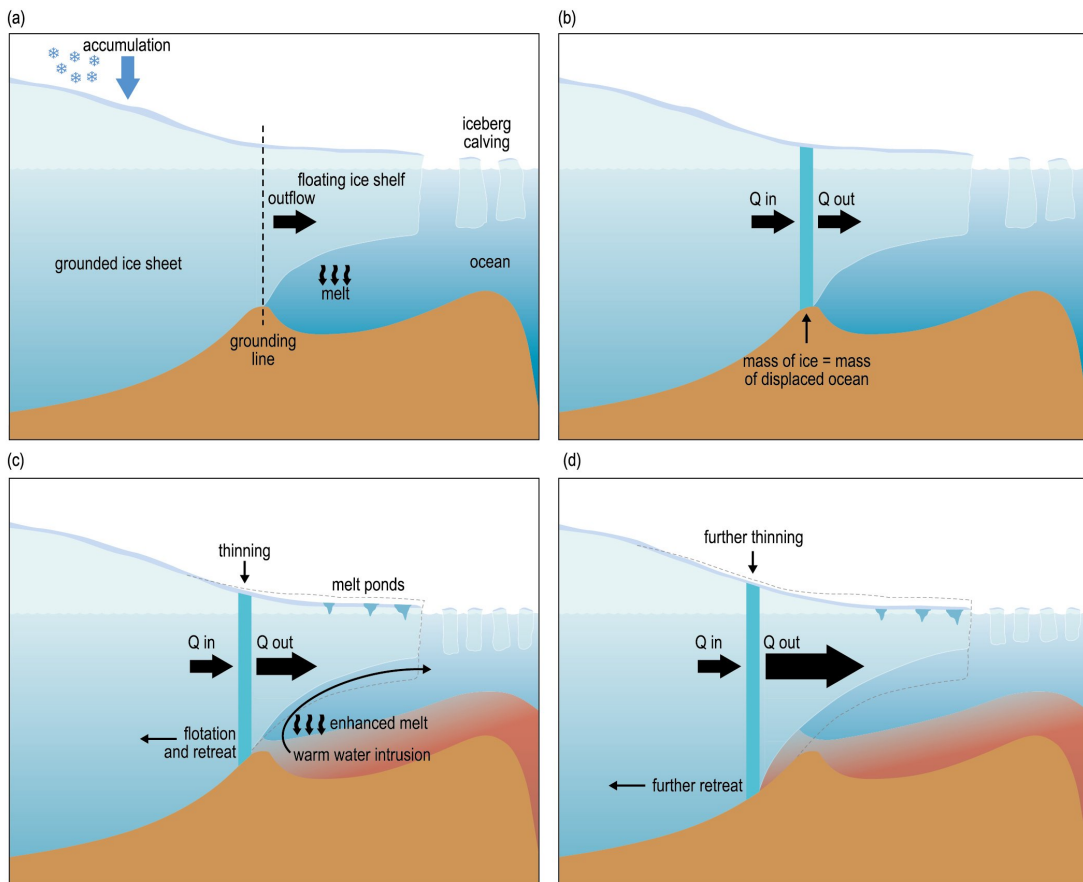


Figure 1.3: Schematic of the main processes of MISI, showing a) a marine ice sheet configuration; b) steady state grounding line position; c) increased flux across the grounding line due to climate forcings; and d) the ongoing unstable retreat of the grounding line to deeper bedrock. From Church et al. (2013), Box 13.2, Fig. 1.

Schoof (2007) demonstrated that for an idealised, laterally unvarying and therefore unbuttressed ice stream there is no stable grounding line position on retrograde (downward sloping) bed and the grounding line will retreat unabated once triggered. As the grounding line retreats onto deeper bed, the volume of ice feeding the floating ice shelf increases due to increased thickness of ice upstream. As the depth of the grounding line increases, the water column deepens and therefore larger buoyancy forces are exerted on the ice, resulting in increased ungrounding and further retreat (Pegler, 2018a).

While Weertman (1974) and Thomas and Bentley (1978) proposed initially that MISI could be stabilised only by regions of prograde or upward sloping bed, Hindmarsh (1993) stated that neutral equilibrium profiles could be reached where perturbations would push the grounding line to new steady states. Schoof's 2007 boundary layer theory demonstrated that removal of a perturbation could result in the grounding line

re-stabilising on its original position on a prograde bed. However, for a retrograde bed following the removal of forcing, grounding line positions are only stable when retreating over a section of locally prograde bed. This finding, however, was only shown in one horizontal dimension and neglected the influence of an ice shelf on the stress balance.

More recent idealized (Cornford et al., 2020; Gudmundsson, 2013) and realistic (Cornford et al., 2015) modelling simulations have shown that when using a three dimensional coupled ice stream ice shelf system that marine ice sheet instability exhibits hysteresis. The hysteresis type behaviour occurs where the retreat triggered by external forcing, such as ice shelf melting, can be reversible, with grounding line advance being possible with the removal of the forcing. Here, a laterally varying ice stream with a confined ice shelf acts to slow the rate of grounding line retreat through buttressing due to lateral and basal shearing (see section 1.2.8 Gudmundsson, 2013; Fürst et al., 2016; Pattyn, 2018).

WAIS is the worlds largest marine ice sheet, resting on bedrock that is on average 1 km below sea level (Bamber et al., 2009). West Antarctic ice streams in deep embayments such as the ASE (the ‘weak underbelly’ of WAIS; Hughes, 1981), are considered highly susceptible to the mechanism. Some modelling studies of the ASE state that MISI is currently underway for Pine Island Glacier (PIG) and Thwaites Glacier (TG; Joughin et al., 2014; Rignot et al., 2014), although more recent studies show that with an optimised model initialisation that this is not currently occurring in the region (Alevropoulos-Borrill et al., 2020) due to stabilising ridges in the bed (Morlighem et al., 2020). Instead, recent research suggests that observed rates of mass loss in the region are consistent with climate drivers rather than MISI (Gudmundsson et al., 2019; Joughin et al., 2021).

There is evidence to suggest that MISI played a role in past ice sheet collapse and ice stream retreat to present day extents. Records of global mean sea level and model inference suggest that WAIS may have collapsed during previous interglacials, even as recently as 125,000 years ago (Steig et al., 2015; Dutton et al., 2015), resulting in global sea level rise of over 5 m (Mercer, 1978). Marine micro-organisms in sediment beneath West Antarctica also supports a reduced ice sheet extent during recent interglacial periods, where ice covered areas were replaced with open ocean (Joughin and Alley, 2011). MISI is even suggested to have occurred in the ASE for individual ice

streams as recently as the 1940s, where marine sediment records indicate irreversible retreat of PIG following ungrounding from a bathymetric ridge over 40 km seaward of the current grounding line (Smith et al., 2017).

Much of the uncertainty associated with the future response of Antarctica to climate change is associated with the occurrence of MISI where rapid instability would result in a rapid growth in uncertainty (Robel et al., 2019; Nias et al., 2019). Subsequently, better understanding the timing of occurrence of MISI is an essential part of narrowing the uncertainty associated with projections of the future Antarctic contribution to sea level (Scambos et al., 2017).

1.2.8 Ice Shelf Buttressing

Ice shelves can provide some resistance to the outward flow of grounded ice upstream in a mechanism known as buttressing (fig. 1.4; Dupont and Alley, 2005). Buttressing can help to limit grounding line retreat (Gudmundsson, 2013). Buttressing occurs when an ice shelf experiences compressive, shear and transverse stress. Compressive longitudinal normal stress is generated as upstream ice flows into slower flowing parts of an ice shelf, such as areas of local grounding, which provides resistance to seaward flow. Confined ice shelves experience shear stress at the ice margins, either through lateral contact with slower flowing ice shelves or along topography where the disparity in velocity creates gradients in flow (Paterson, 1994). Furthermore, basal shear stress is generated beneath an ice shelf where the ice base makes contact with shallow topography causing local grounding. Transverse spreading or ‘hoop’ strain has been recently investigated for its role in buttressing ice streams, however, modelling experiments suggest that the damage induced from extensional stresses as a result of transverse spreading does not provide sufficient hoop stress to resist flow (Wearing et al., 2020). The magnitude of ice shelf buttressing is partly determined by the extent of ice shelf viscous deformation which depends on ice shelf geometry including both the horizontal extent and the thickness, the location and orientation (Still et al., 2019) of pinning points and the rheology and structural integrity of the ice shelf which is controlled by both temperature and damage.

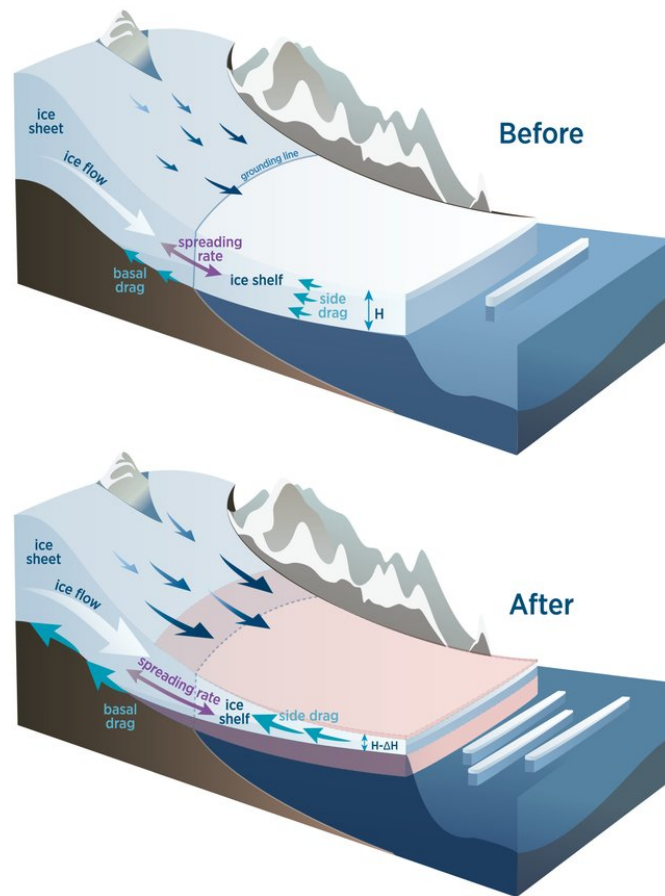


Figure 1.4: Schematic of the consequence of reduced ice shelf buttressing on ice flux. Ice shelf thinning results in increased spreading at the grounding line from increased longitudinal stress which transmits upstream. a) Before the calving event b) after the calving event and onset of ice shelf thinning resulting in increased discharge into the ocean as a result of reduced lateral drag. From Gudmundsson et al. (2019), Fig. 1

As buttressing describes the resistance of an ice shelf to outward flow, reduced buttressing results in an increase in grounding line flux (fig. 1.4; Zhang et al., 2020). Buttressing is reduced through thinning of the ice shelf which results in ungrounding of the shelf from pinning points and, for confined ice shelves, reduces the area in contact with slower flowing ice or topography at the margins resulting in reduced lateral shear stress (Reese et al., 2018b; Goldberg et al., 2018). A reduced seaward extent of an ice shelf through increased calving further reduces the area of ice providing lateral and basal shear (when previously locally grounded or ‘pinned’) and compressive longitudinal stress, leading to reduced buttressing. Furthermore, buttressing can be reduced through increased damage occurring in shear margins or total disintegration of floating parts (Wild et al., 2021).

Fürst et al. (2016) assessed ice shelves around Antarctica for their ability to buttress upstream ice and identified the ‘passive shelf ice’ regions which have minimal impact on upstream ice flow if removed or calved. To calculate the passive shelf ice, buttressing was computed as a normal force exerted by the ice shelf on upstream flow where the stress field for this was taken from an ice flow model. For an area of ice shelf to be considered passive, the ice shelf normal force must be equal to the vertically integrated hydrostatic pressure exerted by the ocean on the front of the ice shelf with the passive region removed. This ratio was used to determine the magnitude of buttressing, where the greater the disparity between the two forces means the greater the importance of the ice shelf in stabilising grounded ice upstream. The lowest ratios of passive and buttressing ice were found in ASE ice streams, demonstrating that the ice shelves in the region play an important role in regulating ice flow.

Reese et al. (2018b) performed a series of ice sheet model experiments to assess ice shelf buttressing around Antarctica through thinning a series of ice shelf grid cells of 20 x 20 km and calculating the grounding line flux in response. A buttressing flux response number, Θ_B , was calculated as $\Theta_B = R/P$ where R is the increase in annual mass flux and P is the ice shelf mass. They found the strongest response in ice flux to be a result of thinning immediately downstream of the grounding line, although this differed between ice streams. This is somewhat consistent with Fürst et al. (2016) who found most passive regions of ice to be at the ice front. Although this does not stand for larger ice shelves such as the Ross and Filchner-Ronne where their stability is more complex.

Ice shelf buttressing can be influenced by sea ice and the presence of an ice mélange. An ice mélange is a dense lattice of calved shelf ice that can form a rigid barrier to outward flow, exerting hydrostatic pressure on the front of a calving front. Massom et al. (2018) showed with both observations and modelling that the loss of sea ice from areas adjacent to Larsen A and B resulted in the ice shelves being exposed to enhanced flexure by storm cells which accelerated disintegration. Ice mélange strength is also influenced by sea ice. Although not a mechanical impact on buttressing, loss of sea ice from the front of ice shelves exposes the ocean surface to radiative forcing which can raise melt rates beneath ice shelves (Stewart et al., 2019).

1.2.9 Topographic Controls

1.2.9.1 Bed Slope

Topography plays an important role in determining the occurrence and extent of MISI. Firstly, the underlying directional slope of the bed determines whether or not the grounding line will retreat over retrograde or prograde bed. Secondly, the presence of features in the bed act to resist and in some cases pin the grounding lines of ice streams (Seroussi et al., 2017), delaying grounding line retreat. Castleman et al. (2021) used a mass conserving bed topography and ice thickness product to explore the migration of the grounding line of Thwaites Glacier TG in the ASE and found that the location and amplitude of bed features have a greater role in dictating grounding line retreat than the sharpness and shape of the feature.

Bed topography has impacts not only for grounded ice but also ice shelves through the local grounding at pinning points. Still et al. (2019) performed an analysis of pinning points over the Ross Ice Shelf and determined that there is no clear relationship between the effective resistance provided by a pinning point and the elevation or area of the pinning points. Instead, Still et al. (2019) found the shape of features to be more important. This finding was also supported by Wild et al. (2021) in the investigation of the role of the eastern TG pinning point.

1.2.9.2 Basal Drag

Lateral shearing or drag at the bed regulates the velocity of ice streams, where basal motion is a function of the friction at the bed and the effective pressure as determined by the thickness of ice and the saturation of water in the subglacial sediment (Cuffey and Paterson, 2010). A soft deformable rheology is considered a prerequisite for fast flow exhibited by ice streams (Bougamont et al., 2014; Anandakrishnan et al., 1998, 2007). While Alley et al. (2007) found increased sediment contact with the base of the ice can lead to increased friction, an increase in the volume of basal meltwater lubricates the ice allowing for accelerated flow (Stearns et al., 2008). The porosity of the sediment material also plays a role, where high porosity leads to weaker sediment that is more easily deformed and therefore less resistive to flow (Brisbourne et al., 2017).

1.3 The Amundsen Sea Embayment (ASE) Ice Streams

The ASE holds the equivalent volume of ice to raise global sea levels by 1.2 m and is dominating records of observed Antarctic mass loss (IMBIE, 2018). Approximately 20 % of the mass of WAIS drains into the ASE through a series of marine terminating ice streams, the largest of which being PIG (Pine Island Glacier) and TG (Thwaites Glacier) in the east of the sector. A group of smaller ice streams, Haynes, Pope, Smith and Kohler Glaciers (PSK) situated in the west feed the Crosson and Dotson ice shelves. The region has experienced a 77 % increase in ice flux across the grounding line since 1973 (Mouginot et al., 2014) which has coincided with catchment-wide thinning and acceleration. The ASE is exposed to warm, saline water that causes melt rates of an order of magnitude greater than elsewhere in the continent (Jacobs et al., 1996), which is responsible for driving observed rapid acceleration, thinning and mass loss (Schodlok et al., 2012; Dutrieux et al., 2013; De Rydt et al., 2014).

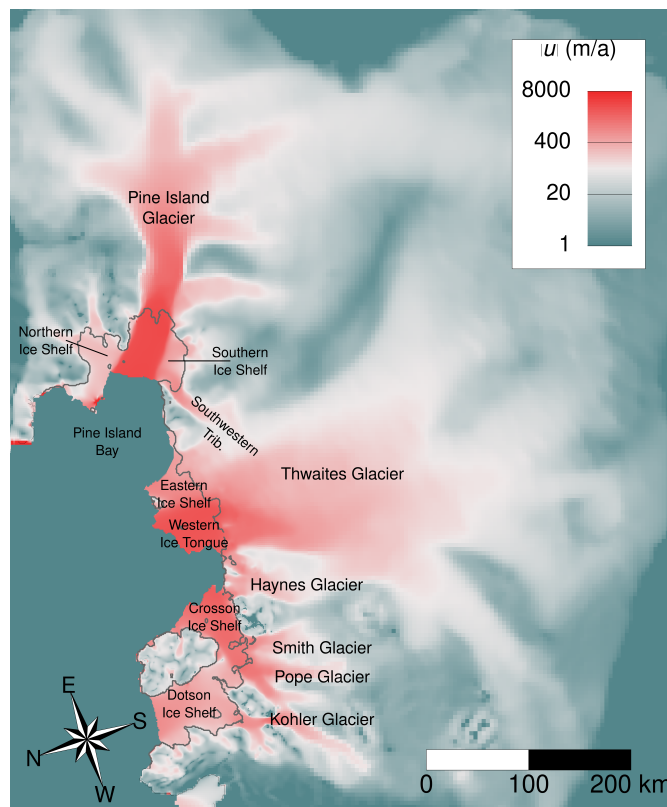


Figure 1.5: Map of Amundsen Sea Embayment domain with background initial velocity field (m yr^{-1}) and initial grounding line position from 1996 (Rignot et al., 2011) in black. Ice streams, ice shelves and tributaries discussed in this chapter are labelled.

1.3.1 Pine Island Glacier

PIG is the single largest contributor to Antarctic sea level rise over the observational period (Shepherd et al., 2018), with present ice loss contributing 0.1-0.15 mm yr⁻¹ to global sea level rise (Bamber et al., 2018) making up 20 % of present day WAIS mass loss. PIG has the potential to contribute 51 cm to global sea level rise (IMBIE, 2018; Morlighem et al., 2020). Payne et al. (2004) first postulated that the cause of velocity changes observed over the ice stream from 1974 to 2000 were dynamic responses to ice shelf thinning forced by ocean induced melting. This since has been agreed upon widely in the literature (Pritchard et al., 2012), where the ice shelf experiences some of the highest melt rates of all Antarctic ice shelves (Shean et al., 2019; Adusumilli et al., 2020) and periods of increased continental shelf ocean temperatures coincide with intermittent phases of high melt, heterogeneous acceleration and retreat (Mouginot et al., 2014; Turner et al., 2017).

In the 1940s, unpinning from a submarine ridge 40 km in advance of its present grounding line triggered rapid retreat replicating MISI type behaviour (Smith et al., 2017; Favier et al., 2014). Since the 1990s, satellite observations have documented sustained increased discharge across the grounding line (Rignot and Jacobs, 2002; Rignot et al., 2011; Mouginot et al., 2014, 2019). Between 1996 and 2009 the grounding line retreated 20 km (Joughin et al., 2010) coinciding with ice shelf acceleration from 1973 to 2013 from 2.3 km yr⁻¹ to 4.0 km yr⁻¹ (Mouginot et al., 2014). However, it appears that the period of acceleration has begun to slow, perhaps showing the ice stream is more stable than previously considered (Konrad et al., 2018; Bamber and Dawson, 2020).

The ice stream feeds a large ice shelf, with a width of 25 km and a length of almost 100 km. The ice stream trunk is fed by nine tributaries that merge 175 km upstream from the grounding line. At the grounding line the ice thickness reaches 1.5 km which decreases with increased distance from the grounding line, reaching 300-400 m at the ice front. The shelf is made up of a fast flowing centre, with a velocity of 4 km yr⁻¹ separated from both a Northern and Southern ice shelf by shear margins, where the two peripheral shelves flow more slowly than the centre (0.1 - 0.5 km yr⁻¹) (Shean et al., 2019). There is a tributary feeding the Southern PIG ice shelf from the Southwest which MacGregor et al. (2012) identifies as the 'Southwestern Tributary' of PIG, however, ice here is discharged from PIG's neighbour, TG. To maintain consistency we continue to

use this name but acknowledge that it could be more appropriate to label the tributary as part of TG.

As PIG has a topographically confined ice shelf, it provides high buttressing forces that resist flow (Fürst et al., 2016; Reese et al., 2018b) and provides stability given that the ice stream is grounded on retrograde bed. As buttressing regulates upstream ice flow, the dynamics of grounded ice upstream are highly sensitive to sub-shelf melt induced thinning (Shean, 2016). Thinning leads to local ice shelf ungrounding (unpinning) from topographic highs, places of higher basal shear stress, which have been identified beneath the ice shelf (Davies et al., 2017). Therefore, ice shelf thinning and ungrounding is expected to impact future flow (Fürst et al., 2016).

While sub-ice shelf basal melting is a dominant control on upstream ice dynamics, more recent investigations have emphasised the importance of appropriately capturing changes to other ice processes and properties in order to better understand the behaviour of ice flow of the glacier. Observed changes in the last two decades such as thinning of the trunk (Bamber and Dawson, 2020), grounding line retreat at irregular intervals (Rignot et al., 2014), and changes in the position of the ice front (Arndt et al., 2018) are all factors responsible for changes in ice dynamics and acceleration. Furthermore, observed mechanical fracture of ice along the shear margins (Sun et al., 2017; Lhermitte et al., 2020) in addition to partial loss of the integrity of the ice shelf (Alley et al., 2019) have been shown to influence the buttressing ability of the shelf and therefore modify overall ice flow. Representing the future evolution of the ice stream is therefore complex.

1.3.2 Thwaites Glacier

TG could control the stability of WAIS (Scambos et al., 2017; Feldmann and Levermann, 2015). The wide ice stream holds the ice volume equivalent to raise global sea level by 65 cm (IMBIE, 2018; Morlighem et al., 2020). Observations have shown thinning upstream of the grounding line currently occurs at a rate in excess of 1 m yr^{-1} over the entire catchment which is a product of the dynamic response to a velocity increase of 100 m yr^{-1} (Milillo et al., 2019; McMillan et al., 2014). TG currently contributes almost 0.1 mm yr^{-1} to sea level, which has doubled since the 1990s (Rignot, 2008; Medley et al., 2014). Due to its observed high rates of mass loss and potential for future collapse, the ice stream is among the most studied in the world (Scambos et al., 2017).

Better understanding how the ice stream is evolving and identifying the causes of observed changes will supplement the understanding of the stability of the ice stream so that future projections can be constrained.

TG has a wide, unconfined ice shelf that can be separated into two counterparts with differing behaviour. The floating ice tongue in the west is 50 km wide and flows at 4 km yr⁻¹ (Tinto and Bell, 2011). In contrast, the eastern ice shelf flows at approximately 0.8 km yr⁻¹ which is slowed due to the presence of two bathymetric pinning points that induce ice shelf crumpling and enhance the buttressing effect of the ice shelf. While it has been suggested that the TG western ice tongue has provided some stability for the eastern ice shelf and upstream flow (Wild et al., 2021), Fürst et al. (2016) found much of the ice tongue to be considered passive ice shelf meaning its removal would have little influence on upstream ice flow.

Following 14 years of steady ice velocity, acceleration in ice flow occurred in 2006 along the main trunk of the TG. By 2013 ice flux increased by 33 % which coincided with a 1 km yr⁻¹ increase in velocity at the grounding line (Mouginot et al., 2014). From 1996 to 2011 the grounding line of TG retreated upstream along retrograde bedrock by up to 18 km (Rignot et al., 2014) and retreated a further 3.2 km along the western trunk by 2017 (Milillo et al., 2019). Although this position is hard to determine exactly due to its considerable variability, with tidally induced ungrounding of up to 2.5 km (Miles et al., 2020). In part due to these tidal oscillations, from 2014 a new cavity opened upstream of the observed grounding line, thinning from beneath (Milillo et al., 2019). However, Bevan et al. (2021) has found this new cavity has not expanded beyond 2017 as thinning rates are matched by the delivery of upstream ice through advection.

Changes to the velocity and grounding line over the last 20 years have been driven by changes to the ice shelf. Following the retreat of the ice front to 80 km upstream from its 2000 position, the TG western ice tongue has rapidly disaggregated (Miles et al., 2020). Structural weakening of the ice tongue over this period coincides with rapid acceleration of ice at the grounding line of TG. The eastern ice shelf and western ice tongue decoupled in 2009 (Tinto and Bell, 2011) which was followed by a large calving event in 2012. From 2006 to 2012 the ice shelf developed a series of rifts and fractures on the ice tongue in the shear zone between the eastern ice shelf and western ice tongue approximately 30 km downstream from the grounding line (Miles et al., 2020). From 2016 to 2018 a series of acceleration and deceleration events resulted in

large rifts opening in the southern shear zone between the eastern and western parts. This acceleration and deceleration has been shown to coincide with periods of ocean warming and cooling indicating that this has been the trigger of the structural weakening and acceleration of the TG ice shelf (Miles et al., 2020).

Recent research has focused on the role of the pinning point at the calving front of TG eastern ice shelf in stabilising the flow of the glacier (Alley et al., 2021; Wild et al., 2021). Jordan et al. (2020) identified that the height of the seafloor ridge acting to pin the ice shelf is -498 m though the average height above floatation of the ice grounded on this ridge is only ~ 8 m meaning modest thinning rates could unpin the ice shelf from this ridge (Wild et al., 2021). Radar measurements have shown that the eastern ice shelf thinned by up to 33% from 1978 to 2008 (Schroeder et al., 2019). Wild et al. (2021) state that should present rates of thinning of the eastern ice shelf continue, the ice shelf will unpin in less than a decade causing increased discharge of 10 %. The longer term implications of this unpinning are yet to be determined but could have extreme consequences.

1.3.3 Pope Smith and Kohler Glaciers

Although PIG and TG receive more scientific attention, Pope, Smith and Kohler, PSK, the smallest ice streams in the ASE, have undergone periods of mass loss exceeding that of their larger neighbours, comprising 23 % of ASE mass loss (Mouginot et al., 2014). While the ice stream catchment contains a mere 6 cm of sea level equivalent (Fretwell et al., 2013), it shares an ice divide with TG and therefore has the potential to drain mass from its neighbour through these smaller ice streams. Ice sheet modelling studies have suggested that continued retreat over the next few decades is likely (Goldberg et al., 2015; Scheuchl et al., 2016) and persistent present day climate could lead to continued retreat over the 21st century (Lilien et al., 2019).

At the peak of observed changes, between 2003 to 2008, PSK thinned at 9 m yr^{-1} upstream of their grounding lines (Pritchard et al., 2009). Furthermore, following a period of heightened thinning and acceleration, the grounding lines retreated by up to 35 km between 1996 and 2011 (Rignot et al., 2014).

PSK ice streams feed the adjacent Dotson and Crosson ice shelves. Crosson Ice Shelf is the easternmost of the two and fed by Pope Glacier and an eastern branch of Smith Glacier, whilst Dotson ice shelf to the west is fed by western Smith and Kohler

Glaciers. Observations from 1992 to 2011 found Smith Glacier to be experiencing the greatest ongoing grounding line retreat at a rate of 2 km yr^{-1} , totalling 40 km of retreat since 1996 (Scheuchl et al., 2016). Pope Glacier experienced 11 km of grounding line retreat at a slower rate of 0.5 km yr^{-1} . Further, Dotson and Crosson thinned by 18 and 10 % respectively from 1994 to 2011. Thinning over this period led to unpinning from a number of locations resulting in reduced buttressing and ice shelf weakening (Scheuchl et al., 2016). Observed thinning rates are a product of both acceleration and sub shelf melting, where the latter is considered presently unsustainable with the potential to thin the Dotson ice shelf completely in the next 50 years (Gourmelen et al., 2017).

While studies have suggested the configuration of PSK in the 1990s was inherently unstable due to the rapid grounding line retreat and thinning that occurred in the years following, Lilien et al. (2019) performed a series of ice sheet model simulations showing that observed changes were driven by elevated melting. In performing simulations forced with small perturbations, observed retreat was not initiated, suggesting a larger driver of retreat was necessary to cause the observed changes. These modest projections indicate a sea level contribution of 6 mm, likely underestimating future mass loss given that the simulations did not capture the full extent of observed retreat as has occurred in reality.

1.4 Amundsen Sea Oceanography

Composite analysis of observational records of mass change over the Antarctic continent from 1979 to 2017 has shown that mass loss occurs in regions where warm CDW has access to the continental shelf and the grounding lines of marine terminating glaciers (Dinniman et al., 2016; Rignot et al., 2019). The warm water reaches up to 4°C above the in situ freezing point, with a salinity of 34.6 psu (Turner et al., 2017) and therefore has high potential for melting ice shelves. CDW originates in the Antarctic Circumpolar Current (ACC) which lies off continent. Around WAIS, the ACC is in close proximity to the continental shelf specifically near the Amundsen and Bellingshausen Seas. Around much of the continent, CDW is blocked from the ice sheet due to a depressed thermocline (between 300 and 700 m) caused by the presence of cold surface waters (Schmidtko et al., 2014; Jenkins et al., 2016; Assmann et al., 2013). In the ASE the continental shelf break at 500-600m depth acts as a barrier to onshore flow of deep water (Arneborg et al., 2012; Wåhlin et al., 2013; Walker et al., 2013). How-

ever, dendritic troughs intersect the shelf break provide deeper access points for CDW (Nitsche et al., 2007).

Once driven toward the continental shelf break by circumpolar westerly winds (Thoma et al., 2008), CDW upwells onto the shelf and is routed toward the grounding line of the ice streams through these bathymetric troughs (Nitsche et al., 2007). CDW mostly flows through the troughs that intersect the continental shelf break at 113 °W and 102-108 °W in Pine Island Bay (Walker et al., 2013) and is directed toward the ice streams. Measurements of on shelf flow in the western branch of the trough has shown 0.2-0.4 sverdrup of CDW travelling toward the ice sheet (Walker et al., 2007). Once it is on the continental shelf, CDW is modified through mixing with cooler fresher shelf water. The thickness of the modified CDW (mCDW) layer that surpasses the topographic barrier of the continental shelf determines the heat supply to the grounding line meaning the variability of thermocline depth determines the heat available for basal melting of ice shelves (Davis et al., 2018; De Rydt et al., 2014; Dutrieux et al., 2014a).

There remains debate as to what processes are responsible for increased CDW upwelling in the ASE. Most studies agree that wind forced mechanisms are responsible (Dinniman et al., 2015, 2016; Thoma et al., 2008). With a temporally high resolution dataset, Davis et al. (2018) showed that surface heat flux anomalies (Webber et al., 2017) are inconsistent with the observed temporal variability in the heat content in Pine Island Bay through thermocline depth and subsequent basal melt rates. Instead, they find a positive correlation between the strength of vertical Ekman velocity (Kim et al., 2017) and basal melt rates, where the former explains 74 % of the monthly variability in the latter (Davis et al., 2018). That being said, while this relationship is valid for short term variability, the long term influence is yet to be determined, with additional processes such as shelf edge winds (Wåhlin et al., 2013), heat fluxes, sea ice extent changes and teleconnections and large scale climate variability driven by features including El Niño/Southern Oscillation and the Southern Annular Mode (Paolo et al., 2018; Jenkins et al., 2018).

Thermocline height varies seasonally and inter-annually in the ASE, where the mCDW layer is deeper, more saline and warmer in winter compared with summer (Mallett et al., 2018). A landward upward tilting of the thermocline between 1994 and 2009 has resulted in an increase in the thickness of CDW layer accessing the continental shelf, meaning an increased heat content of mCDW and higher basal melt rates (Jacobs

et al., 2011). This event was followed by a reduction in basal melting as a result of a cooling driven by thermocline depressing between 2010 and 2012 (Dutrieux et al., 2014b).

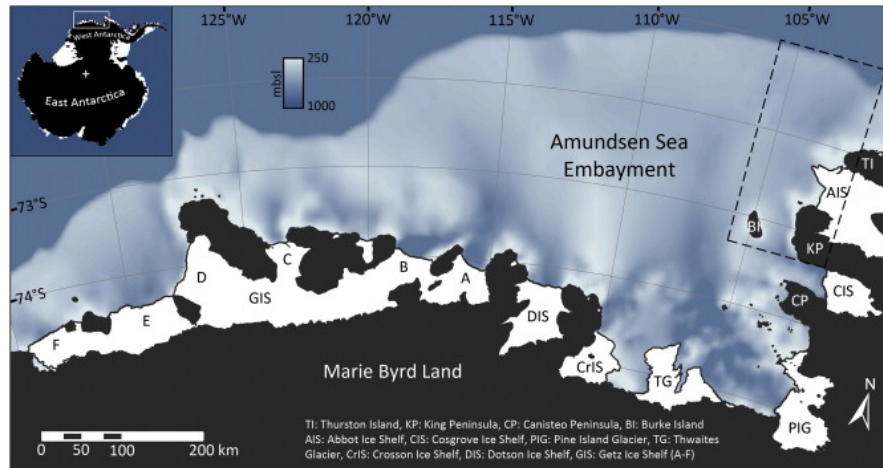


Figure 1.6: Bathymetry of the Amundsen Sea and Marie Byrd Land continental shelf with location marked on map of Antarctica. From Klages et al. (2015), Fig. 1.

El Niño/Southern Oscillation is the strongest inter-annual climate fluctuation influencing the globe, and is responsible for observed climatological variability in the Amundsen Sea. El Niño/Southern Oscillation has been associated with changes in snowfall, air temperature, sea ice extent and delivery of CDW into Pine Island Bay (Paolo et al., 2018). The Southern Annular Mode influences Southern Ocean climatology, in addition to modifying the effect of El Niño/Southern Oscillation. A positive Southern Annular Mode phase (high pressure over Antarctica) combined with la Niña and a negative Southern Annular Mode phase combined with El Niño result in a strengthening of Antarctic atmospheric anomalies, particularly in the Pacific Sector of the Southern Ocean. El Niño alone drives enhanced circumpolar westerly strength causing increased basal melting through the increased delivery of CDW to the continental shelf (Paolo et al., 2018).

Although the observational record of ocean properties in the Amundsen Sea is temporally limited due to the presence of sea ice and therefore inaccessibility of the region (Mallett et al., 2018), the limited measurements that have been taken suggest that the Amundsen Sea deep ocean has warmed by 0.2 °C per decade since the 1990s (Schmidtke et al., 2014). Furthermore, Nakayama et al. (2018) find CDW to have warmed off-shelf by 0.2 °C between the periods 2001-2006 and 2009-2014 where off-

shore warming is controlled by large scale ocean circulation processes and more specifically the strength of the Ross Gyre. However, more recent work has shown there to be less of a clear trend due to the large variability in ocean temperatures in the region forced by teleconnections with the tropical Pacific and other large scale climatological variability such as El Niño/Southern Oscillation and the Southern Annular Mode (Jenkins et al., 2016).

Climate model simulations demonstrate that the decadal scale variability from the Pacific acts as an anomaly superimposed on a longer term trend of a poleward shift in circumpolar westerlies (Holland et al., 2019). However, historical oceanographic observations in the ASE are lacking, with observations only being available since 1994 (Jacobs et al., 1996). As is consistent with the climate model simulations, the eastward zonal wind trend results in a warming at mid depth of $0.33\text{ }^{\circ}\text{C}$ per century in addition to a 0.021 psu per century salinification which coincides with a 47% increase in ice shelf melting (Naughten et al., 2022). During this period, a strengthening of horizontal heat transport across the shelf as an undercurrent coincides with a strengthening in circumpolar westerlies at the shelf break (Naughten et al., 2022). Although observations of recent decades suggested no clear trend in ASE ocean temperature due to oscillations from the Pacific, Naughten et al. (2022) confirmed a historical trend of increased CDW delivery to the ASE as a result of strengthening winds which supports the theory that anthropogenic climate change will result in increased mass loss from ASE ice streams (Bracegirdle et al., 2013; Goyal et al., 2021). With evidence of a warming trend since the 1920s, it is supported that this is likely to continue overall, combined with the effects of Pacific oscillations which will likely contribute to fluctuations in warming events in the region (Jenkins et al., 2016; Holland et al., 2019; Naughten et al., 2022).

1.5 Amundsen Sea Sub-Ice Shelf Basal Melting

Observational records demonstrate that the grounding lines in the ASE have retreated since the 1970s (Konrad et al., 2018) driven by high sub-ice shelf melt rates (Pritchard et al., 2012; Khazendar et al., 2016) of $100\text{-}120\text{ Gt yr}^{-1}$ of freshwater equivalent (Medley et al., 2014). Basal melting at the grounding line of glaciers alters the stress balance (Waibel et al., 2018), where localised changes at the grounding line propagate upstream, perturbing the state of the ice stream (Payne et al., 2007). Ocean forced melt induced thinning at the grounding line results in a local surface draw-down around the

grounding line, causing an increased gradient in surface slope and therefore greater gravitational driving stress; a process that influences upstream ice (Payne et al., 2004). Furthermore, reduced buttressing through ocean forced thinning of confined ice shelves through melting drives ice stream acceleration and grounding line retreat. Basal melting is the primary control on present and future ASE mass loss and will be the trigger of instability in the region.

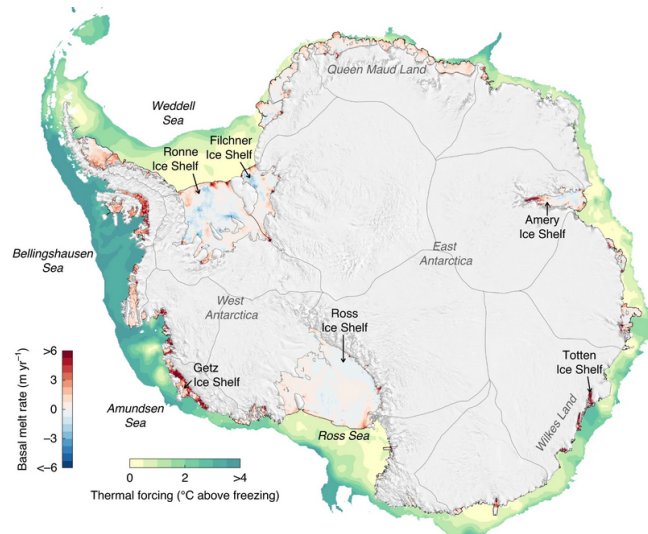


Figure 1.7: Map of Antarctic ice shelf melt rates and potential temperature (thermal forcing) averaged over 2010-2018 over the continental shelf. From Adusumilli et al. (2020), Figure 1.

In warm-water cavities such as the ASE, basal melting occurs as part of a feedback (Holland et al., 2020). Intense melting at the base where the ice is in contact with warm, saline mCDW drives the production of cold fresh meltwater which is more buoyant than the mCDW at depth. Buoyant meltwater rises along the curved base of the ice shelf, causing a stronger circulation with higher turbulence meaning more CDW is drawn toward the base of the ice shelf (Lazeroms et al., 2018). Given the presence of CDW on the shelf, there is little to no marine ice formed on the base of ice shelves toward the terminus given that in-situ temperatures are above freezing (Holland et al., 2020).

Observations of basal melt rates in the ASE are necessary for use in validating ocean models and forcing ice sheet models (Holland et al., 2020). Net melt rates beneath ice shelves can be estimated with a variety of techniques such as in situ glaciological observations (Rignot and Jacobs, 2002) and satellite data (Depoorter et al., 2013; Rignot et al., 2013a). Ground based observations of basal melting of ASE ice shelves are

limited due to the challenges in obtaining oceanographic measurements in the region (Mallett et al., 2018). Satellite measurements of ice shelf surface changes can be used to calculate basal melt rates by accounting for the flux divergence with mass conservation (Rignot et al., 2013a). Alternatively, high resolution cavity resolving ocean models can be used to reconstruct basal melt rates beneath individual ice shelves (Holland et al., 2009, 2010; Schodlok et al., 2012; Hellmer et al., 2012). Bernales et al. (2017) combined ice sheet modelling with output from climate models to develop a basal melt field for all Antarctic ice shelves and found the results were similar to satellite derived estimates. Recently a suite of detailed melt rate datasets have been published (Adusumilli et al., 2020; Das et al., 2020; Hirano et al., 2020).

Given the control of basal melting on present day mass loss in the ASE, it is important that the processes driving basal melting be understood but the lack of in situ measurements of the ice-ocean boundary layer (Wählin et al., 2020; Dinniman et al., 2016) makes this challenging. Uncertainties in the bathymetric datasets of both ice geometry and bathymetry make it difficult to appropriately model processes occurring within ice shelf cavities (Goldberg et al., 2018, 2019). Furthermore, differences exist in the coefficients for the equations that describe basal melting, resulting in vast uncertainty in melt rate output from ocean models (Malyarenko et al., 2020).

1.6 Future Simulations of the Amundsen Sea Embayment

1.6.1 Future Climate

The Intergovernmental Panel on Climate Change (IPCC) adopted a series of future scenarios for atmosphere ocean general circulation models (AOGCM) to capture the evolution of global climate in response to current and future estimated greenhouse gas emissions. The Representative Concentration Pathways (RCP) and Shared Socioeconomic Pathways (SSPs) provide different trajectories of climate change based on an estimate of future socioeconomic changes as well as changes in radiative forcing as a result of the greenhouse effect arising from increased emissions. The Coupled Model Intercomparison Project 5 (CMIP5) (Taylor et al., 2012) was performed whereby AOGCM groups all over the world have performed the same experiments to explore the response

of the climate system to scenarios of changed radiative forcing over the 21st century. The updated CMIP6 experiments include both RCPs and SSPs in addition to extended simulations until 2300.

Observations have shown that the strength of the Southern Annular Mode has increased over the last century, where the phase has become more positive resulting in a southward migration and strengthening of circumpolar westerlies (Thompson and Solomon, 2002) which has led to increased CDW delivery to the ASE (Naughten et al., 2022). Ozone depletion over Antarctica and an increase in greenhouse emissions are shown to intensify the positive Southern Annular Mode phase (Arblaster and Meehl, 2006; Arblaster et al., 2011), suggesting that if current emissions continue then a long term trend of a strengthening of this climatology is expected (Thompson and Solomon, 2002; Gillett et al., 2013; Bracegirdle et al., 2013). A southward shift in circumpolar westerlies will drive the ACC closer to the coast in the ASE and projected weakening of the Amundsen Sea Low will encourage CDW to upwell onto the shelf (Raphael et al., 2016), causing increased thermal forcing of ASE ice shelves.

Projecting basal melt rates beneath ice shelves in the ASE is challenging. AOGCM such as those involved in CMIP5/6 have a coarse resolution that is unable to capture eddies responsible for CDW upwelling in the ASE, furthermore, these models do not resolve ice shelves and therefore do not simulate sub-ice shelf processes (Jourdain et al., 2020). Bracegirdle et al. (2013) also found that several CMIP5 AOGCMs have an equatorward bias in the position of the ACC leading to cold biases in the ASE (Naughten et al., 2018b). While high resolution cavity resolving ocean models can be used to directly project basal melt rates, the theoretical understanding of ice shelf processes is limited by a lack of observations due to the inaccessibility of ice shelf cavities with modern observational methods (Mallett et al., 2018; Wåhlin et al., 2020) and gaps in the representation of processes in ocean models (Malyarenko et al., 2020), meaning exacerbated uncertainty when considering the translation of projected future ocean properties and subsequent projected melt rates. That being said, existing cavity resolving ocean model projections project increasing melt rates in the ASE (Donat-Magnin et al., 2017; Naughten et al., 2018b; Jourdain et al., 2017).

Donat-Magnin et al. (2017) explore the role of pole-ward migration of winds in altering ocean circulation and properties in the Amundsen Sea over the 21st century using a cavity resolving ocean model. They found a 6% and 21% increase in melting

beneath PIG and TG respectively due to changing winds. However, Donat-Magnin et al. (2017) show that when accounting for ice shelf cavity evolution by incorporating an offline, asynchronous coupling with an ice sheet model, that ice shelf basal melt rates increase by 2.5 due to retreating grounding lines and increased overturning circulation within ice shelf cavities. This highlights that ice-ocean interactions and representation of such is an important component of projecting the future evolution of the ASE.

With a warming atmosphere in response to increased emissions, Antarctica is expected to receive increased snowfall due to the increased ability of the atmosphere to hold moisture (Medley and Thomas, 2019). Model simulations show for an RCP8.5 scenario, AIS SMB could increase by 13 to 25 % by 2100 (Lenaerts et al., 2016; Agosta et al., 2013; Palerme et al., 2017). This increased precipitation will offset mass loss through increased surface melt which is also projected in response to increased surface temperatures (Donat-Magnin et al., 2021). However, given that accumulation through precipitation occurs over longer timescales, this expected to be insufficient to offset the fast paced mass loss through basal and surface melt Donat-Magnin et al. (2021); Holland et al. (2020).

1.6.2 Future Ice Evolution

Given their vulnerability to unabated retreat and mass loss, future projections of the ASE are a focus of modelling investigations. The strongest controlling mechanisms for past and future evolution include the evolution of sub-ice shelf melting (Robel and Banwell, 2019), the control of topography on retreat (Castleman et al., 2021; Wernecke et al., 2022; Schlegel et al., 2018; Waibel et al., 2018), and changes to ice shelf properties in the form of mechanical damage and calving events (De Rydt et al., 2021; Lhermitte et al., 2020; Joughin et al., 2021). As there are large uncertainties associated with the evolution of ocean circulation and properties within ASE ice shelf cavities, observations of the bed and numerical representation of dynamic ice evolution, future projections of the region often differ. Here, a select few investigations are presented that incorporate both the modelled response of the ASE ice streams to future climate and of the role of internal ice sheet model uncertainty in diverging projections.

Cornford et al. (2015) performed simulations of the future evolution of WAIS in response to climate forcing associated with CMIP3 emissions scenarios. They forced the ice sheet model BISICLES with seven sets of projected accumulation anomalies

and eight sets of ocean forced ice shelf melt anomalies from published atmosphere and ocean modelling investigations for up to 200 years. Ocean model projections used to parameterize ice shelf melting exhibited increases in shelf wide melting of up to 20 m yr⁻¹ by 2100. The results from Cornford et al. (2015) projected a mass loss equivalent to 15-40 mm of global mean sea level rise from the ASE by 2100. The trajectory of mass loss was found to be dominated by the timing and extent of retreat of TG.

Nias et al. (2019) explored the projected evolution of the ASE in response to ocean forced increases in sub-ice shelf melting of up to 20 m yr⁻¹ at the grounding line, while accounting for uncertainty in the model initialisation. They found an upper end (95% confidence interval) 100 year future sea level contribution of 123 mm, with a median estimate of 56 mm. Furthermore, Nias et al. (2019) found parameter uncertainty amplified the linearity of the response of the mass loss to ocean forced melting, which coincided with the extent of grounding line retreat given that a lengthening of grounding line increased both the size of the flux gate and the thickness of ice at the grounding line. The long upper tail of the mass loss distribution was consistent with Robel et al. (2019), where simulations with more extreme rates of grounding line retreat due to the instability of retrograde beds resulted in the largest mass loss.

Castleman et al. (2021) and Wernecke et al. (2022) explored the interplay between future climate evolution and uncertainty in the representation of bedrock topography in the ASE. Castleman et al. (2021) found a bimodal distribution of future sea level contribution ranged between 40 to 210 mm from the TG basin over 200 years from simulations of statistically perturbed bed topographies forced with perturbed sub-ice shelf melt forcings. A similar investigation performed by Wernecke et al. (2022) for a model domain of PIG found the uncertainty in the bed topography of one standard deviation can lead to uncertainty in projected mass loss from the ice stream of up to 5 mm of global sea level equivalent. In response to a high climate forcing, the mean mass loss from PIG is 19 mm by 2100 (Wernecke et al., 2022).

Schlegel et al. (2018) explored uncertainty in the projected evolution of Antarctica in response to climate perturbation. They performed simulations with alternative bed topographies, ice shelf collapse, and perturbations of climate forcing, basal friction and ice viscosity. The ASE was found to dominate the uncertainty in future sea level rise from Antarctica, making up 89% of quantified uncertainty and accounting for 47% of the mean mass lost from the continent which ranged from -16 mm to 99 mm over 100

years.

Alevropoulos-Borrill et al. (2020) forced a regional ASE domain with six parameterizations of RCP8.5 forced ice shelf basal melt rates from high performing CMIP5 models. With an optimised initial model domain, 21st century mass loss from the region was projected to be between 20 to 45 mm where ice discharge was positively related to increased melting. Furthermore, when accounting for uncertainty in the initialisation procedure, the range in mass loss increased to -0.2 mm to 121 mm where modifications to ice sheet model parameters increased the sensitivity of ice streams to melting. Their study reinforced the importance of considering both uncertainty in ice sheet model initialisation and climate forcing when performing projections of future ice sheet evolution given the interplay between the two features.

Differences in models, model set-up and the ranges of uncertainty explored within model based investigations results in a wide range in the projected evolution of the ASE and Antarctica as a whole. Narrowing this uncertainty will be important for constraining sea level rise estimates. What most investigations do agree on, however, is that mass loss from the ASE is expected to increase in the future in response to a changing climate.

1.7 Summary

Future mass loss from Antarctica is the most uncertain component of the sea level rise budget. The ice sheet is currently in a state of disequilibrium, where dynamic mass loss exceeds ice sheet growth. Unstable retreat and the potential collapse of regions of the ice sheet on inland sloping beds skews the uncertainty in mass loss projections. Better understanding the stability and dynamics of these regions will help constrain estimates of future sea level rise.

The ASE ice streams have experienced rapid changes over the last few decades, with intermittent, climate driven periods of acceleration and grounding line retreat. ASE ice streams are being melted from beneath due to the presence of warm CDW on the continental shelf which is routed toward the region's grounding lines. High basal melt rates reduce the stabilising effect of ice shelves, promoting acceleration. Observations of historical trends and future model projections suggest delivery of CDW to ASE grounding lines will increase in the future, driving further mass loss from the region.

Although there have been periods of stability over the satellite record, FIG, TG

and PSK modelling investigations suggest mass loss will increase in the future due to internal ice dynamic feedbacks, external climate forcing, and ice-climate feedbacks which could amplify mass loss. The future sea level contribution from the ASE can be better constrained by exploring the uncertainties associated with future projections and understanding the interplay between ice sheet behaviour and external climate forcing.

Chapter 2

The History and Future of Ice Sheet Modelling

2.1 Introduction

As the AIS contains a global sea level equivalent of 58.3 m (Fretwell et al., 2013), quantifying the contribution of the ice sheet to sea level over the coming century is a focus of global research. With large sectors of the ice sheet susceptible to instability and collapse, it is important that processes controlling ice sheet flow are understood. Ice flow is the product of a balance of stresses, where driving stresses due to gravity are balanced by resistive stresses such as lateral and basal drag. Numerical ice sheet models mathematically solve the balance between these opposing forces and therefore simulate ice sheet evolution. Ice sheet models can be used as diagnostic tools to reproduce and understand processes or as prognostic tools to simulate the change in ice flow under different conditions.

Over 13 international continental ice sheet modelling groups exist (Seroussi et al., 2019), with varying representations of the physics of ice flow, parameterisations, initialisation methods and grid resolution (Levermann et al., 2019). Continental-scale ice sheet modelling is a relatively recent practice (Blatter et al., 2010), emerging only at the beginning in the 1980s (Huybrechts, 1990; Jenssen, 1977; Oerlemans, 1983; Hertenich, 1988). The field has since advanced with improved representation of the ice sheet system, processes, and the variables influencing ice flow (Cornford et al., 2020). Furthermore, with the supplement of remote sensing techniques and datasets available for

model assimilation (Morlighem et al., 2020), the present-day state of the AIS is better captured in models (Rignot et al., 2011; Pattyn, 2018). Ice sheet models are widely used for simulating the response of AIS to future climate change (Cornford et al., 2015; Pattyn, 2018; Levermann et al., 2019; Martin et al., 2019; Golledge et al., 2015, 2019) and such practices are imperative for estimating future sea level rise. However, with a diverse spread of ice sheet models and their capabilities, there is disagreement in projections of future AIS evolution resulting in large uncertainties in future sea level contribution from the ice sheet (Seroussi et al., 2020; Edwards et al., 2021).

While improvements in the representation of the coupling between ice streams and shelves and the treatment of the grounding zone has provided more consistency between models (Cornford et al., 2020), treatment of schemes such as subglacial friction and sub-ice shelf melting are causing simulations to diverge (Brondex et al., 2017; Schlegel et al., 2018; Burgard et al., 2022). Furthermore, incomplete understanding of ice flow and ocean processes require the inclusion of tuning parameters to represent present conditions of ice which results in differences between initial states of model simulations (Cornford et al., 2020; Seroussi et al., 2019), requiring model drift to be removed from projections (Seroussi et al., 2020).

This Chapter describes the history of ice sheet models and their development to the continental scale ice sheet models that are available today. Firstly, the equations underlying ice flow in modern ice sheet models are presented and described. Given that integral differences between models are in their approximation of englacial stresses, the approximations to ice flow equations are described and the different ice sheet model types are introduced. Further differences in ice sheet models are presented such as model initialisation methods, representation of friction and the inclusion of surface fluxes. The trajectory of ice sheet model development is discussed with a focus on ice-ocean model coupling. Finally, the primary model used throughout this thesis, BISICLES, is described.

2.2 The Introduction and Development of Ice Sheet Models

In 1947 the Journal of Glaciology was launched, prompting the intuitive observational study of glaciers to progress toward a focus on the mechanics and thermodynamics of

glaciers which began a new chapter in glaciology. While the first recorded work to represent and understand ice flow beginning in the late 1700s, may have incorrectly theorised the mechanisms responsible for glacier motion, the work encouraged observations of glaciers to become more systematic over the coming centuries (Blatter et al., 2010). Following observation and surveying of individual glaciers, researchers began to present mathematical formulations to explain observed flow behaviour. Laboratory experiments quantifying ice deformation (Glen, 1952, 1955) prompted the first ever ice sheet models that related stress to ice motion through flow approximations (Campbell and Rasmussen, 1970; Rasmussen and Campbell, 1973). The mathematical representation of ice flow in two dimensions was then adapted for three dimensional models (Mahaffy, 1976) to better represent the real world. These three dimensional models included a power-law relation between stress and strain rate (Glen, 1955) and approximated the Stokes equations of viscous fluid flow to account for the large aspect ratios of ice sheets (see 2.3.3.4), but neglected the temperature dependence of ice viscosity.

The first comprehensive three-dimensional model of Antarctica was developed by Morland (1987) based on the work of Huybrechts and Oerlemans (1988). The model included coupled ice shelves and a transition model between grounded and floating components that included gradients in membrane stresses, disparity in basal sliding and an element of vertical motion through isostatic bed adjustment. The model was run on supercomputers and incorporated 10 vertical layers with a grid resolution of 40 km. By the mid 1990s, a total of five European continental ice sheet models existed, which prompted the first ever intercomparison of ice sheet models to be performed (Huybrechts et al., 1996; Blatter et al., 2010). While the models were able to capture continental scale ice flow, ice flow through internal deformation was represented in the form of the shallow ice approximation (see Section 2.3.3.4) making them poorly suited for the study of smaller glaciers and ice streams. From the early 21st century, more researchers began to challenge the simplicity of these models and progress was made to represent more of the stress balance of ice flow using the full Stokes equations (e.g. Gudmundsson (1999)) though this had a far greater computational expense.

The first full-Stokes AIS model was presented by Pattyn (2008) and was initially used to investigate the dynamics of ice flow over subglacial lakes. The progression of models toward higher-order (the most complex of Stokes equation approximations; Blatter, 1995; Greve and Blatter, 2009) prompted the first intercomparison of modern,

advanced ice sheet models in the Higher-Order Model intercomparison (Pattyn et al., 2008), a subdivision of the ongoing Ice Sheet Model Intercomparison Project (ISMIP). In requiring ice sheet models to perform a series of benchmark simulations it permitted the quantification of the role of differences in model physics and approximations to be assessed (Pattyn et al., 2012). The results demonstrated that for both steady state diagnostic simulations and time varying prognostic (or transient) simulations that there was consistency between the models.

Ice sheet models have improved in the last decade (Pattyn et al., 2017) with more constrained representation of physical processes such as grounding line migration (Cornford et al., 2020) and ice shelf fracture, and with the increased availability of observational data used to tune and calibrate models (Rignot et al., 2019; Shepherd et al., 2018). While models are able to reproduce known and understood processes such as a stable grounding line for a laterally varying ice stream and hysteresis in the grounding line position following perturbation, differences arise when considering real world domains for time dependent problems (Edwards et al., 2019; Seroussi et al., 2020).

Realistically representing grounding line migration is an important part of performing simulations of AIS evolution given the dependence of the mass loss on flux at the grounding line (Schoof, 2007). The first models that provided suitable representation of the stresses at the grounding line were higher-order models (Hindmarsh, 2006; Pattyn et al., 2006). At the grounding line, the flow regime changes from shear dominated flow over grounded ice to flow dominated by membrane stresses (the horizontal normal and shear stresses on the horizontal plane). The transition between the two schemes is gradual and has a large dependence on the representation of friction at the base of the ice. Vieli and Payne (2005) found that in order to represent the mechanical coupling of flow regimes at the grounding line, ice flow models must have a horizontal grid resolution in this region of below 1 km. This promoted widespread advance in the capabilities of numerical models which diversified to account for this fine resolution while compromising to save computational expense. Models began to introduce sub-grid interpolation schemes (Feldmann et al., 2014), anisotropic unstructured mesh (Larour et al., 2012) and time varying adaptive refinement of mesh (Cornford et al., 2013).

The diversity of the capabilities of modern ice sheet models means models can be selected to target specific research interests. Coarse resolution models with more simple approximations of ice flow are well used in palaeo-climate simulations (Lowry et al.,

2019) for example, where finer resolution simulations performed by full-stokes models would be too computationally expensive. Alternatively, fine resolution adaptive mesh models are best able to represent processes at the grounding line in fast flowing ice streams (Cornford et al., 2015; Nias et al., 2016) and models with interactive hydrological schemes are better suited to exploring the flow of ice streams that are heavily influenced by sliding through till deformation (Smith-Johnsen et al., 2020). And with international model intercomparisons, the differences arising from choice of model and their configuration can be assessed.

2.3 The Hierarchy of Ice Sheet Models

2.3.1 Stokes Equations

The Stokes Equations approximate the Navier Stokes Equations for fluid flow, where the approximation neglects inertia and momentum advection making the equations better suited to describing viscous flow. The flow of ice differs from other fluids as it is non-Newtonian and viscous, meaning there is a non-linear relationship between the applied stress and resulting strain rate of the material most commonly described by Glen’s flow law (Glen, 1955). The Stokes Equations describe conservation laws that are related to the thermal and mechanical properties of the material. This section, inspired by Nias (2017), introduces the Stokes Equations.

2.3.1.1 Field Equations

The field equations describe the conservation of mass, momentum and energy.

Mass conservation is captured by the continuity equation,

$$\frac{\delta \rho_i}{\delta t} + \nabla \cdot (\mathbf{u} \rho_i) = 0 \quad (2.1)$$

where $\rho_i = 918 \text{ kg m}^{-3}$ is the density of ice and \mathbf{u} is the velocity vector and t is a unit of time. As ice is considered incompressible and therefore constant density, Equation 2.1 can be reduced to the incompressibility condition,

$$\nabla \cdot \mathbf{u} = 0 \quad (2.2)$$

Conservation of linear momentum is described by

$$\rho_i \frac{\delta \mathbf{u}}{\delta t} = \nabla \cdot \boldsymbol{\sigma} - \rho_i \mathbf{g} \quad (2.3)$$

where $\boldsymbol{\sigma}$ is the Cauchy stress tensor, $|g| = 9.81 \text{ m s}^{-2}$ is gravitational acceleration. We neglect the Coriolis force and the acceleration term in Equation 2.3 due to the density and volume of the ice sheet.

For a constant ice density, the momentum balance can be rewritten to

$$\nabla \cdot \boldsymbol{\sigma} + \rho_i \mathbf{g} = 0 \quad (2.4)$$

The conservation of angular momentum ensures that the Cauchy stress tensor is symmetric

($\boldsymbol{\sigma} - \boldsymbol{\sigma}^T = 0$, where $\boldsymbol{\sigma}^T$ is the transpose of $\boldsymbol{\sigma}$).

There is one final field equation but this relates to the thermodynamics of ice which is not something considered on the timescales that are investigated in this project and therefore are not described here.

2.3.1.2 Constitutive equations

To solve the field equations for ice, a single constitutive equation for material law is required. Glacier ice is polycrystalline fluid with a stress dependent viscosity, meaning there is a nonlinear relationship between applied stress and resulting strain or deformation. This is most widely represented through Glen's flow law (Glen, 1955). Polycrystalline ice is also treated as an isotropic fluid so that there is no defined direction from crystal orientation within the ice which is a crude representation of reality (McCormack et al., 2022).

Firstly, Glen's flow law describes the power law between stress and deformation (strain rate), which is dependent on ice rheology, a term that has a number of other dependencies such as local ice temperature and damage.

$$\dot{\boldsymbol{\epsilon}} = A \sigma_e^{n-1} \boldsymbol{\tau} \quad (2.5)$$

A is the Arrhenius' law temperature-dependent rate factor, σ_e is the effective stress,

defined as the second invariant of the stress tensor $\sigma_e = \sqrt{\frac{1}{2}tr\sigma^2}$. The power law exponent derived from both lab and field experiments is a constant, typically assigned a value of 3 (Cuffey and Paterson, 2010). Although this is often debated and higher values have recently been proposed (Millstein et al., 2022). Here, $\boldsymbol{\tau}$ is the deviatoric stress tensor that exists once the hydrostatic stresses $p\mathbf{I}$ are removed

$$\boldsymbol{\tau} = \boldsymbol{\sigma} + p\mathbf{I} \quad (2.6)$$

and

$$p = -\frac{1}{3}tr\boldsymbol{\sigma} \quad (2.7)$$

As ice is considered incompressible, deformation depends on the deviation from the isotropic pressure p which is positive when compressed. Isotropic pressure alone does not induce deformation.

The inverse of Glen's flow law is used so $\boldsymbol{\tau}$ is described as a function of $\dot{\boldsymbol{\epsilon}}$ which can be directly incorporated in the momentum equation:

$$\boldsymbol{\tau} = 2\eta\dot{\boldsymbol{\epsilon}} \quad (2.8)$$

Here, η is the effective viscosity of the ice which is dependent on strain given that polycrystalline ice is a strain rate softening material

$$\eta = \frac{1}{2}A^{-\frac{1}{n}}\dot{\boldsymbol{\epsilon}}_e^{\frac{1-n}{n}} \quad (2.9)$$

The components of $\dot{\boldsymbol{\epsilon}}$ are defined as

$$\dot{\epsilon}_{ij} = \frac{1}{2} \left(\frac{\delta v_i}{\delta x_j} + \frac{\delta v_j}{\delta x_i} \right) \quad (2.10)$$

Finally, the equation of motion is produced by substituting Equation 2.6.

$$-\nabla p + \nabla \cdot [\eta(\nabla \mathbf{u} + (\nabla \mathbf{u})^T)] + \rho_i g = 0 \quad (2.11)$$

In representing ice flow with these equations, the elastic effects are neglected which

is considered reasonable for the longer timescales represented. Stress and strain are collinear meaning a shear stress leads to a shearing strain rate and an extensional stress leads to an extensional strain rate.

2.3.2 Boundary conditions

Boundary conditions must be included to close the system of equations for ice surfaces. At the upper surface of the ice sheet s , we assume a stress-free condition,

$$\boldsymbol{\sigma} \cdot \mathbf{n} = 0 \quad (2.12)$$

where \mathbf{n} is the outward-pointing unit normal vector.

Basal drag, $\boldsymbol{\tau}_b$, is the shear component of the stress vector at the bed, $\sigma|_{z=b}$

$$\boldsymbol{\tau}_b = \begin{cases} -C|\mathbf{u}|^{\frac{1}{m}-1}\mathbf{u} & \text{if } \frac{\rho_i}{\rho_{sw}}h > -r \\ 0 & \text{otherwise} \end{cases} \quad (2.13)$$

Basal drag takes into account the ice thickness, h , the bedrock elevation r and the density of seawater ρ_{sw} . Basal drag is often computed as a function of ice velocity in the form of a sliding law; in equation 2.13 Weertman (1957) sliding is described but there are alternative laws used in modelling (See Section 2.5). Basal drag is set to zero where the ice is floating as an ice shelf. Velocity outwardly normal to the base is zero where in contact with the base.

Where ice is in contact with water, pressure is applied at the interface,

$$\boldsymbol{\sigma} \cdot \mathbf{n} = \rho_s w g z \mathbf{n} \quad (2.14)$$

where z is the ice base.

2.3.3 Model Approximations

The Stokes equations are computationally expensive to solve, especially on the timescales of interest to many researchers e.g. centennial to millennial. To compromise, models include some form of approximation of the Stokes equations by neglecting parameter

variation over different dimensions e.g. neglecting vertical velocity. Approximations minimise the impact of reduced process representation whilst ensuring enhanced computational efficiency and are therefore well suited for simulations performed on larger domains (Blatter et al., 2010; Pattyn, 2018). The sets of approximations and model types are presented below in descending complexity, Full Stokes through to the Shallow Ice Approximation (SIA; section 2.3.3.4), with hybrid models included last.

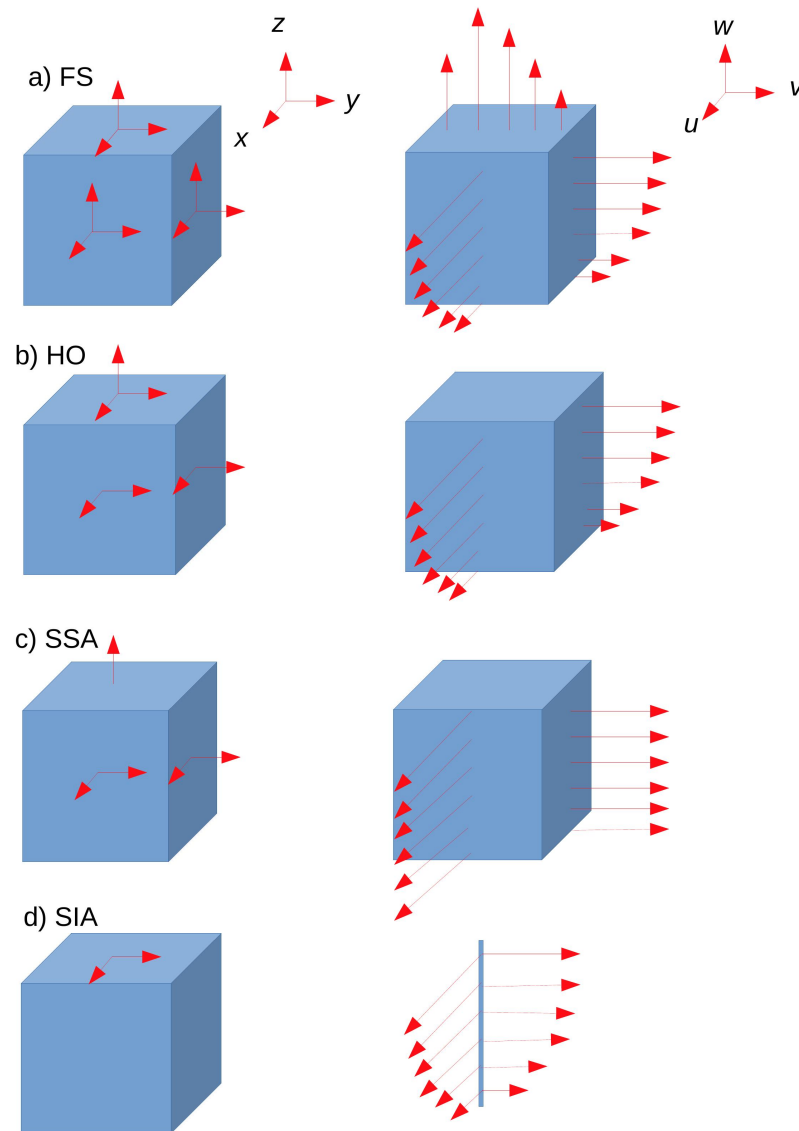


Figure 2.1: Schematic of the principal stresses included in each of the ice sheet model approximations; FS: Full Stokes, HO: Higher Order, SSA: Shallow Shelf Approximation and SIA: Shallow Ice Approximation. The right column shows the corresponding velocities. Arrows x , y and z mark the directions of the principal stresses and planes and u , v w show the directional velocity components.

2.3.3.1 Full Stokes Models

Though computationally expensive, models solving the full Stokes equations (aptly called Full Stokes models) do exist. Full Stokes models (fig. 2.1a) such as Elmer/Ice (Durand et al., 2009; Cheng et al., 2019) provide the most complete mathematical de-

scription of ice sheet dynamics (Pattyn et al., 2013). However, solving these equations with a mesh of a suitably fine resolution is exceptionally computationally expensive so tend to be reserved for regional catchment scale domains or even domains of single ice shelves.

2.3.3.2 Higher Order Models

The Ice Sheet System Model (ISSM) is an example of a higher order model (fig. 2.1b; Larour et al., 2012), though the model is capable of using other approximations also. Higher order or Blatter–Pattyn (Blatter, 1995; Pattyn, 2003) models are based on two main assumptions, first, that horizontal gradients in vertical shear stresses are small relative to the vertical gradient of the vertical normal stress.

$$\frac{\delta\tau_{zx}}{\delta x}, \frac{\delta\tau_{zy}}{\delta y} \ll \frac{\delta\tau_{zz}}{\delta z} \quad (2.15)$$

where τ_{zx} is the shear stress component in the vertical (z) direction exercised on the horizontal x normal surface and τ_{zy} is the equivalent for the lateral y surface. The normal stress τ_{zz} here is the vertical stress component acting in the vertical z direction. This equation can be integrated to give an expression for p , the hydrostatic pressure, which can then be eliminated from the momentum balance equations.

The second simplification allows terms to be eliminated through the aspect ratio of ice sheets, where the horizontal extent greatly exceeds the vertical. This simplification therefore assumes that the horizontal derivatives of the vertical velocity component ($\frac{\delta w}{\delta x}$ and $\frac{\delta w}{\delta y}$) are sufficiently small compared with vertical derivatives of the horizontal velocity ($\frac{\delta u}{\delta z}$ and $\frac{\delta v}{\delta z}$) allowing them to be neglected:

$$\frac{\delta w}{\delta x} \ll \frac{\delta u}{\delta z} \quad (2.16)$$

and

$$\frac{\delta w}{\delta y} \ll \frac{\delta v}{\delta z} \quad (2.17)$$

These simplifications ease the computational expense of the Full Stokes through providing an analytical solution for pressure and eliminating the computational expense

deriving vertical velocity gradients.

2.3.3.3 Shallow Shelf Approximation

The Shallow Shelf Approximation (SSA; fig. 2.1c; MacAyeal, 1989; Morland, 1987) builds upon the simplifications of the Higher Order, Blatter-Pattyn approximations. Úa is a finite element SSA model. SSA neglects the vertical shear stresses above the ice base with the assumption that ice flow is dominated by basal sliding as opposed to ice deformation and vertical shear (fig. 2.2). In SSA models, horizontal, longitudinal and lateral compression and stretching, otherwise known as membrane stresses, dominate the stress balance. The following terms are therefore neglected:

$$\frac{\delta\tau_{xz}}{\delta z} \approx \frac{\delta\tau_{yz}}{\delta z} \approx 0. \quad (2.18)$$

Membrane stresses are non-local, meaning that the driving stress is balanced by far-field ice stretching. In neglecting the above terms and eliminating pressure, vertical deviatoric stresses are written in terms of horizontal normal deviatoric stresses and then vertically integrated. For grounded ice, some SSA schemes will incorporate some form of vertical shear at the base of the ice such as deformable sediment beneath the bed that can be combined into the friction law (Bueler and Brown, 2009). Alternatively, these approximations can be applied for fast flowing grounded ice such as ice streams with the incorporation of a friction parameter that can be introduced as a function of velocity. However, for slow-flowing parts of the ice sheet where ice is frozen to the bed, SSA will underestimate the velocity as membrane stresses here account for very little of the driving stress (Pattyn et al., 2013).

2.3.3.4 Shallow Ice Approximation

The greatest simplification of the Stokes equations is the Shallow Ice Approximation (SIA; fig. 2.1d Hutter, 2017) which neglects all membrane stresses. Although not well suited to fast flowing ice streams or shelves, this approximation is suited to large scale simulations as this regime captures the flow of the majority of an ice sheet. SIA models solve the stress balance equations without the need for partial differential equations, making them computationally efficient and well suited to performing large ensembles on multi-millennial timescales.

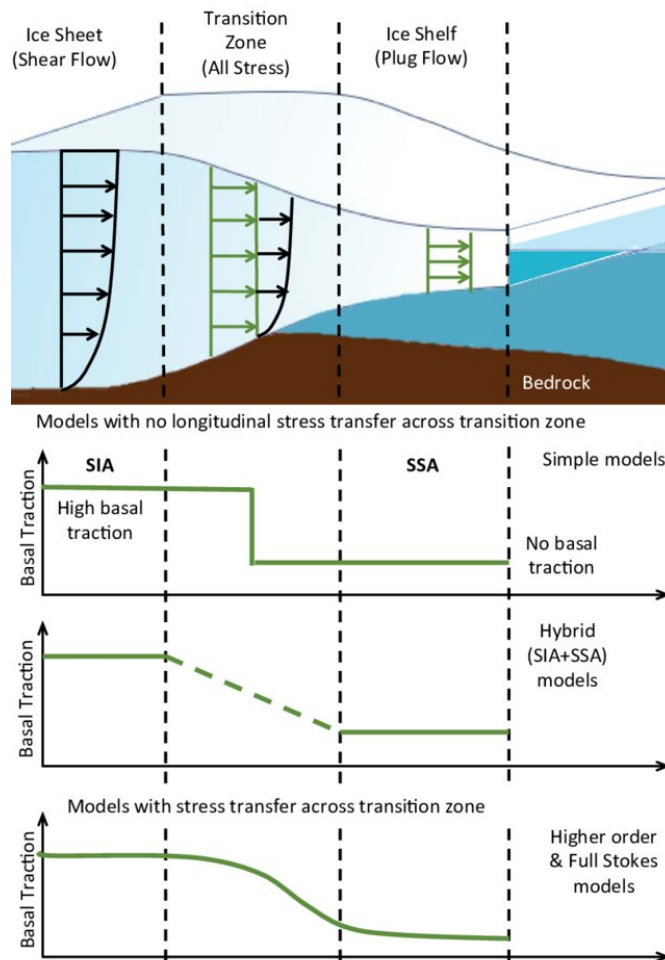


Figure 2.2: Diagram of model approximations of ice flow at the transition from grounded to floating ice in an ice shelf as basal friction is reduced. Figure is from Nowicki and Seroussi (2018).

In the SIA it is assumed that

$$\frac{\delta\tau_{xx}}{\delta x} + \frac{\delta\tau_{xy}}{\delta y} \ll \frac{\delta\tau_{xz}}{\delta z} \quad (2.19)$$

and

$$\frac{\delta\tau_{yx}}{\delta x} + \frac{\delta\tau_{yy}}{\delta y} \ll \frac{\delta\tau_{yz}}{\delta z} \quad (2.20)$$

Here, the vertical gradients of the vertical shear stresses exceed the horizontal normal and shear deviatoric stresses which are therefore neglected. These equations can be explicitly solved with known surface elevation, ice thickness and surface slope as diffusion equations as opposed to advection (SSA) which depends on the behaviour of upstream and downstream flow. While SIA has the benefit of computational efficiency, a lack of membrane stresses means stress transfer across the grounding line is absent and therefore dynamic sectors of Antarctica such as the ASE are poorly represented. Instead, SIA schemes are better used for modelling ice sheets on palaeo-timescales.

2.3.3.5 Hybrid Models

Hybrid models include the Parallel Ice Sheet Model (PISM; Winkelmann et al., 2011), SICOPOLIS (Greve and Blatter, 2016) and f.ETISH (Pattyn et al., 2004). Hybrid models fill the gap between the more complex Higher-Order models and the SSA/SIA approximations that over simplify the flow of ice. There is considerable variety in Hybrid models (Hindmarsh, 2004), with examples of higher-order approximations being variations of the one layer longitudinal stress balance approximation solved in one dimension (L1L1), L1L2 (one layer longitudinal stress balance approximation solved in two dimensions), and further variants such as LMLa, LTSML and L1L1*. The approximations of these Hybrid models will not be discussed in this section, instead the L1L2 model BISICLES is described in Section 2.9.

2.3.4 Grid Representation

Grid size is a primary control on the accuracy of an ice sheet model (Vieli and Payne, 2005; Durand et al., 2009). Horizontal resolution of an ice sheet model domain directly impacts the computational cost of the model, where finer resolution models better rep-

resent reality but take longer to run. While coarser model domains are therefore less computationally demanding, the compromise of these domains is through smoothing of important datasets such as ice geometry and misrepresenting important transitional regions such as the grounding line. Modelling investigations have shown that grounding lines require fine-scale horizontal grid resolution of at least 1 km (Cornford et al., 2013; Vieli and Payne, 2003). However, continental scale simulations at this uniform resolution are computationally demanding.

In order to deal with fine resolution representation of grounding lines while mitigating computational expensive, several approaches of non-uniform grids have been developed including nested grids (Pattyn et al., 2012), unstructured (Larour et al., 2012) and adaptive mesh grids (Cornford et al., 2013). Adaptive mesh grids allow the finest grid resolution to surround the grounding line, maintaining the finest resolution as the grounding line migrates through time. Adaptive grids are most often based on the surface velocity of ice, where the fastest velocities occur around the grounding line (Hecht, 1998; Cornford et al., 2013).

2.4 Model Initialisation Methods

For prognostic simulations of real world domains, models commonly are initialised to replicate a state of the ice sheet that represents conditions during a particular time period. While many simulations performing future projections will initialise for a modern period somewhere between 1996-present day where remote sensing data is available for model calibration, investigations for past periods where there is less available data may require an alternative approach.

2.4.1 Inverse Methods

Many modern ice sheet models (e.g. Gudmundsson et al., 2019; Cornford et al., 2013; Larour et al., 2012; Fürst et al., 2015) use inverse methods to estimate the initial conditions for both material ice and bed properties that are not directly measured. In essence it is a tuning procedure to better calibrate the initial state of a model to observations. Inversions are iterative, beginning with an initial estimate of the unobserved variable fields which are produced based on its relation to a known property. Parameter fields are then modified while minimising the misfit between the model and observations,

which is typically ice surface speed. Parameter fields produced relate to either the ice rheology, the amount of sliding at the bed and the bed topography in some instances. Inverse methods in glaciology were initially proposed by MacAyeal (1992), who first determined basal friction beneath the MacAyeal Ice Stream. Since then, the data available for model assimilation and initialisation have improved, particularly with the introduction of satellite based observations.

Inverse methods are not well posed, as one dataset is used to produce multiple (normally two) outputs meaning there can be an infinite number of solutions which produce near identical representations of the initialised model with equivalent overall misfit. Subsequently, simulations with varying parameters might produce an equally good fit with observations whilst diverging during prognostic simulations. Nias et al. (2016) produced an ensemble of simulations with perturbed parameter fields to explore the sensitivity of the ASE ice streams to these tuned parameters. Having constrained these simulations with observations, Nias et al. (2019) performed prognostic simulations with time varying melt rates and found perturbed parameters resulted in a divergence in the response of the ice to surface fluxes. Small differences in parameter fields can have a large impact on transient simulations, making these parameters a notable source of uncertainty (Schlegel et al., 2018; Lowry et al., 2021).

Whilst BISICLES solves for both basal friction and ice rheology parameter fields simultaneously, models such as ISSM and Úa perform an inversion for rheological parameters over ice shelves followed by friction parameters for grounded ice (Larour et al., 2012; Barnes et al., 2020). This means the solutions are marginally more constrained, though the latter models therefore have a greater dependence on the basal traction coefficient as it is the only tuned parameter over grounded ice.

Barnes et al. (2020) compared inversion methods and output with three different ice flow models over the ASE. They found that after performing a 40 year forward run with the three different models initialised with the same data, that the contribution to sea level differed by 4.8 mm. The similarity between the pattern of inversion parameters less reflect model specific behaviour and more reflect the underlying equation systems that are near universal in ice sheet models.

2.4.1.1 L-curve Analysis

For models that initialise using an inverse procedure, an element of smoothing of parameters is required. While noisy parameter fields might result in a better match between modelled and observed velocity, the noise could be some amalgamation of errors in the velocity data which could skew results of forward simulations. Instead, smoothing is performed with use of a regularization parameter. Regularization parameters can be chosen based on L-curve analysis (Hansen, 1992). The regularization is plotted against the misfit between the modelled initial velocity and surface velocity observations (Cornford et al., 2015). The relationship between model misfit and regularization is commonly not linear and more commonly an L shape, where the relationship transitions from a small change in regularization resulting in a small change in the misfit to a small change in the regularization resulting in a large change in the model misfit. In an L-curve analysis, the corner point of the L shape is most often chosen where both the regularization and the misfit values are lowest. This process helps to ensure that inversions are able to replicate observed velocity well while not being overly smoothed. Examples of different practices of the L-curve analysis are described in Barnes et al. (2020).

2.4.2 Spin-ups

Given a lack of observational data available for inversions, the first ice sheet model simulations were generally performed using model spin-ups (e.g. Pollard and DeConto, 2012; Winkelmann et al., 2011). These models are frequently used for palaeo-climate studies but have wider applications. The model initialisation process requires ice sheets to reach a thermal equilibrium state and often a steady state ice geometry. While this method works well for simulations performed over long timescales, performing a spin up to reach an equilibrium ice sheet state will result in an initial model that may not represent the present ice sheet disequilibrium. Furthermore, this procedure often results in a different initial ice sheet geometry than that which is currently observed, meaning the representation of variables such as ice velocity are not well matched with observations (Goelzer et al., 2018). Models combining the two approaches do exist, where transient spin-ups over glacial-interglacial timescales are performed with a simple inversion to match the ice thickness of present day (Pollard and DeConto, 2012). Additional examples include a nudging procedure performed by Golledge et al. (2019) to reset thickness

to match observations while evolving the ice flow. With improvements in both the quality and temporal extent of observations, in addition to the methods of data assimilation in models, models that are initialised with a tuning to observations are most widely used for future projections (Pattyn, 2018).

2.5 Representation of Basal Friction

The differences in flow regimes observed over Antarctica are controlled by basal processes, where sliding at the bed is an important component of ice stream flow (Cuffey and Paterson, 2010). Although it is widely accepted that deformable sediment, sediment with high porosity, and water saturated sediment are prerequisites for fast flow, the processes of subglacial sediment deformation are poorly observed and constrained (Tulaczyk et al., 2000). Subsequently, representation of basal sliding in ice sheet models has some uncertainty. Ice flow models incorporate a friction law or sliding law (or slip law) that defines the relationship between basal drag, τ_b and the basal velocity u_b (fig. 2.3). In some cases, additional variables such as effective pressure, N , are incorporated in the law to include the effects of subglacial water pressure (Tsai et al., 2015; Budd et al., 1979a; Schoof, 2005).

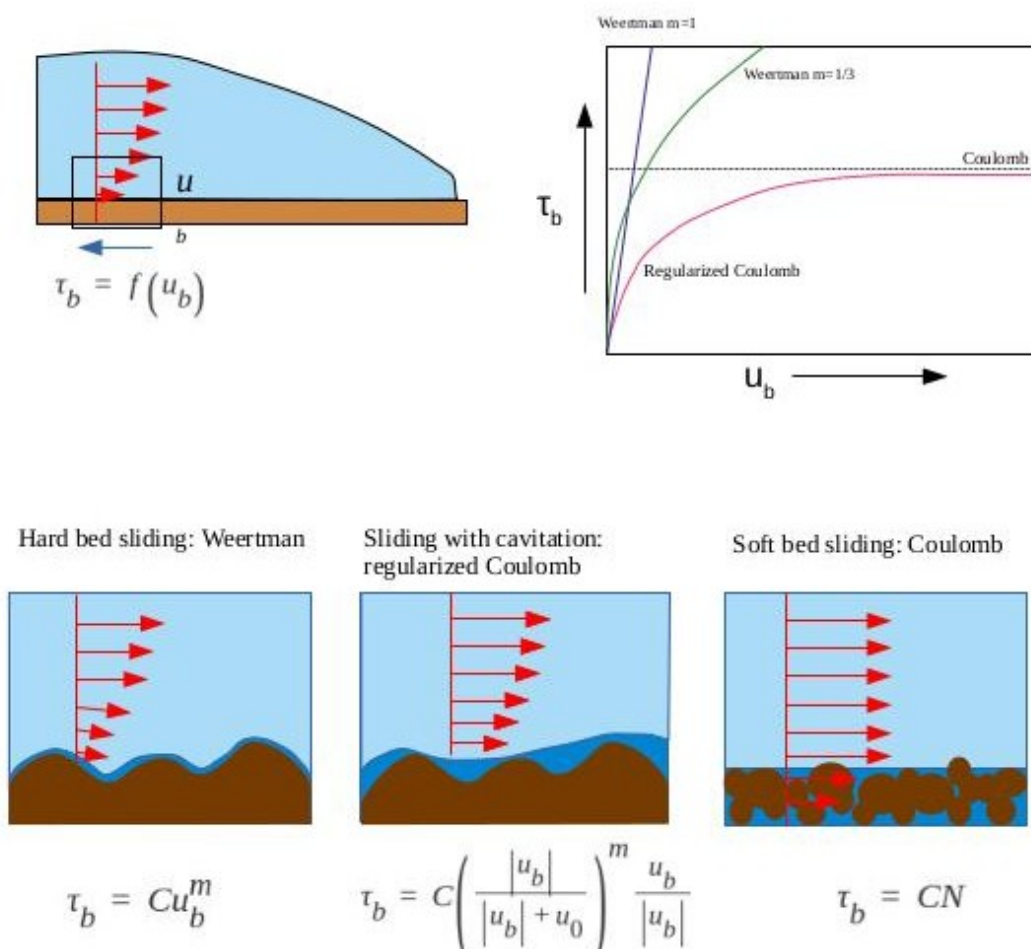


Figure 2.3: Schematic of basal sliding mechanisms and the associated sliding laws. Three bottom panels depict hard bed sliding, sliding with cavitation and soft bed sliding at the ice-bed interface with basal velocity depicted by the red arrows. Beneath each figure is the equation for the respective sliding law, here m is equivalent to the inverse of the m described in the text. Top right panel depicts the simplified relationship between basal velocity, u_b , and basal drag, τ_b , for each of the sliding laws.

In data assimilation models, a basal traction coefficient, C , is incorporated to account for some of the unresolved basal properties over a model domain and is used in the sliding law as a scaling factor. The basal traction coefficient field is held constant through time due to a lack of constraints on its temporal evolution (Favier et al., 2014). Gong et al. (2017) performed an inversion for basal friction over a terminating glacier in Svalbard for 1995 and 2011 and extrapolated the trend to attempt to predict the flow evolution of the glacier for the following year but was unsuccessful in capturing the

observed surging of the glacier. Subsequently, models without temporally evolving coupled subglacial-hydrology models will generally hold inverted parameters constant.

The use of an effective pressure, N (2.21), term in a friction law has been shown to support representation of friction around the grounding line. Vieli and Payne (2003) found an area over which the basal traction coefficient gradually reduces upstream from the grounding line. This supports the presence of a hydrological scheme linked to the ocean that becomes disconnected upstream over a transition zone between grounded and floating ice. The distribution of effective pressure would replicate this zone, where ice thickness increases inland, increasing ice overburden pressure (P_i) as the water saturation (or water pressure, P_w) decreases with distance from the ocean.

$$N = P_i - P_w \quad (2.21)$$

Sliding laws are used to describe different regimes of basal motion, which in continental scale ice sheet modelling studies is reduced to three categories: hard bedded sliding, sliding with cavitation and soft bedded sliding or till deformation. The below sliding laws therefore each relate to one of these modes of sliding. The sliding laws included to not cover the full range seen in glaciological literature.

Weertman Sliding Weertman sliding (equation 2.13) was introduced to represent sliding over a hard bed (Weertman, 1957, 1974). Here, free slip is allowed given the presence of a thin film of water at the bed which permits sliding. Resistance occurs through the presence of bed features and flow occurs in the form of regelation and viscous creep over hard obstacles.

For Weertman sliding τ_b is non-linearly related to the mean velocity u by an exponent m . Here, a basal traction coefficient C is incorporated which is obtained through an inversion. Some studies previously proposed a linear relationship between velocity and drag with $m = 1$ but this was shown to drastically overestimate basal drag in fast flowing ice streams (Nias et al., 2016). Instead $m = 3$ has been shown to better represent mass change in the region and is more commonly used in modelling investigations (Nias et al., 2019; Alevropoulos-Borrill et al., 2020; Brondex et al., 2019; Weertman, 1974).

Coulomb Plastic Sliding Coulomb plastic sliding was introduced to represent sliding over soft, deformable sediment which has been proposed to best represent basal conditions around the grounding line (Tulaczyk et al., 2000; Schoof, 2006; Pimentel et al., 2010). The Coulomb sliding law states that basal drag is independent of basal velocity and instead dependent on water pressure at the bed. In fast flowing areas around the grounding line, N is low given that water pressure within the subglacial sediment is high relative to the ice overburden pressure resulting in low basal drag and high rates of sediment deformation. Soft bedded sliding is therefore assumed to be controlled not by slip at the ice bed interface but instead through deformation of sediment.

With a Coulomb type sliding law, basal shear stress is proportional to the effective pressure, N , and scaled by a basal traction coefficient, C . This sliding law is perfectly plastic, where subglacial till only deforms above a yield stress but with a strain-rate independent behaviour above this yield stress (Iverson and Zoet, 2015; Zoet and Iverson, 2020).

$$\tau_b = CN \quad (2.22)$$

Regularized Coulomb Sliding A number of sliding laws exist that lie between the representation of sliding over both hard rigid and soft deformable beds. Such laws support the presence of both soft and hard bedded sliding regimes but over different parts of an ice stream. This can be represented in a number of ways. Tsai et al. (2015) proposed a friction law that incorporates Coulomb friction around the grounding line where N is low, but a transition to Weertman friction when N reaches a transitional threshold. Thereby introducing a shear stress with an upper dependence on N . This is similar to that proposed by Schoof (2005) and Joughin et al. (2019) where the latter incorporates a transition based on a threshold velocity rather than N .

The regularized Coulomb regime is thought to represent a third mode of sliding which involves the formation of subglacial cavities (Joughin et al., 2019). When velocity is low, no cavities exist beneath the bed and therefore hard bedded sliding dominates. As velocity increases, cavities begin to form in the sediment, reducing the contact of the ice with the sediment and reducing N as cavities fill with water which lowers basal drag. The process of cavitation is therefore velocity dependent and incorporates both regimes of hard bedded sliding and soft bedded sliding where basal drag is limited due

to the formation of cavities.

Comparisons Tsai et al. (2015) provided a detailed description of the effects Coulomb and Weertman type sliding have on the stress balance of an ice stream. The main differences between the two sets of equations occur near the grounding line, where Coulomb friction tends to approach zero as effective pressure tends to zero which contrasts with a Weertman friction regime where basal shear stress is highest around the grounding line where velocity is greatest.

The Marine Ice Sheet Model Intercomparison Project 3D+ (MISMIP3D+, Cornford et al., 2020) found that while models with different representations of englacial stresses were able to produce similar responses, the choice of friction law dictated divergence in model results. Brondex et al. (2019) performed an analysis of four friction laws from literature and found that with model tuning, friction laws were able to produce equivalent initial flow but the results diverged over time-dependent simulations. Over a century scale projection, Weertman sliding resulted in the lowest contribution to sea level than the Budd (Budd et al., 1979b), Schoof (Schoof, 2005) or Tsai (Tsai et al., 2015) sliding laws given that there is no upper limit of the dependence of basal drag on velocity. Brondex et al. (2019) suggested that use of an effective pressure-dependent friction law with a coupled model of subglacial hydrology would produce the most physically realistic results, though models of this sort currently lack observations to constrain them.

2.6 Surface Fluxes

In continental ice sheet models, surface fluxes describe changes to the upper and lower surfaces alternatively called the surface and the base respectively. Surface fluxes can be incorporated with surface mass balance parameterizations that include changes in surface elevation, or can simply be read into ice sheet models as direct changes in ice thickness where mass change occurs at the surface. Basal fluxes again are often incorporated in the form of melting (or refreezing) by directly altering the thickness of floating ice shelves from the base. Changes in surface fluxes are most regularly applied to ice sheet models to simulate a changing climate e.g. increased melting at the base through greater thermal forcing.

In the ASE, the dominant process controlling mass loss and sea level contribution is sub-ice shelf basal melting which is applied as a basal flux in ice sheet models. Incorporating basal fluxes in models has been shown to have great uncertainty (Nias et al., 2016) and existing differences in default applications of melting in models is in part responsible for disagreement between the simulated AIS response to climate changes. Methods of applying basal fluxes or basal melt rates in ice sheet models are discussed.

2.6.1 Melt Rate Parameterization

As explained in Chapter 1, basal melting of floating ice acts to reduce buttressing, which leads to ice shelf thinning, driving upstream acceleration, thinning and grounding line retreat (Gudmundsson, 2013; Reese et al., 2018b; Konrad et al., 2018). Both the magnitude of total ice shelf melting and the spatial distribution matters (Goldberg et al., 2019), where melting in shear zones and at grounding lines can influence ice dynamics most. Capturing realistic basal melt rates is essential for both reproducing observed changes in ice flow and projecting future mass loss from the continent. However, currently the treatment of sub-ice shelf melting within models is one of the greatest sources of uncertainty in future AIS simulations (Seroussi et al., 2020).

In order to perform future simulations on real world domains, it is common practice for melt rates representative of present day to first be applied. While present day melt rates such as Rignot et al. (2013b) can be read directly into models, there can be discrepancies between observed melt rates and observed thinning rates of ice shelves in the ASE. In order to determine an initial melt field, Cornford et al. (2015) produced a basal melt field that balanced ice flux across the grounding line, resulting in an unchanging ice shelf thickness. An alternative method is that performed by Gолledge et al. (2019) who introduced a ‘melt factor’ term in order to tune parameterized basal melt rates, represented as a function of temperature and salinity, to observed basal melt rates. This melt factor term is spatially varying and ensures both cold and warm cavity ice shelves have more realistic basal melt rates. Jourdain et al. (2020) also incorporated two tuning parameters to reproduce present day melt fields. The advantage of this melt factor (or alternative tuning parameters) is that it can be applied through time to temperature and salinity anomalies in order to produce melt rates for future simulations.

2.6.1.1 Cavity Resolving Ocean Models

Regional cavity resolving ocean models able to capture the high resolution output of basal melting beneath ice shelves can be used to directly force ice sheet models; though at present, this is a challenging task and few have successfully managed to produce reasonable responses for the whole of Antarctica (Asay-Davis et al., 2017; Naughten et al., 2018b). Using direct output from regional ocean models that fully resolve the Stokes equations within cavities, appropriately capturing the exchange of heat between the ocean boundary layer and the ice, is considered the most comprehensive way of applying basal melting to ice sheet models (Favier et al., 2019). While these models may capture the one-way influence of the ocean on the ice, they often fail to account for important processes that influence ocean circulation. Additional parameterization must be implemented to account for grounding line retreat in offline (un-coupled) simulations where an evolving cavity is not incorporated in an ocean model (Donat-Magnin et al., 2017). Furthermore, some ocean model simulations have been shown to be biased by the AOGCM boundary conditions (Naughten et al., 2018b). While suitable regional ocean model projections of ice shelf basal melting are currently a work in progress, parameterization of melt rates by ice sheet models themselves remains a viable practice (Berdahl et al., 2020).

2.6.1.2 AOGCM Parameterization

Numerous existing studies parameterize melting directly based on ocean model (or AOGCM) output for temperature and salinity (Nowicki et al., 2020; Jourdain et al., 2020) following the three equations that relate ocean properties, namely in-situ temperature and salinity, to ice shelf melting (Hellmer and Olbers, 1989). The benefit of this method is that ice sheet model simulations can generally be directly forced with emissions scenarios from more complex earth system models. Using AOGCM output to directly force ice sheet models means processes of ocean circulation within ice shelf cavities are not accounted for and therefore additional processes must be parameterized.

Function of Depth As the highest melt rates are concentrated around the grounding line at the deepest point in the ice shelf, where the melting point of ice is lower due to increased pressure, parameterizations exist as a function of depth. This is most commonly implemented as a piecewise linear function of depth with an initial calibration

to ensure the magnitude of melt rates are appropriate for a given ice shelf (Favier et al., 2014; Joughin et al., 2014). Though this parameterization has been criticised for overestimating grounding line retreat when compared with more physically realistic coupled ice-ocean models (Seroussi et al., 2017; Jordan et al., 2018; De Rydt and Gudmundsson, 2016), it is beneficial given its simplicity. However, for future simulations, melt anomalies or ‘perturbation coefficients’ must be calculated based on ocean model output and therefore scaling based on temperature and salinity is required. Alternatively, idealised simplified scalings can be applied such as the x1.8 increased melt rate performed by Barnes et al. (2020) to represent a melt rate in a high emissions scenario.

Function of Distance from Grounding Line The melt rate parameterization used by Nias et al. (2019) and Alevropoulos-Borrill et al. (2020) applies a melt rate anomaly that is related to distance from the grounding line. The distance decay function ensures the highest melt rates anomalies exist closest to the grounding line, as is consistent with the current observed pattern of melt rates (Shean et al., 2019). This parameterization negates the issue of which melt rates to apply to newly floating ice, a problem that must be considered when performing offline forcing simulations using regional ocean modelled melt rates. The limitation of this parameterization is that prescribed melt rate anomalies are applied uniformly across the grounding line which is in reality varies with cavity geometry and ocean circulation. While this parameterization is suited to smaller ice streams in the ASE which retreat over deepening bed, it may be less suited to larger ice shelves such as the Ross where some of the highest melt rates occur at the ice front (Stewart et al., 2019). Furthermore, for future simulations, melt anomalies must be calculated based on ocean model output and therefore scaling based on evolving local ocean temperature and salinity is required. Alternatively, idealised simplified scalings can be applied. Nias et al. (2019) used a linear increase in melt rate anomaly to 20 m yr^{-1} over 100 years to represent a melt rate in a high emissions scenario based on Hellmer et al. (2012).

Linear/Quadratic Dependence Arguably more physically realistic parameterizations, yet still simplified, include the linear and quadratic parameterizations initially presented by Rignot and Jacobs (2002) and Holland et al. (2008) respectively. While a linear relationship between thermal forcing and ice shelf melting was suggested by Rignot and Jacobs (2002) based on observations, it was later modified by Holland et al. (2008)

who found melting had a quadratic dependence on local thermal forcing. The quadratic component was introduced to account for ocean turbulence, where buoyancy driven circulation has been found to increase linearly with increased thermal forcing (Jourdain et al., 2017). The quadratic dependence of melt on thermal forcing (temperature above the in situ freezing point) therefore somewhat accounts for the velocity of a buoyant meltwater plume.

Plume/Box Model More complex parameterizations incorporate simplified models to capture more of the understood processes occurring beneath the ice shelves. For example, Lazeroms et al. (2018) incorporated a plume model in order to replicate the buoyancy driven circulation observed beneath ice shelves where high basal melting results in high meltwater production. Fresh, buoyant meltwater rises beneath the ice shelf as a plume which acts to entrain warmer bottom water toward the ice shelf while the freshwater is transported away at the surface.

Pelle et al. (2019) built upon this parameterization by coupling the plume model from Lazeroms et al. (2018) with the box model, PICO, presented in Reese et al. (2018a). The product, PICOP, uses the box model PICO to modify far field temperature and salinity from ocean models to better represent ocean properties within ice shelf cavities. PICO then provides more realistic temperature and salinity from which melt rates can be calculated and distributed beneath ice shelves with the buoyant plume model. The product was found to broadly reproduce the pattern of melting beneath ice shelves in the ASE. However, Burgard et al. (2022) suggested that PICOP does not perform well when compared with a cavity resolving ocean model and discourage the use of this parameterization in its current form.

2.6.2 Parameterization Assessments

Assessment of parameterizations of basal melting have generally been compared with modelled melt rates (Lazeroms et al., 2018). Favier et al. (2019) use the ice sheet model Elmer/Ice coupled with the ocean model NEMO (Nucleus for European Modeling of the Ocean) to assess the performance of a series of simplified parameterizations in addition to a box model (Reese et al., 2018a) and a plume parameterization (Lazeroms et al., 2018) on an idealised ice shelf. While the ice sheet model was able to simulate the subsequent dynamic response of the ice shelf to these varied parameterizations, this

method gives little indication as to the real world impact of parameterizations, and therefore is yet to provide an indication of the uncertainty in sea level rise projections for a given parameterization applied over the continent. This can be particularly important when considering the spatial variation in buttressing given the presence of ice rumples and rises and shear zones, each of which influence the buttressing (Goldberg et al., 2019; Reese et al., 2018a; Sun et al., 2017). Therefore, applying varied parameterizations to present day configurations of regions in Antarctica, we can better understand the performance of different idealised melt rates that are applied to real world simulations.

While basal melt parameterizations in ice sheet models broadly capture the observed pattern of melting beneath ice shelves (Favier et al., 2019), offline forcing and parameterizations fail to account for the interplay between the ocean processes driving melting and the subsequent influence of ice shelves and meltwater on ocean properties (Donat-Magnin et al., 2017). Issues arise with offline forcings when the grounding line of the ice shelf migrates and the ice shelf cavity evolves, where areas that un-ground in the ice sheet model simulation remain grounded in the ocean model simulation. This modified cavity geometry affects ocean circulation (Donat-Magnin et al., 2017) through changing the ice shelf draft and therefore the space in which ocean masses can circulate (Mueller et al., 2018). Furthermore, a changing cavity geometry, specifically the gradient of slope of the ice shelf, can influence the velocity of the ocean masses interacting with the ice shelf and therefore the heat capacity.

2.7 Ice Sheet Model Intercomparison Project (ISMIP)

The ISMIP6 project was designed in 2016 (Nowicki et al., 2016) as a successor to existing model comparisons for idealised domains (Cornford et al., 2020; Pattyn et al., 2012, 2013). The goal of ISMIP6 was to build upon existing work in the climate modelling community and use the diversity in AOGCM climate projections to explore the future evolution of Greenland and Antarctica. ISMIP6 is a subdivision of CMIP6 with a focus on ice sheets which had previously been neglected from the CMIP process. While ISMIP6 primarily included standalone ice sheets with forcings parameterized from CMIP6 model output (Seroussi et al., 2020), the progression of the ice sheet modelling community toward coupling means fully interactive ice sheets within existing AOGCMs will be included in the next phase of the intercomparison.

Existing ice sheet model intercomparisons, as mentioned in Section 2.2, demonstrated a need to better understand the causes of spread in model results. While many studies explore intramodel uncertainty through performing large parameter ensembles (Schlegel et al., 2018; Ritz et al., 2015; Nias et al., 2016; Lowry et al., 2019), differences in results due to alternative model initialisation are harder to quantify. Therefore, as part of ISMIP6, a comparison of initial model states was performed in initMIP-Antarctica (Seroussi et al., 2019). The goal of initMIP was not to constrain future sea level estimates by accounting for disparities in the impacts of model initialisation. Instead, the project aimed to understand the effects of these differences.

The results of initMIP showed a difference in the volume above floatation of present day ice of 32 % across the 25 simulations from 16 international groups (Seroussi et al., 2019). Further, they found a range in the Antarctic sea level contribution of -243 to +167 mm after performing a 100 year experiment with controlled climate. This range was a result of differences in model initialisation, treatment of melting at the grounding line due to the unconstrained experimental design and model parameterization, including grid resolution. The primary finding of the study demonstrated that models initialised with inverse methods better reproduce initial ice thickness and velocity than those performed with spin-ups. However, there is a greater divergence in the response of ice to forcing for models initialised with inverse methods compared with those that used spin-ups. Combining the two methods will be important for constraining these differences, with temporally varying observations to be used in the initialisation procedure (Goldberg et al., 2015; Larour et al., 2014).

The current suite of AOGCM used in CMIP phases do not yet include resolved ice shelf cavities meaning there is no representation of the ocean properties beneath ice shelves to be used directly in ice sheet model simulations (Eyring et al., 2016). The basal melt parameterization designed by Jourdain et al. (2020) accounted for the lack of cavities by applying a thermal forcing field based on temperature and salinity and tuned to best match observations (Favier et al., 2019). Three dimensional temperature and salinity fields produced by a subset of CMIP5 models (Barthel et al., 2020) under various future forcing scenarios were extrapolated over the continent to account for the future ungrounding of ice and exposure to the ocean. To account for biases in model set ups, the temperature and salinity fields were taken as anomalies and added to present day ocean climatologies from observations.

In order to obtain a thermal forcing field, following the advice of Favier et al. (2019) both the local and non-local temperature and salinity fields should be included. The ‘local’ forcing assumes that the far field forcing has no change in stratification and simply advects into the ice shelf cavity with each ice shelf depth interacting with a vertically varying ocean. The non-local forcing accounts for the sector averaged values of temperature and salinity rather than those directly in contact with the base of ice shelves. The chosen ISMIP6 forcing includes both local and non-local thermal forcing in the quadratic parameterization implemented. Parameterizations are defined over separate sectors of Antarctica and include a temperature correction, δT , for each sector and a tuned ‘uniform coefficient’, γ_0 , which roughly represents the exchange velocity used for solving the three equations. The γ_0 is a single coefficient tuned for the whole continent.

In addition to the ‘local’ and ‘non-local’ parameterizations relating to the dependence of thermal forcing on the surrounding ocean properties, there are an additional two sets of alternative parameterizations that involve tuning the γ_0 value to reproduce different patterns of melting. The MeanAnt method tunes γ_0 so that, when multiplied by the thermal forcing field, melt rates around Antarctica are summed to match observations of Rignot et al. (2013b) and (Depoorter et al., 2013). For the ‘PIGL’ method, γ_0 is tuned to ensure melt rates adjacent to the grounding line are represented in the ‘local’ and ‘non-local’ parameterisations. While the PIGL method more closely captures melting in the ASE, where present day melt rates in the ASE are double that for PIGL relative to MeanAnt, maximum melt rates for this parameterization remain below half of those found in observations (Jourdain et al., 2020).

The results of ISMIP6 show a range in the AIS sea level contribution of -7.8 to 30 cm by 2100, showing the models even disagree on the net sign of future mass change (Seroussi et al., 2020). That being said, these values are relative to a control simulation to account for model drift as a result of differing initialisation procedures (Seroussi et al., 2019) and therefore describe the sensitivity of the ice sheet to climate perturbations. Furthermore, the majority of simulations show mass gain, exhibited as a fall in global sea level, to be occurring through increased accumulation in East Antarctica. Conversely, the majority of simulations show mass loss in West Antarctica. Use of the PIGL forcing over the MeanAnt forcing results in an additional upper sea level contribution of 3 cm, demonstrating an increased sensitivity to melting has only a small impact

on the total mass contribution over the century. Overall the greatest uncertainties in the continental projections were associated with the choice of AOGCM, the implementation of the melt parameterization and differences in initialisation (though this should have been accounted for somewhat by the subtraction of the control simulation). Part of the uncertainty with the implementation of the melt parameterization is due to the calibration to present day melt rates, lumping the uncertainty of the poor representation of physics into two tuning parameters δT and γ_0 .

A total of six different types of parameterizations were included by different modelling groups as part of the open parameterization framework simulations. While the cumulative melt was found to be 50% higher and lower compared with the standard framework, the total mass loss from the open framework simulations was generally greater, with a mean sea level contribution of 45 mm when forced with RCP8.5 AOGCM output (Seroussi et al., 2020). The open framework also resulted in a greater standard deviation in projections of mass loss over the 21st century.

2.8 The Future of Ice Sheet Modelling: Coupling

As an interactive component of the Earth system, processes that influence ice sheet behaviour are often linked to the atmosphere-ocean through feedbacks. Although atmospheric feedbacks are vastly important (Ridley et al., 2005), most of the uncertainty in AIS evolution from ice sheet modelling studies is associated with uncertainties in future basal melting (Seroussi et al., 2020). Subsequently, the focus here lies with the ice-ocean interactions and model coupling.

Ice-ocean interactions are complex, and feedbacks that exist can be both positive (amplifying) and negative (subduing). While Section 2.6.1 introduced some of the limitations of capturing ice shelf melting using ice sheet model parameterizations alone, fully coupled models not only better capture the influence of the ocean on ice shelf melting but also the influence of ice shelf meltwater on ocean processes. Golledge et al. (2019) performed an asynchronous, ‘offline’ coupling with an intermediate complexity earth system model and the ice sheet model PISM (Martin et al., 2011). The experiment performed ‘hosing’ where a prescribed quantity, or flux, of freshwater is added into the Southern Ocean according to a continuous timeseries flux that was derived from the ice sheet model. With increased freshwater flux around Antarctica, the

ocean masses adjacent to the continent become more strongly stratified resulting in less mixing between warm deep water and the colder fresher surface, where the former instead spreads laterally resulting in concentrated melting at AIS grounding lines (Bintanja et al., 2015b; Bronselaer et al., 2018). Representation of this process in model simulations will likely have consequences for Amundsen Sea glaciers which are already vulnerable to increased intrusion of warm deep water on the continental shelf.

When coupling an ice sheet model to an ocean model there must be an exchange of information between the two. The timestep over which the information is exchanged generally defines the level of complexity of the coupling and where it falls within the three categories defined by Jordan et al. (2018). Generally, the required information for the ocean model from ice sheet model will depend on the type of ocean model. The ocean model requires a horizontal and lateral boundary for an ice shelf in order to resolve the circulation within a cavity, therefore, as a grounding line retreats (advances) and an ice shelf grows (shrinks) these updated horizontal and vertical extents must be updated in the ocean model. For a cavity resolving ocean model (e.g. ROMS, Naughten et al., 2018b) that directly calculates melt rates, freshwater from ice shelf melt is already represented by the ocean model. Conversely, in an ocean model that does not resolve ice shelf cavities, such as the ocean models of AOGCMs, sub-ice shelf melting must be parameterized by an ice sheet model and a freshwater flux given to the ocean model. For a thermodynamic ice sheet model, the temperature of the ice at the base can also be provided for the ocean model. As previously discussed, the ice sheet model requires basal mass balance inputs and therefore either directly calculated or parameterized melt rates.

One of the hopes of ISMIP6 was to include fully coupled atmosphere-ocean general circulation models with a fully interactive ice sheet model (AOGCM-ISM) but this had not been achieved prior to the deadline. That being said, many AOGCM-ISM models are currently under development. Smith et al. (2021) successfully coupled the UK Earth System Model (UKESM1) with BISICLES. Development of coupled models open new possibilities for research on the role of the ice sheet within the climate system, providing a better understanding of the role of feedbacks in the future evolution of the ice sheet.

2.9 BISICLES

The ice sheet model used throughout this thesis is the Berkeley Ice Sheet Initiative for Climate at Extreme Scales model (BISICLES) developed by Cornford et al. (2013). BISICLES is an L1L2 model based on the Schoof-Hindmarch approach (Schoof and Hindmarsh, 2010) and is described in detail in Cornford et al. (2013). In comparison to SSA, this L1L2 model takes into account the vertical shear stresses (shear stress acting on the vertical plane) in the second invariant of the deviatoric stress tensor. These approximations therefore calculate the depth-integrated effective viscosity with the incorporation of vertical shear stress so that the momentum balance can be solved in two dimensions. While standard hybrid SIA/SSA models linearly combine SSA and SIA stress balance regimes in flow, BISICLES couples vertical shear and membrane stresses.

Assuming hydrostatic equilibrium:

$$s = \max \left[h + r, \left(1 - \frac{\rho_i}{\rho_s w} \right) h \right], \quad (2.23)$$

Where s is the surface elevation, h is ice thickness and r is the bedrock elevation. Accounting for mass conservation

$$\frac{\delta h}{\delta t} + \nabla \cdot [\mathbf{u}h] = a - M \quad (2.24)$$

thickness change $\frac{\delta h}{\delta t}$ and flux divergence $\nabla \cdot (\mathbf{u}h)$ balance surface (a) and basal fluxes (M).

Ice thickness and horizontal velocity also satisfy a two-dimensional stress balance equation

$$\nabla \cdot [\phi h \bar{\mu} (2\dot{\boldsymbol{\epsilon}} + 2tr(\dot{\boldsymbol{\epsilon}})\mathbf{I})] + \boldsymbol{\tau}_b = \rho_i g h \nabla s, \quad (2.25)$$

where $\dot{\boldsymbol{\epsilon}}$ is the horizontal strain rate tensor,

$$\dot{\boldsymbol{\epsilon}} = \frac{1}{2} [\nabla \mathbf{u} + (\nabla \mathbf{u})^T] \quad (2.26)$$

and \mathbf{I} is the identity tensor. Vertically integrated effective viscosity, $\phi h \bar{\mu}$, is com-

puted from a stiffening factor ϕ and a vertically varying effective viscosity μ that is derived from Glen's flow law with an n value of 3 (Cuffey and Paterson, 2010). Here, the ice sheet is sub-divided into 10 layers which progressively thin from the surface to the base.

$$\phi h \bar{\mu}(x, y) = \phi \int_{s-h}^s \mu(x, y, z) dz \quad (2.27)$$

Vertically varying effective viscosity $\mu(x, y, x)$ includes vertical shear strains and satisfies

$$2\mu A(T)(4\mu^2 \varepsilon^2 + |\rho_i g(s-z) \nabla s|^2)^{(n-1)/2} = 1, \quad (2.28)$$

Here, $A(T)$ depends on the ice temperature T through the Arrhenius law (Cornford et al., 2013). Uncertainty in temperature T and the rate factor are accounted for by the tuned viscosity parameter ϕ . Finally, basal drag τ_b is included with a sliding law related to basal velocity (Section 2.5).

BISICLES is an adaptive mesh refinement (AMR) ice sheet model which is able to represent the domain with a fine horizontal resolution near the grounding line and a coarser resolution elsewhere. Throughout this thesis, the BISICLES simulations performed implement five resolution levels with mesh grid spacing of $\Delta x^l = 2^{-l} \cdot 4000$ m, where l is an integer between 0 and 4. The grounding line is therefore represented with a mesh resolution of 250 m.

2.9.1 Model Initialisation

With surface elevation (s), bedrock elevation (r), surface mass balance (a) and temperature T , the model equations can be solved to calculate modelled velocity. However, given uncertainties in observed parameters in addition to uncertainties associated with unknown spatially varying parameters, the model must be tuned in order to better match observed velocity. An inverse problem is solved in order to find two un-observable parameter fields for basal friction (C) and ice rheology (ϕ). Such inversion methods are well established and practiced (Morlighem et al., 2010; Joughin et al., 2010; Cornford et al., 2013; Barnes et al., 2020, ; see Section 2.4.1).

The following objective function is minimised in the inversion by changing $C(x, y)$

and $\phi(x, y)$ fields

$$J = \int_{\Omega} (|u| - |u_{obs}|)^2 + \alpha_C \int_{\Omega} (\nabla C)^2 d\Omega + \alpha_{\phi} \int_{\Omega} (\nabla \phi)^2 d\Omega \quad (2.29)$$

The first term in the equation calculates the misfit between modelled $|u|$ and observed $|u_{obs}|$ velocity over the domain, Ω . The remaining terms regularize the solution.

2.9.2 Model Application

Throughout this thesis BISICLES is used to perform prognostic simulations of century scale. The model is not re-introduced in each Chapter, however, the data used in the model initialisation is described for each set of experiments and the boundary conditions namely the applied friction law, modification to the calving front and surface fluxes are described. Furthermore, with the adaptive mesh refinement scheme, century scale simulations can be performed to with a suitably high resolution (sub kilometer) around the grounding line without additional computational expense (Cornford et al., 2013).

All BISICLES simulations presented in this thesis are performed on the New Zealand eScience Infrastructure Cray XC50 supercomputer, Māui, on 80 hyperthreaded computer processing units (CPUs).

2.10 Summary

Continental scale ice sheet models were introduced in the late 1980s and have undergone vast improvement over recent decades. The development of multiple international ice sheet modelling groups and models prompted the model intercomparison studies, for which models were required to perform benchmark experiments to better represent the mechanical coupling between ice streams and ice shelves. The community has since grown, with the most recent intercomparison of models involving 26 different ice sheet model simulations from 13 modelling groups. Modern ice sheet models have a wide extent of capabilities and diverge in their solutions to englacial stresses, grid structure and parameterization of boundary conditions. The diversity of available models provides the cryospheric science community a greater range of tools from which to choose in order to answer specific research questions.

With improvements in the availability of satellite observations of AIS change, models are better representing present day ice flow over the continent. However, discrepancies in the representation of present day ice flow due to differences in initialisation procedures are hindering agreement in the simulated response to future climate. Furthermore, uncertainties in the representation of ice shelf basal melting in models due to both a lack of observational data and poorly understood ice shelf cavity processes, exacerbates the projected response of the AIS to future climate. Areas identified to cause uncertainty in projections are the focus of future model development, with updated initialisation as data availability increases and progress to couple ice sheet models to cavity resolving ocean models and full earth system models.

Chapter 3

Re-advancing the grounding lines of marine terminating glaciers in the Amundsen Sea Embayment

3.1 Introduction

The Amundsen Sea Embayment (ASE) dominates mass loss from the Antarctic continent (Rignot et al., 2019; Mouginot et al., 2014), with rapid grounding line retreat and dynamic mass loss driven by ocean forced basal melting of the region's ice shelves (Pritchard et al., 2012; Rignot et al., 2011, 2019). Between 1973 and 2014 ice discharge from the ASE increased by 77 % as a result of glacier acceleration, making the region responsible for 10 % of global sea level rise contribution (Mouginot et al., 2014). Acceleration of glaciers in the ASE is caused by reduced buttressing from ice shelves through thinning and local ungrounding as a result of ocean induced melting (Gudmundsson, 2013; Fürst et al., 2016). Elevated sub-ice-shelf basal melt rates and increased ice discharge across the grounding line are not matched by mass gain through accumulation in the region, meaning the system is out of balance.

The high rates of observed sub-ice-shelf melting are attributed to the presence of CDW on the continental shelf which reaches 2-4 °C above the in situ freezing point (Jacobs et al., 2011, 2012; Rignot and Jacobs, 2002). While blocked from much of the continent by a deep thermocline and shallow continental bathymetry, in the ASE CDW upwells onto the continental shelf and flows through deep troughs toward ice

shelf cavities, causing melting from beneath (Thoma et al., 2008; Nakayama et al., 2014; Wåhlin et al., 2013; Deb et al., 2018). Present melt rates beneath PIG (Shean et al., 2019; Adusumilli et al., 2020) and TG ice shelves reach up to 250 myr^{-1} and 207 myr^{-1} (Milillo et al., 2019) respectively. The depth of the CDW layer on the shelf determines the heat available for ice shelf melting where upwelling occurs as a result of strong circumpolar westerly winds (Thoma et al., 2008; Walker et al., 2013). While onshore transport of CDW is increasing due to a long term trend of strengthened westerlies (Naughten et al., 2022), decadal oscillations in far field temperature (Jenkins et al., 2016; Steig et al., 2012; Paolo et al., 2018) and changes to the strength and position of local synoptic systems (Assmann et al., 2013; Dotto et al., 2020; Hosking et al., 2016) also cause temporal variability in CDW upwelling. With increased delivery of warm water coinciding with periods of acceleration and mass loss from the region (Pritchard et al., 2012), it is widely accepted that future changes in the quantity of CDW on the shelf in the ASE will dictate future mass loss (Naughten et al., 2018b; Turner et al., 2017; Donat-Magnin et al., 2017).

Climate model projections under high emissions scenarios indicate a shift in the position and intensity of circumpolar westerlies (Bracegirdle et al., 2008, 2013) in association with a more positive Southern Annular Mode (Zheng et al., 2013). Subsequently, delivery of CDW to the ASE is projected to increase (Donat-Magnin et al., 2017). Furthermore, increased ice shelf melting and a freshening of the ocean surface has been shown to result in a positive ice shelf melting feedback caused by a warming of the subsurface and deep water (Golledge et al., 2019). Most ice sheet modelling studies focus on the ice sheet response to increased basal melting in response to a warming of the subsurface in the ASE (Nias et al., 2019; Ritz et al., 2015; Gladstone et al., 2012), in addition to forcing widespread ice shelf and whole sector collapse (Martin et al., 2019). Such experiments permit the response of the region to a ‘business as usual’ (RCP8.5) emissions scenario to be explored, and provide estimates of the upper limit of future sea level contribution from the region.

Many recent ice sheet modelling studies investigate the upper-end of projected mass loss from the (ASE; Alevropoulos-Borrill et al., 2020; Robel et al., 2019; Nias et al., 2019), however, few studies investigate the stability of the region in response to a reduced climate forcing following a period of retreat over future decades (Seroussi et al., 2014). The RCP2.6 scenario involves a decline in global temperature in response to a

curbing of global emissions, which implicitly includes carbon removal and sequestration schemes in order to prevent global temperatures from rising (Moore et al., 2010; Van Vuuren et al., 2011). This scenario, however, does little to reduce the projected ocean temperatures in the ASE to below present day (Alevropoulos-Borrill et al., 2020). Moore et al. (2018) proposed that warm water can be blocked from ice shelves in the ASE by dredging gravel to build a berm of 10-50 cubic kilometers on the sea floor in front of the glacier termini. Gürses et al. (2019) used a coupled sea ice-ocean model to explore the effects of this wall and found cooling in the water column within the walled region, resulting in a reduction in basal melting from PIG by 85 %. While the implications of a blocking of CDW on basal melting in the region were considered, there was no further consideration of whether this blocking would help to stabilise the disequilibrium of the ice streams that are presently in a state of mass loss.

Here, the ability of the ASE ice streams to stabilise in response to reduced basal melting is investigated through a 182 simulation ensemble of ice sheet model simulations. Basal melting is initially increased beneath ASE ice shelves to varying magnitudes over different durations to cause the ice streams to retreat. The investigation is extended by exploring the blocking of CDW from the continental shelf in the ASE (Gürses et al., 2019) by implementing different magnitudes of reduced basal melting, to replicate local ocean cooling. The purpose of these idealised sensitivity experiments is to better understand how the ASE ice streams respond to reduced melting and whether reduced melting can act to offset the present high rates of mass loss from the region.

3.2 Methods

3.2.1 Regional Model Domain

The BISICLES ice sheet model is used to perform the described simulations (see Chapter 2). Simulations are performed for the regional ASE domain used by Nias et al. (2019) and Alevropoulos-Borrill et al. (2020). Topography and thickness are derived from a modified Bedmap2 (Nias et al., 2016; Fretwell et al., 2013). The surface mass balance field from Arthern et al. (2006) is held constant in order to focus on the ocean forced response of the region. A three-dimensional temperature field produced by Pattyn (2010) is applied, which does not evolve through time. Basal friction and flow enhancement (ice rheology) coefficients are determined through an inverse procedure

so that the initial modelled velocities are consistent with observations, specifically observed velocity over 2007 to 2009 (see Chapter 2; Rignot et al., 2011). This tuning process produces two spatially varying parameter fields, a basal traction coefficient and ice rheology (Cornford et al., 2013).

A fixed calving front is applied for numerical stability, combined with a calving flux parameterized as a function of velocity. While the ice front remains fixed, a minimum ice thickness of 10 m is prescribed, allowing floating ice to thin almost completely with a negligible effect on upstream buttressing (Cornford et al., 2015).

An initial basal melt rate field (fig. 3.1) produced by Cornford et al. (2015) is applied to replicate present day melt rates over the ASE. This product was tuned to reproduce observed ice shelf thinning rates when accounting for ice flux divergence. It has been further smoothed and scaled with the highest melt rates concentrated at the grounding line (Nias et al., 2016). This melt rate field is applied throughout the simulations as a background melt rate to which the anomalies are added.

3.2.2 Ensemble Description

A 182 member ensemble of simulations is performed, with each simulation lasting 200 years. Two reference simulations are performed, one with constant present-day melting (Control) and one with no sub-ice shelf melting (Zero, where ice shelf thickness changes are purely dynamic). For the 180 externally forced simulations, temporally evolving melt rate anomalies are applied (fig. 3.2a). Anomalies are scaled according to observed patterns of basal melting, where the highest melting is concentrated at the grounding line (Nias et al., 2016; Rignot et al., 2013b). A grounding line proximity parameter p is used as a multiplier where $p = 1$ at the grounding line and decays exponentially with increasing distance according to the equation $p = \exp(-x/\lambda)$. Here, λ is a length scale of 10 km. This method is implemented in Nias et al. (2019) and repeated by Alevropoulos-Borrill et al. (2020).

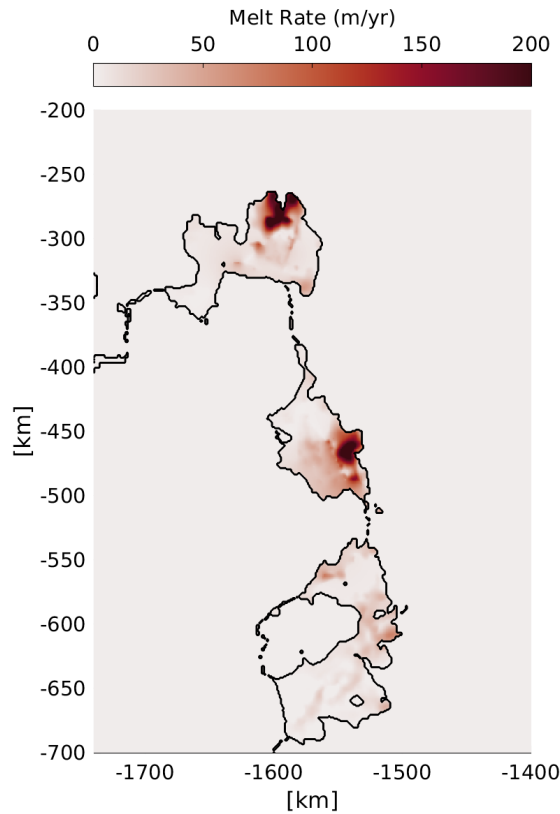


Figure 3.1: Background basal melt rate field (m yr^{-1}) applied beneath ice shelves in the Amundsen Sea Embayment from Cornford et al. (2015). Black lines define the ice shelf boundaries of the initialised model using Bedmap2 (Fretwell et al., 2013) ice thickness and topography. Positive melt rates describe mass loss.

For 180 of the simulations, there are 30 different retreat phases with positive basal melt anomalies and six different advance phases with negative melt anomalies. Initially, melt rate anomalies are linearly increased to six different magnitudes, from 5 m yr^{-1} to 30 m yr^{-1} at 5 m yr^{-1} intervals. Each magnitude is reached over five different durations, from 20 to 100 years at 20 year intervals (fig. 3.2). The duration relates to the duration of positive forcing, i.e. increased basal melting. Upon removal of the positive anomaly, once the duration of positive forcing is reached, the melt rates are reduced relative to the background field. Each of the 30 simulations experiences reduced melting, applied as a negative anomaly, to six different magnitudes. Negative melt anomalies vary from 0 m yr^{-1} (no anomaly, only the background melt field) to -5 m yr^{-1} . These negative melt rate anomalies are held constant for the remainder of the 200 year simulation. The simulation codes represent the duration of positive melt anomaly (YR) the magnitude

to which the anomaly was linearly increased (M) and the magnitude of the negative anomaly (R). Therefore, the simulation YR80-M20-R4 (fig. 3.2b) is forced with 80 years of melt rates that are linearly increased to 20 m yr^{-1} before being removed and reduced to -4 m yr^{-1} relative to the initial basal melting field, which is applied for 120 years to fulfil the 200 year simulation. When referring to the applied anomalies throughout this chapter, periods of increased basal melt rates are described as positive and reduced basal melt rates as negative, in relation to the background melt field. When the anomaly and background melt field are combined, areas of positive melting reflect thinning through the removal of ice while negative melting reflects thickening through marine ice accretion or refreezing.

The anomaly varies spatially, where the largest magnitudes of anomaly (both the M and R values) are applied at the grounding line, and decrease toward the calving front. The negative anomaly is also applied in this way with the greatest reduction in melting occurring at the grounding line. Subsequently, for negative anomalies, the anomaly is subtracted from the background basal melt rate field so that the largest reductions in melting occur in regions where the greatest positive melting is observed (Rignot et al., 2013a). Areas where basal melt rates are low to begin with are therefore replaced with low magnitudes of refreezing as the overall melt rate becomes negative. Given the current high rates of basal melting in the region (Adusumilli et al., 2020) and limited observations of periods when these melt rates are consistently lowered, observations of the pattern of melt rates with a lowered average are lacking. Maintaining elevated basal melting at the deepest parts of the shelf is consistent with the physical processes of melting, while plume models indicate refreezing occurs over shallower portions of the ice shelf with a flatter basal gradient (Lazeroms et al., 2018) which is replicated here.

Throughout this chapter, the period over which the basal melt forcing (anomaly) is positive and negative are described as the retreat and advance phases respectively. In some simulations there may not be any grounding line advance or mass gain in the advance phase. The term ‘forcing’ is used synonymously with sub-ice shelf melt anomaly.

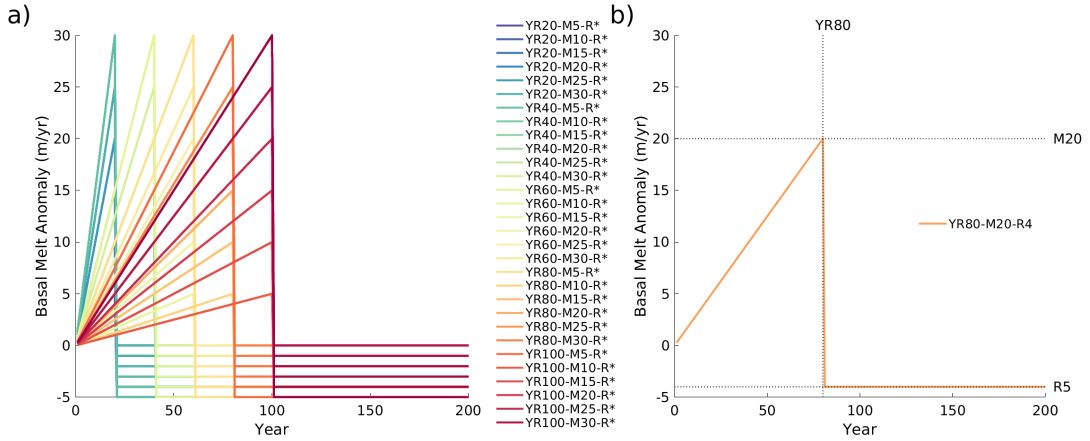


Figure 3.2: a) Ensemble of ASE ice shelf melt rate anomalies (m yr^{-1}) that are concentrated at the grounding line, line colours are grouped by the retreat phase. b) Example of individual simulation forcing, YR80-M20-R4.

Here, and throughout the following research chapters, mass loss from the region is quantified as the change in the ice volume above floatation relative to the initial state of the model and presented as an equivalent sea level (SLE) contribution. The change in ice volume above floatation (ΔVAF) is the amount global eustatic sea level changes by through a change in displacement which is the ice equivalent volume. The ΔVAF of ice equivalent is converted to its equivalent mass in gigatonnes

$$\text{Mass (Gt)} = \Delta\text{VAF (km}^3) \times \rho_i \text{ (Gt km}^{-3}) \quad (3.1)$$

which is then converted to freshwater volume equivalent as 1 Gt of freshwater = 1 Gt of ice

$$\text{Volume of freshwater equivalent (km}^3) = \text{Mass (Gt)} \times \rho_w \text{ (Gt km}^{-3}). \quad (3.2)$$

The height of sea level change is then calculated using the following equation

$$\text{Height (km)} = \frac{\text{Volume (km}^3)}{\text{Area (km}^2)} \quad (3.3)$$

Giving,

$$SLE (km) = \frac{Freshwater Volume (km^3)}{361 \times 10^6 (km^2)} \quad (3.4)$$

where $361 \times 10^6 \text{ km}^2$ is an estimate of the total area of the Earth's oceans.

Finally, units are converted from kilometers to millimetres by

$$SLE (mm) = SLE (km) \times 10^{-6}. \quad (3.5)$$

3.3 Results

3.3.1 Sea Level Contribution

In response to the ensemble of forcings, the ASE contributes an equivalent mass to raise global mean sea level by 28 to 84 mm (fig. 3.3) over 200 years. For each subset of negative melt rate (R) values, the SLE at the end of the simulation is related to both the magnitude and duration of the initial forcing. Simulations with longer durations of positive basal melt anomalies (e.g. YR100-M30-*) result in the greatest SLE contribution while the forcing is applied. Although positive basal melting is increased linearly, SLE increases non-linearly for all simulations while positive forcing is applied. The rate of SLE contribution ($\delta SLE \delta t^{-1}$) reaches a peak (fig. 3.4), and declines at the end of the positive melting phase as the positive melt anomaly is removed. For every simulation, the $\delta SLE \delta t^{-1}$ declines following the removal of forcing and application of negative melt rate anomaly (fig. 3.4) which curbs and limits the total SLE contribution.

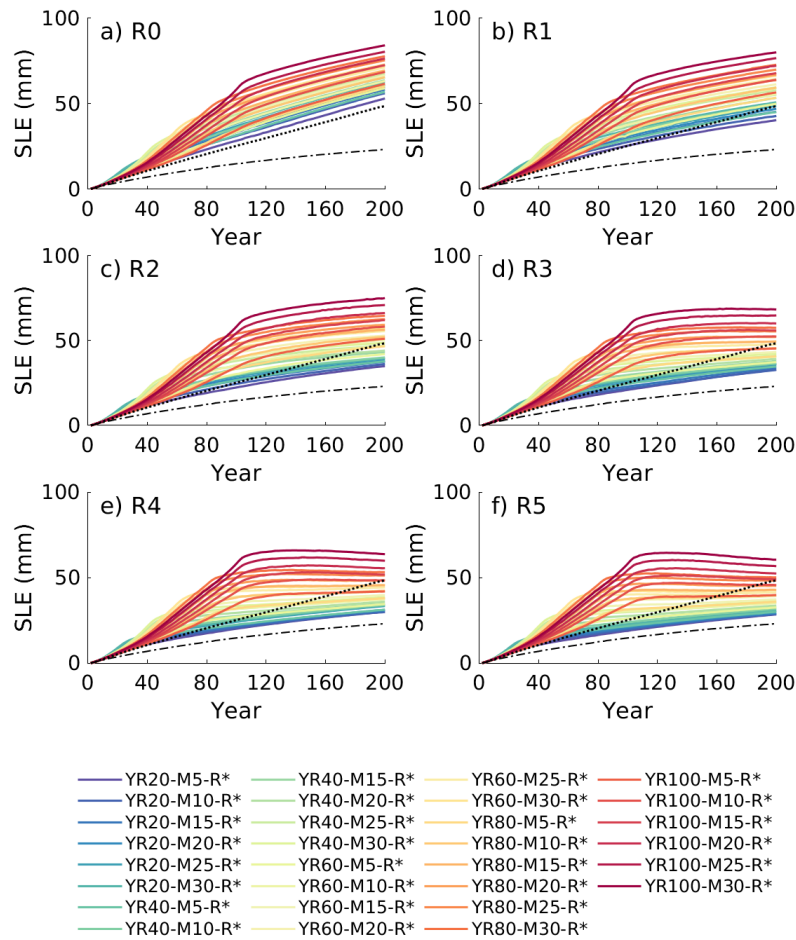


Figure 3.3: Total sea level equivalent (SLE) contribution over the 200 year simulations. Each panel includes simulations for a single set of negative melt rate anomalies (R). Black dotted line shows the contribution for the control simulation and the dot-dash line is the Zero simulation.

The $\delta\text{SLE } \delta t^{-1}$ contribution in the advance phase is dependent on the magnitude of the retreat phase, where simulations of longer durations of positive anomalies with higher magnitudes are most inclined to gain mass during the advance phase with negative anomalies. Simulations with the greatest magnitude and duration of positive forcing such as YR100-M30-*, result in the lowest $\delta\text{SLE } \delta t^{-1}$ contribution during the advance phase with negative melt rate forcing. In YR100-M30-R5, $\delta\text{SLE } \delta t^{-1}$ reaches a peak of 0.9 mm yr^{-1} at 110 years in the simulation which decreases to -0.09 mm yr^{-1} at year 140. As the $\delta\text{SLE } \delta t^{-1}$ becomes negative, the region experiences mass gain which re-

sults in a fall in global sea level. In contrast, shorter retreat phases of lower magnitudes such as the YR20-M5* simulations result in a reduction in the rate of SLE contribution after the negative melt rate is applied, the rate of mass loss remains positive for all magnitudes of negative melt rate (R values). Therefore, simulations with greater positive phases are more prone to regrowth following retreat.

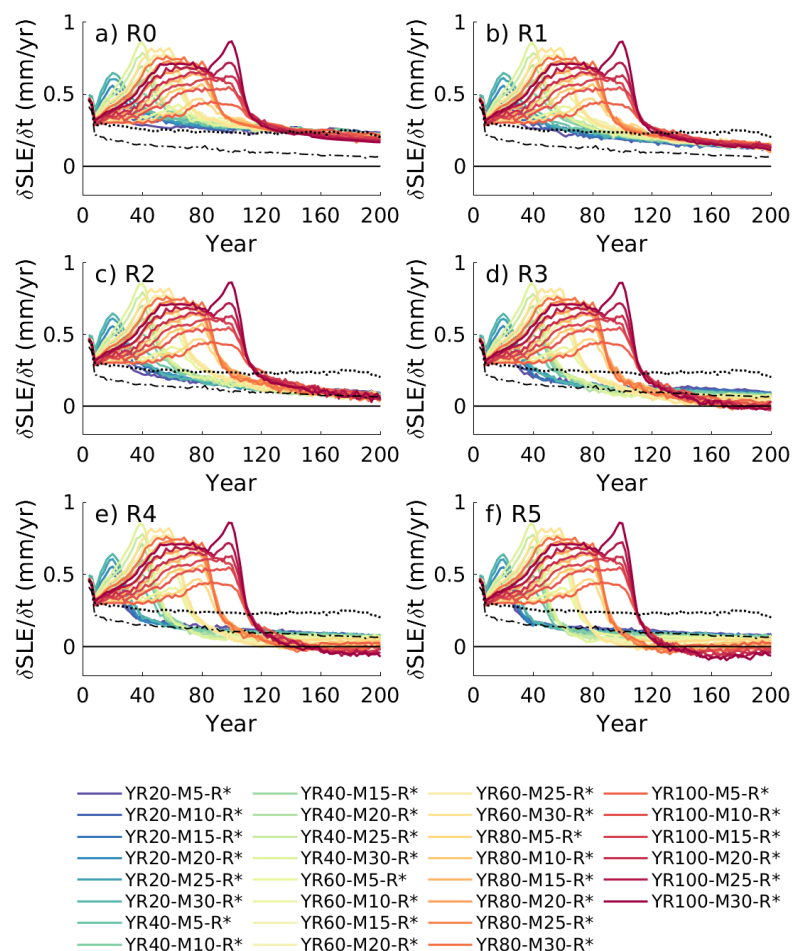


Figure 3.4: Rate of sea level equivalent ($\delta\text{SLE} \delta t^{-1}$) contribution with ten year averaging applied. Each figure panel includes simulations for a single set of negative melt rate (R) values. Black dotted line shows the rate of SLE contribution for the control simulation and the dot-dash line is the Zero simulation.

There is a minimum committed SLE contribution from the ASE (fig. 3.5) which is demonstrated by an asymptotic decrease in SLE at the lower end of the distributions as basal melting is linearly reduced. By contrast, there is an almost linear reduction

in the upper bound of the SLE envelope. The largest reduction in the lower tail end SLE contribution of 12.7 mm occurs between the R0 and R1 subsets, with the smallest reduction of 1.4 mm occurring from R4 to R5. This contrasts with the simulations with the highest cumulative forcing (upper tail), where an increase in the magnitude of negative basal melt anomalies leads to a consistent reduction in SLE of ~ 5 mm. Furthermore, with an increase in the R value, the distribution of SLE from each set of 30 simulations becomes more positively skewed, with a greater upper tail on the distribution and with medians closer to the lower quartile of the distribution.

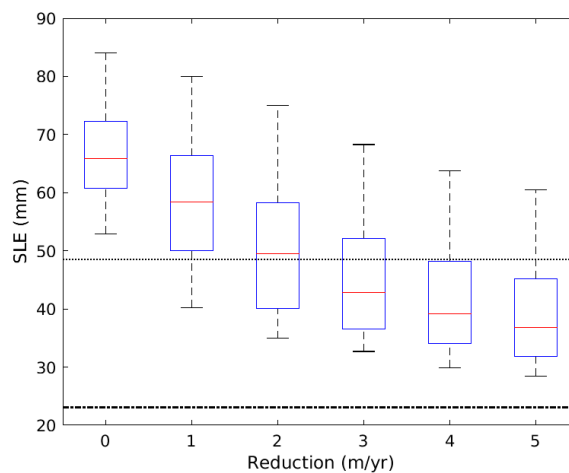


Figure 3.5: Distribution of SLE contribution at the end of the simulations, each box-plot represents a subset of 30 simulations each with the same magnitude of negative basal melt anomalies (R). Dashed black line shows the SLE contribution for the control simulation. Dash-dot black line shows the SLE contribution for the zero basal melting simulation.

3.3.2 Grounding Line Positions

In year 200 of the simulations, the grounding line positions cluster according to the magnitude of negative melt rate anomaly (fig. 3.6). For the R0 simulations, the grounding lines of PIG and TG retreat to the same position while the grounding lines of PSK vary according to the cumulative positive melt anomaly (both duration and magnitude), where simulations with the greatest cumulative positive forcing show the greatest extent of grounding line retreat. In contrast, the close proximity of grounding lines for simulations with varying cumulative positive forcings suggest that the PIG and TG grounding lines are retreating to a position of stability upstream of the initial grounding lines.

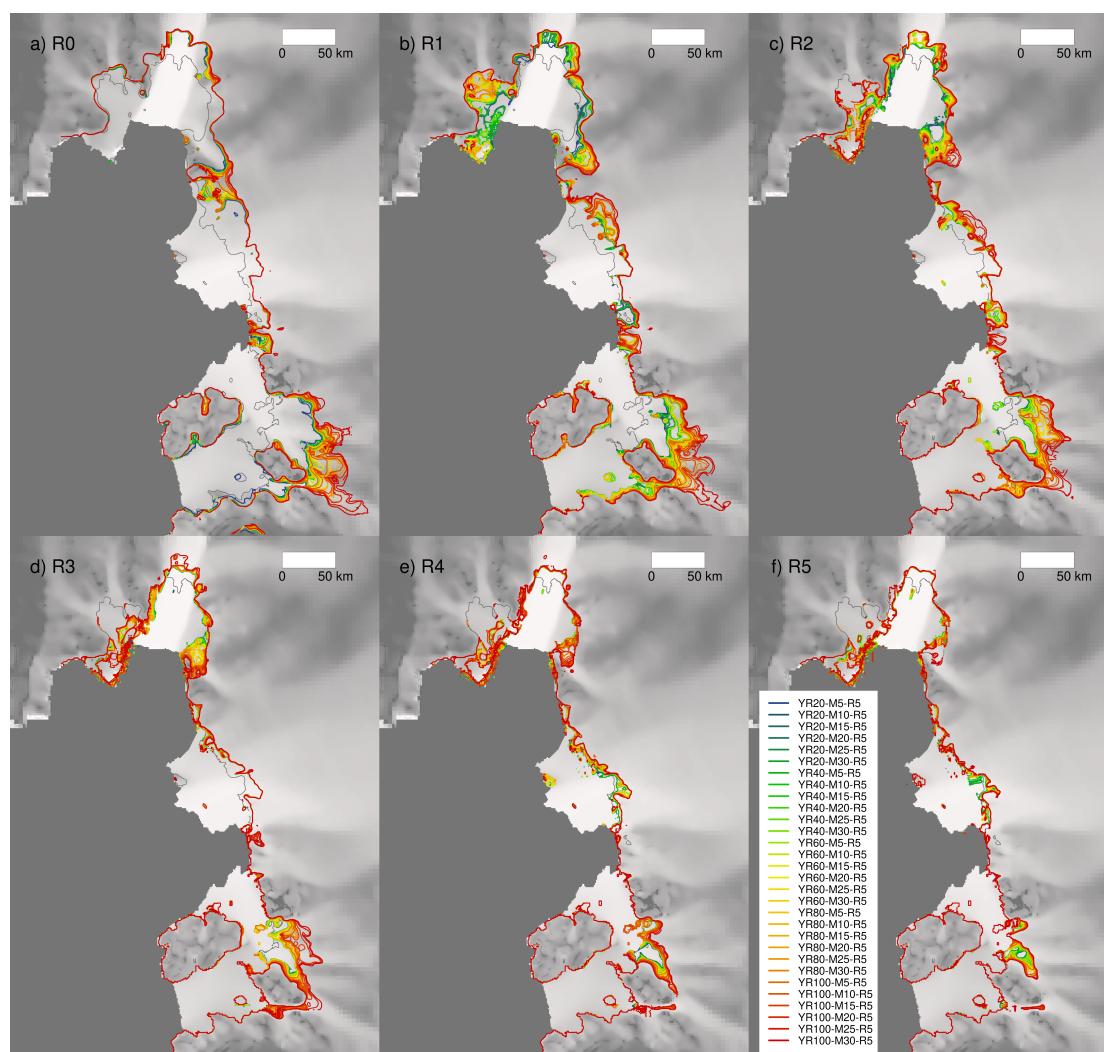


Figure 3.6: a-f) Grounding line positions in the year 200 for each simulation. Panels are separated by the magnitude of the negative melt rate anomaly in m yr^{-1} (R^*). Grey lines in each panel represent the initial grounding line position in year 0.

The R1 and R2 subsets have the greatest spread in end of simulation grounding line positions, where greater positive cumulative forcing results in greater retreat. The differences in end of simulation grounding line position for these two subsets is consistent with the large range in SLE contribution at the end of the simulation (fig. 3.5). The most notable differences in grounding line positions for simulations within each subset occur along the Southwestern Tributary of PIG, and PSK (fig. 3.6).

The largest difference in final grounding line positions between different sets of R values occurs from R0 and R1, which is consistent with the change in the spread of SLE contribution over the period (fig. 3.5). The Southwestern Tributary retreats into

TG in R0, resulting in a lengthening in the grounding line due to a retreat of TG eastern grounding line $\sim 40\text{km}$ inland. In contrast, while the central grounding line of TG is seen to retreat inland in the R1 simulation, the retreat of the Southwestern Tributary of PIG is more limited. For both R0 and R1 there is a dependence of grounding line position of PSK on the magnitude of increased basal melt and therefore grounding line position is determined by the retreat phase. That being said, the spread in grounding line position is greatest for R1 where the reduction in basal melting causes an advance in grounding line positions for simulations with lower cumulative forcing.

A negative melt rate anomaly of 4 m yr^{-1} (R4) is required to re-advance the grounding line of TG to approximately its initial position (fig. 3.6). Though the grounding line of PIG advances following removal of forcing for R1-5, the grounding line along the main trunk does not advance over the 10 km of retrograde bed that is situated upstream of the initial grounding line. The grounding lines of Pope and Smith Glaciers remain retreated, while Kohler Glacier, the smaller of the three ice streams advances.

3.3.3 Individual Drainage Basin Response

The drainage basin (drainage basin) contribution varies due to the difference in sensitivity to forcing (fig. 3.7). PIG loses the most mass in these simulations, with a maximum SLE contribution of 32 mm, compared with 28 mm and 24 mm for TG and PSK respectively. PIG is the most sensitive to melt forcing of all ASE drainage basins, which is shown through the large range in end of simulation SLE contribution from 8 to 32 mm. When no melting occurs beneath the ice shelf in the Zero simulation, the SLE contribution after 200 years is 2 mm while the Control simulation results in a linear SLE contribution, reaching a total of 17 mm following 200 years of constant present day basal melt rates. The large difference in mass loss between the Zero and Control simulations demonstrates the sensitivity of the ice stream to present day forcing.

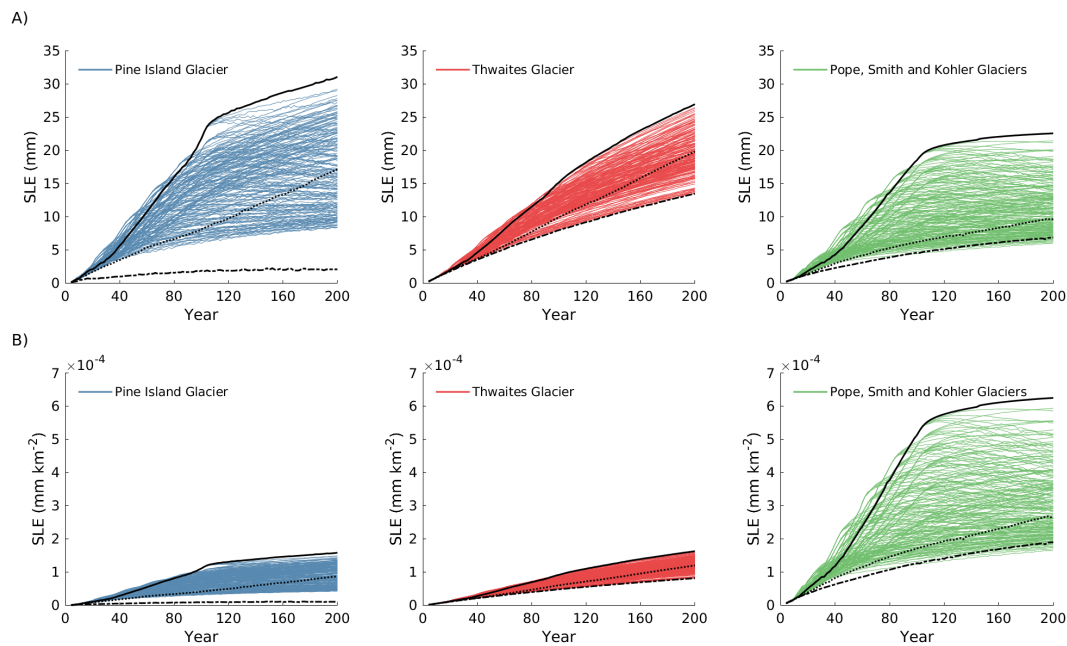


Figure 3.7: A) Sea level equivalent (SLE) contribution for all simulations separated by drainage basin. B) SLE per square kilometer of drainage basin area for each drainage basin. Black filled lines define the YR100-M30-R0 simulations for each drainage basin. Black dotted lines and dash dotted lines define the SLE contribution from the control simulation and the Zero simulation respectively.

TG has the greatest committed dynamic mass loss of all ASE ice streams (fig. 3.7). The Zero simulation results in a SLE contribution of 13 mm by the end of the simulation from TG, demonstrating that projected mass loss is dominated by present-day behaviour. Further, the YR100-M30-R0 simulation results in a quasilinear increase in mass loss from TG over the period, with a $\delta\text{SLE } \delta t^{-1}$ of 0.1 mm yr^{-1} from years 120 to 200 during the advance phase, again demonstrating that the dynamic mass loss from the drainage basin is substantial and removal of the positive forcing does little to mitigate mass loss from the ice stream.

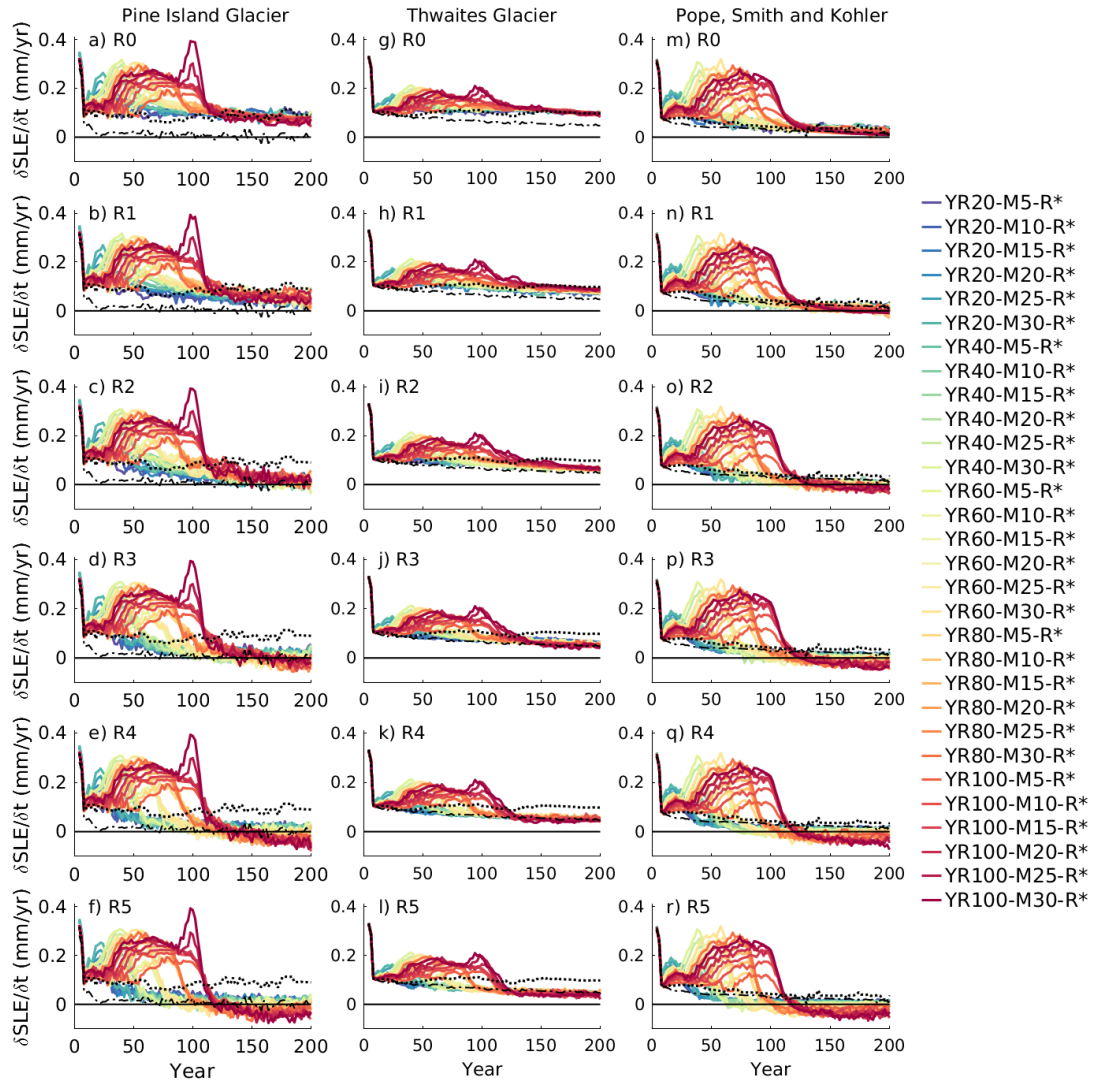


Figure 3.8: Rate of sea level equivalent ($\delta\text{SLE } \delta t^{-1}$) contribution for each ice stream separated into panels based on magnitude of reduction. Black dotted lines and dash dotted lines define the SLE contribution from the Control simulation and the Zero simulation respectively.

The large dynamic mass loss from TG may not be indicated by the position of the grounding line. Unlike PIG, a negative melt rate anomaly of 5 m yr^{-1} is insufficient to result in mass gain of the TG basin, with the mass loss gradient remaining positive during the advance phase for the entire ensemble (fig. 3.8). However, for all R5 simulations, the grounding line of the ice stream advances to its initial position (fig. 3.6), despite a rate of mass loss of $\sim 0.1 \text{ mm yr}^{-1}$.

PSK are most sensitive to the removal of forcing, where the $\delta\text{SLE } \delta t^{-1}$ in the advance phase in R0 simulations is the lowest of all ASE drainage basins, averaging 0.03 mm yr^{-1} from years 150 to 200. Furthermore, the magnitude of mass loss diverges during the retreat phase which also demonstrates mass loss is sensitive to perturbed positive melt anomalies. The smaller ice streams show the greatest SLE contribution accounting for the area of the drainage basin also, ranging from $1.9 \times 10^{-4} \text{ mm km}^{-2}$ to $6.4 \times 10^{-4} \text{ mm km}^{-2}$.

With the individual basin SLE response, there appears to be basin dependent differences in the relationship between positive and negative phases and the SLE contribution. To assess the basin dependent response to forcing (fig. 3.7), three multiple linear regression analyses are performed for each drainage basin (Table 3.3.3) with the response variable being end of simulation SLE (mm). The predictor variables are β_1 the duration of forcing in years (YR), β_2 is the maximum magnitude of positive basal melt anomaly (M) and β_3 is the magnitude of negative melt rate anomaly (R*). The models each have high R-squared values of 0.93, 0.95 and 0.9 for PIG, TG and PSK respectively.

Linear Regression Model Coefficients			
	PIG	TG	PSK
β_0 (mm)	13.35	17.92	5.69
β_1 Duration (yr)	0.12	0.05	0.09
β_2 Magnitude (m yr^{-1})	0.20	0.12	0.19
β_3 Reduction (m yr^{-1})	-2.55	-1.46	-1.16

TG is observed and predicted to contribute the greatest amount of mass to sea level rise in the absence of additional melting, whereas the projected mass evolution of PIG is the most sensitive to perturbations in melt rate anomaly. The β_0 value of 17.9 mm of SLE contribution from TG is a result of dynamic mass loss in the absence of forcing. The TG β_1 is 0.07 mm lower than that for PIG, therefore the larger ice stream is less sensitive to the duration of elevated basal melting than its neighbour. Furthermore, TG is less sensitive to the magnitude of negative anomaly than PIG, with -1.46 mm of SLE from a 1 m yr^{-1} reduction compared with PIG's -2.55 mm.

PSK are more sensitive to positive melt forcing than TG as shown by their higher β_1 and β_2 values. However, the dynamic mass loss from the region shown by the β_0 of

5.69 mm, is less than half of that for PIG and a third of TG. Furthermore, the regression model suggests that the smaller ice streams are less sensitive to the negative melt rate anomaly, as shown in the lowest β_3 value.

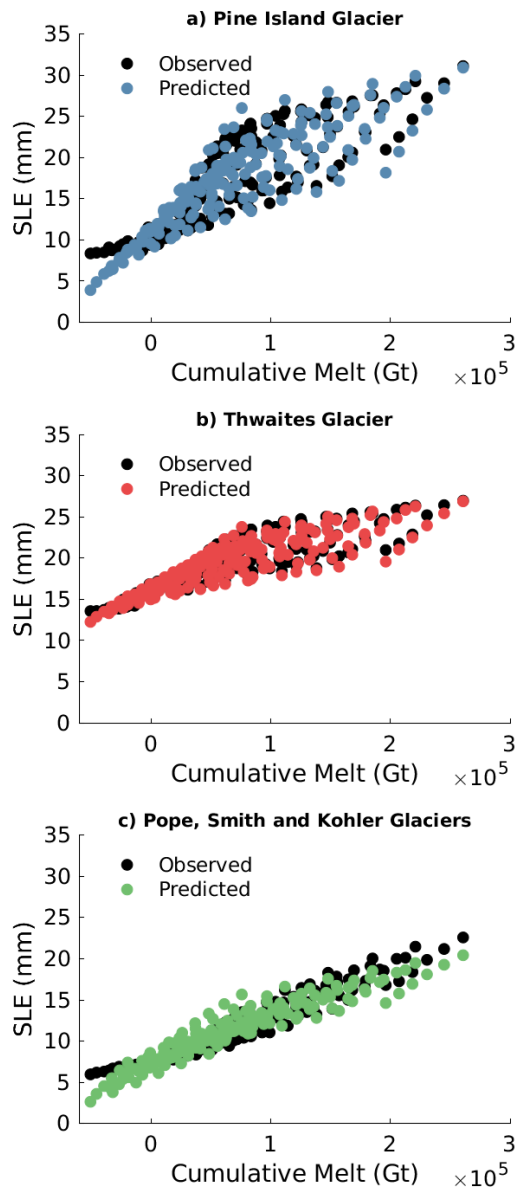


Figure 3.9: Relationship between cumulative melting (total meltwater production over the simulation) and SLE contribution for each drainage basin. Coloured markers indicate the measured values while the black markers represent the predicted values according to the multilinear regression model.

3.3.4 Specific Simulations: Equivalent Sea Level Contribution

The relationship between cumulative basal melt and SLE contribution is complex because it depends on the duration and magnitudes of positive and negative melt rate anomalies for each simulation. This can be seen with two example simulations, YR20-M5-R0 and YR100-M20-R5, which have different forcings and cumulative melt but the same SLE at the end of the simulation of ~ 53 mm. The higher cumulative forcing simulation YR100-M20-R5 experiences a high SLE contribution while the positive forcing is being applied over the first 100 years with an accelerating mass contribution. However, after 100 years, as the melt rate anomaly becomes negative there is a curbing in the SLE contribution, where the rate of SLE becomes negative after 120 years of the simulation. In contrast, the YR20-M5-R0 simulation experiences near linear SLE contribution over the 200 years despite the removal of forcing. This insensitivity to the removal of forcing is consistent with the earlier results.

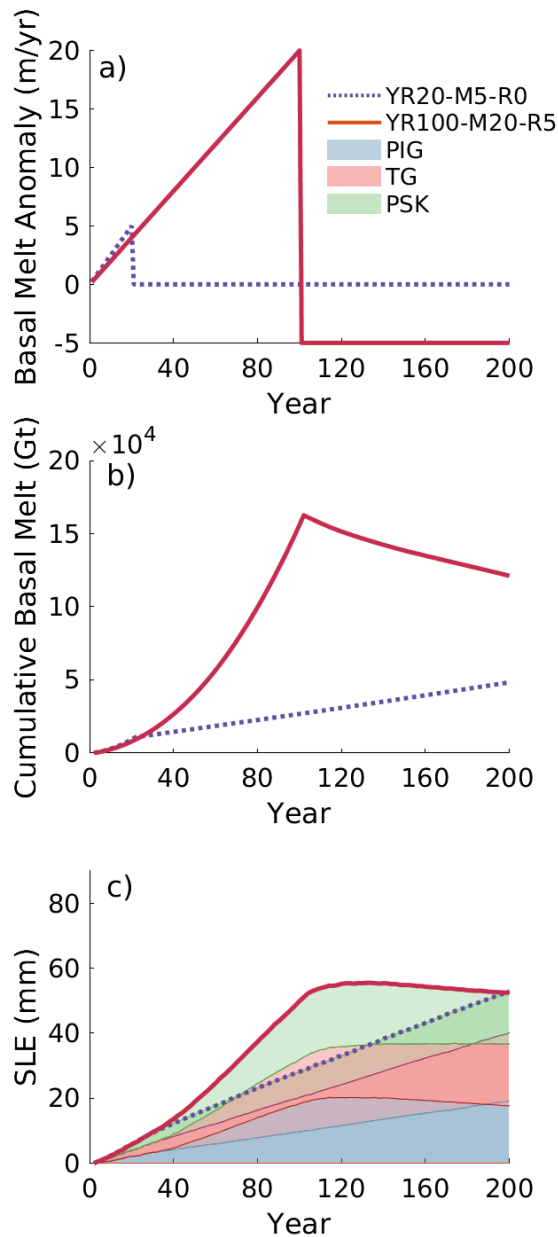


Figure 3.10: Time series of a) annual basal melt anomalies b) cumulative basal melt and c) SLE contribution for simulations YR20-M5-R0 and YR100-M20-R5 over 200 years. SLE contribution (c) is separated into individual drainage basin contribution for the two simulations shown by coloured shading.

The linear SLE contribution (fig. 3.10) is replicated in the consistent grounding line retreat in the YR20-M5-R0 simulation over the 200 year simulation (fig. 3.11). Over the first 50 years the grounding line of the PIG trunk retreats 10 km upstream with 20

km of retreat along the Southwestern tributary. The TG grounding line retreats 15 km upstream in the first 50 years with more retreat occurring in the eastern side of the ice stream. The greatest extent of retreat during this time occurs in the PSK ice streams. Following the removal of forcing 20 years into the simulation, the grounding line retreat continues, with little evidence of any pause in retreat in response to the lowered forcing. Furthermore, both grounded and floating ice thins over the domain by an average of 300 m.

In contrast, the pattern of grounding line change is different for YR100-M20-R5. While the grounding lines of PIG and TG retreat to almost the same position as YR20-M5-R0, this occurs over the first 100 years and is followed by grounding line advance back to its original position. PSK grounding lines retreat by up to 40 km more in the 100 years of forcing than the YR20-M5-R0 simulation does over 200 years. For PIG the final grounding line position in the YR100-M20-R5 simulation sits ~ 10 km upstream from the initial grounding line and the Smith Glacier grounding line also does not advance to its original position. Grounding line advance coincides with ice shelf thickening relative to the initial thickness, though grounded ice over the domain experiences thinning. Furthermore, this grounding line advance helps to explain the reduction in cumulative melt following the application of the negative anomaly where reduced ice shelf area means a reduced area experiencing melting and lower overall melting (fig. 3.10b).

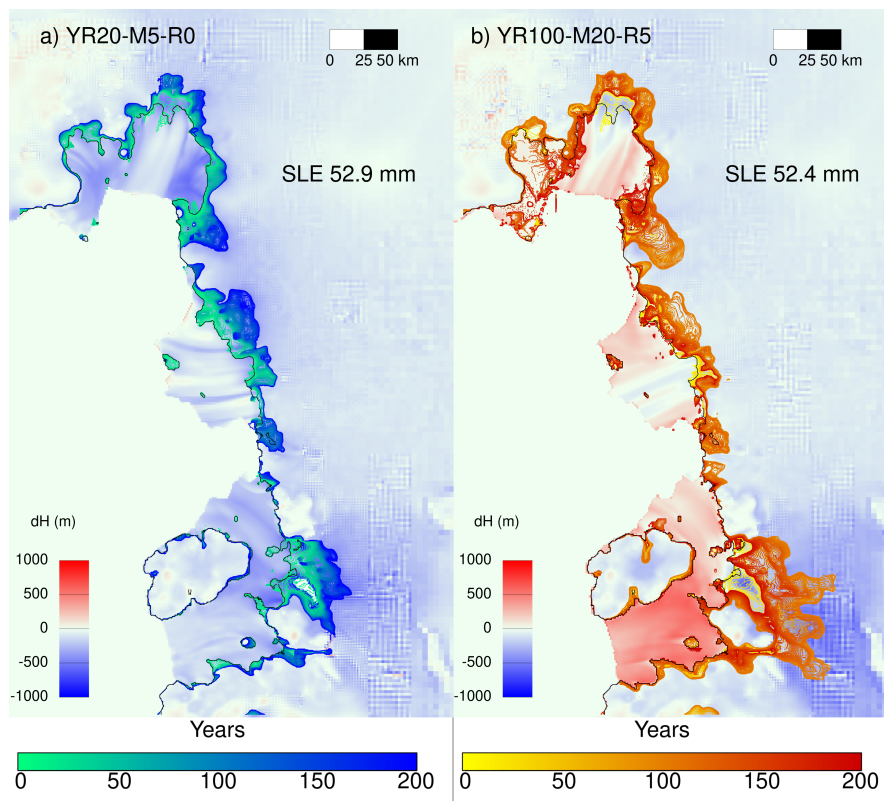


Figure 3.11: Grounding line positions for the a) YR20-M5-R0 and b) YR100-M20-R5 simulation plotted every 2 years of the simulation where the colour gradient evolves through time. Background is the thickness change (δH) in the year 200 relative to the initial thickness.

3.4 Discussion

In these experiments, sub-ice shelf melting in the ASE is reduced following a period of forced retreat in order to explore the regrowth and re-advance of the region's ice streams. While the magnitude and spatial pattern of the melt rate anomalies are idealised, the experiment gives insight to the dynamic behaviour of the region should a prolonged reduction in basal melting take place through local ocean cooling. These results show that total ASE mass loss is sensitive to positive perturbations in basal melting but can be limited with prolonged periods of reduced melt rates relative to present-day. In all simulations, the removal of the positive melt rate anomaly results in a reduction in the rate of sea level contribution (fig. 3.4), where large negative melt anomalies cause ice to thicken both dynamically and through marine ice accretion, and cause grounding lines to re-advance (fig. 3.6). Even with ice shelf melt rates over the retreat phase reaching up to 30 m yr^{-1} above present day over 100 years, mass loss from the ASE

is limited to 84 mm with relatively moderate grounding line retreat over TG and PIG. Therefore, extended periods of reduced melting beneath ASE ice shelves can help to stabilise ASE ice streams, limit mass loss and mitigate collapse of the region in the next two centuries.

Reducing the minimum contribution from the ASE will require mass gain to equilibrate the system and offset the committed mass loss. As the melt anomaly becomes sequentially more negative, there are diminishing returns in the amount by which SLE is reduced at the lower end of the ensemble range (fig 3.5). The convergence on a minimum value coincides with the 22 mm contribution from the Zero simulation, suggesting that the reduction in forcing explored in this ensemble is insufficient to compensate for the committed dynamic mass loss. This committed SLE contribution occurs because of the high rates of ice discharge due to increased velocities in the last few decades (Mouginot et al., 2014), with the ASE being already in a state of disequilibrium (IMBIE, 2018). Offsetting this minimum mass contribution will therefore require increased mass gain, most realistically through increased surface accumulation, to balance the mass loss and discharge. As precipitation is expected to increase with a warming climate (Donat-Magnin et al., 2021; Previdi and Polvani, 2016), future trends could provide some of this offset.

Although some simulations show grounding line advance with application of a negative melt anomaly, this does not necessarily coincide with mass gain. In YR100-M20-R5 for example, despite large extents of retreat and mass loss, the grounding lines of TG, Smith and Kohler re-advance to near their initial position. While the grounding lines advance, TG continues to lose mass with a $\delta\text{SLE}/\delta t^{-1}$ above zero (fig. 3.8). TG mass loss is mostly committed (table 3.3.3) as a result of the disequilibrium of the initial state of the glacier combined with high discharge as a result of its wide trunk and fast flow (Mouginot et al., 2019; Milillo et al., 2019). This finding would suggest that although grounding line position, namely whether or not it is situated on retrograde or prograde bed, is widely discussed as being a key indicator of ice stream health, here, grounding line advance does not necessarily indicate reduced ocean displacement and net mass gain. That being said, the reduction of basal melting and occurrence of re-freezing in simulations that experience extensive grounding line retreat and thinning does curb the upper limit of mass loss and slow mass loss through re-grounding and ice shelf thickening.

The dynamic response of the ASE to positive forcing may reflect MISI. The reduction of positive melt anomalies to present day values following perturbation, as are shown in the R0 simulations, gives an indication of the dynamic response to multi-decadal periods of increased melting. Despite the differences in cumulative melting, the simulations with R0 forcings result in an equivalent extent of grounding line retreat for PIG and TG. The end of simulation grounding line position occurs where local topographic highs exist (Morlighem et al., 2020), which act to pause the retreat (Schoof, 2012, 2007). However, whilst grounding lines retreat to the same position, the total range in mass loss for R0 simulations is 31 mm (fig. 3.5). This range in total mass loss is dictated by the divergence in the rate of mass loss during the retreat phase, which varies according to the cumulative forcing (fig. 3.4). Subsequently, upon removal of forcing, these differences are sustained. Therefore, whilst all R0 simulations may experience grounding line instability, the range in end of simulation SLE differs according to the magnitude and duration of the positive retreat phase.

Simulations with the greatest cumulative melting in the retreat phase have the greatest reduction in SLE contribution in the advance phase. An example of this is YR100-M20-R5 (fig. 3.10). Although the grounded ice over the domain experiences thinning relative to its initial state, overall the ice shelves thicken (fig. 3.11). In response to increased positive melt anomalies, YR100-M20-R5 experiences high rates of ice shelf thinning leading to reduced buttressing which drives upstream dynamic thinning and grounding line retreat (fig. 3.11). This thinning and subsequent lowering in surface slope around grounding lines lowers the driving stress (Paterson, 1994) in this vicinity. Therefore, upon reduction in the positive melt forcing, the velocity in the central trunk is lowered. In the advance phase, as the anomalies become more negative, the grounding lines advance with increased delivery of thick ice toward the grounding line (fig. 3.11). Furthermore, thicker ice shelves, especially those that thicken and locally ground, result in increased buttressing which therefore provide more resistance to flow. As a result, ice discharge into the ocean is lowered for simulations with high positive followed by negative anomalies.

Here the ice streams that flow into topographically confined ice shelves are most sensitive to the application of positive melt anomalies. PIG and PSK have higher β_1 and β_2 values than TG meaning these ice streams have a greater mass change response to equivalent perturbations in forcing. PIG, Dotson and Crosson ice shelves are shown to

have high buttressing potential (Fürst et al., 2016) and control the flow of upstream ice (Gudmundsson, 2013; Gudmundsson et al., 2019). Therefore, with increased thinning and reduced buttressing through increasing durations of positive melt anomalies, mass loss as a result of increased discharge is expected. While this sensitivity to positive melt anomalies is not replicated in the absolute response to the negative anomaly, where PSK has a lower β_3 than TG, the relative sensitivity is higher for PSK given the size of its basin. The PSK β_3 is equivalent to 20 % of its committed SLE contribution (shown by the β_0) while the TG β_3 is 12 % of its β_0 . Therefore, while the dynamics of ice streams with confined ice shelves are sensitive to positive basal melting anomalies, the relative contribution and size of the ASE drainage basins need to be accounted for when considering the sensitivity to negative forcing.

Although the regression model is unable to capture the lower end of the cumulative forcing simulations (fig. 3.9) with high reduction (R) values and low durations (YR) and magnitudes (M), the model does well at capturing the overall spread and range of data. The inability to capture the SLE contribution from simulations with the lowest cumulative melting could stem from the non-linearity of the response. The lower end of SLE contributions exhibit diminishing returns in the magnitude of reduction (fig. 3.5) where reductions in melt rate at the lowest end of the range do little to further offset the dynamic, committed contribution to SLE.

Limitations and Future Work The basal melt anomaly parameterization scales the magnitude of the anomaly as a function of distance from the grounding line, where the highest anomalies occur at the grounding line and are reduced with increased distance. Applying this melt rate as an anomaly means focal points of high melting in the background melt field experience a relatively small reduction in basal melting, specifically the main trunk of PIG and Western TG. However, not all areas at the grounding line have initially high melting (Dutrieux et al., 2014b; Rignot et al., 2013a). Areas initially with low magnitude basal melting along the grounding lines experience a high reduction in basal melting resulting in a wide area of refreezing occurring simultaneously with points of high melting. Alternative idealised parameterizations based on depth could be employed (Favier et al., 2014), but there is no clear relationship between ice shelf melting and depth for ASE ice streams (Seroussi et al., 2014) due to the role of cavity circulation and local geometric variability (Goldberg et al., 2019; Gourmelen et al., 2017).

The amount by which the melt rate is reduced in the advance phase is limited to -5 m yr^{-1} . With this magnitude of negative anomaly there is evidence of grounding line advance past the initial grounding line, though this occurs in areas which impact the main ice stream dynamics little such as the northern ice shelf of PIG. When the grounding line advances past its initial position, ice begins to slide over bedrock with a sliding coefficient of zero, given that the inversion of this parameter in the initialisation procedure can only take place for grounded ice. With this in mind, the magnitude of reduction is restricted to a maximum value that resulted in the grounding line position returning to near its initial position, which has been achieved with this ensemble. Furthermore, areas with grounding line advance have been masked from the calculations to obtain SLE. However, in some simulations where the grounding line advances past the initial position, the ice that grounds in advance of the initial grounding line will be represented more closely to an ice shelf with zero basal shear stress, more representative of a lightly grounded ice plain providing equivalent buttressing to a thick ice shelf rather than grounded ice which is not entirely unrealistic.

This investigation uses a fixed calving front as a numerical solution to ensure the model behaviour remains regular, a practice that is common in ice sheet modelling investigations (Seroussi et al., 2014; Cornford et al., 2015). Setting a minimum ice thickness ensures ice shelves that may have disintegrated in response to elevated melt rates and dynamic thinning will not act to buttress the grounded ice upstream. However, in the advance phase when ice shelf thickening occurs this happens over a predefined extent. Therefore, for example, thickening the PIG ice shelf will enhance the ice shelf buttressing which contributes to the sensitive response of the ice stream to basal melting (Gudmundsson, 2013). In reality, in response to elevated basal melting and increased ice flux the calving front has been shown to retreat and the ice shelf geometry to change (Lhermitte et al., 2020). As ice shelf geometry controls upstream ice dynamics (Fürst et al., 2016; Joughin et al., 2021), calving front migration of confined ice shelves would likely impact the response of the ice stream to reduced basal melting.

The behaviour of the grounding line in these simulations is controlled by the topography. This is shown most clearly in the R0 simulations where the grounding lines of PIG and TG experience dynamic retreat to positions on topographic maxima. Subsequently, the role of grounding line retreat and advance and the promotion of re-growth will be partly dictated by the use of the Bedmap2 topography product. With an alterna-

tive topography, the modelled response of ice streams to forcing may differ. To explore this, the use of an alternative product could be used such as BedMachine (Morlighem et al., 2020) or statistically produced bed topographies to explore the uncertainty associated with the bed topography could be explored (Wernecke et al., 2022; Castleman et al., 2021). Furthermore, this investigation neglects topographic uplift through vertical land movement which has been shown to occur over decadal timescales in the ASE Barletta et al. (2018); Gomez et al. (2015) which could promote stability (Castleman et al., 2021; Whitehouse et al., 2019).

3.5 Conclusion

Here, a 182 member ensemble of ice sheet model simulations was performed to investigate the regrowth of ASE ice streams following retreat. The results show that mass loss in response to increased ocean forced basal melting can be limited for simulations with high cumulative forcing through the reduction of basal melting and refreezing. For simulations with 80-100 years of elevated basal melt rates, removal of a positive melt anomaly allows the ice shelves to thicken and grounding lines to re-advance. Prolonged reductions in sub-ice shelf melting limits the upper end of mass loss contribution from the region, with glaciers that have experienced the greatest extent of thinning subsequently resulting in the greatest reduction in the rate of mass loss in response to reduced melting and refreezing. In contrast, limiting the mass contribution from simulations with lower initial perturbation of basal melting is more challenging, with a diminishing return on the magnitude of reduction due to the disequilibrium of the initial system and high committed dynamic mass loss. As a result, even with a curbing of mass loss following the reduction of forcing, the minimum contribution of 23 mm over 200 years from the region which occurs despite grounding line advance to near its initial position.

There is a clear ice stream dependence in the response to both positive and negative melt anomalies. Of the three drainage basins in the ASE, the ice streams with the confined ice shelves, PIG and PSK, are most sensitive to changes in basal melting through reduced buttressing. In comparison, TG has the greatest committed mass loss due to its initial dynamic disequilibrium and wide fast flowing trunk. For TG, a reduction in basal melting to -5 m yr^{-1} below its initial background melt field continues to contribute mass to sea level rise which occurs even with advance of the grounding line to

its initial position. These findings suggest that grounding line position, while a metric of overall ice stream stability, does not necessarily directly represent the health of the ice stream, as a re-advanced grounding line and thickening ice shelf can continue to result in a positive contribution to sea level rise.

This work could be augmented by the incorporation of an alternative method of parameterizing melt anomalies to incorporate the relationship between ice shelf melting and depth and the inclusion of a migrating calving front. However, this would require further computational expense and may be numerically challenging to implement.

Chapter 4

Understanding the modelled response of Pine Island Glacier to varied basal melting

4.1 Introduction

Pine Island Glacier (PIG) in West Antarctica is the single largest contributor to sea level rise from Antarctica (Shepherd et al., 2018; Bamber et al., 2018). Since the 1990s, the satellite record has captured acceleration of the ice stream (Rignot et al., 2011; Mouginitot et al., 2017; Joughin et al., 2019) which has coincided with grounding line retreat (Konrad et al., 2018) and spatially heterogeneous thinning (Bamber and Dawson, 2020). Additionally, optical remote sensing has provided high resolution imaging of large calving events (Arndt et al., 2018), ice front retreat and crevassing in the shear zone (Alley et al., 2019) which has lead to mechanical weakening of the glacier's floating ice shelf (Lhermitte et al., 2020; Arndt et al., 2018; Sun et al., 2017). Recent changes in the geometry of PIG have been dated back to the 1970s (Smith et al., 2017), when the ice stream unpinning and retreated from a ridge, initiating the current period of widespread ice front calving and grounding line retreat. Although modelling studies suggest the current rate of grounding line retreat could be evidence of the onset of instability (Favier et al., 2014), recent satellite based observations of surface elevation change of grounded ice suggest there could be negligible grounding line retreat over the next two decades (Bamber and Dawson, 2020; Joughin et al., 2010). With a complex history of ice flow

and geometry change, the present health of the glacier therefore remains uncertain.

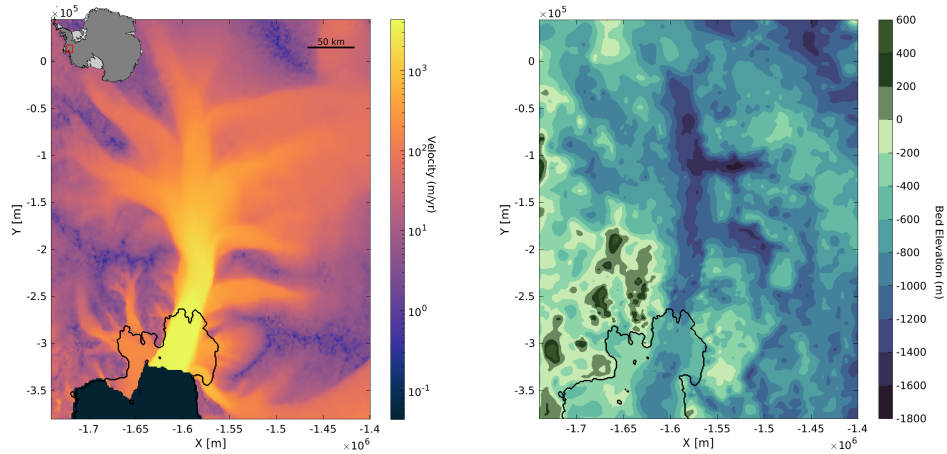


Figure 4.1: a) Map of Pine Island Glacier velocity over 2007-2009 (Rignot et al., 2011), red box shows location of glacier in Antarctica. b) Map of Pine Island Glacier bed topography elevation, black contour represents the grounding line.

The stability of PIG is dependent on the health of the ice shelf (Fürst et al., 2016; Haseloff and Sergienko, 2018; Pegler, 2018a). As the PIG ice shelf is constrained topographically, it provides a strong buttressing force on the grounded ice in the form of longitudinal membrane stresses that regulate the acceleration of ice upstream (Fürst et al., 2016; Gudmundsson, 2013; Gudmundsson et al., 2019). The high buttressing from the ice shelf is a key control on the present and future mass loss from the glacier (Fürst et al., 2016). Buttressing limits ice stream acceleration and mitigates the occurrence of MISI (Gudmundsson, 2013; Fürst et al., 2016; Reese et al., 2018b) to which PIG is vulnerable (Schoof, 2007). Although the central calving front of the ice shelf is considered passive (Fürst et al., 2016), the remainder of the ice shelf actively stabilises the flow of upstream ice (Reese et al., 2018b). Mechanical weakening and melt induced and dynamic thinning of the ice shelf reduces the buttressing of grounded ice causing increased ice flux into the ocean. As the extent and integrity of the ice shelf is critical for stability of the ice stream, changes to the material properties and geometry of the shelf will play an important role in the evolution of the ice stream.

Basal melt induced thinning of the ice shelf, and subsequent reduced buttressing, is responsible for the high rates of mass loss from PIG (Pritchard et al., 2012; Payne et al., 2007). The PIG ice shelf experiences melt rates of up to 250 m yr^{-1} (Shean

et al., 2019) adjacent to the grounding line. High magnitudes of melting at depth are attributed to the presence of a warm, saline, CDW which is transported toward Pine Island Bay causing ice shelf melting (Pritchard et al., 2012; Shean et al., 2019; Nakayama et al., 2014, 2018; Donat-Magnin et al., 2017). Circumpolar westerly winds are responsible for driving CDW toward the ASE (Thoma et al., 2008; Walker et al., 2013). In response to anthropogenic climate change, a more intense positive Southern Annular Mode phase is projected, causing a southward migration and strengthening in westerly winds (Bracegirdle et al., 2013) which are expected to increase the volume of CDW in Pine Island Bay. Subsequently, higher melt rates beneath PIG are projected under a variety of future warming scenarios (Gladstone et al., 2012; Ritz et al., 2015; Donat-Magnin et al., 2017). Furthermore, investigations show increases in melt rates can be enhanced by positive feedbacks through acceleration of meltwater plumes (Lazeroms et al., 2018) and a subsurface accumulation of heat from CDW due to increased meltwater at the surface (Golledge et al., 2019). Enhanced ice shelf melting and reduced buttressing could determine the occurrence of MISI (Gudmundsson, 2013). Capturing the future magnitude of basal melting beneath PIG is an essential component of projecting the future mass loss from the ice stream.

Recent modelling studies show the ice stream response to external forcing depends on ice sheet model parameters and tuning (Alevropoulos-Borrill et al., 2020; Nias et al., 2019; Brondex et al., 2019; Lowry et al., 2021). De Rydt et al. (2021) combined remote sensing data from 1996 to 2016 and ice flow modelling to diagnose the dominant drivers of change in flow of PIG by considering how processes such as calving, shelf thinning, material ice and bed properties influenced ice dynamics. When prescribing observed thinning and calving rates to the model, only 64 % of the observed change in flow over the 20 year period was accounted for (De Rydt et al., 2021). Instead, a modified representation of the bed in the model was necessary to fully capture observed changes in ice flow (Joughin et al., 2019). The calving front position, ice rheology and bed properties are shown to impact the ability of an ice sheet model to represent ice flow over a two decade period, rather than external climate forcing alone.

Here, the modified sensitivity of PIG to basal melting is explored when a retreating ice front and a viscous-plastic bed are incorporated in model simulations. A series of ice sheet model simulations are performed, first to understand the sensitivity of PIG to sub-ice shelf melting, and then to consider the role of model set up in altering ice

stream sensitivity to melting. The work builds upon De Rydt et al. (2021) by applying external forcing in the form of basal melting which incites geometry change, allowing for a natural evolution instead of prescribing direct thickness changes. Furthermore, by performing 200 year simulations the long term implications of geometry change and bed representation can be considered.

4.2 Methods

4.2.1 Experimental Design

The ice sheet model BISICLES is used to simulate the 200 year evolution of PIG in response to a series of 20 idealised scenarios of basal melting with three different model set ups or configurations. Twenty simulations with varied sub-ice shelf melt rate anomalies are performed using a reference model configuration to explore the ice stream sensitivity to melting. For two alternative model configurations, the low and high melt anomalies, or forcings, from the 20 member ensemble are applied (YR20-M5 and YR100-M20; see Section 4.2.5). The end member forcings produce the largest range in ice stream response to forcing so that the sensitivity of the model to different magnitudes of sub-ice shelf melting can be considered. In this section the three model configurations are described which consist of the reference model (Bedmap2-W-fixed), the viscous-plastic bed representation (Bedmap2-rC-fixed) and the migrated calving front (Bedmap2-W-retreated). Then, the ensemble of basal melt rate anomalies are described.

4.2.2 Reference Model

The reference model is consistent with that of Chapter 3. The regional domain of the ASE is initialised to the year 2000 following the method described in Nias et al. (2019, 2016) and Alevropoulos-Borrill et al. (2020). Bed topography and ice thickness are derived from a modified Bedmap2 (fig. 4.1; Nias et al., 2016; Fretwell et al., 2013). The surface mass balance field from Arthern et al. (2006) and temperature field from Pattyn (2010) are held constant through time. The model domain is initialised by performing an inversion to ensure modelled velocities match observations (Rignot et al., 2011) through a tuning process to produce two spatially varying parameter fields; a coefficient for basal friction (C) and ice rheology (ϕ ; Cornford et al., 2013, 2015). An initial or

background two dimensional basal melt field from Nias et al. (2016) and Cornford et al. (2015) is used. This spatially distributed basal melt rate field is tuned to ensure modelled ice shelf thinning rates match observations (Cornford et al., 2015), with the highest melt rates concentrated adjacent to the grounding line of PIG (Rignot et al., 2013a; Shean et al., 2019). For PIG ice shelf the total basal melting is 100 Gt yr^{-1} , which is of the same order as the latest observational estimates from Shean et al. (2019) of $83\text{-}92 \text{ Gt yr}^{-1}$ and Rignot et al. (2013a) of 101 Gt yr^{-1} for the same period.

The following equation is used to approximate Weertman sliding in the reference model (Eq. 4.1), which is also included in Chapter 2. τ_b denotes the basal shear stress which is non-linearly related to the mean velocity u by an exponent m which in this case is 3. The inversion for the basal traction coefficient C is first performed for a linear viscous friction ($m = 1$) and then scaled to represent a nonlinear viscous field with $m = 3$. C is produced only for grounded ice over the domain (where ice is floating C is zero).

$$\tau_b = -C|\mathbf{u}|^{\frac{1}{m}-1}\mathbf{u} \quad (4.1)$$

Unless otherwise stated in the simulations, a fixed calving front is applied for numerical stability, combined with a calving flux parameterized as a function of velocity. While the ice front remains fixed, a minimum ice thickness of 10 m is prescribed, allowing floating ice to thin almost completely with a negligible effect on upstream buttressing (Cornford et al., 2015).

4.2.3 Alternative Sliding Law

Recent work has proposed that a combination of Weertman and Coulomb sliding regimes should be implemented in ice sheet models (Joughin et al., 2019; De Rydt et al., 2021; Schoof, 2010; Tsai et al., 2015), with the former representing sliding over hard bedrock and the latter representing sliding over soft water-saturated sediment. The regularized Coulomb friction law proposed by Joughin et al. (2019) (Equation 4.2) represents both the sliding over deformable sediment and hard bedrock where effective pressure is subsumed into a transition velocity value u_0 of 300 m yr^{-1} . Below the transition velocity, basal drag is represented as Weertman type sliding, while above the transition velocity basal drag as Coulomb type sliding. This transition velocity acts as a way of evolving

the areas of weak till over time as the grounding line migrates and velocity evolves. The friction law has been shown to capture both the slower flow of ice over hard bedrock combined with fast flow of ice in the central trunk of PIG (Joughin et al., 2019).

To incorporate regularized Coulomb sliding (Joughin et al., 2019), the domain is re-initialised. As per the Bedmap2-W-fixed simulation, the inversion for the basal traction coefficient is performed for a linear viscous friction ($m = 1$) and then scaled to match a nonlinear viscous field for $m = 3$ but with the inclusion of a threshold velocity for which the sliding scheme transitions from viscous to plastic. For the regularized Coulomb (rC) sliding implemented here, effective pressure N is for the most part subsumed into the basal friction term. However, in some variations of the sliding law N is explicitly calculated (Schoof, 2010; Tsai et al., 2015). For the regularized Coulomb simulations values of $m = 3$ and $u_0 = 300 \text{ m yr}^{-1}$ are used to maintain consistency with Joughin et al. (2019).

$$\boldsymbol{\tau}_b = -C_{s,m} \left(\frac{|\mathbf{u}|}{|\mathbf{u}| + u_0} \right)^{\frac{1}{m}} \frac{\mathbf{u}}{|\mathbf{u}|} \quad (4.2)$$

4.2.4 Migrated Calving Front

Since Bedmap2 was released (Fretwell et al., 2013), the geometry of the AIS has evolved, including changes to the thickness and extent of PIG (Bamber and Dawson, 2020; Lhermitte et al., 2020). Satellite imagery has captured the calving and retreat of PIG's calving front since 1996 (Lhermitte et al., 2020). The ice front of PIG is forced to retreat over years 14 to 20 of the simulations using the observed migration of ice front position (Joughin et al., 2021) captured by Sentinel-2 and provided by Anna Hogg (fig. 4.2). This same ice front retreat was implemented in De Rydt et al. (2021), but here this is extended with the addition of the observed retreat from 2016 to 2020. The ice front retreat is prescribed by applying an extreme melt anomaly of $1 \times 10^4 \text{ m yr}^{-1}$ to retreated areas in order to remove the ice rapidly over the years 2014 to 2020. During this time the minimum ice thickness is returned to 0 m so that the ice front can migrate. After 20 years of the simulation as the ice front reaches its modern position, the minimum ice thickness is returned to 10 m and the ice front position remains fixed for the remainder of the simulations. The simulation with a retreated ice front position is called Bedmap2-W-retreated.

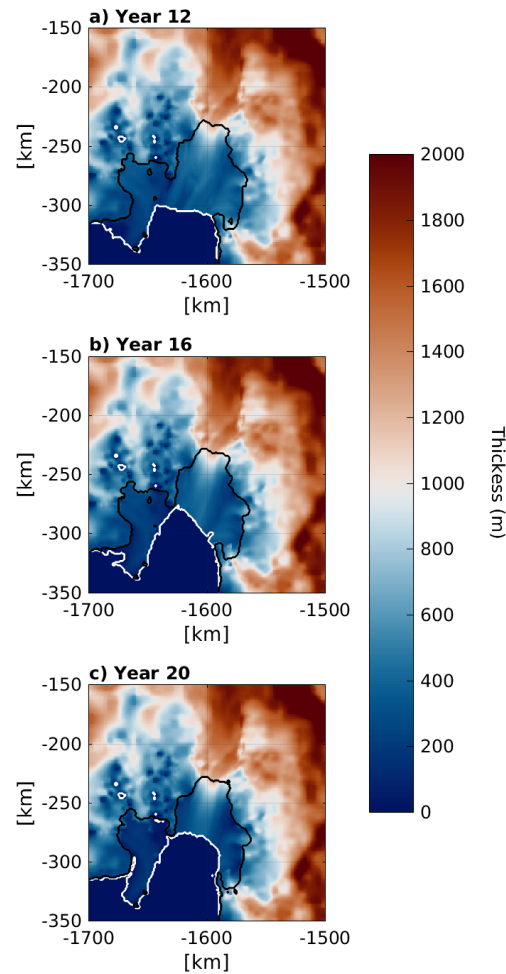


Figure 4.2: Pine Island Glacier ice thickness and calving front migration prescribed in years a) 12, b) 16 and c) 20 in Bedmap2-W-retreated simulations. White contour defines boundary between the ice and the ocean. Black line defines the grounding line based on hydrostatic floatation.

4.2.5 Basal Melt Forcing

The full 20-member ensemble of simulations for the reference model are forced with 20, 200-year, idealised projections of temporally evolving basal melt rate anomalies. The basal melt anomaly is scaled and spatially distributed to match the observed pattern of melting occurring beneath PIG ice shelf, with the greatest melting occurring adjacent to the grounding line (Nias et al., 2016) where the pressure melting point is lower and highest melt rates often found (Shean et al., 2019). The scaling relates to distance, with

an exponential decay in the absolute melt anomaly with increasing distance from the grounding line. A grounding line proximity parameter p is used as a multiplier where $p = 1$ at the grounding line which decreases exponentially for increasing distance (x) according to $p = \exp(-x/\lambda)$. Here, λ is a length scale of 10 km. Melting is applied solely to fully floating grid cells. The anomalies are applied in addition to the (Cornford et al., 2015) background melting field described above.

The temporal evolution of the basal melt forcing applied is idealised so that the dynamic response to perturbation can be explored. The magnitude of the basal melt anomaly varies through time, increasing linearly to four different magnitudes over five different time periods (fig. 4.3). Melt anomalies are increased over different durations, from 20 to 100 years at 20 year intervals. In each simulation, once the forcing period is met, the anomaly is removed so that the present day Cornford et al. (2015) melt field is applied for the remainder of the 200 year simulation (fig. 4.3). For each duration (20, 40, 60, 80, 100 years), the melt rate is increased linearly to four different maximum values (5, 10, 15, 20 m yr⁻¹). The magnitude of anomalies lie within the range of melt rate anomalies explored in existing studies (Nias et al., 2019; Alevropoulos-Borrill et al., 2020).

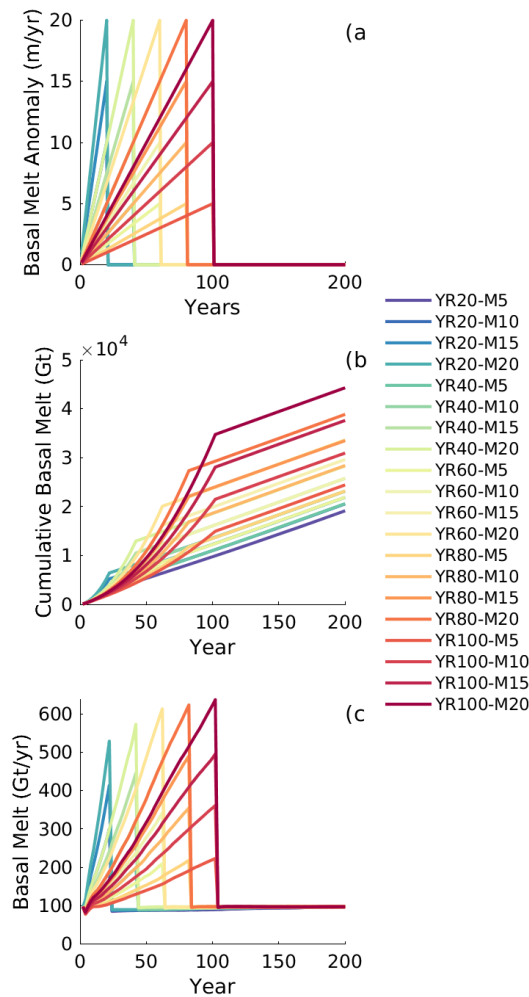


Figure 4.3: a) Two hundred year mean melt rate anomaly (m yr^{-1}) forcing ensemble of 20 simulations. b) Cumulative sub-ice shelf melting (Gt) c) Total ice shelf melting (Gt yr^{-1}).

Each simulation is referenced by a code that indicates both the duration of the positive anomaly (YR*) and the magnitude of the basal melting (M*) to which the anomaly was increased. For example, YR20-M5 describes a simulation with 20 years of additional basal melting that is increased linearly to 5 m yr^{-1} before being removed for the remaining 180 years of the 200 year long simulation.

The cumulative melt forcing describes the total basal mass balance change over time applied to the models as an anomaly (fig. 4.3), this metric incorporates both the magnitude and duration of the applied anomaly. Despite the removal of the forcing (fig. 4.3), the cumulative basal melt continues to increase as the initial basal melt field continues to thin the ice.

4.3 Results

First, the sensitivity of PIG to the full 20-simulation ensemble is discussed for the reference model Bedmap2-W-fixed (Section 4.3.1) using Bedmap2 topography and ice geometry with Weertman sliding ($m = 3$) and a fixed ice front (Bedmap2-W-fixed). The comprehensive presentation of the sensitivity to basal melting for this configuration provides continuity with existing investigations (Nias et al., 2016, 2019; Alevropoulos-Borrill et al., 2020). The response of the ASE to end member sub-ice shelf forcings for an alternative sliding law (Bedmap2-rC-fixed) and ice front (Bedmap2-W-retreated) are presented.

4.3.1 Bedmap2-W-fixed

4.3.1.1 Sea Level Contribution

Over 200 years, PIG loses a quantity of mass equivalent to raise global sea level by 18-28 mm (fig. 4.4). For each set of durations (YR* values), the greater the magnitude of forcing, the greater the overall SLE contribution. As the forcing is applied, the rate of SLE contribution ($\delta\text{SLE } \delta t^{-1}$) is dependent on the magnitude of the forcing, where greater magnitudes lead to a greater rate of SLE contribution. This is illustrated by the increase in spread of SLE as the forcing is applied due to a divergence in the basal melt forcings. When the forcing is removed, the spread in SLE converges, as shown by a reduction in $\delta\text{SLE } \delta t^{-1}$ to equivalent values regardless of initial magnitude of forcing.

In the year 200 the total SLE is positively, non-linearly related to the cumulative basal melt, where an incremental increase in cumulative melt leads to a smaller increase in the overall mass loss (fig. 4.4f). When the forcing is removed, simulations with a greater overall cumulative melting have a greater reduction in $\delta\text{SLE } \delta t^{-1}$ which acts to limit the overall mass loss (fig. 4.4). This can be seen in the convergence of the SLE following removal of forcing (fig. 4.4) and is evident in the negative nonlinear relationship between cumulative forcing and the $\delta\text{SLE } \delta t^{-1}$ averaged over the last 40 years, where simulations with greater cumulative forcing have a lower rate of mass contribution after the forcing has been removed (fig. 4.4).

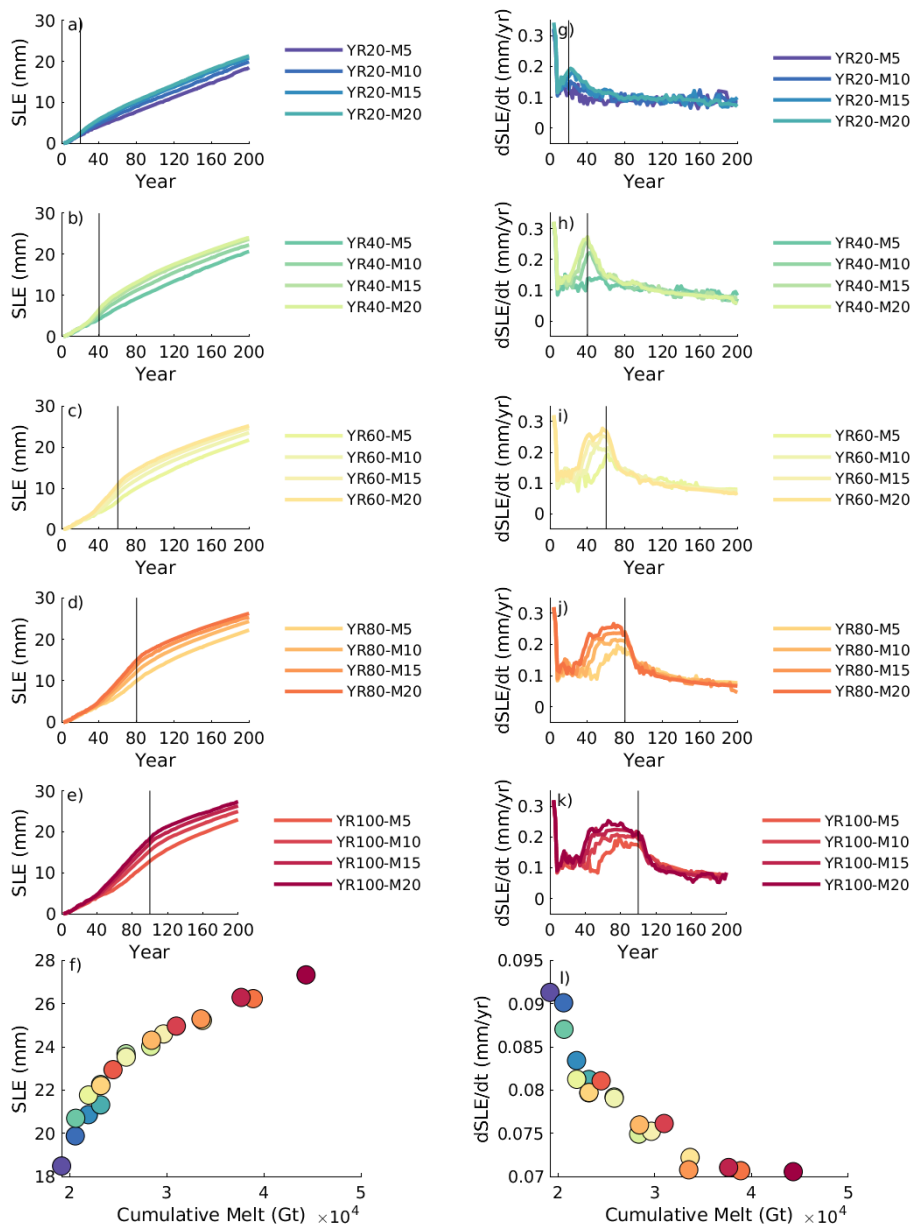


Figure 4.4: a-e) Sea level equivalent contribution (mm) g-k) rate of sea level equivalent contribution (mm yr^{-1}) for each simulation separated by the magnitude of forcing. Vertical black line marks the year in which the forcing is removed. f) Relationship between the sea level equivalent for $t = 200$ and the cumulative melt anomaly at the end of the simulation. l) Relationship between the mean rate of sea level equivalent averaged over the last 40 years of the simulation against the cumulative melt anomaly at the end of the simulation.

4.3.1.2 Grounding Line Position

Despite the ensemble range in SLE after 200 years of varied cumulative forcing, the end of simulation grounding line position is similar for the 20 simulations, with a 24 km retreat upstream along the trunk of the ice stream occurring (fig. 4.5). Along the trunk all simulations result in the same extent of retreat due to the existence of a topographic high (fig. 4.5) which pauses the retreat of the grounding line. The southern boundary of the ice shelf migrates inland resulting in a widening of the ice shelf with 50km of retreat along the tributary connecting TG to the PIG ice shelf. The differences in the end of simulation grounding line positions along the Southwestern Tributary are attributable to the shallow topography at the front of the initial ice shelf which promotes ice shelf grounding (fig. 3.1), causing buttressing and resulting in some sensitivity to varying melt rates.

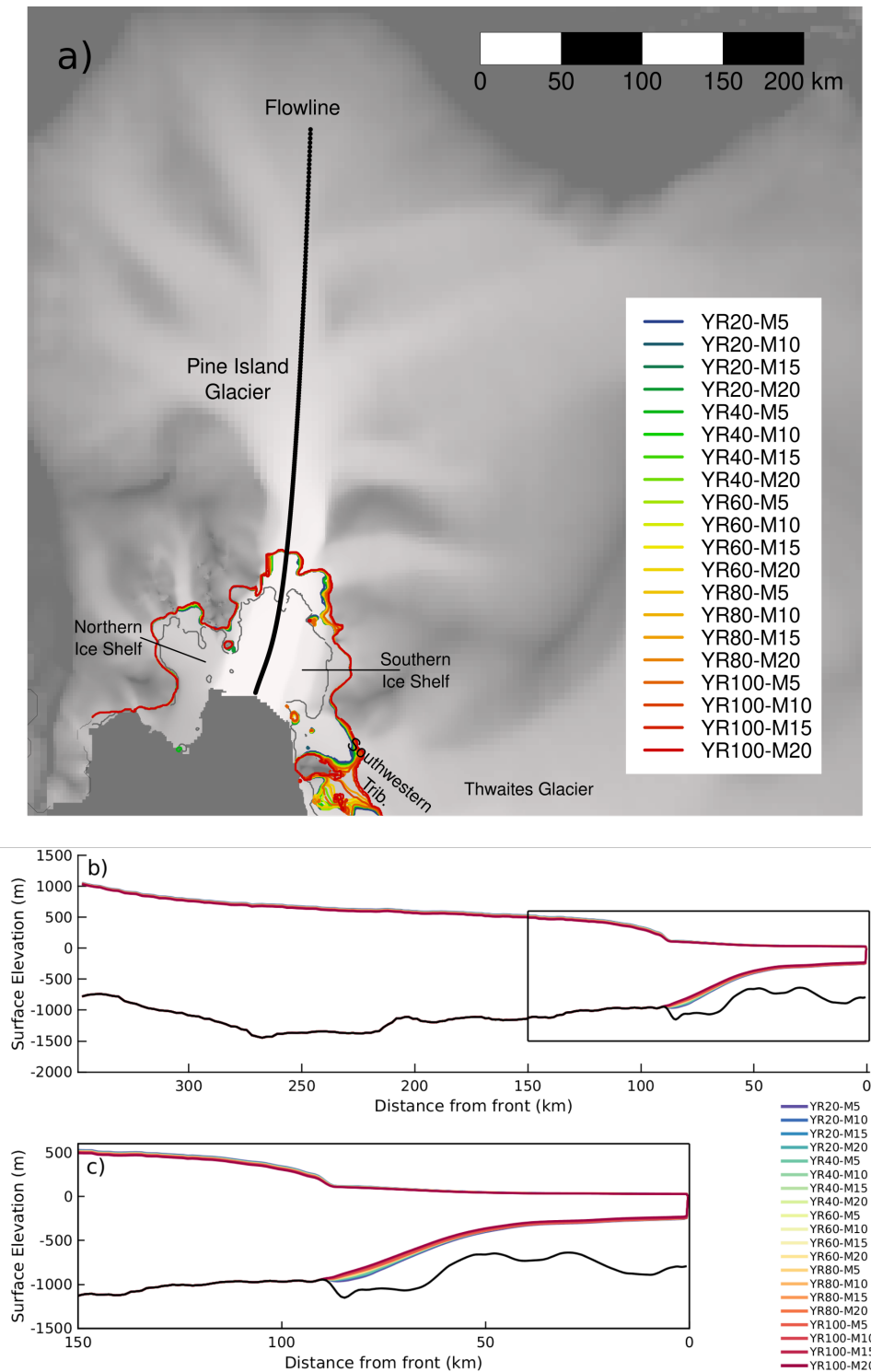


Figure 4.5: a) Grounding line position at the end of the 200 year simulations with added initial grounding line position in grey. Solid black line marks the transect used for cross sections and to measure grounding line retreat. b) End of simulation cross-section of surface elevation and base along flowline where coloured lines represent different simulations. Black contour marks the topography. c) Enlarged inset of b).

The flowline marks the centre of a 16 km wide window over which the grounding line position is averaged in order to determine the mean grounding line position over the central trunk of the ice stream (fig. 4.5). The pattern of retreat is broadly step-wise, indicating intermittent pauses in the rate of retreat where the grounding line position remains pinned by underlying topography (fig. 4.6) before retreating rapidly upstream until a new position of stability is reached.

The timing of retreat is dependent on the duration of applied forcing. The YR20* simulations retreat to 24 km the slowest (fig. 4.6), where the grounding line temporarily stabilises at a position 14 km upstream from the initial grounding line. While all simulations retreat to the same position, the rate of retreat can be slowed by topography.

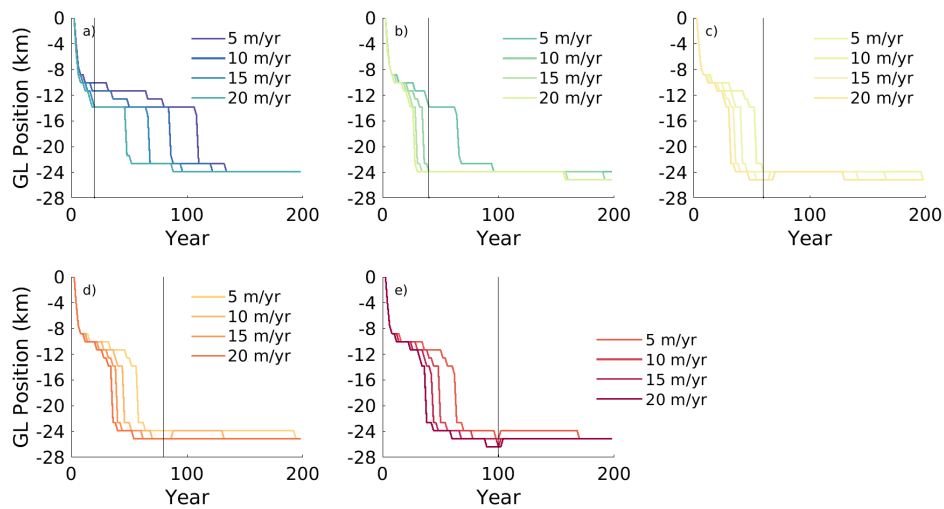


Figure 4.6: Distance of grounding line migration through time relative to the initial position for a) YR20* b)YR40* c)YR60* d)YR80* e)YR100*. Black vertical line marks the time at which the forcing is removed for each set of simulations.

Over the first 20 years, the grounding line retreats 10 km upstream along the trunk which is consistent across all the simulations (fig. 4.6). The difference in grounding line positions begins at 60 years into the simulation, where all simulations with a duration of forcing greater than 40 years results in retreat to the 24 km position along the trunk. After 60 years there is a divergence in grounding line position that is dependent on the magnitude of melting. By 160 years all simulations show 24 km of retreat upstream from the initial grounding line. The grounding line position retreats first up the narrow trunk before widening due to retreat inland of the southeastern grounding line. The difference in grounding line position along the southwestern tributary begins to converge

following $t = 160$ where the grounding line reaches approximately the same position.

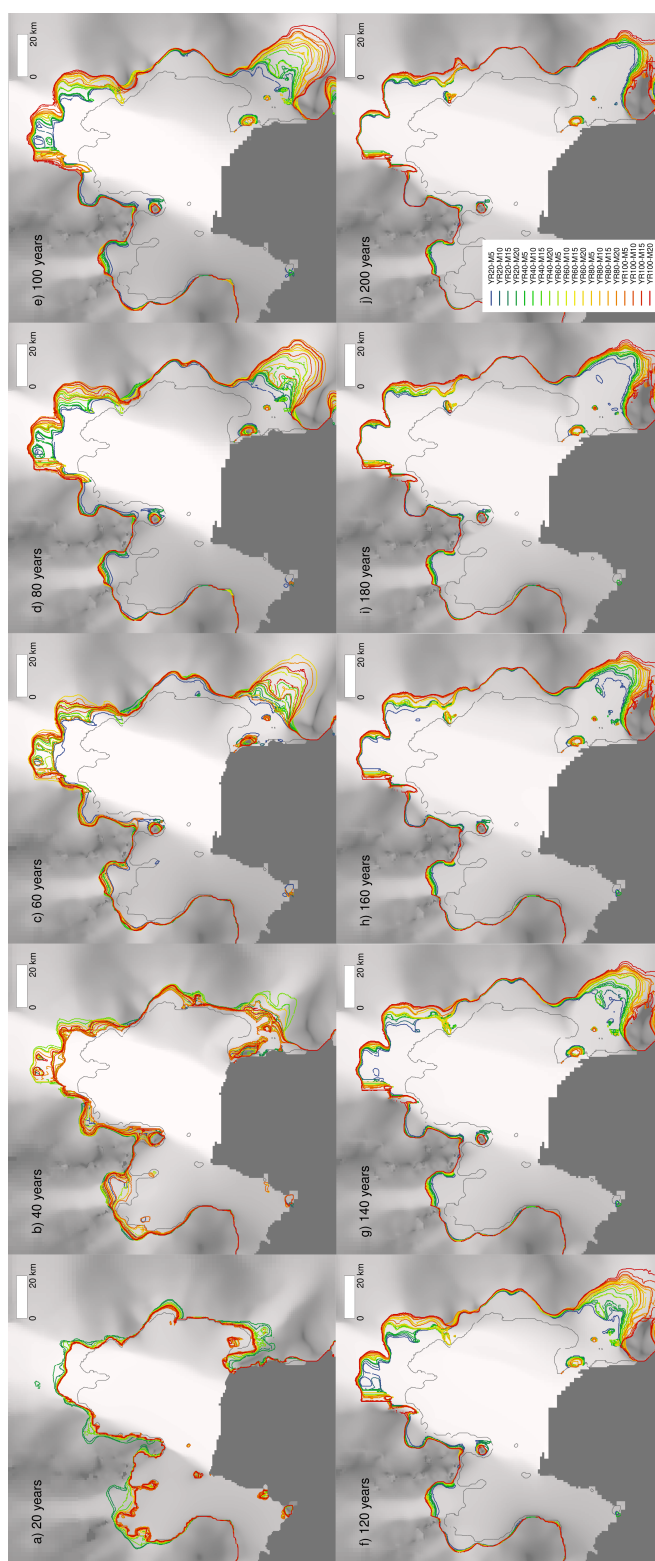


Figure 4.7: a-j) Grounding line position at 20 year intervals for each simulation with added initial grounding line position in black.

4.3.2 Alternative Model Configurations

The high (YR100-M20) and low (YR20-M5) melt simulations are compared for model domains with a migrated calving front (Bedmap2-W-retreated) and regularized Coulomb sliding (Bedmap2-rC-fixed) with the reference model configuration described above. The SLE contributions at the end of the simulation differs for each of the model configurations (figs. 4.8 & 4.9). For the low (fig. 4.8) melt forcing the SLE is highest for Bedmap2-W-retreated, which results in a 21 mm SLE at the end of the simulation compared with 19 mm for Bedmap2-W-fixed and 13 mm for Bedmap2-C-fixed. While the Bedmap2-W-fixed and Bedmap2-W-retreated both result in a near linear increase in SLE over the 200 years, the Bedmap2-rC-fixed simulation has a nonlinear, lowered rate of SLE contribution which is consistent with a lesser extent of grounding line retreat along the trunk (fig. 4.8d).

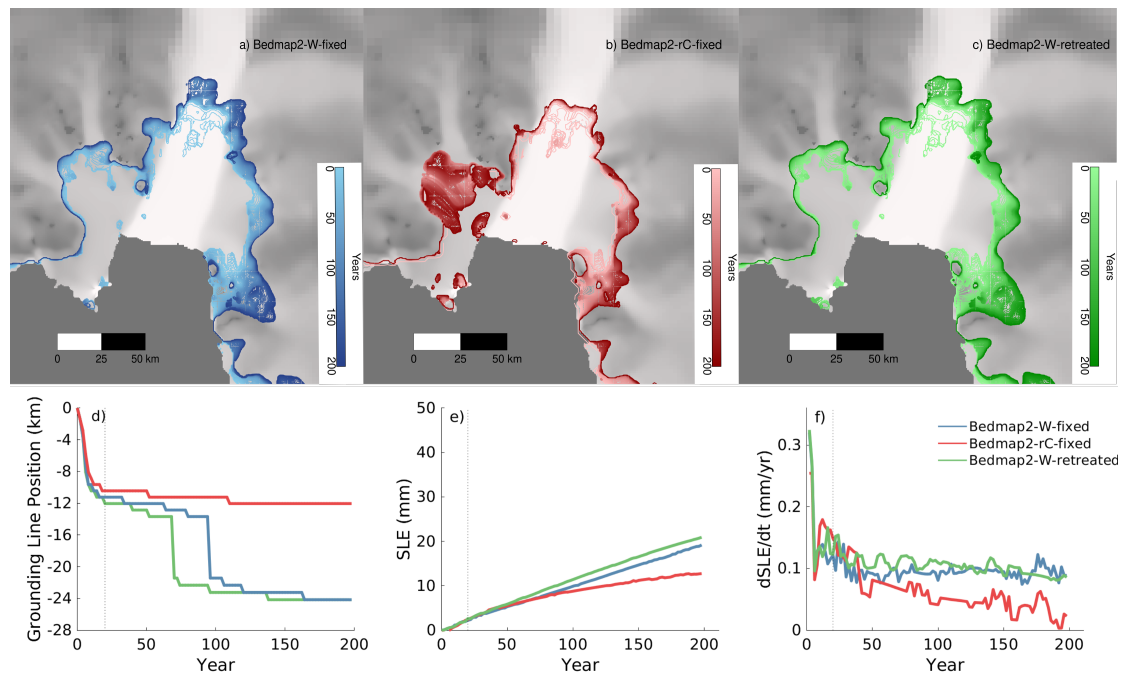


Figure 4.8: Map of grounding line positions plotted every 2 years for a) Bedmap2-W-fixed b) Bedmap2-rC-fixed and c) Bedmap2-W-retreated, for YR20-M5 low melt simulations. Time series of d) grounding line retreat along trunk flowline e) sea level equivalent contribution f) rate of sea level equivalent contribution for alternative low melt simulations.

In contrast, for the high melt forcing Bedmap2-rC-fixed experiences the greatest mass loss of 35 mm of SLE (fig. 4.9), 25 % greater than the Bedmap2-W-fixed reference model at the end of the 200 years. Furthermore, Bedmap2-W-retreated results in a SLE

contribution 3 mm greater than Bedmap2-W-fixed, a 9 % greater mass loss. The end of simulation grounding line position and pattern of retreat remains similar, despite the difference in SLE, with all three simulations retreating 24 km along the trunk of FIG. Bedmap2-W-retreated experiences the fastest retreat, reaching 24 km of retreat upstream 5 years before the high melt forced Bedmap2-W-fixed and Bedmap2-rC-fixed simulations.

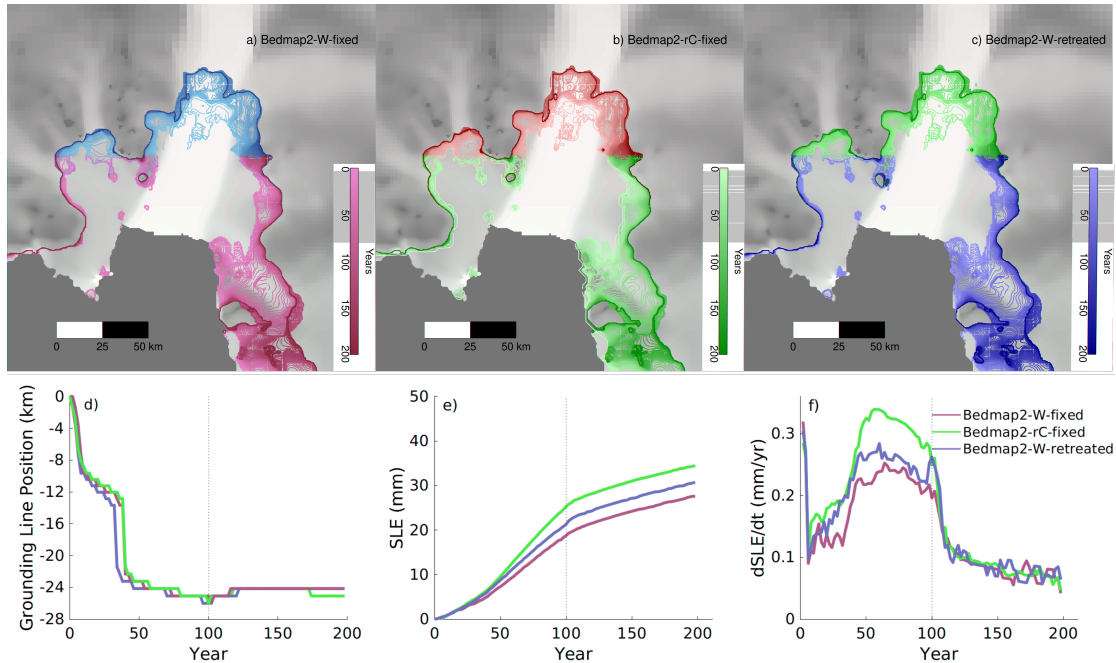


Figure 4.9: Map of grounding line positions plotted every 2 years for a) Bedmap2-W-fixed b) Bedmap2-rC-fixed and c) Bedmap2-W-retreated, for YR100-M20 high melt simulations. Time series of d) grounding line retreat along trunk flowline e) sea level equivalent contribution f) rate of sea level equivalent contribution for alternative high melt simulations.

The ice stream geometry change over time is similar for both Bedmap2-W-fixed and Bedmap2-rC-fixed (fig. 4.10) for the high melt simulation which is consistent with the equivalent extent of grounding line retreat occurring over the simulation. The primary difference in the evolution occurs with the extent of thinning of the ice shelf. While both simulations experience the same melt rates over the ice shelf, the thinning rates vary as a result of both the spreading rate of the ice shelf and the ice flux across the grounding line and therefore the volume of ice being fed into the ice shelf. All high melt forced simulations show thickening of the ice shelf in response to the removal of positive forcing.

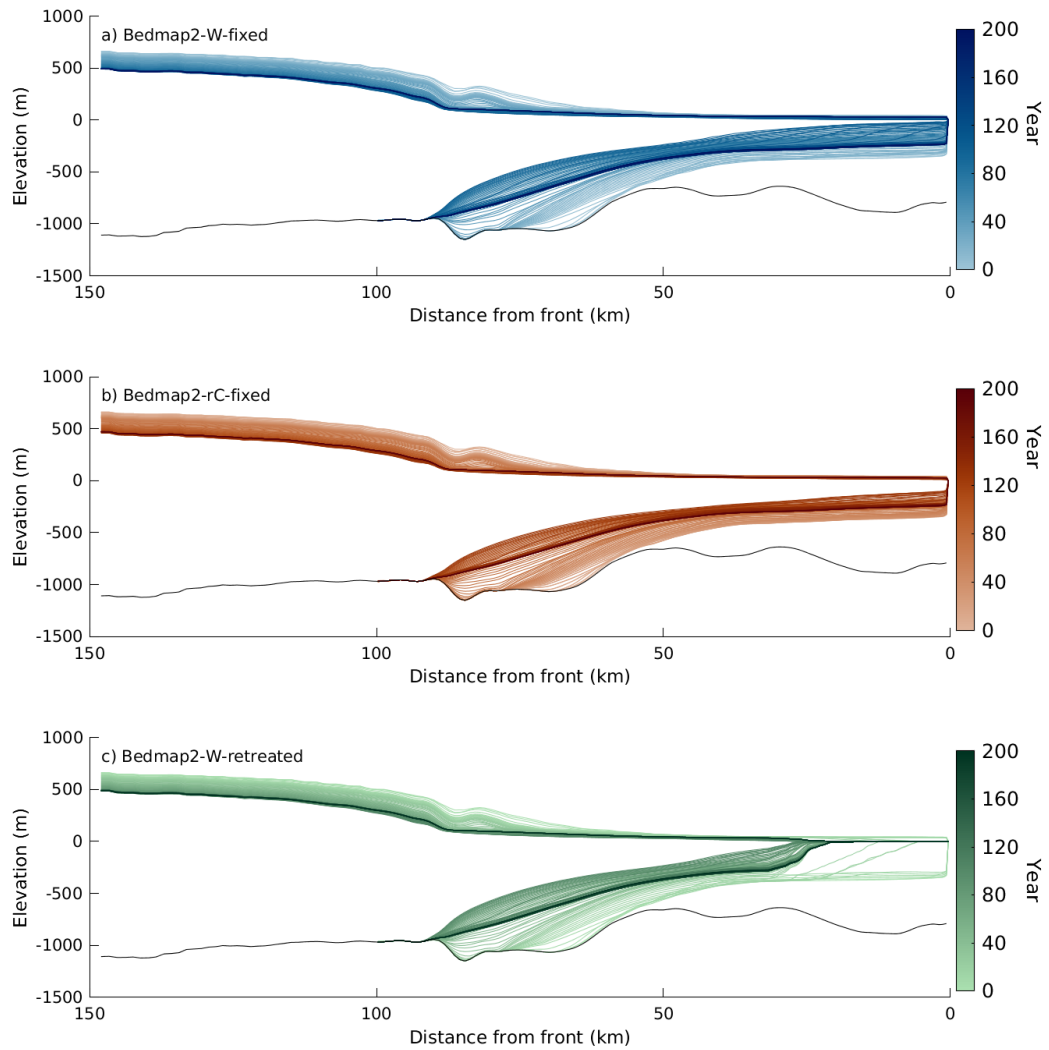


Figure 4.10: Ice geometry evolution along cross-section for high melt (YR100-M20) forced simulations for a) Bedmap2-W-fixed b) Bedmap2-rC-fixed and c) Bedmap2-W-retreated.

For the low end basal melt forcing, the Bedmap2-rC-fixed simulation is more sensitive to the removal of basal melt rate anomaly than Bedmap2-W-fixed (fig. 4.8f), with the rate of SLE contribution plateauing following removal 20 years into the simulation. After peaking at 0.17 mm yr^{-1} the $\delta\text{SLE } \delta t^{-1}$ falls to around 0.001 mm yr^{-1} . This contrasts with the high melt simulation, where the $\delta\text{SLE } \delta t^{-1}$ rises to 0.34 mm yr^{-1} after 70 years of the simulation before falling to 0.08 mm yr^{-1} after the forcing has been removed (fig. 4.9f).

Whilst the pattern and timing of grounding line retreat is near equivalent for the three simulations with the high melt forcing, there is a 10 mm range in the SLE contribution from these simulations (fig. 4.9e) indicating that total mass loss is not necessarily solely dictated by the total extent of grounding line retreat (fig. 4.9d). Bedmap2-W-retreated experiences the fastest retreat, reaching 24 km of retreat upstream 30 years before the low melt forced Bedmap2-W-fixed, while Bedmap2-rC-fixed retreats only 11 km upstream.

Aside from the Bedmap2-W-fixed low melt simulation, the final grounding line positions differ very little, with the most notable differences being the movement of the southern ice shelf grounding line (fig. 4.8 & 4.9). The main differences between the lower and higher melting simulations lies in the southward retreat of the trunk margins in addition to the retreat of the southwestern tributary. The high melt simulations experience over 50 km of retreat toward TG, connecting the ice shelves, whereas the retreat in response to the lower magnitude forcing is insufficient to connect these ice shelves. The Bedmap2-rC-fixed simulation experiences 10 km of retreat long the trunk in addition to 10 km of retreat of the southern ice shelf.

At $t=200$ the velocity change relative to $t=0$ is almost equivalent for Bedmap2-W-fixed and Bedmap2-W-retreated (fig. 4.11), though the latter experiences a greater increase in velocity of up to 300 m yr^{-1} over the ice shelf, most notably toward the new calving front. Bedmap2-rC-fixed shows the biggest contrast, with slower ice shelf flow than the initial in the low melt forcing but in response to the high melt forcing the model configuration exhibits the greatest acceleration over the trunk and ice shelf.

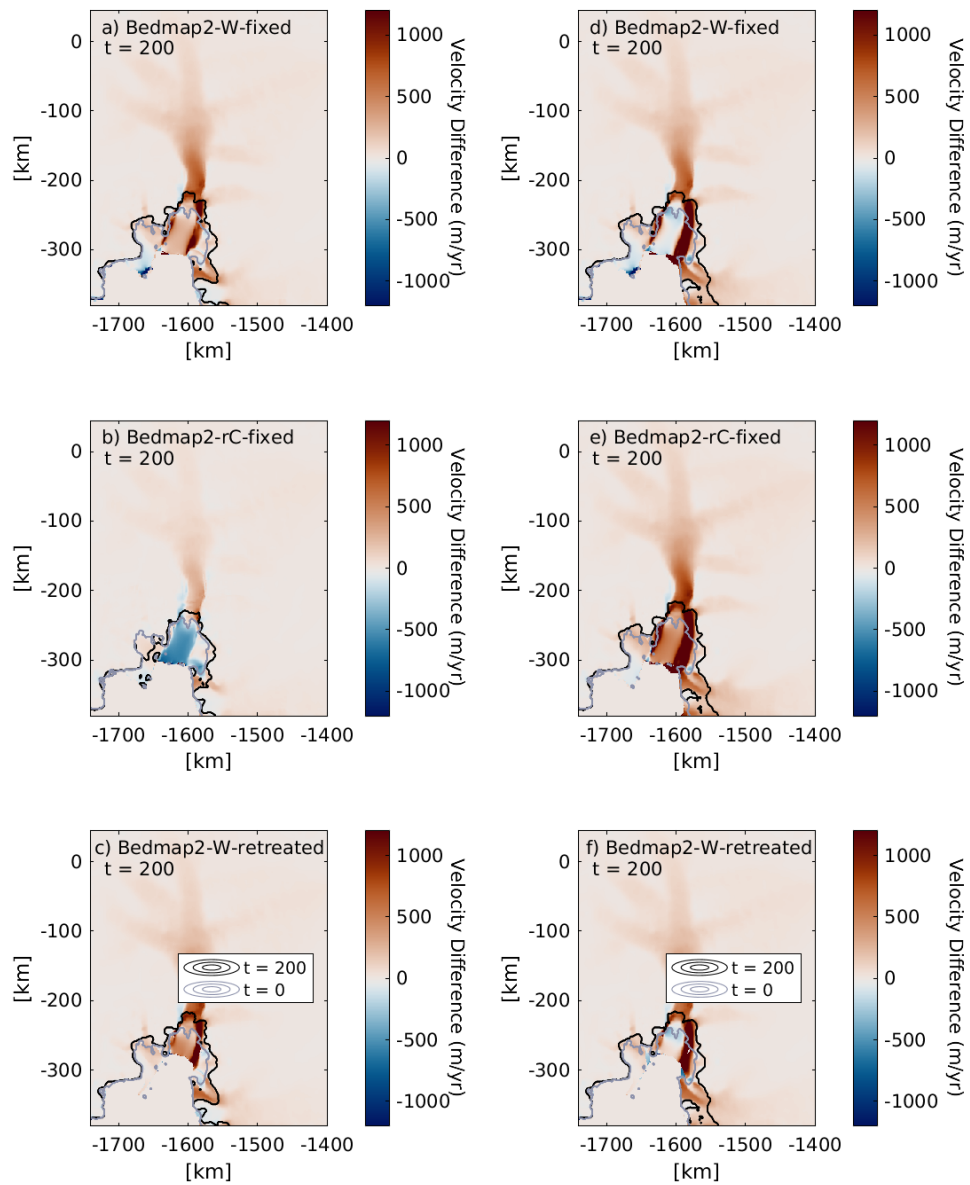


Figure 4.11: End of simulation ($t=200$) velocity difference relative to the initialised model ($t=0$) in response to the a-c) low melt forcing and d-f) high melt forcing for each of the model configurations. Black and grey contours mark the grounding line positions in $t=200$ and $t=0$ respectively.

4.4 Discussion

4.4.1 Reference Model

In every simulation, small perturbations in basal melting of PIG ice shelf results in an increased SLE contribution, even with the removal of the positive basal melt anomaly and reduction of melt to present-day values. These findings are consistent with Seroussi et al. (2014), who found a 5 year perturbation in basal melting impacted ice stream dynamics for up to 50 years. Instead, these simulations show that perturbation in basal melting of 20 years can alter ice flow and mass loss for up to 180 years. Increased ice shelf melting results in ice shelf thinning that reduces buttressing (Gudmundsson, 2013) and causes grounding line retreat (fig. 4.7). As the ice stream accelerates in response to reduced buttressing, this propagates inland, with acceleration reaching tributaries 120 km upstream (fig. 4.13c). This highlights the dynamic sensitivity of PIG to ice shelf melting, as found in existing studies (Payne et al., 2004; De Rydt et al., 2021; Seroussi et al., 2014). That being said, the future relevance of this behaviour is conditional on a prolonged reduction in the ocean thermal forcing of the ASE to present day rates which is not yet seen in even the lowest future emissions pathways (Alevropoulos-Borrill et al., 2020; Jourdain et al., 2020).

Mass loss of PIG is dependent on both the magnitude of basal melting and the duration of elevated basal melting applied, which is best described with the metric of cumulative melting. The relationship between SLE and cumulative melt indicates that in some cases, simulations with the same magnitude of basal melting will result in differences in SLE depending on the duration of forcing. An example of this is YR60-M5 and YR20-M15, with the former contributing 1 mm more SLE over the 200 year period (fig. 4.4). Both the duration and magnitude of elevated melt forcing is important for the future evolution of PIG (Seroussi et al., 2014). With a wide uncertainty in projections of future ocean evolution in the ASE (Naughten et al., 2018a; Alevropoulos-Borrill et al., 2020), proving the ongoing sensitivity of mass loss from the ice stream to melting reinforces the importance of narrowing uncertainty in future melt projections.

The dynamic response of the ice stream to the removal of the basal melt forcing results in a logarithmic dependence of total mass loss on the cumulative basal melting (fig 4.4). Over the final 40 years of the simulations, the rate of mass loss is lowest (highest) for the simulations with the greatest (least) overall cumulative melting (fig 4.4).

This occurs due to the enhanced thinning of the ice shelf in the high melt simulation that drives thinning of grounded ice upstream (Payne et al., 2004). As the grounded ice thins along the trunk, the surface slope gradient from grounded to floating ice is lowered, reducing gravitational driving stress around the grounding line and decreasing ice flux across the grounding line (fig. 4.12). For the higher melt simulations, thinner ice with a lower velocity upon removal of forcing results in reduced flux across the grounding line and therefore a lower rate sea level contribution, causing the upper end curbing in SLE in relation to cumulative melting. This behaviour, however, is dependent on the equivalent end of simulation grounding line position which could be unique to this investigation and the bed topography used. Should the grounding line positions differ, this would result in an increased rate of mass loss for a more retreated grounding line where grounding line retreat leads to reduced basal drag which drives acceleration (Payne et al., 2007). Additionally, in the high melting simulations, surface gradients while lowered in the trunk will be increased toward the interior and therefore the long term response to forcing could result in increased discharge from these simulations.

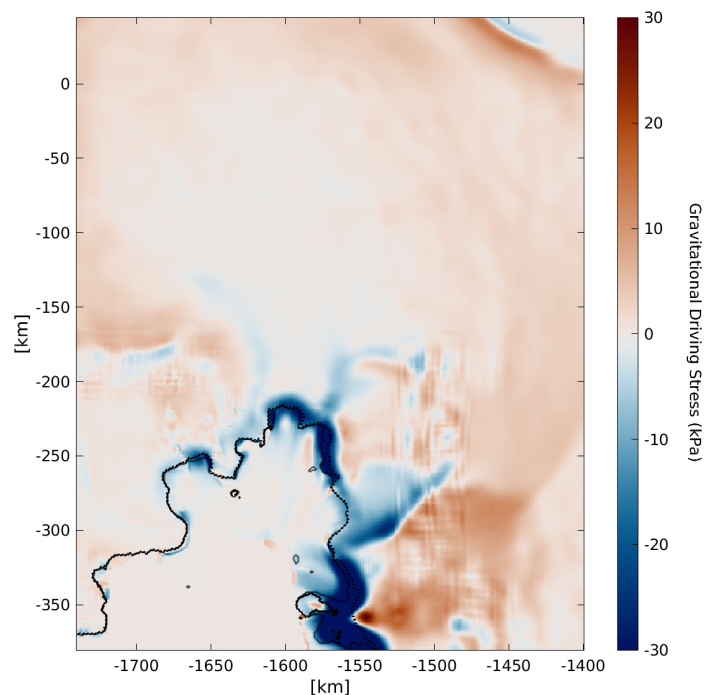


Figure 4.12: Difference in gravitational driving stress between high and low melt Bedmap2-W-fixed simulations at $t = 200$. Red (blue) shows that the high melt simulation for Bedmap2-W-fixed has higher (lower) gravitational driving stress than the low melt simulation in the same year.

The extent of grounding line retreat is dictated by bed topography. Despite a difference in cumulative ice shelf melting of up to 2.5×10^4 Gt over 200 years (fig. 4.3b), all simulations result in an equivalent extent of grounding line retreat (fig. 4.5). The end of simulation grounding lines retreat to a stable position on a ridge 24 km upstream of the initial grounding line along the trunk of the glacier (fig. 4.5). As the initial grounding line resides on a portion of downward sloping bed, retreat upstream from this position is expected given the MISI mechanism, which explains the retreat to this position for each of the simulations and the stepped pattern of retreat (fig. 4.6). The occurrence of MISI here would indicate that the thickness and confinement of the ice shelf provides insufficient buttressing to prevent this retreat (Gudmundsson, 2013). While the grounding line position at the end of the simulation is considered temporarily stable, retreat upstream from this position would result in grounding line retreat over a large portion of retrograde bedrock with few sections of prograde bed or topographic maxima upstream (fig. 4.5). Therefore, while a stable grounding line position is reached in all simulations, this does not negate the possibility of instability should retreat occur past 24 km. Furthermore, this equivalent extent of grounding line retreat of simulations with varied magnitudes and durations of basal melting indicates that while grounding line position is important for determining the occurrence of MISI, grounding line position does not directly predict SLE.

4.4.2 Comparison of Configurations

Relative to the reference model, the choice of sliding law has a greater influence on total mass loss and grounding line retreat in response to basal melting than the effect of a modified calving front position (fig. 4.8 & 4.9). The representation of the bed with a plastic-type friction law results in an increased sensitivity of the ice stream to the applied basal melt forcing, where there is a 22 mm range in SLE contribution between simulations with low and high melt forcings (fig. 4.8d & 4.9d). In regions of fast flowing ice such as the grounding zone of PIG, the effects of cavitation on weak sediment, as represented in the Bedmap2-rC-fixed simulations, promotes faster ice flow over the domain given that there is an upper limit to the dependence of friction on velocity (Schoof, 2010; Joughin et al., 2019). The sliding law impacts the representation of velocity over the entire domain, whereas the effects of a migrated calving front on ice velocity are more localised (fig. 4.11). Subsequently, the sliding law has a greater

impact on ice discharge from PIG than the modelled ice front position.

The plastic bed acts to limit mass loss and grounding line retreat for low magnitudes of basal melting. Bedmap2-rC-fixed low melt simulation experiences the least grounding line retreat (fig. 4.13f) and advance occurs over the northern ice shelf. The velocity increases over the first 20 years while the positive melt forcing is applied (fig. 4.13), where more acceleration occurs over a greater area of the ice stream in Bedmap2-rC-fixed compared with Bedmap2-W-fixed, due to reduced basal resistance (Joughin et al., 2010; Tsai et al., 2015). This leads to both an increase in thick ice delivered to the grounding line. With increased delivery of thick grounded ice to the ice shelf in the initial 20 years of the simulation, due to faster flow and reduced basal resistance, the ice shelf remains thicker in Bedmap2-rC-fixed and the grounding line further downstream. As the forcing is removed, PIG decelerates in Bedmap2-rC-fixed, resulting in the ice shelf velocity reaching 500 m yr^{-1} below than the initial velocity. In contrast, Bedmap2-W-fixed experiences a more localised increase in velocity around the grounding line (fig. 4.13), more localised thinning and more grounding line retreat. The ice stream experiences less deceleration following the removal of forcing in Bedmap2-W-fixed than Bedmap2-rC-fixed, with a thinner ice shelf and more retreated grounding line. The regularized Coulomb sliding law therefore limits retreat and mass loss for low magnitude melt forcing compared with Weertman sliding (Wernecke et al., 2022).

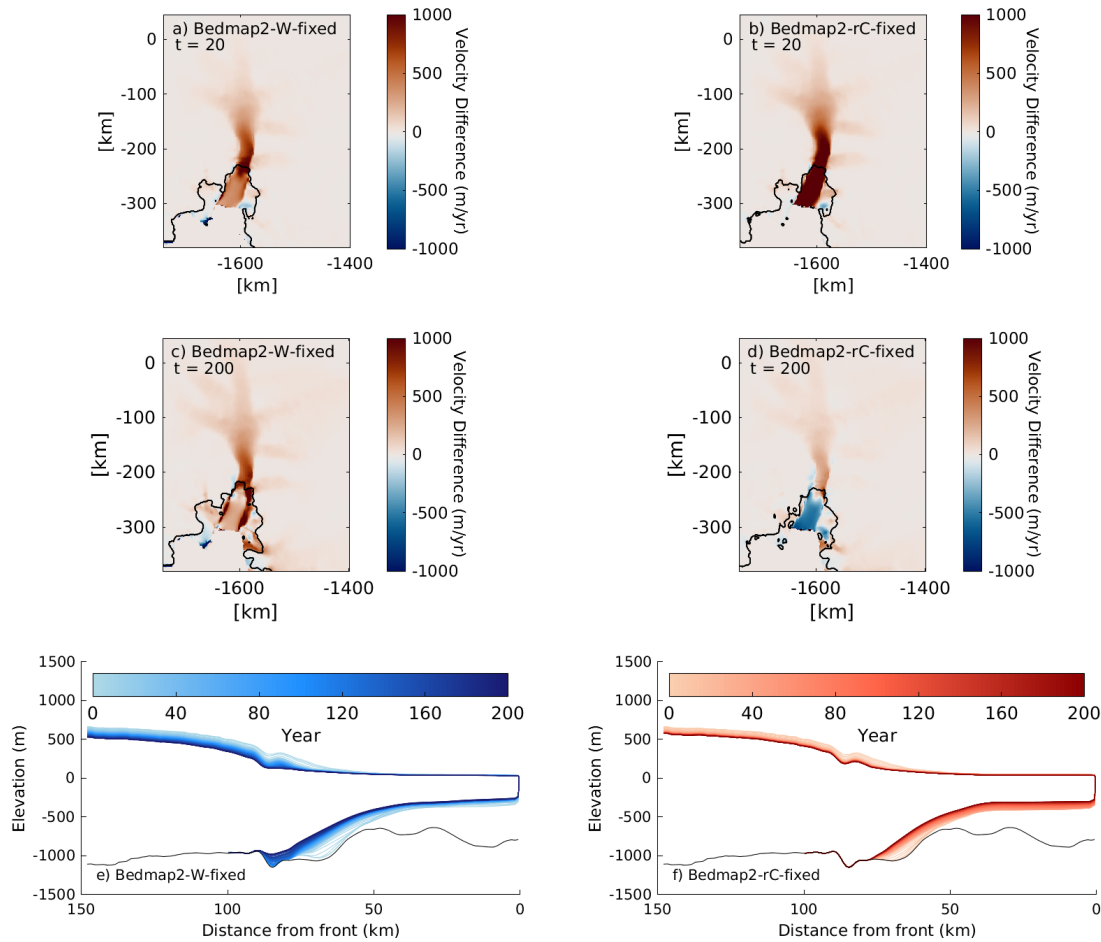


Figure 4.13: Velocity change relative to $t = 0$ for respective simulations a) Bedmap2-W-fixed YR20-M5 in $t = 20$ b) Bedmap2-rC-fixed YR20-M5 forced for $t = 20$, c) Bedmap2-W-fixed YR20-M5 for $t = 200$, d) Bedmap2-rC fixed YR20-M5 for $t = 200$ with grounding lines plotted for the comparative year. e) cross section along flowline of ice geometry change with lines representing every two years in Bedmap2-W-fixed YR20-M5 and f) the same but for Bedmap2-rC-fixed. Black line marks the topography along the flowline.

The role of friction representation in determining the behaviour of PIG differs for the high melt simulation, where the elevated velocity and mass loss is sustained for Bedmap2-rC-fixed despite the removal of forcing. In the high melt simulation there is greater mass loss for Bedmap2-rC-fixed (fig. 4.9e) but almost the same extent of grounding line retreat as Bedmap2-W-fixed. Both Bedmap2-W-fixed and Bedmap2-rC-fixed experience acceleration (fig. 4.14) in response to elevated ice shelf melting resulting in increased discharge (fig. 4.9d) over the first 50-60 years, although Bedmap2-rC-fixed reaches a velocity 1500 m yr^{-1} greater than Bedmap2-W-fixed. After 60 years,

there is deceleration over the trunk for both simulations. While Bedmap2-rC-fixed decelerates more, the end of simulation velocity remains greater than the initial due to a greater area of acceleration over the domain (fig. 4.14), consistent with Joughin et al. (2010). In both simulations, the PIG ice shelf thickens following the removal of forcing (fig. 4.10), but remains thinner than the initial geometry therefore providing less buttressing. High prolonged periods of melting result in greater mass loss with a regularized Coulomb sliding and higher sustained velocity. This finding is consistent with existing investigations, where plastic-type sliding laws used in modelling the ASE resulted in a greater extent of mass loss compared with viscous linear sliding laws (Brondeux et al., 2019; Bulthuis et al., 2019; Wernecke et al., 2022).

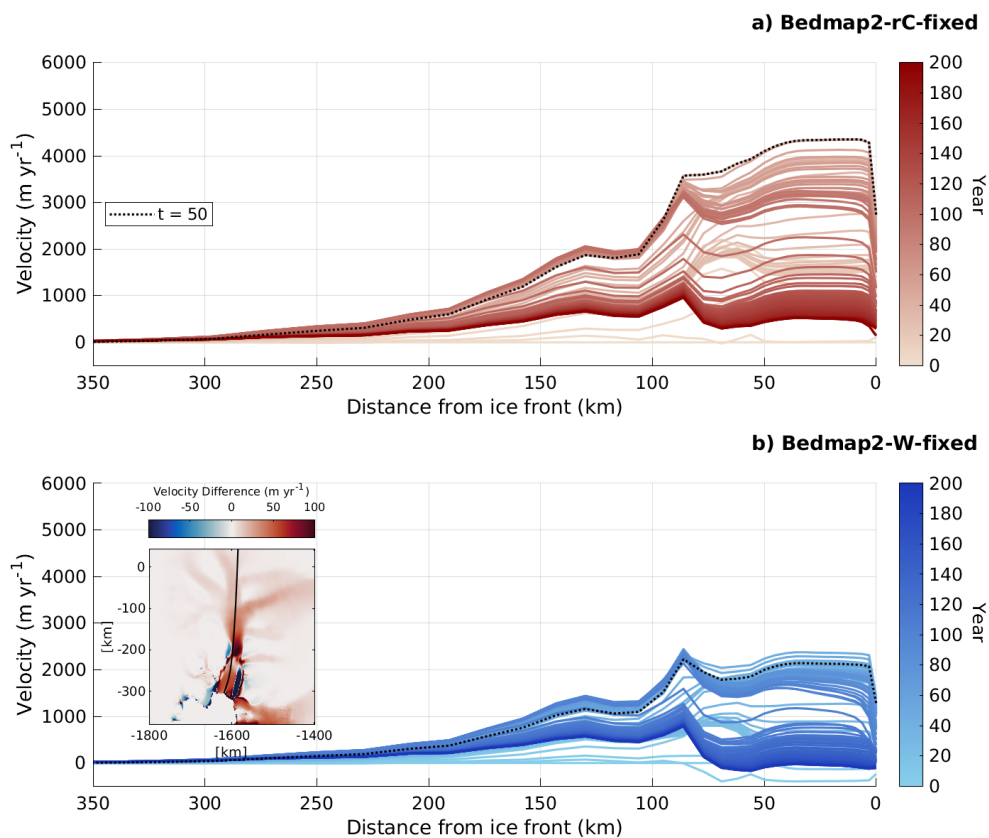


Figure 4.14: Velocity profile along PIG transect (identified in inset) relative to $t = 0$. Contours plotted every 2 years in simulations a) Bedmap2-rC-fixed and b) Bedmap2-W-fixed in response to the high melt forcing. Black dotted line represents the velocity at $t = 50$. Inset shows velocity difference between the simulations at $t = 200$ where red (blue) shows Bedmap2-rC-fixed is faster (slower) than Bedmap2-W-fixed.

The retreated ice front position in Bedmap2-W-retreated that is prescribed using

observations of retreat driven by large calving events from 2014 to 2020 results in a 9-11 % greater mass loss from the ice stream over the 200 year simulations, where the sensitivity of the PIG to calving front migration is dependent on the magnitude of melting. The absence of a portion of confined ice shelf that is buttressed through both basal and lateral drag has an impact on the longitudinal compressional force of upstream ice (fig. 4.15), thus the forces opposing downstream flow are reduced overall. The result of this reduced buttressing is an immediate increase in velocity relative to the reference domain Bedmap2-W-fixed (fig. 4.15) which is consistent with literature (Gudmundsson et al., 2019; Payne et al., 2007; Seroussi et al., 2014), and confirms that the area of shelf calved includes non-passive ice (Fürst et al., 2016; Lhermitte et al., 2020; De Rydt et al., 2021). The acceleration of grounded ice initially reaches up to 50 km upstream of the grounding line in $t = 14$ but this propagates up the trunk over the following 16 years reaching 100 km upstream of the grounding line. Faster ice flow means increased ice discharge and subsequent greater rates of sea level rise that are observed (fig. 4.9d and 4.11). The rate of mass loss increases most for higher magnitudes of ice shelf melting with a retreated calving front when compared with the reference model.

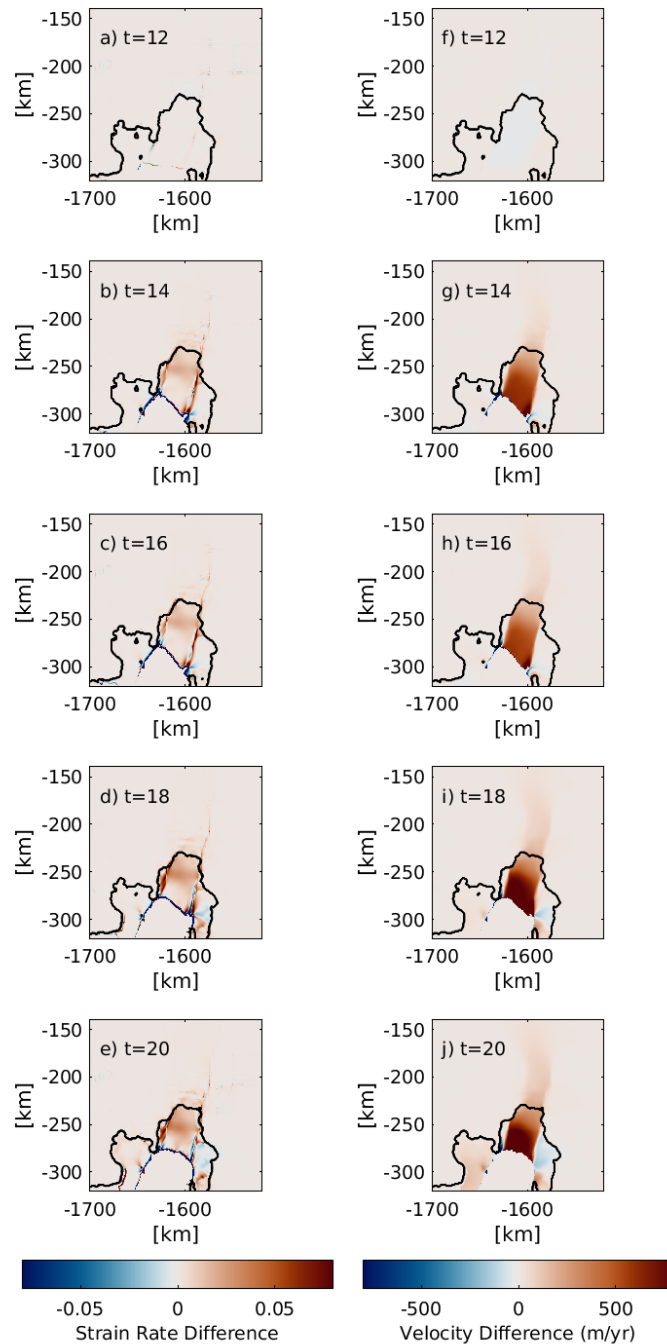


Figure 4.15: Velocity (a-e) and strain rate (f-h) differences between Bedmap2-W-retreated and Bedmap2-W-fixed high melt simulations. Each panel represents a different year of the simulation from $t = 14$ and $t = 30$. Red (blue) shows higher (lower) velocity/strain rate in Bedmap2-W-retreated. Grounding line position for both simulations is equivalent for the years presented and is represented by the black contour.

grounding line retreat along the main trunk of the ice stream is fastest for Bedmap2-W-retreated in both low and high melt forced simulations compare with Bedmap2-W-fixed and Bedmap2-rC-fixed (figs. 4.8 and 4.9). As discussed previously, in simulations with Weertman sliding the ice stream acceleration is more localised around the grounding line, and this is exacerbated with calving front retreat reducing the resistive stresses from the ice shelf, promoting faster grounding line retreat. This is most notable in the low melt simulation where retreat to the end of simulation position occurs 25 years before the reference model of Bedmap2-W-fixed. Although the difference in mass loss between Bedmap2-W-fixed and Bedmap2-W-retreated is greater for the high melt forcing, calving front migration has a greater impact on grounding line retreat for the low magnitude forcing, this mass loss difference could be greater should the rate of grounding line retreat continue with the absence of the topographic high at 24 km upstream.

Limitations The application of regularized Coulomb sliding by Joughin et al. (2019) incorporated a term h_T which describes a threshold thickness where basal friction, C , is linearly decreased to zero toward the point of floatation. This is partly to account for the incorporation of effective pressure, N into the basal traction coefficient (Brondex et al., 2019; Nias et al., 2018). With large uncertainties associated with the water content within subglacial sediment, determining a time evolving N with the use of a hydrological model is challenging (Schoof, 2010). Therefore the use of h_T by Joughin et al. (2019) accounts for seawater incursion into sediment beneath the grounding line causing weakening of sediment. The simulations performed in this chapter include no such reduction in friction toward the grounding line. Subsequently it is possible that the velocity acceleration at the grounding line would be more modest than if a h_T term were to be included.

Additionally, the transition velocity u_0 of 300 m yr^{-1} has been introduced by Joughin et al. (2019) as it was found to result in a model response that best matches observed velocity changes. Although this may be the case for the velocity data used in the study, that is not to say that there are no uncertainties associated with observations of velocity nor that a longer period of observations may result in a different transition velocity. Future work should therefore consider a greater range of these values, perhaps more specifically for lower values of u_0 which would result in speed up over a greater area of the drainage basin in response to forcing.

An investigation by Brondex et al. (2019) of the role of friction laws on ice flow is

performed on an idealised ice shelf domain described in the (Pattyn et al., 2012) MIS-MIP experiment 3 where the effects of friction are considered in response to reduced buttressing. Brondex et al. (2019) provides an ideal platform upon which to explore the effects of a realistic loss of buttressing on a real, not idealised, ice stream as is explored here. This investigation therefore could be expanded by incorporating the retreated ice front with the regularized Coulomb sliding.

Here, all simulations, with the exception of Bedmap2-rC-fixed with low melting, result in an equivalent extent of grounding line retreat due to the presence of a stabilising portion of prograde bed approximately 24 km upstream from the initial grounding line (fig. 4.10). The extent of grounding line retreat is consistent with the equivalent rate of mass loss following removal of forcing occurring for these simulations. With an alternative bed topography such as BedMachine Antarctica (Morlighem et al., 2020) or DeepBedMap (Leong and Horgan, 2020), the grounding line may not stabilise at this position for all simulations which would impact the sensitivity to the removal of forcing, where grounding line position impacts ice discharge. Subsequently, repeating this experiment for alternative bed topographies may impact the sensitivity of the ice stream to melting with alternative model configurations.

Finally, to explore the amount to which dynamic ice shelf thickening is responsible for promoting the observed ice stream stability upon the removal of the positive melt anomaly, further investigations can be performed. In fixing the geometry of the ice shelf following the removal of forcing, preventing dynamic thickening, the ongoing response of the ice stream to the initial increase in melting can be explored. This will also account somewhat for the fixed calving front, where dynamic thickening to the full extent of the initial ice shelf will be partly responsible for promoting stability through increased buttressing. These experiments will therefore provide more of an understanding of ongoing behaviour of ice flow within the trunk and tributaries in response to perturbed forcing.

4.5 Conclusion

In this Chapter a 20-member, ensemble of 200 year long ice sheet model simulations was performed to explore the sensitivity of PIG to positive perturbations in sub-ice shelf melting of different durations and magnitudes. In each of the simulations, following a

period of forcing, basal melting is reduced to investigate the unforced, dynamic response of PIG. The results show that the dynamic response of PIG depends on both the magnitude and duration of sub-ice shelf basal melt forcing. Longer durations of lower magnitude forcing can experience greater overall mass loss than shorter durations of higher magnitude melting. Therefore, while achieving a conservative future emissions pathway such as RCP2.6 has been shown to limit the future warming in the region, a prolonged period of a modest increase in basal melting can have similar outcomes to shorter periods of higher melting for the ice stream.

The standard experiments reveal an element of stability in the present and near future state of the ice stream, with a period of 100 years of increased sub-ice shelf basal melting leading to a relatively modest extent of grounding line retreat of 24 km over 200 years. Upon reduction in the sub-ice shelf melt forcing, PIG tends to equilibrate, with a lower rate of mass loss occurring for simulations that experience the greatest cumulative melt throughout the simulations. This stability however is conditional on a lowering of elevated melt rates to present day magnitudes after a century of forcing, which is not currently projected, and strong grounding line pinning on a prominent ridge. That being said, while the grounding line may reach a point of stability, even the shortest duration low magnitude forcing results in increased velocity over 200 years. Therefore it may be that MISI is triggered in these simulations, but the result of which is not observed over the time frame explored.

Here, two end-member simulations forced with low and high magnitudes of sub-ice shelf melt anomalies were repeated to explore some of the uncertainty in future projections that is created through ice sheet model set-up. The experiments show there is a modified sensitivity of the ice stream to sub-ice shelf melting with an alternative sliding law and migrated calving front, where the end of simulation range in sea level contribution of 18-28 mm increases to 15-34 mm over 200 years. The greatest differences in the rate of mass loss for the different model configurations occurs during periods of elevated melting, with most simulations experiencing the same rate of mass loss following reduction of melting to present-day values. A plastic-type sliding law that represents cavitation of sediment beneath the ice stream has the greatest impact on dynamic mass loss in response to melting, and alters the response of PIG to the removal of forcing. In contrast, although it has less of an impact on overall mass loss, the migrated calving front has a greater impact on the rate of grounding line retreat.

The findings reiterate the importance of using the most up to date input data and best practices for model parameterizations when running ice sheet model simulations to project the response of the ice to basal melting. While present and future sub-ice shelf basal melting remains the largest uncertainty in projecting the future of the ice stream, the sensitivity of the ice stream to melting, as determined by other ice sheet model parameters, can amplify the ice response and future uncertainty.

Chapter 5

The Influence of Topography and Thickness Products on Future Simulations of the Amundsen Sea Embayment

5.1 Introduction

The future response of the ASE ice streams to climate change remains a large uncertainty in projections of global mean sea level rise (Schlegel et al., 2018; Yu et al., 2018; Nias et al., 2019; Lowry et al., 2021). The region is vulnerable due to its grounding on retrograde bedrock below sea level (Fretwell et al., 2013), in addition to the presence of warm water in the Embayment melting the ice streams from below (Pritchard et al., 2012; Jenkins et al., 2016). Increasing delivery of warm water toward ASE ice shelves is responsible for observed speed up of ice streams in the ASE (Pritchard et al., 2012; Naughten et al., 2022), a trend which is projected to increase into the future (Donat-Magnin et al., 2017), and therefore will determine much of the future mass loss from the region. Topographic features such as ridges stabilise ice flow (Morlighem et al., 2017), and observational records show that unpinning from subglacial ridges has preceded large speed up events of ice streams (Smith et al., 2017; Tinto and Bell, 2011). Thus, both topography and ice shelf melting exert first order controls on mass loss from the ASE (Seroussi et al., 2017). While the full extent of the uncertainties associated with

melt rate projections have yet to be quantified (Jourdain et al., 2020), improvements in the availability of topographic measurements have allowed for the uncertainty in the role of topography on ice dynamics to be better examined (Sergienko and Wingham, 2021; Castleman et al., 2021).

High rates of sub ice shelf melting in the ASE could trigger unstable retreat in the region. Grounding line retreat over retrograde bed could initiate MISI, where increased melting can initiate self-sustained retreat (Weertman, 1974; Schoof, 2007; Robel et al., 2019). While the original proposal of the MISI hypothesis suggests marine based ice sheet cannot exist in a steady state with a grounding line situated on a retrograde bed (Weertman, 1974), this has since been further examined (Schoof, 2007; Robel and Tziperman, 2016; Tsai et al., 2015; Pegler, 2018b; Gudmundsson, 2013). In reality, short wavelength high amplitude features exist in the bed, modulating the flux across the grounding line through varied topographic gradients (Sergienko and Wingham, 2021) which would indicate the relationship is not as simple as previously suggested. Furthermore, three-dimensional modelling of coupled floating ice shelves have been shown to limit upstream flow and provide stability for ice streams on retrograde bed (Gudmundsson, 2013; Fürst et al., 2016; Reese et al., 2018b; Gudmundsson et al., 2019), particularly when the ice shelves are topographically confined and provide lateral friction (Fürst et al., 2016; Reese et al., 2018b; Gudmundsson, 2013). While some studies suggest MISI is currently underway in the ASE (Favier et al., 2014), it remains unclear what consequences this mechanism could have on ice dynamics in the region.

Advances in ice sheet modelling have shown that uncertainties in model parameters (Nias et al., 2016; Brondex et al., 2019; Alevropoulos-Borrill et al., 2020), physical laws governing the flow of ice (Brondex et al., 2019; Joughin et al., 2019; Tsai et al., 2015) and initialisation data (Kyrke-Smith et al., 2018) can result in different responses of ice flow to both external forcings and boundary conditions, resulting in a broader range of uncertainty for projected mass loss and subsequent sea level rise estimates. With topography providing a first order control on ice dynamics through its influence on grounding line positions, understanding the role it plays in moderating flow is important (Castleman et al., 2021).

Several studies explore the role of topography in modulating ice flow in the ASE (Castleman et al., 2021; Wernecke et al., 2022; Schlegel et al., 2018; Nias et al., 2016), finding generally that higher resolution topography data leads to increased mass loss.

For example, Schlegel et al. (2018) compared the flow of ice over topography from both Bedmap1 (Lythe and Vaughan, 2001) and a modified Bedmap2 (Fretwell et al., 2013) using mass conservation techniques to refine resolution of the bed to 150 m in the ASE (Morlighem et al., 2011), finding that over a century, the better resolved newer topography model resulted in 0.14 m greater sea level rise. Castleman et al. (2021) applied perturbations to the BedMachine topography product (Morlighem et al., 2020) over TG within the range of error associated with the product and found topographic uncertainty could amplify the range in projected SLE contribution to 22 cm over 200 years. Furthermore, Wernecke et al. (2022) compared the Bedmap2 and BedMachine datasets over PIG and the interplay between melting and topography in influencing ice flow, finding the latter product, of a finer horizontal resolution, resulted in increased projected mass loss.

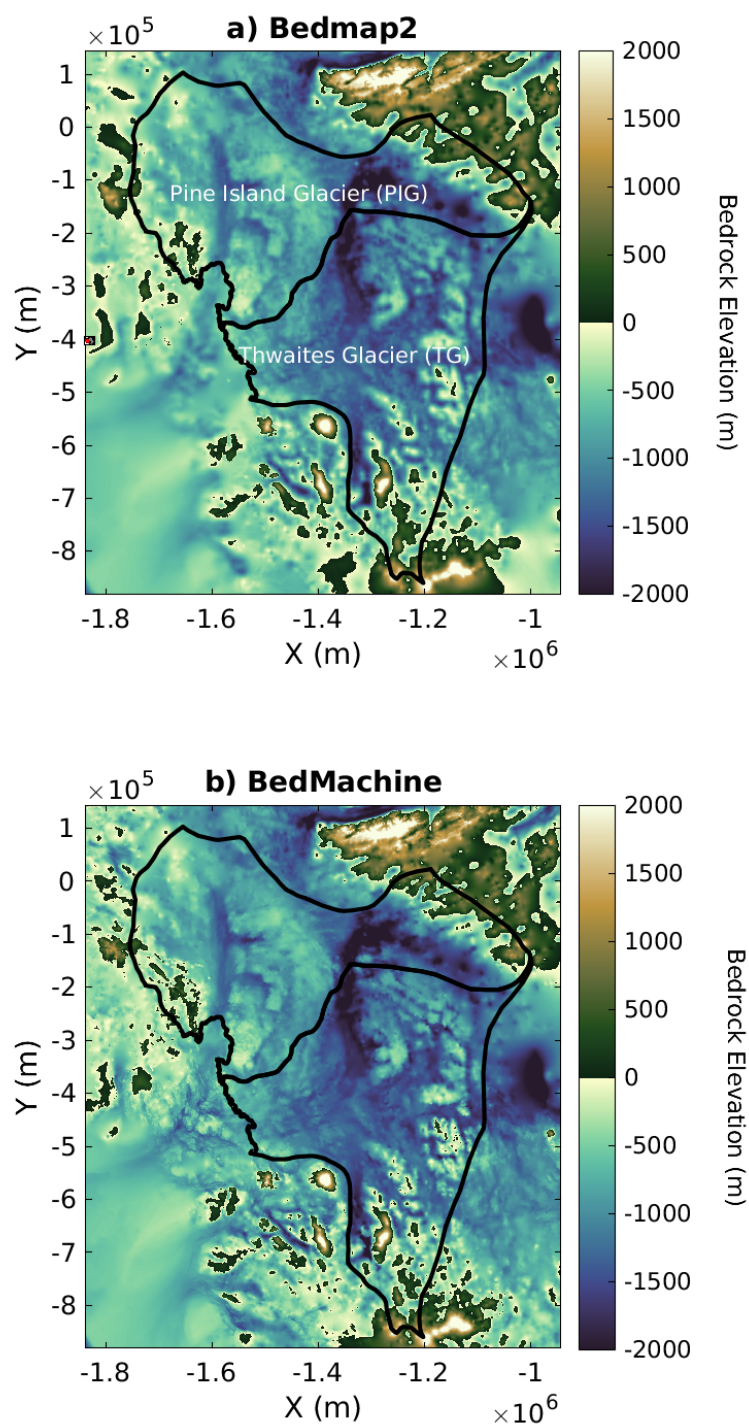


Figure 5.1: Amundsen Sea Embayment (ASE) bedrock elevation from a) Bedmap2 and b) BedMachine. Inset in a) shows location of region in Antarctica in the outlined red box. Black outlines represent the boundaries of Pine Island Glacier and Thwaites Glacier drainage basins. Produced with Greene et al. (2017) mapping tools.

Here, ice sheet model simulations of the ASE are performed with two geometry

(ice thickness and topography) products (fig. 5.1), BedMachine Antarctica version 1 (Morlighem et al., 2020) and a modified version of Bedmap2 (Fretwell et al., 2013; Nias et al., 2016), to examine the role of bed topography in controlling the response to varied magnitudes of sub-ice shelf melting of ASE ice streams. The melt forcings applied throughout the simulations are designed to explore both the bedrock dependent response of the ice streams to different magnitudes of melting, in addition to the ability of ice streams to stabilise following the removal of forcing (Schoof, 2007). Furthermore, to investigate the relative importance of representation of basal sliding with alternative geometry products, two sliding laws are implemented, also providing continuity with previous chapters. This research builds on Castleman et al. (2021) and Wernecke et al. (2022) by exploring melt forcing of a greater magnitude and providing a direct comparison between the ASE's two largest ice streams.

5.2 Method

The BISICLES ice sheet model (see Chapter 3) is used to simulate the evolution of PIG and TG in response to idealised scenarios of basal melting using the variables of bed topography and ice thickness from two separate geometry products, BedMachine version 1 (henceforth referred to as BedMachine, Morlighem et al., 2020) and a modified Bedmap2 (henceforth simply Bedmap2, Nias et al., 2016, ; fig. 5.1). The simulations are performed with an adaptive mesh, where the grid resolution varies between 4000 m and 250 m. As such, this ice sheet model will be able to capture the roughness of the bed of BedMachine, which coarser models are unable to do. Generally, the Bedmap2 dataset is consistent with observations from around the year 2000 and BedMachine from 2007, though the data obtained is often a composite over longer time periods.

5.2.1 Initialisation

5.2.1.1 Bedmap2

The regional domain of the ASE is initialised for the year 2000, following the method described in Nias et al. (2016); Alevropoulos-Borrill et al. (2020). Bed topography and ice thickness are derived from a modified Bedmap2 (Nias et al., 2016; Fretwell et al., 2013) with 1 km horizontal resolution. The product succeeds Bedmap1 (Lythe and Vaughan, 2001) with updated thickness measurements and a more refined grid. Further-

more, the modified Bedmap2 is considered an improved version of the original product (Nias et al., 2016). The method to produce this modified bed ensured modelled thinning rates better matched those observed in the region (Nias et al., 2016), and the resulting product ensured transient mass loss estimates were more consistent with observations (McMillan et al., 2014). The most distinct differences between the modified Bedmap2 and the original are the inclusion of a -600 m elevation area beneath the Crosson Ice Shelf where data is absent and the removal of a bed feature at the 1996 grounding line of PIG that resulted in erroneous thickening at the grounding line, discussed in Cornford et al. (2015). The use of the modified Bedmap2 instead of the original dataset is partly to maintain consistency with previous chapters. Furthermore, the modified Bedmap2 is an improvement of the original product as it was found to produce more realistic ice behaviour (Nias, 2017) meaning differences between the modified Bedmap2 and mass conserving BedMachine could be less stark.

The surface mass balance field from Arthern et al. (2006) and temperature field from Pattyn (2010) are held constant through time. The model domain is initialised by performing an inversion (see Chapter 3) to match modelled velocities to observations (Rignot et al., 2011), 2007 - 2009 average, through a tuning process to produce two spatially varying parameter fields, a traction coefficient (C) and ice rheology (ϕ) (Cornford et al., 2013). The domain is initialised with both Weertman (Weertman, 1957) and regularized Coulomb (Joughin et al., 2019) sliding laws (see Chapter 2).

5.2.1.2 BedMachine

BedMachine Antarctica succeeds Bedmap2 in two ways, firstly, the dataset is resolved to 0.5 km as opposed to 1 km (Morlighem et al., 2020). As the mechanical coupling between grounded and floating ice must be resolved over fine horizontal spatial resolutions (Vielé and Payne, 2003), the finer horizontal resolution of BedMachine provides more detail of the topographic influence on grounding line position and therefore the ice dynamics in this area. Secondly, the generation of the BedMachine product involved the use of mass conservation methods (Morlighem et al., 2011), correcting for both changes in surface mass balance and temporal ice thickness changes in order to improve the thickness calculation.

The BedMachine data product of bed topography and thickness has been derived from a combination of in situ radio echo sounding data, satellite derived surface ve-

locity, modelled surface mass balance and surface elevation data (Morlighem et al., 2020) to obtain the grounded ice topography and thickness fields. The surface elevation data used in BedMachine was taken from the Reference Elevation Model of Antarctica (Howat et al., 2019). Further, seismic and gravity derived bathymetry data was obtained to compute the topography for areas covered by floating ice. BedMachine is considered an updated dataset, revising topography of over half the existing Bedmap2 data for regions flowing faster than 50 m yr^{-1} .

To perform simulations with the topography and ice thickness from BedMachine (Morlighem et al., 2020), a new domain is initialized to produce an alternative field of C and ϕ so that the velocity field is consistent with observations. The velocity product used for the initialisation is Mouginot et al. (2017), which is the dataset used in the mass conservation methods by Morlighem et al. (2020) used to create BedMachine, and which is an average from 2013 to 2017. Surface mass balance is from Arthern et al. (2006) and a temperature field is taken from Pattyn (2010) to maintain consistency with the Bedmap2 simulations. Again, the domain is initialised with both Weertman (Weertman, 1957) and regularized Coulomb (Joughin et al., 2019) sliding laws.

5.2.1.3 Comparison of Parameters

Pine Island Glacier The C field impacts the sliding of ice along bedrock, and combines with the sliding law to determine the basal drag resisting ice flow. Along the main trunk and tributaries the BedMachine C is greatest (fig. 5.2a), where ice that exists outside of the ice stream has a lower C relative to Bedmap2. Within 40 km of the initial grounding line of BedMachine, there is an area of difference with BedMachine having both higher and lower C within the same area. Of the entire PIG drainage basin, 35 % of the area has a greater C in BedMachine relative to Bedmap2. This is also shown with the upper tail of the distribution showing a greater portion of higher traction values (fig. 5.2c), in addition to Bedmap2 having a greater mean and median C than BedMachine. However, the 35 % of the domain with greater C for BedMachine is occurring over the trunk and tributaries where the velocity is greatest and has the greatest influence on ice flux.

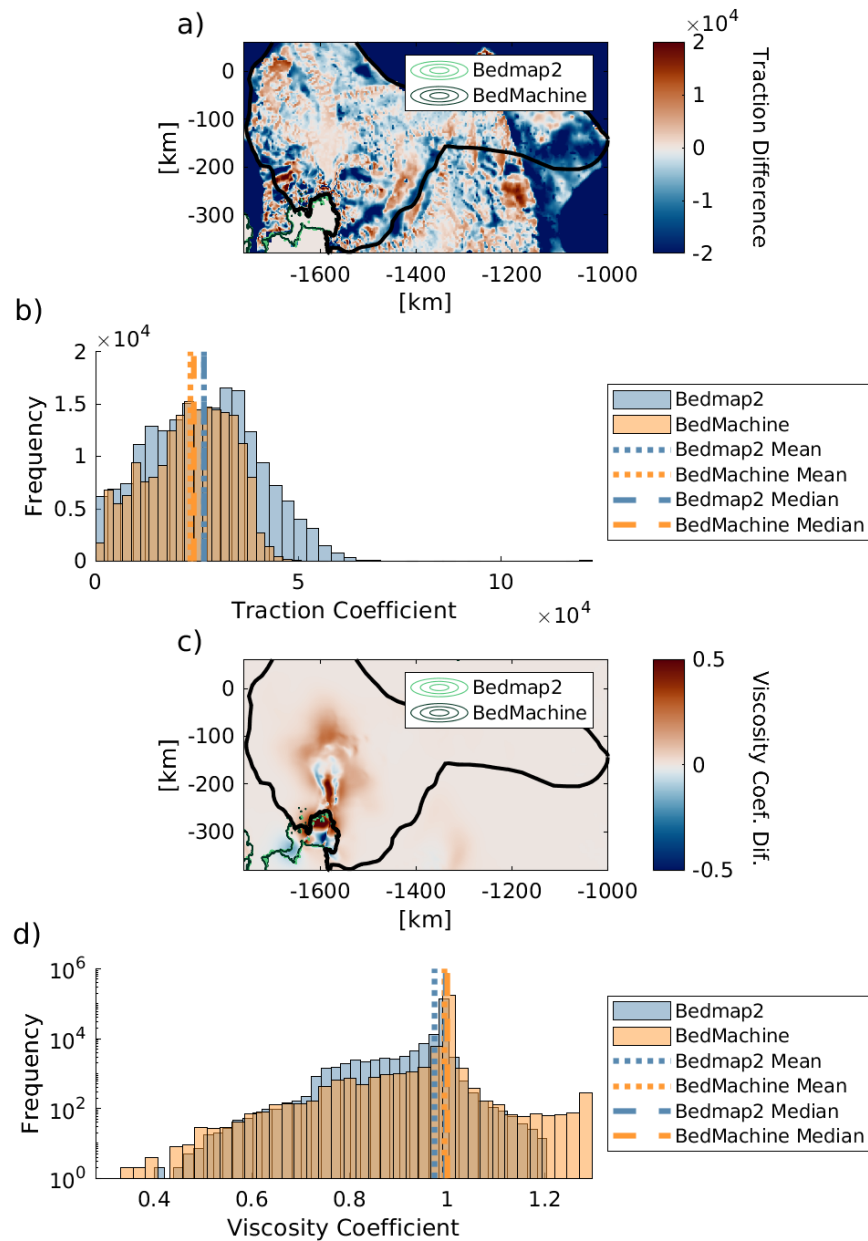


Figure 5.2: a) Difference in BedMachine basal traction over PIG relative to Bedmap2. b) Difference in BedMachine viscosity coefficient field relative to Bedmap2. Red (blue) shows BedMachine parameter is higher (lower) than Bedmap2. Black contour marks the outline for the PIG drainage basin. Friction parameters presented are those obtained for the regularized Coulomb sliding law. Histogram of Bedmap2 and BedMachine c) traction coefficient and d) viscosity coefficient over outlined drainage basin. Orange and blue vertical lines mark the mean and medians from the distributions.

The ϕ describes the material properties of the ice. During model tuning, ϕ becomes more rigid or soft and deformable to better match ice flow. Over 90 % of the PIG domain, the BedMachine ϕ is greater than Bedmap2 (fig. 5.2b) meaning the ice is made more rigid. This can also be noted in the distribution of ϕ values where the upper tail of the distribution is greater for BedMachine (fig. 5.2d) and the greater mean and median ϕ values in BedMachine. The southern portion of the ice shelf has a lower ϕ in BedMachine compared with Bedmap2, meaning ice is softer. Furthermore, upstream along the main trunk of the ice stream at the shear margins ϕ is lower for BedMachine.

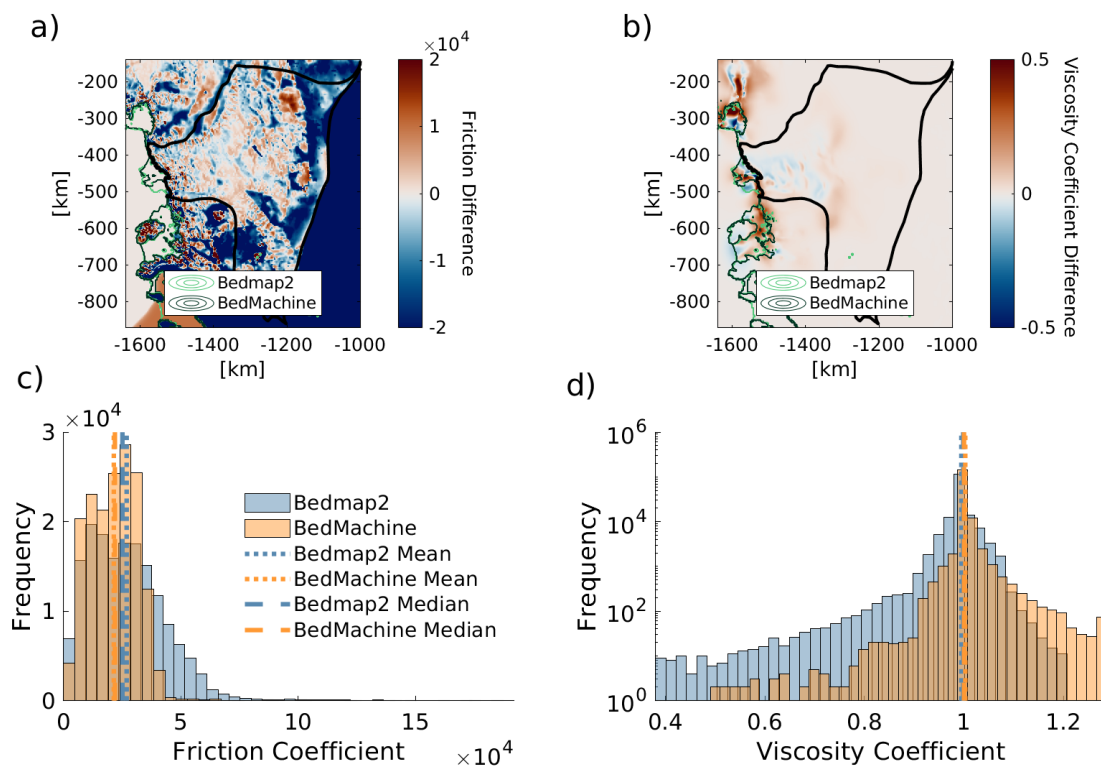


Figure 5.3: a) Difference in BedMachine basal traction over TG relative to Bedmap2. b) Difference in BedMachine viscosity coefficient field relative to Bedmap2. Red (blue) shows BedMachine parameter is higher (lower) than Bedmap2. Black contour marks the outline for the TG drainage basin. Friction parameters presented are those obtained for the regularized Coulomb sliding law. Histogram of Bedmap2 and BedMachine c) traction coefficient and d) viscosity coefficient over outlined drainage basin. Orange and blue vertical lines mark the mean and medians from the distributions.

Thwaites Glacier Basal traction beneath TG has a different pattern (fig. 5.3a), with the wide trunk showing both higher and lower C , with the greatest magnitudes of difference occurring at the grounding line. Of the grounded area included in the figure, 36 %

of the area has greater overall traction in BedMachine which is supported with the lower median and mean C values for BedMachine (fig. 5.3c). The ϕ however appears to be marginally lower along much of the main trunk of TG for the BedMachine initialisation though overall 85 % of the area has higher ϕ and BedMachine has a higher median and mean ϕ over the basin (fig. 5.3d). A large portion of the trunk of TG shows lower ϕ in BedMachine and the greatest differences in ϕ occurs over the floating ice shelves.

5.3 Control Simulations

5.3.1 Basal Mass Balance

For the control simulations, a two-dimensional basal melt used by Nias et al. (2016) and Cornford et al. (2015) is applied. This spatially distributed basal melt rate field is tuned to ensure modelled ice shelf thinning rates match observations (Cornford et al., 2015), with the highest melt rates concentrated adjacent to the grounding line of PIG (Rignot et al., 2013a; Shean et al., 2019). For PIG ice shelf the total basal melting is 100 Gt yr^{-1} which is consistent with Rignot et al. (2013a)'s estimates of $101.2 \pm 8 \text{ Gt yr}^{-1}$. The background melt field underestimates the total annual melt from TG with a value of 62 Gt yr^{-1} compared with $97.5 \pm 7 \text{ Gt yr}^{-1}$ from Rignot et al. (2013a). This melt rate field is read into BISICLES with a function that ensures melting is stretched toward the grounding line as this retreats. Although the melt rate field was calculated for Bedmap2 data, in order to control for differences in the forcing and ensure the ice response is due to the different initial ice thickness and topography, this has also been used for the BedMachine simulations.

All simulations have a fixed calving front, unless otherwise described, and a minimum thickness of 10 m is prescribed for numerical stability.

5.3.2 Simulations

Control simulations for Bedmap2 and BedMachine are performed using both Weertman sliding (Weertman, 1957) and regularized Coulomb sliding (Joughin et al., 2019). As the plastic bed rheology was found to better represent sliding beneath ASE ice streams, simulations with regularized Coulomb sliding will be the focus of the analysis. However, for comparison of uncertainty, the results of the Weertman sliding simulations

are presented in the discussion. Simulation codes therefore include the bed topography product, the sliding law and the basal melt forcing e.g. Bedmap2-rC-ctrl is the control melt simulation (ctrl) for Bedmap2 with regularized Coulomb (rC) sliding. BedMachine simulations are abbreviated to Bmach-*, again with the sliding law and melt forcing.

5.3.2.1 Relaxation

Initially, the control experiments are performed for 200 years and compared directly as though they were initialised for the same year. The velocity of PIG in the BedMachine simulation decreases over the first two years of the simulation as it relaxes (fig. 5.4). The average velocity of the ice shelf along the transect decreases from $\sim 5100 \text{ m yr}^{-1}$ to 4050 m yr^{-1} . Conversely, the velocity of PIG in the Bedmap2 simulation increases over the first 10 years of the simulation, with mean ice shelf velocity along the transect being $\sim 3200 \text{ m yr}^{-1}$ and increasing to 4800 m yr^{-1} .

To account for this disparity in velocity, a 10 year relaxation is performed for Bedmap2 and a 2 year relaxation is performed for BedMachine. The relaxation holds the present day melt rates constant during the first years of the experiment. This has been performed for both the control simulations and the perturbed simulations. From henceforth, when presenting the results, year 11 and year 3 for Bedmap2 and BedMachine simulations are described to represent conditions in 2010, which is $t = 0$.

While this relaxation period captures the speed up in velocity of PIG over the first 10 years of the simulation to better match the velocity of Mouginot et al. (2017) used to initialise BedMachine, capturing this equivalent speed up in TG is more challenging. As a result, it is acknowledged that the initial velocity of Bedmap2 and BedMachine over TG is inconsistent and this will be accounted for in the analysis of the results. A further justification of the requirements to generate this speed up of TG will be discussed in Section 5.5.2.

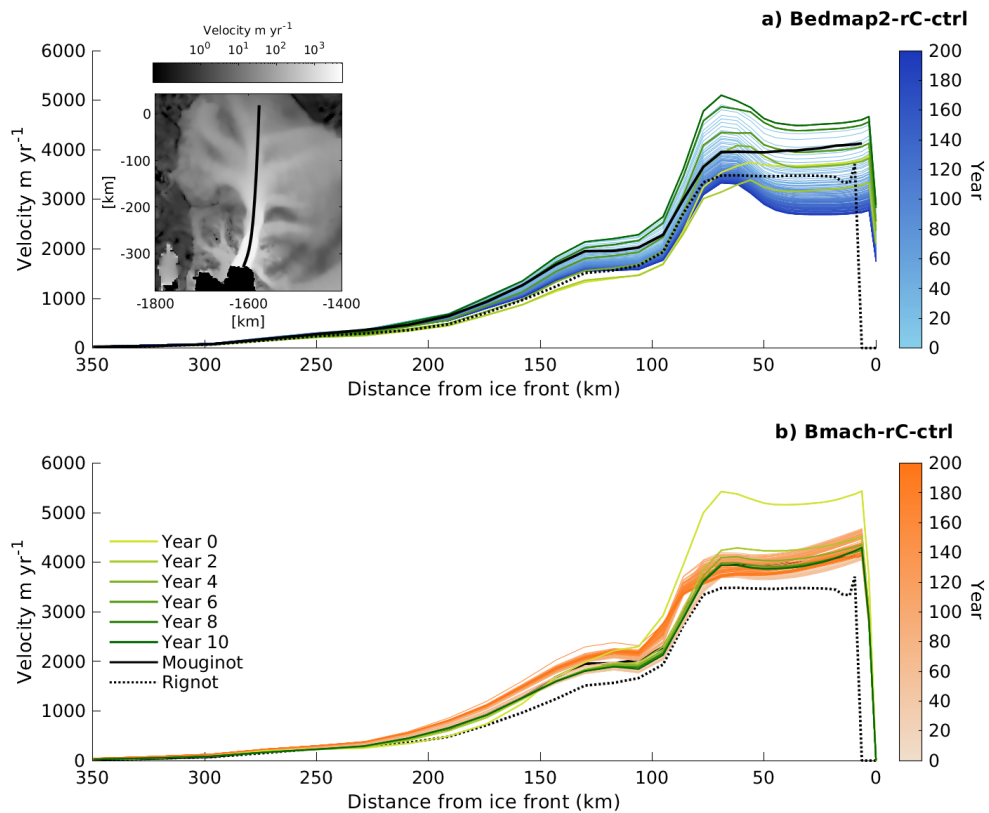


Figure 5.4: Velocity along PIG trunk transect plotted every two years over the 200 year simulations for a) Bedmap2-rC-ctrl b) Bmach-rC-ctrl with constant present day basal melting. Black solid line represents Mouginitot et al. (2014) velocity and black dotted line represents Rignot et al. (2011) velocity along the transect. Inset shows map of initial PIG velocity for Bedmap2-rC-ctrl with location of transect marked by a black line. Years 0 to 10 are plotted in an alternative color scale as shown in the legend.

5.3.3 Results

For each ice stream the differences in the initial conditions of the bed, ice thickness and surface elevation are described before then describing the results of the control simulations. While figures present rectangular insets of each drainage basin, percentages of thickness and elevation area quoted in the text correspond to values for the whole drainage basin outlined in figure 5.1.

5.3.3.1 Pine Island Glacier

The pattern of thickness difference over PIG is spatially variable (fig. 5.5a). Over PIG, 56 % of the area has thicker ice in BedMachine relative to Bedmap2 at $t=0$. Within 40

km of the initial grounding line position, BedMachine has ~ 150 m thicker ice than Bedmap2. This thickness difference in the central trunk extends into the central ice shelf. The surface elevation over the majority of the domain is approximately 30 m lower in BedMachine (fig. 5.5b). Around the grounding line and over the central ice shelf BedMachine has a 50 m higher elevation than Bedmap2. BedMachine also has a greater area of deeper bed than Bedmap2 (fig. 5.5c), which is consistent with areas of thicker ice upstream of the grounding line (fig. 5.5a). Over the mountainous region to the north of the PIG trunk, there is a large area of positive bedrock difference of up to 500 m which is consistent with thinner ice in the same location.

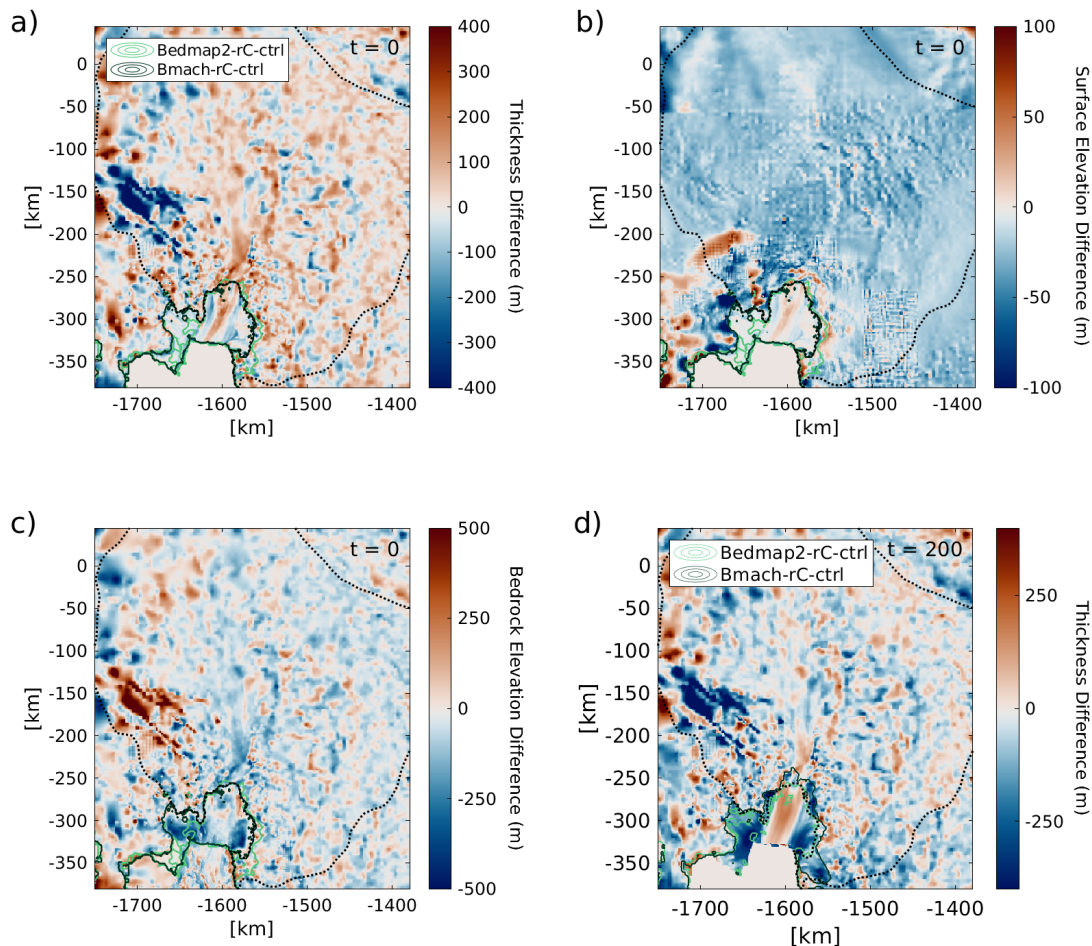


Figure 5.5: Comparison of a) initial thickness b) initial surface elevation, c) bedrock elevation and d) thickness difference in the year 200 of control simulations. Red (blue) shows the BedMachine variable is greater (lesser) than Bedmap2. d) Dashed coloured lines show the grounding line positions in the Year 200, blocked coloured lines show the respective initial grounding line positions.

The difference in ice thickness at the end of the 200 year -ctrl simulation (fig. 5.5d) shows increased thinning of the northern and southern ice shelves of PIG in BedMachine with a thicker central ice shelf than Bedmap2. This thinning corresponds with areas of increased grounding line retreat in BedMachine, around the central trunk and along the Southwestern Tributary of PIG.

Despite the same melt rate forcing being applied to both domains, the Bmach-rC-ctrl simulation results in a greater velocity along the main trunk of PIG than Bedmap2 over much of the 200 year simulation (fig. 5.6), which coincides with greater mass loss of 29 mm compared with 12 mm from Bedmap2. Until $t=40$, the Bedmap2 simulation has greater velocity than BedMachine, starting with a difference of 400 m yr^{-1} and decreasing in difference over time as PIG accelerates in Bmach-rC-ctrl. From $t=30$ onward Bmach-rC-ctrl experiences faster ice flow where the difference increases throughout the simulation. At $t=200$ there is a difference in ice velocity of over 1500 m yr^{-1} over the ice shelf of PIG and over 700 m yr^{-1} over the trunk of the ice stream, extending over 150 km upstream from the grounding line but with the difference decreasing with increased distance from the grounding line.

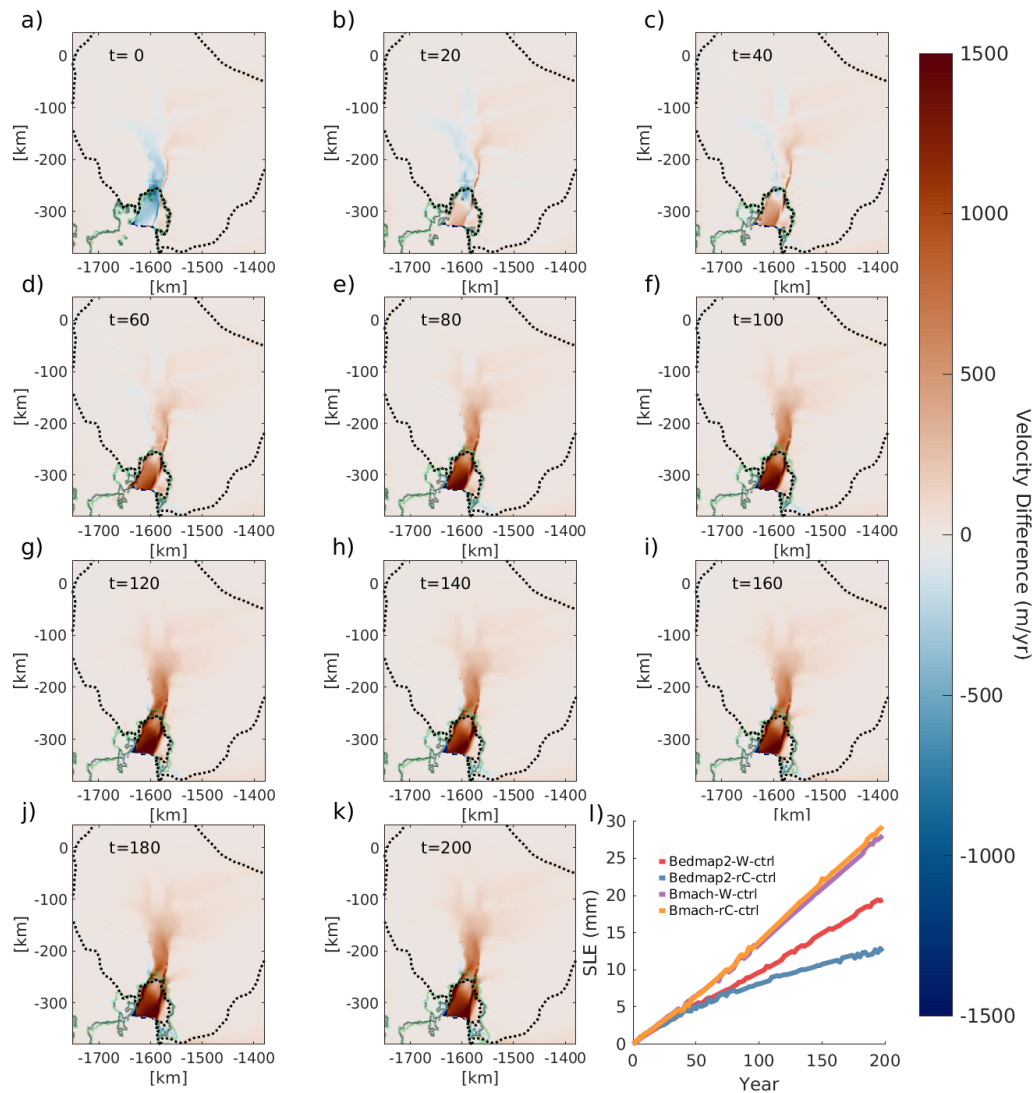


Figure 5.6: a-k) Velocity difference at 20 year intervals between BedMachine and Bedmap2 control runs with constant present day basal melting. Red (blue) shows BedMachine has a higher (lower) velocity. l) Sea level equivalent contribution from PIG over the 200 year control simulations.

5.3.3.2 Thwaites Glacier

By the end of the control simulations, mass loss from TG equates to 21 mm of global sea level rise in the Bedmap2 simulation compared with 34 mm for BedMachine. The initial ice geometry of TG is different between Bedmap2 and BedMachine, most notably the horizontal extent of the ice shelf. The absence of a large area of the western ice tongue

of TG is evident from the 400 m difference in thickness (fig. 5.7a). There are a number of areas over the domain where ice is both thicker and thinner in BedMachine which has a random distribution, though overall 61 % of the area of TG is thicker. The surface elevation for BedMachine is lower than Bedmap2, as is consistent with PIG (fig. 5.7b). A large positive difference in bedrock elevation of approximately 500 m occurs where an absence of bathymetry data beneath the Crosson Ice Shelf was replaced with a -600 m elevation sea floor by Nias et al. (2016), which has been filled in with bathymetry from Millan et al. (2017) in BedMachine. BedMachine has both a deeper and shallower bed beneath TG over the domain with the largest difference occurring beneath the ice shelf and at the initial grounding line of the ice stream where the bed resides at up to 400 m deeper than Bedmap2.

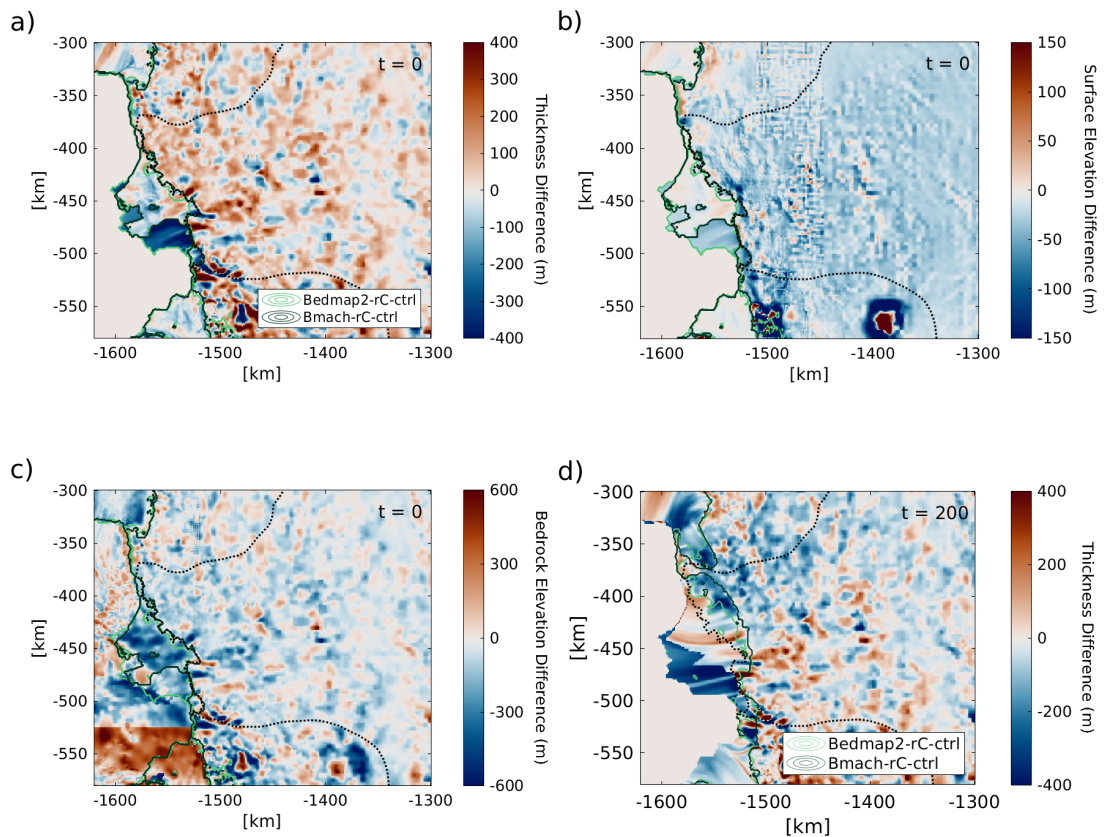


Figure 5.7: Comparison of a) initial thickness b) initial surface elevation, c) bedrock elevation and d) thickness difference in the year 200 of control simulations. Red (blue) shows the BedMachine variable is greater (lesser) than Bedmap2. d) Dashed coloured lines show the grounding line positions in the Year 200, blocked coloured lines show the respective initial grounding line positions.

Much of eastern TG shows greater thinning in BedMachine relative to Bedmap2

(fig. 5.7d), most notably around the retreated grounding line. The ice shelf shows strips of increased thickness in BedMachine at the end of the simulation relative to Bedmap2. Overall the extent of ice shelf in the BedMachine simulation reduces further with much of the western ice tongue disappearing and the eastern ice shelf front retreating, resulting in a large difference in the thickness where ice is present in the Bedmap2 simulation but non-existent for BedMachine.

Considering areas of equivalent ice shelf extent, the western ice tongue in BedMachine initially exceeds the velocity of Bedmap2 by $\sim 1500 \text{ m yr}^{-1}$ (fig. 5.8). Upstream of the grounding line along the central trunk of the ice stream, velocity for BedMachine is up to 500 m yr^{-1} greater in BedMachine extending 20 km upstream, with differences of up to 100 m yr^{-1} extending further inland. For the first 60 years of the simulation the area of largest velocity mismatch extends, with the biggest difference in velocity occurring around the retreating grounding line along the western trunk of TG in the BedMachine simulation. From $t=20$ until the end of the simulation the entire TG ice shelf has a greater velocity by up to $\sim 500 \text{ m yr}^{-1}$ in BedMachine, though the magnitude of the difference decreases from $t=60$ onward.

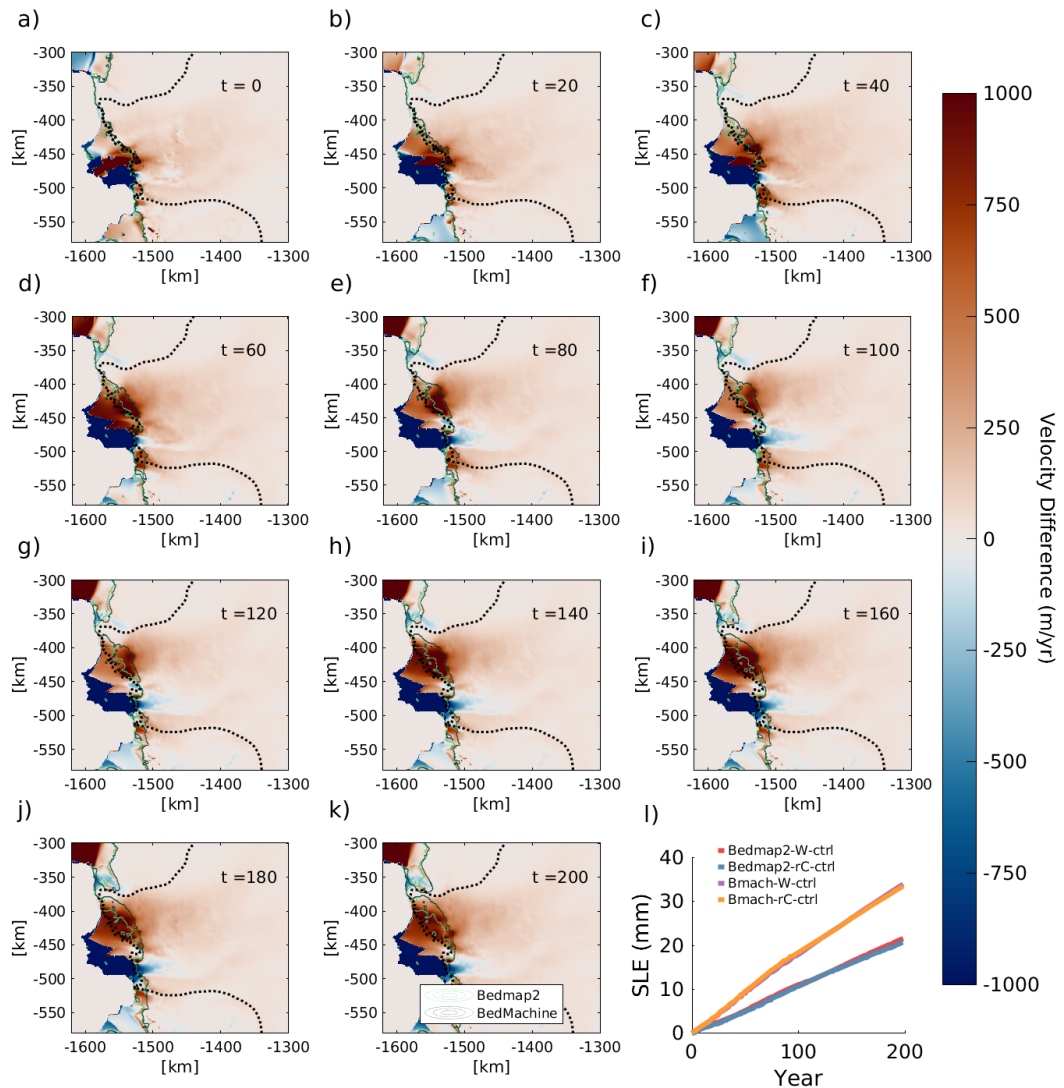


Figure 5.8: a-k) Velocity difference at 20 year intervals between BedMachine and Bedmap2 control runs with constant present day basal melting. Red (blue) shows BedMachine has a higher (lower) velocity. l) Sea level equivalent contribution from TG over the 200 year control simulations.

5.4 Perturbed Simulations

5.4.1 Simulations

To explore the domain response to perturbations in melting, two simulations are performed to represent a low (-low) and high (-high) magnitude ice shelf melt forcing

for each bed geometry product. In these simulations the grounding line localised melt anomaly (See Chapter 4 for more detail) is increased linearly to 5 and 20 m yr^{-1} over 20 and 100 years respectively, before this anomaly is removed and only the initial background melt continues for the remainder of the 200 year simulation. The purpose of these perturbations is to explore both the response to elevated sub-shelf melting in addition to the ability for the grounding line position to stabilise following an initial period of retreat.

5.4.2 Results

5.4.2.1 Pine Island Glacier

Over 200 years, PIG contributes 58 mm of SLE in Bmach-rC-high compared with 37 mm for Bedmap2-rC-high (fig. 5.9a) and 33 mm and 14 mm for Bmach-rC-low and Bedmap2-rC-low respectively. In response to increased melting, both BedMachine and Bedmap2 result in an acceleration in SLE, where the gradient is greatest for BedMachine 5.9b). Upon the removal of forcing at 100 years, both Bmach-rC-high and Bedmap2-rC-high exhibit a reduction in the rate of mass loss. Bmach-rC-high contributes 43 mm to SLE over the first 100 years and 14 mm over the second 100 years, meaning the second century contribution from BedMachine is equivalent to the 200 year contribution from a control or low melt simulation with Bedmap2. There is some overlap in the range of SLE contribution over the 200 years, with Bedmap2-rC-high SLE contribution being only 4 mm greater than Bmach-rC-low.

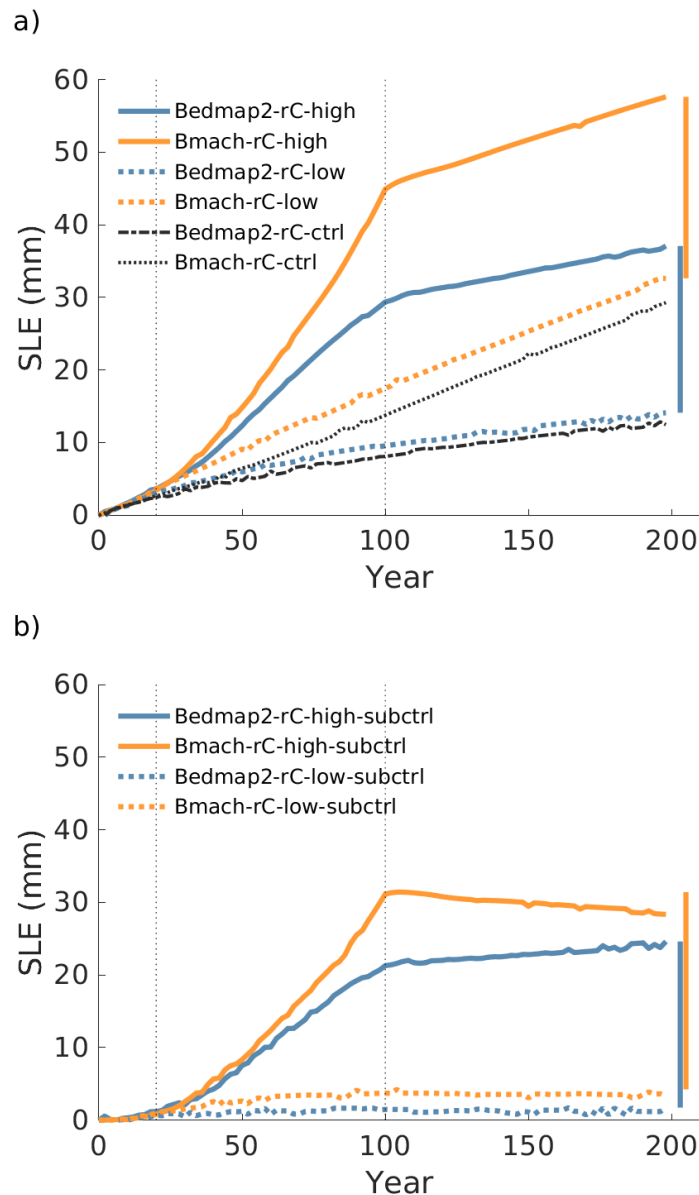


Figure 5.9: a) PIG SLE over 200 years for regularized Coulomb simulations. Coloured block and dotted lines show high and low melt simulations respectively. Black block and dotted lines show Bedmap2 and BedMachine control simulations respectively. b) SLE contribution from Bedmap2 and BedMachine over high and low melt forced simulations with the control simulation SLE subtracted (-subctrl). Vertical black dotted lines mark the years in which the melt anomaly is removed.

Subtracting the control simulation from the perturbed simulations gives an indication of the response to forcing alone, without including dynamic behaviour of the model as a result of the initialisation. Overall the Bmach-rC-high-subctrl simulation

experiences greater mass loss from PIG than Bedmap2-rC-high-subctrl by 4 mm when considering the forced response alone (fig. 5.9b). There is a reduction in the SLE contribution from PIG from 100 to 200 years in the BedMachine simulation whereas the Bedmap2 simulation shows a near negligible increase in SLE contribution, relative to the control.

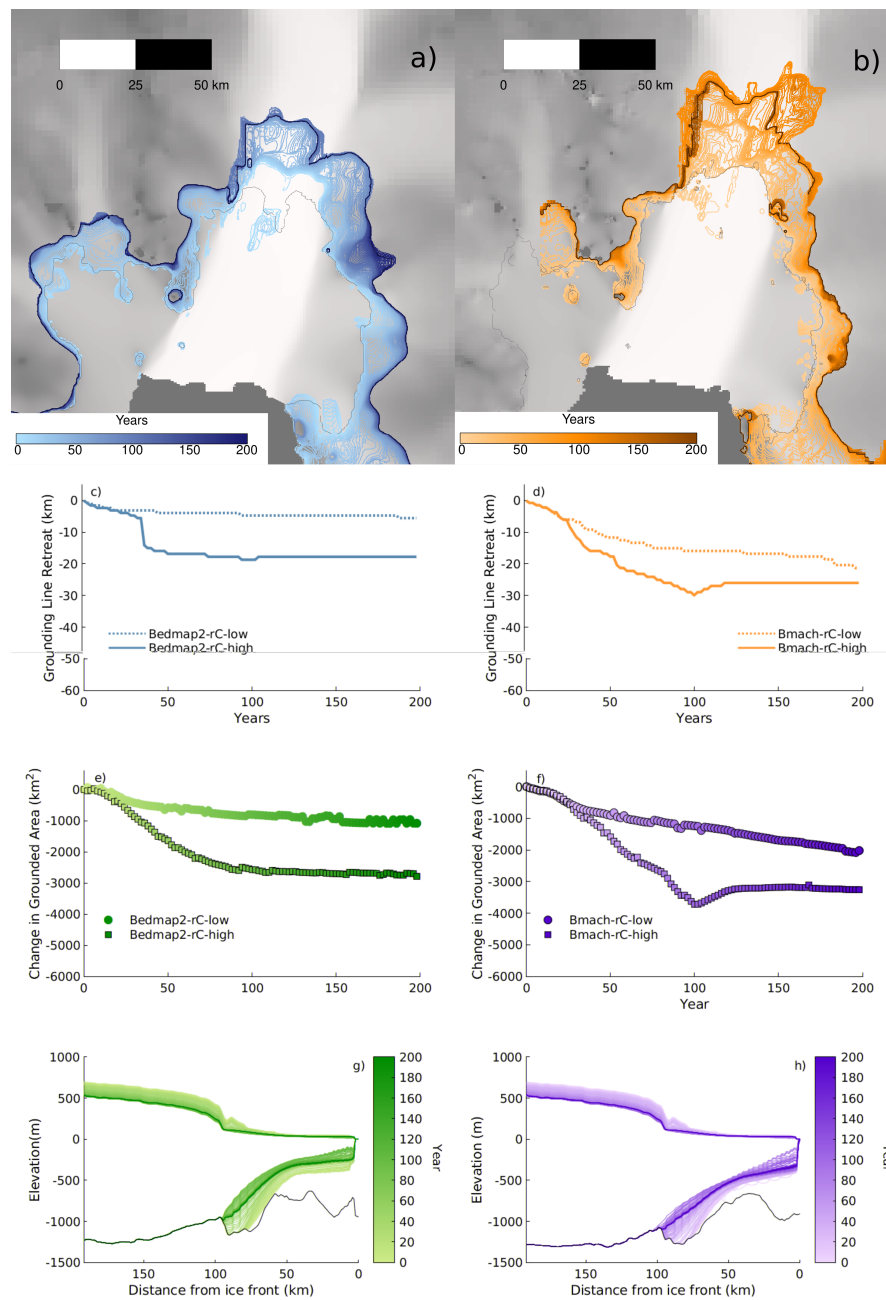


Figure 5.10: Pine Island Glacier grounding line positions plotted every two years over the high melt simulation for a) Bedmap2-rC and b) Bmach-rC. Grounding line retreat along transect over time for c) Bedmap2-rC and d) Bmach-rC simulations with both low and high melt. Scatter plot of change in the grounded area of the drainage basin over time relative to the initial position for e) Bedmap2-rC and f) Bmach-rC. Surface and basal elevation profiles along transects for g) Bedmap2-rC h) Bmach-rC plotted every two years. Black contour represents bed topography along PIG flowline.

In Bmach-rC-high, the grounding line retreats further than Bedmap2 by up to ~ 25 km along the main trunk over the 200 year simulation. Following the removal of forc-

ing in Bedmap2-rC-high, there is minimal change in the total grounded area of the ice stream, where the grounding line advance at the northern margin of the trunk offsets the continued retreat of the southern ice shelf margin. In contrast, the PIG grounding line in Bmach-rC-high advances by 5 km in the northern margin of the trunk and the southeastern trunk and up to 20 km of grounding line advance along the central trunk of the ice stream. Overall the Bmach-rC-high experiences grounding line advance equivalent to a re-grounding of $\sim 500 \text{ km}^2$. For both Bedmap2-rC-high and Bmach-rC-high simulations, the grounding line retreat over time appears to be consistent with a clustering in grounding lines around the final position.

5.4.2.2 Thwaites Glacier

There is no overlap in the end of simulation SLE contribution from the TG for simulations with different bed geometries (fig. 5.11a). Bmach-rC-high contributes 64 mm compared with 31 mm from Bedmap2-rC-high, and Bmach-rC-low and Bedmap2-rC-low contribute 35 mm and 22 mm respectively. In Bmach-rC-high, following the removal of forcing in year 100, TG continues to lose mass albeit at a reduced rate. The control simulations for both domains result in a similar end of simulation SLE contribution from TG as the low melt simulations. Removing the control shows that there is a more pronounced difference in the response of the ice stream in both domains to perturbed basal melting, with a 30 mm SLE contribution in Bmach-rC-high-subctrl compared with 10 mm in Bedmap2-rC-high-subctrl (fig. 5.11b).

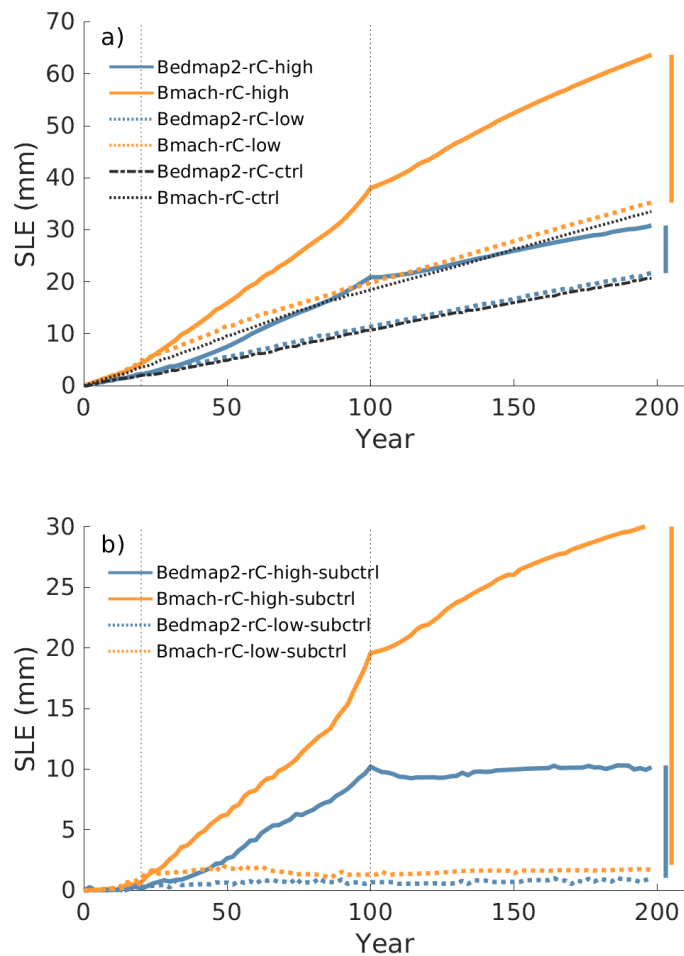


Figure 5.11: a) TG SLE over 200 years for regularized Coulomb simulations. Coloured block and dotted lines show high and low melt simulations respectively. Black block and dotted lines show Bedmap2 and BedMachine control simulations respectively. b) SLE contribution from Bedmap2 and BedMachine over high and low melt forced simulations with the control simulation SLE subtracted. Vertical black dotted lines mark the years in which the melt anomaly is removed.

The grounding line of TG continues to retreat throughout Bedmap2-rC-high and Bmach-rC-high, although the majority of the retreat occurs over the first 100 years of the simulation while basal melting is increased (fig. 5.12). In Bedmap2-rC-high the grounding line stabilises at a position 36 km upstream from the initial grounding line over the eastern trunk of TG. Initially the retreat is slow, with only 15 km of grounding line retreat over the first 80 years followed by 18 km over 20 years which then remains in this position for the second 100 years in the simulation with reduced melt-

ing. There is evidence of stabilisation on an eastern ridge 29-32 km upstream from the initial grounding line in Bmach-rC, which is in close proximity to the end of simulation Bedmap2-rC-high grounding line, 36 km upstream from the initial Bedmap2 grounding line. Bmach-rC-high experiences two stages of rapid grounding line retreat along the flowline in the eastern trunk, retreating 28 km in the first 35 years of the simulation followed by 20 km of grounding line retreat from the years 80 to 100. Although the grounding line in the eastern trunk appears to remain stationary for the second century of the simulation, the grounding line in the west continues to retreat throughout the simulation which is responsible for the continued reduction in grounded area in the second half of the simulation (fig. 5.12f).

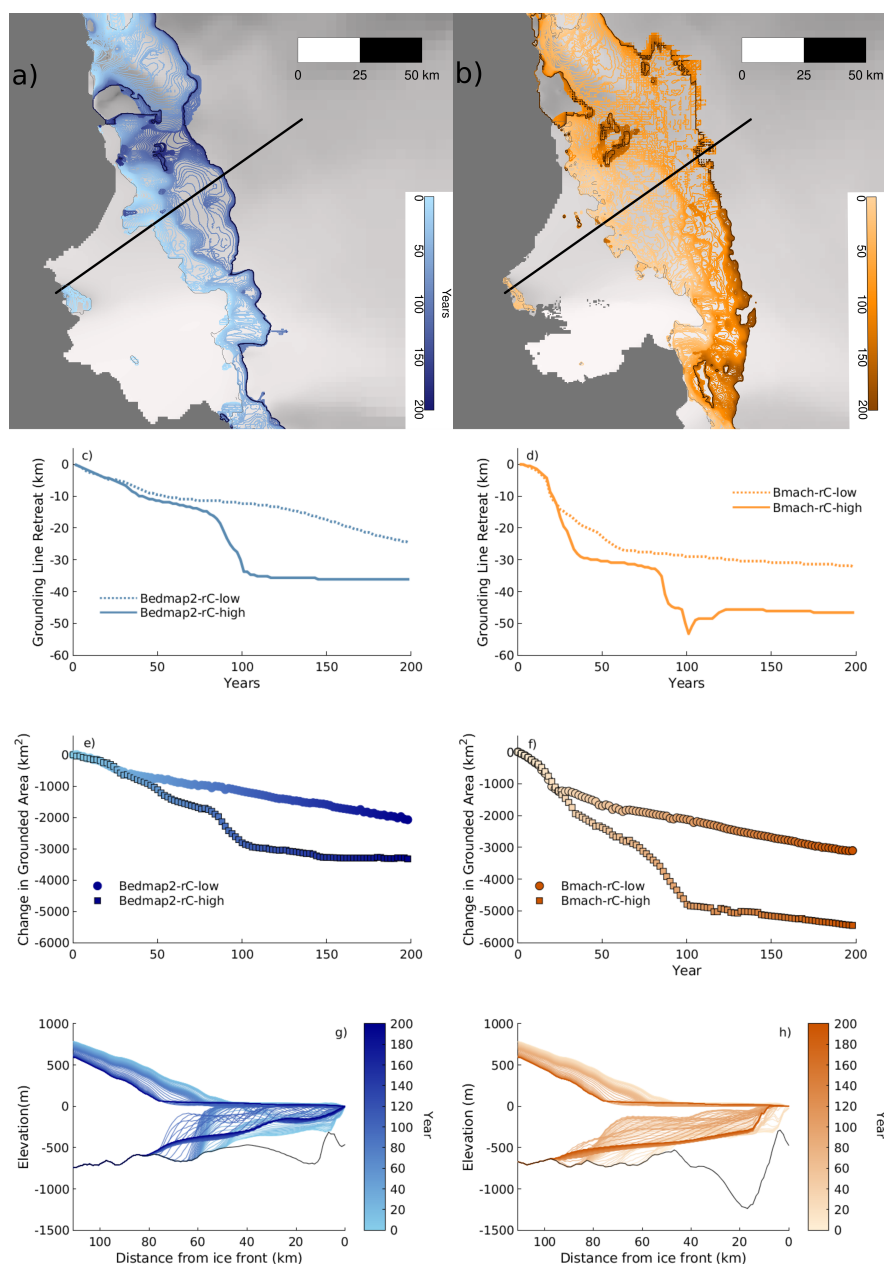


Figure 5.12: Thwaites Glacier grounding line positions plotted every two years over the high melt simulation for a) Bedmap2-rC and b) Bmach-rC. Grounding line retreat along transect over time for c) Bedmap2-rC and d) Bmach-rC simulations with both low and high melt. Scatter plot of change in the grounded area of the drainage basin over time relative to the initial position for e) Bedmap2-rC and f) Bmach-rC. Surface and basal elevation profiles along transects for g) Bedmap2-rC h) Bmach-rC plotted every two years. Black contour represents bed topography along TG flowline.

5.5 Discussion

The results presented here highlight the relative sensitivity of two major Antarctic ice streams to sub-ice shelf melting when alternate bed geometry and representations of basal drag are incorporated in the model simulations. This investigation builds upon that of Wernecke et al. (2022), who compared the two geometry products for PIG in response to high and low climate forcings over the 21st century. Here, a comparison of the two ice streams, PIG and TG, is presented with the response to high and low forcing explored over 200 years, with a focus on both the response to perturbed melting and the stability of the respective ice streams following removal of forcing. Furthermore, the topography product for Bedmap2 used here is a modified version of the bed which has been shown to permit ice flow behaviour that better represents observations (Nias et al., 2016; Nias, 2017). Therefore, these findings present new insight to the modelled behaviour of ASE ice streams using alternative, realistic, domains.

For both PIG and TG, the higher resolution BedMachine geometry product results in greater grounding line retreat and mass loss than Bedmap2 over perturbed and control simulations (fig. 5.15), which was also found by Wernecke et al. (2022) for PIG. The depth of the bed, the ice thickness and the role of topography in promoting and hindering grounding line migration control the differences in the ice stream response for the two geometry products, although the relative contributions of these factors cannot be directly determined here. While there is no statistical difference in the distributions of ice thickness and bedrock elevation of the two products for each ice stream basin (fig. 5.13), observed retreat of the grounding line in these simulations occurs mostly over bed that is deeper in BedMachine relative to Bedmap2 (fig. 5.14). Marine based ice grounded over deeper bed is more prone to grounding line retreat given that buoyancy forces are greater and therefore thicker ice may reach floatation (Schoof, 2007) leading to increased ice discharge and mass loss. Moreover, the simulations performed with BedMachine exhibit greater grounding line retreat due to fewer high amplitude topographic pinning points meaning retreat is exacerbated with elevated melting (Castleman et al., 2021), this will be discussed further in the following sections.

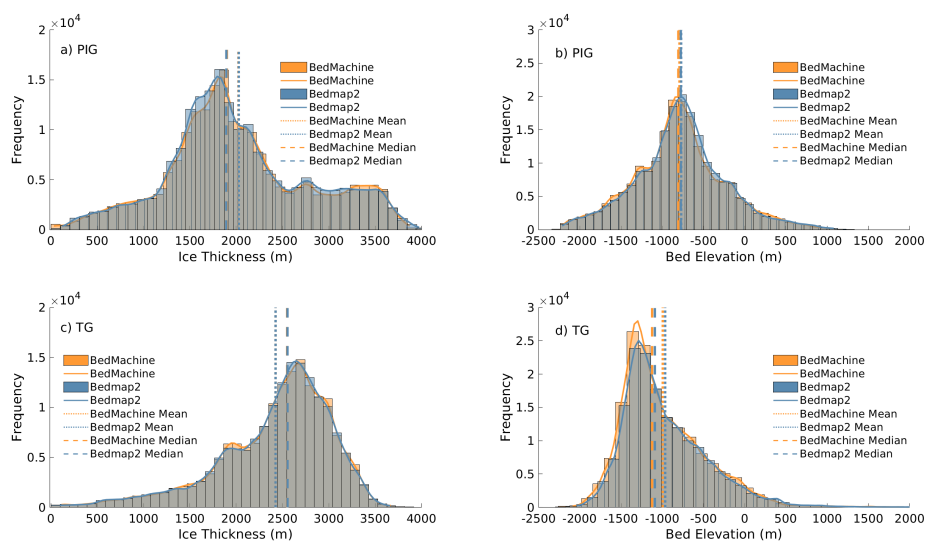


Figure 5.13: Distribution of ice thickness (a) and bedrock elevation (b) over the PIG drainage basin and TG basin (c-d). Vertical coloured lines mark the median and mean of the distributions. Note that ice thickness for both geometry products are from the raw datasets rather than the relaxed start year in these simulations, meaning they relate to different time periods.

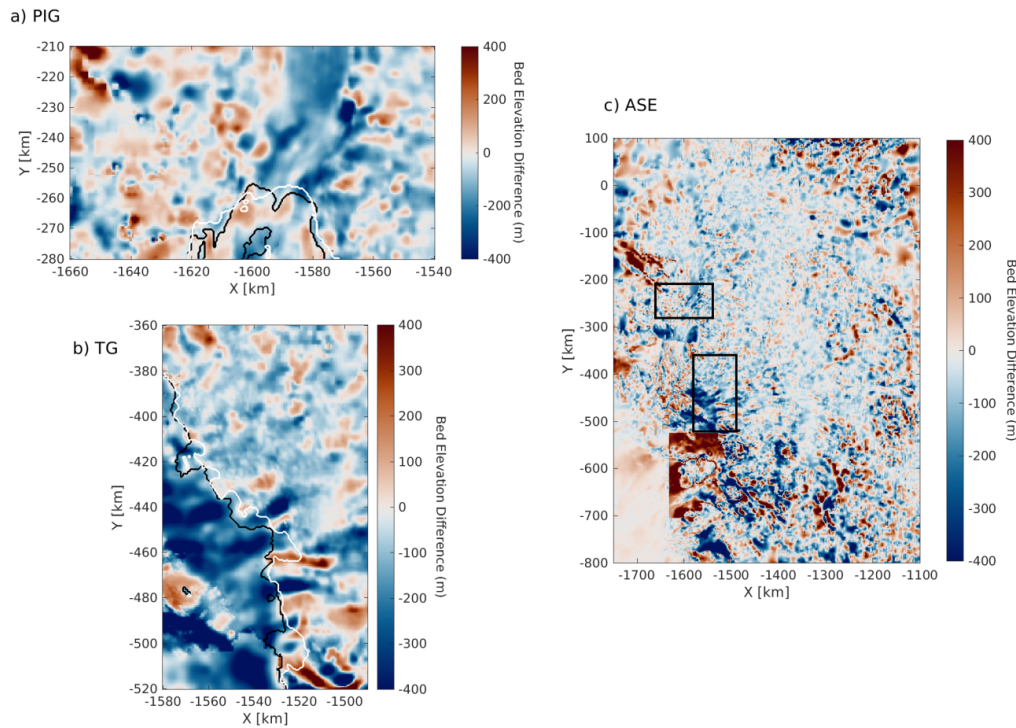


Figure 5.14: Differences in bedrock elevation between BedMachine and Bedmap2 for insets of the central trunk of a) Pine Island Glacier and b) Thwaites Glacier around the initial grounding line. The initial grounding lines for Bedmap2 are shown in black and BedMachine in white. c) Differences in bedrock elevation over the Amundsen Sea Embayment with black boxes marking the locations of a) and b) insets.

There is a topographic dependence in the ice stream sensitivity to perturbed melting for both ice streams (fig. 5.15). For the high melt simulations there is a 50 mm difference in the end-of-simulation combined SLE from PIG and TG for the two bed topographies which compares with a 32 mm difference for the low melt forcing. This highlights an interplay between the modelled ice stream sensitivity to topography and basal melting, where higher melt rates amplify the differences between the modelled ice dynamics for the two geometry products, which is consistent with Wernecke et al. (2022). Increased external forcing of the ice shelf drives grounding line retreat over deepening bed (fig. 5.1), where in BedMachine, there are fewer high amplitude points upstream from the initial grounding line that pause retreat (Castleman et al., 2021; Morlighem et al., 2020). Subsequently, while melting is increased, the rate of mass loss and grounding line retreat diverges, with a greater non-linearity of SLE contribution for BedMachine simulations. Thus, as the high melt forcing has a greater duration of increased melting, there is a greater duration over which the topographic dependent

ice dynamics can be exacerbated.

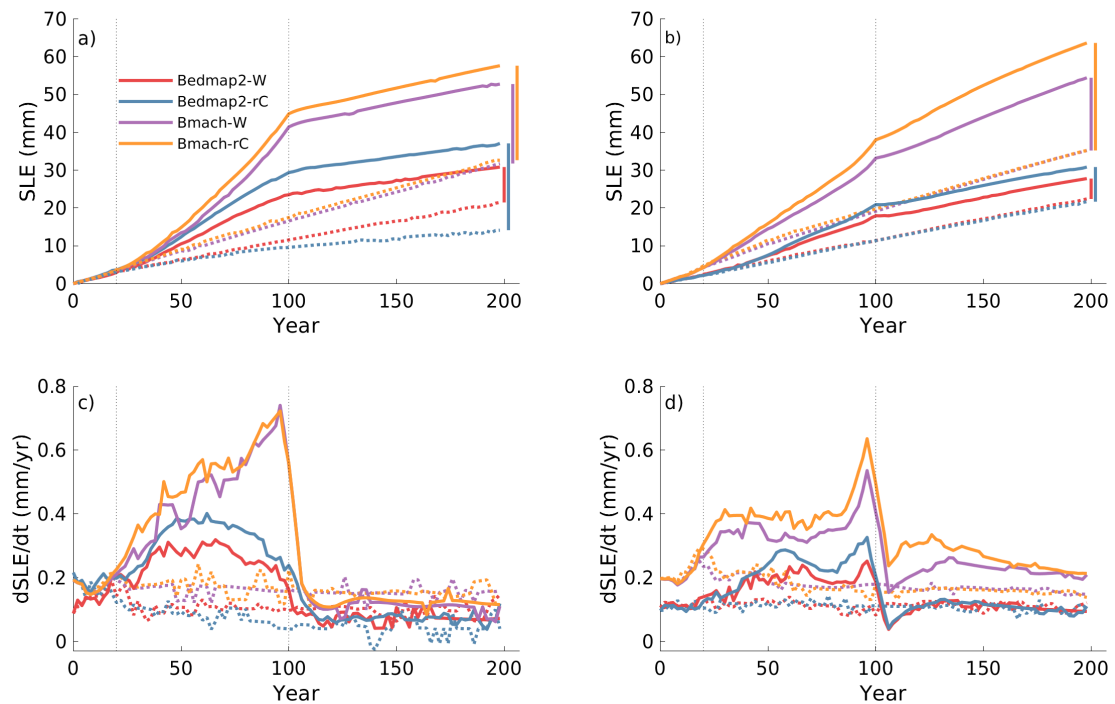


Figure 5.15: SLE for perturbed melt simulations for Bedmap2, BedMachine and the two sliding laws for a) PIG and b) TG. Rate of SLE contribution ($\delta SLE \delta t^{-1}$) for perturbed melt simulations for Bedmap2, BedMachine and the two sliding laws for c) PIG and d) TG. Dotted lines represent low melt simulations and block lines represent high melt simulations.

5.5.1 PIG

5.5.1.1 Control Simulations

Over PIG, the initialised model has a geometry more prone to mass loss in BedMachine than Bedmap2. Bmach-rC-ctrl results in 10 years of acceleration of PIG before remaining constant (fig. 5.16). In contrast, Bedmap2-rC-ctrl exhibits deceleration over the entire simulation as the grounding line becomes pinned on a prominent ridge ~ 16 km upstream from the initial position (fig. 5.10). While the initialisation parameters could play a part, the BedMachine domain has greater traction and viscosity over much of the trunk and tributaries which would act to slow ice flow relative to Bedmap2 simulations (fig. 5.2), contrary to the results. The increased velocity and discharge from the Bmach-rC-ctrl simulation, relative to Bedmap2-rC-ctrl, coincides with a greater extent of grounding line retreat (fig. 5.5) occurring due to fewer high amplitude pinning

points (Castleman et al., 2021). Furthermore, as the grounding line in Bmach-rC-ctrl retreats over deeper bed than Bedmap2, the volume of ice being discharged into the ice shelf is greater. Therefore, the difference in topography and ice thickness controls the differences in dynamic ice stream behaviour simulated.

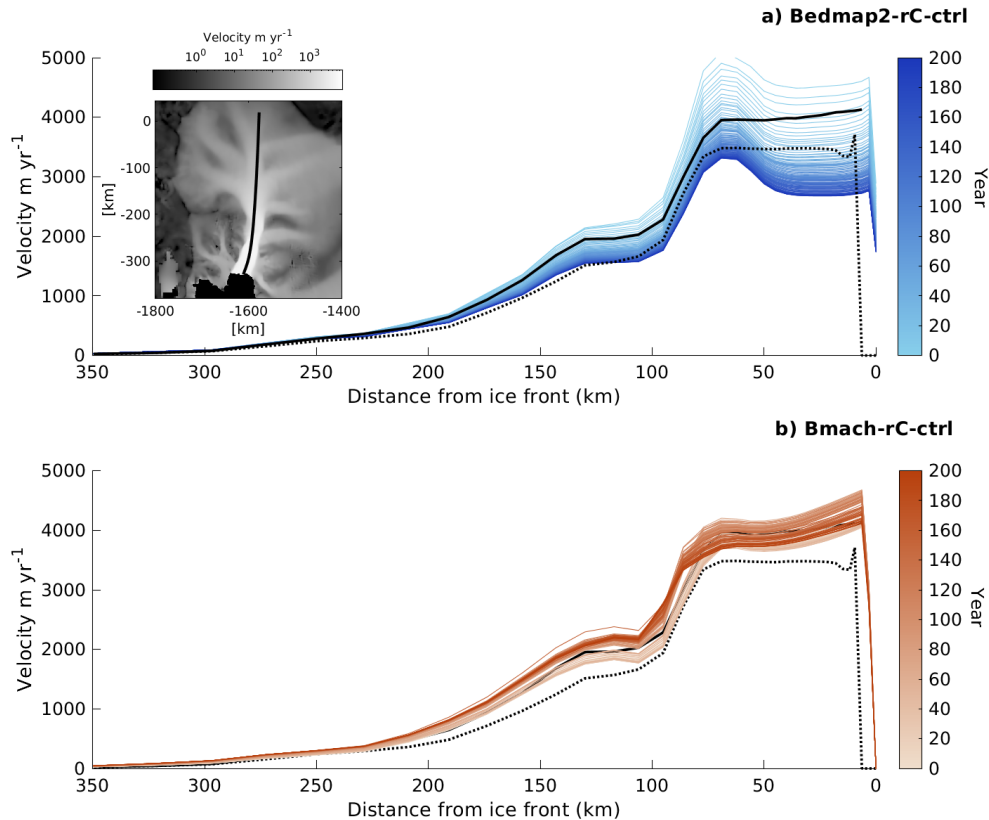


Figure 5.16: Velocity along PIG trunk transect plotted every two years over the 200 year simulations for a) Bedmap2-rC-ctrl b) Bmach-rC-ctrl with constant present day basal melting. Black solid line represents Mouginito et al. (2014) velocity and black dotted line represents Rignot et al. (2011) velocity along the transect. Inset shows map of initial PIG velocity for Bedmap2-rC-ctrl with location of transect marked by a black line.

5.5.1.2 Perturbed Simulations

The divergence in the rate of mass loss between Bmach-rC-high and Bedmap2-rC-high in response to prolonged forcing is a product of the presence of a strong pinning feature in Bedmap2 (Wernecke et al., 2022; Nias et al., 2016). With more consistent initial velocities following relaxation, it is shown that the rate of SLE contribution from PIG follows a similar trajectory for the two geometry products over the first ~ 20 years of

the simulation. Approximately 50 years into the simulations, the rate of SLE contribution for the Bedmap2-rC-high peaks and plateaus while Bmach-rC-high experiences accelerated mass loss. Wernecke et al. (2022) found a divergence in the bedrock driven response to occur in the year 2050 for PIG with the original Bedmap2 (Fretwell et al., 2013), which contrasts with the divergence at the equivalent of 2040 in these experiments after ~ 30 years. This divergence in the rate of mass loss (fig. 5.15) can also be seen in the change in grounded area (fig. 5.10) where the rate of retreat slows approximately 40 years into the simulation where the grounding line position stabilises on a ridge ~ 16 km upstream and elevated melt rates are insufficient to drive continued retreat. While this ridge exists in BedMachine (fig. 5.10), the elevation is lower and therefore its strength of pinning is reduced (fig. 5.14). Furthermore, with grounding line retreat occurring over deeper bed in BedMachine simulations, mass loss is expected to be greater due to an increase in ice volume crossing the grounding line.

Both Bedmap2 and BedMachine geometries promote grounding line stability for PIG following the removal of forcing. While the rate of mass loss in Bmach-rC-high and Bedmap2-rC-high diverges while forcing is applied, following the removal of forcing the rate of mass loss converges below 0.2 mm yr^{-1} (fig. 5.15). In fact, the rate of mass loss following $t=100$ in Bmach-rC-high becomes lower than the control, as shown by the decrease in SLE in Bmach-rC-high-subctrl (fig. 5.9). This is consistent with the grounding line retreat over the simulations exceeding that for Bedmap2 (fig. 5.10), where the grounding line retreats along the southern side of the trunk at the end of the forcing period before advancing. This indicates that PIG is sensitive to the removal of forcing, where Bedmap2 and BedMachine topographies permit slowed grounding line retreat, and advance, which stabilises the mass loss from the ice stream to near initial rates.

While the higher mass loss for simulations with BedMachine and a plastic rheology was found by Wernecke et al. (2022) over PIG, the magnitude of the differences disagrees with findings here. Wernecke et al. (2022) found a plastic bed rheology and high melt forcing resulted in 19 mm by 2100, which compares with our 45 mm for the same period for Bmach-rC-high at $t = 90$. As Wernecke et al. (2022) also used BISICLES, the differences in mass loss are attributed to differences in the applied melt forcing, where the background Dutrieux et al. (2014b) melt rates used in Wernecke et al. (2022) are lower than those from Cornford et al. (2015) used here. The low mag-

nitude ocean forcing used in Wernecke et al. (2022) is a constant initial melt field, the mass loss from which for their BedMachine simulation results in 5 mm of mass loss from PIG which compares with 11 mm for the control simulation in this investigation. Furthermore, Wernecke et al. (2022) use an increasing SMB field for an RCP8.5 scenario which would offset increasing mass loss with increasing accumulation which also explains their lower projected mass loss.

5.5.2 Thwaites Glacier

5.5.2.1 Control Simulations

The relaxation performed is deficient in matching velocities for Bedmap2 and BedMachine simulations over TG (fig. 5.8) where the western ice tongue flows at speeds of 1500 m yr^{-1} greater than Bedmap2 at $t=0$. While the magnitude of the velocity difference in the western ice tongue decreases over time in the control simulation, the velocity difference over the whole ice shelf increases and spreads eastward and upstream, consistent with grounding line retreat that occurs throughout the BedMachine simulation. The initialisation parameters could be influencing this behaviour, where a lower viscosity particularly downstream of the grounding line could be permitting the faster flow observed in BedMachine (fig. 5.17). With a lower viscosity coefficient, ice is able to deform faster and therefore experience increased creep which would also increase the sensitivity of the ice stream to forcing (Alevropoulos-Borrill et al., 2020). However, the role of ice shelf calving and the topography around the grounding line could also be responsible for the faster initial ice velocity of BedMachine.

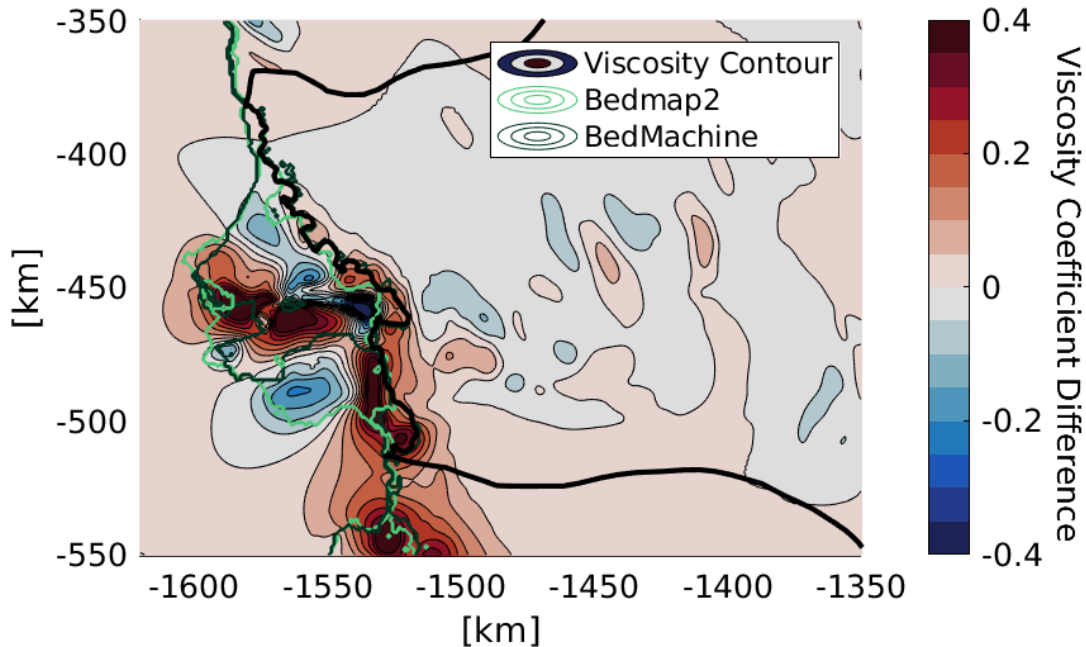


Figure 5.17: Thwaites Glacier viscosity coefficient parameter difference between BedMachine and Bedmap2 model domains with contoured bands. Red (blue) marks areas where the viscosity is higher (lower) in the initialised BedMachine model relative to Bedmap2.

To explore whether the reduced ice shelf extent of TG is responsible for the sustained increase in velocity in Bmach-rC-ctrl, a calving experiment is performed with a Bedmap2 simulation (fig. 5.18). Over the 10 year relaxation period, the ice shelf is calved to match the initial geometry of BedMachine and a uniform thinning rate of 50 m yr^{-1} is simultaneously applied over the whole ice shelf. The results show that even with extreme thinning and calving, the velocity of the Bedmap2-calve does not match the equivalent BedMachine simulation, with ice shelf velocity being on average 300 m yr^{-1} too slow. In response to calving of the western ice tongue, and thinning of the ice shelf, there is a marginal increase in ice stream velocity 15 km upstream from the grounding line in the west, suggesting that the western ice tongue did provide some buttressing to upstream ice (Parizek et al., 2013; Fürst et al., 2016). Despite ice shelf thinning of over 200 m, acceleration and grounding line retreat is not initiated until later in the Bedmap2-calve simulation. In Bedmap2 a series of high amplitude features

around the grounding line act to prevent grounding line retreat even with elevated forcing, meaning acceleration is reduced relative to BedMachine (fig. 5.19). Therefore, initialisation parameters (fig. 5.17) and topography around the grounding line are most responsible for the difference in initial velocity and the elevated rate of mass loss in the BedMachine control simulation.

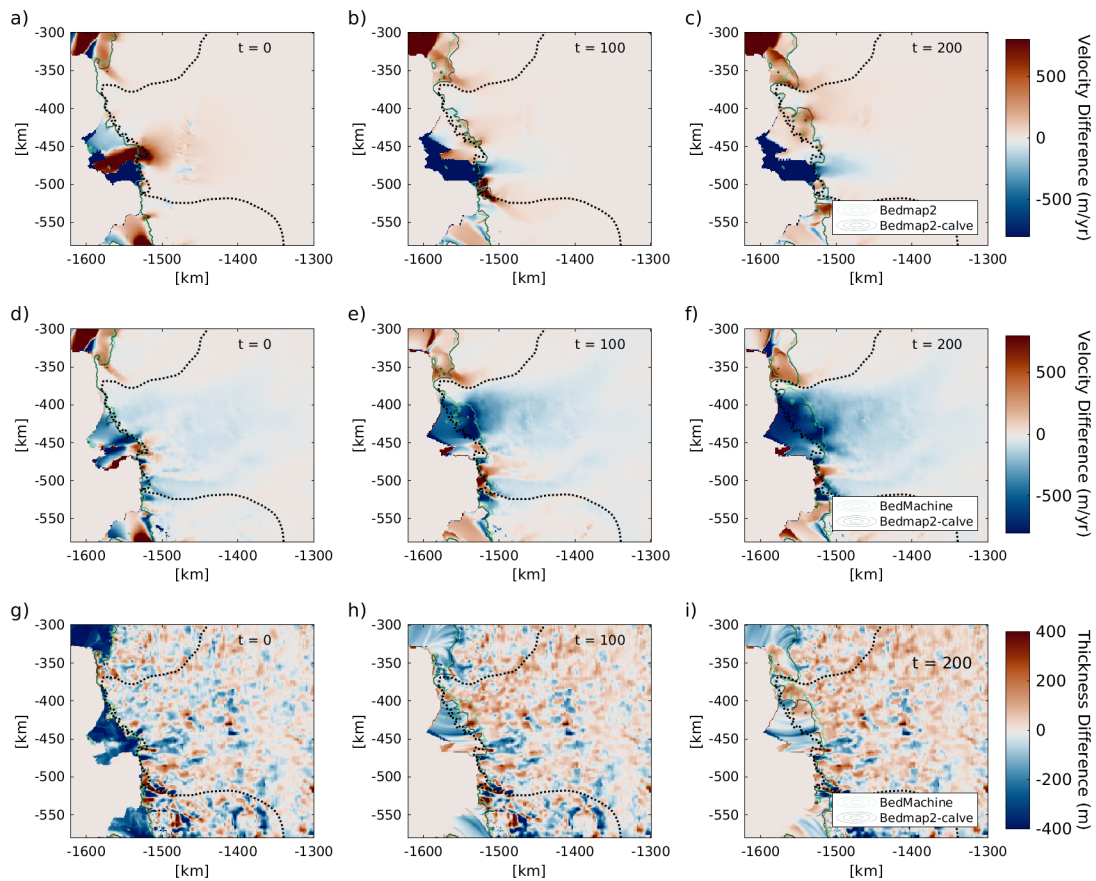


Figure 5.18: a-c) Velocity difference between Bedmap2-calve and Bedmap2 simulations at 100 year intervals over TG. d-f) Velocity difference between Bedmap2-calve and BedMachine over TG. g-i) Thickness difference between Bedmap2-calve and BedMachine.

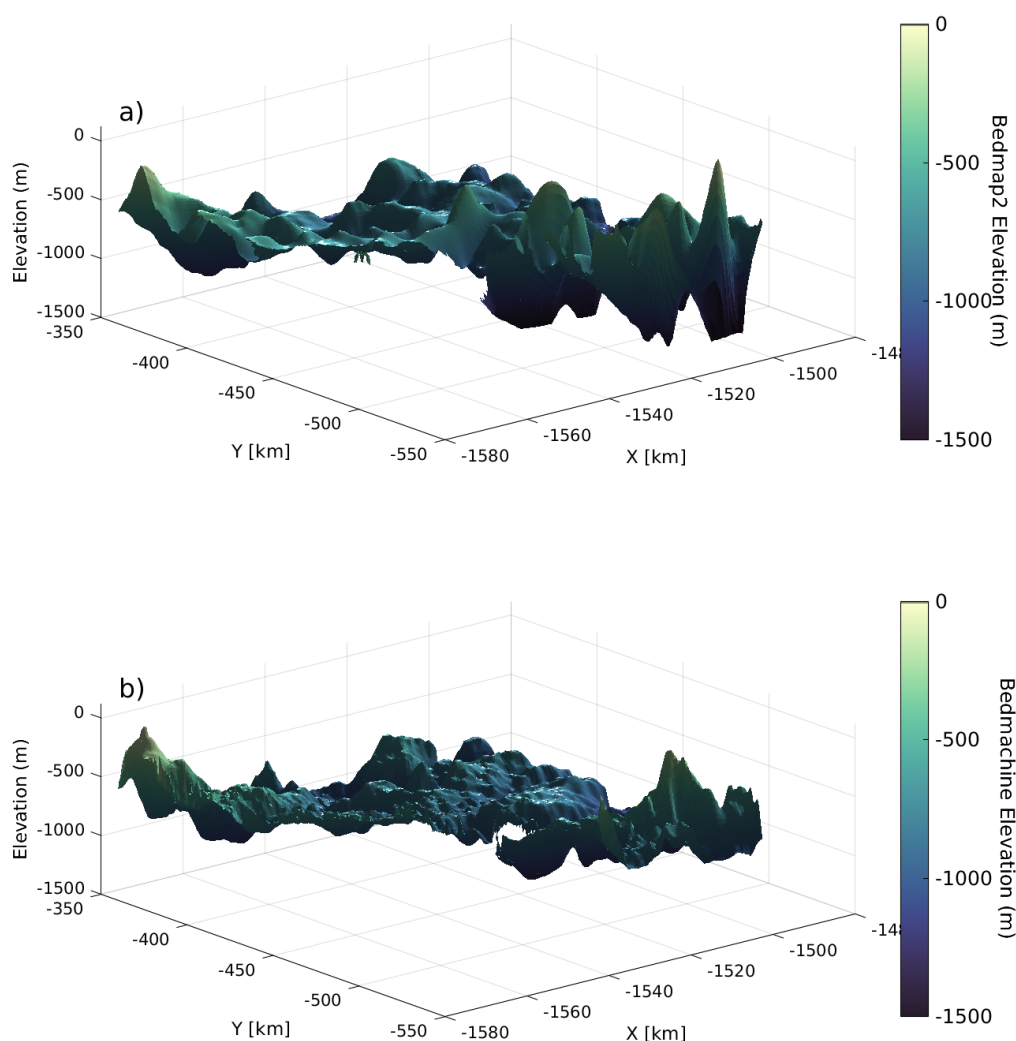


Figure 5.19: 3-D topography of a) Bedmap2 and b) BedMachine along the main trunk of Thwaites Glacier. Plotted areas include only grounded ice of $t=0$.

Despite the differences in the initial velocity leading to a disparity in the projected mass loss from the ice stream, the velocity product used for the BedMachine domain initialisation is a more recently observed dataset. Therefore an important takeaway of this is that investigations using more recent velocity observations will project greater mass loss from TG due to a greater committed mass loss which may be amplified with elevated melting.

5.5.2.2 Perturbed Simulations

The pattern of grounding line retreat of TG differs in the high melt simulation for the two model domains where Bmach-rC-high shows faster and more extensive grounding line retreat than Bedmap2-rC-high. There is a more pronounced clustering of grounding lines during the retreat of TG in the Bedmap2 simulation which limits the overall extent of retreat. In contrast, the pattern of grounding line retreat in the BedMachine simulations have less defined features of clustering or pinning. The result of this again is partly due to a deeper bed, which is too low for topographic highs to create resistance (Castleman et al., 2021), with higher frequency lower amplitude topographic features (fig. 5.19) which have also been shown to lower the resistance from the bed (Sun et al., 2014). The retreated grounding line in BedMachine simulations shows temporary stabilisation on two ridges identified by Morlighem et al. (2020) that reside either side of the trough where the southwestern tributary connects PIG to TG. The second trough ~ 50 km upstream of the initial grounding line is likely the final stabilising ridge in the TG trunk acting to limit retreat. (fig. 5.12). Therefore, the differences in bedrock amplify the sensitivity to elevated melting as a result of differences in grounded area with BedMachine having fewer prominent bed features providing grounding line stability.

Following 100 years of increased melting, the reduction of basal melting results in a curbing in mass loss from PIG for both simulations Bedmap2 and BedMachine simulations. In contrast, the BedMachine simulations result in continued mass loss from TG at a higher rate than the control run following the removal of forcing (fig. 5.15 and 5.11). Although the grounding line position appears to stabilise in the East over the second century, there is a continued loss of grounded area which occurs gradually over the Western trunk (fig. 5.12); though the rate at which this recedes is considerably lower than the rate of ungrounding during the period of increased melting until $t=100$. Therefore, despite a stabilised TG grounding line position in the Bmach-rC-high simulation, continued mass loss from TG is expected given the elevated rate of SLE contribution relative to the control.

5.5.3 Sliding Law Comparison

There is an ice stream dependent difference in the interplay between topography and the representation of sliding. The mass contribution from both PIG and TG using the Weertman sliding law falls within the range of SLE contribution from simulations using regu-

larized Coulomb sliding (fig. 5.15) but PIG is more sensitive to the choice of sliding law than TG. The regularized Coulomb sliding law results in increased mass loss in response to higher melting but also lower mass loss in response to lower melting than Weertman sliding for both ice streams, resulting in a wider range in the end-of-simulation SLE contribution. In contrast, for TG the regularized Coulomb sliding results in increased mass loss relative to Weertman sliding for both the control, low and high simulations. Furthermore, there is a difference in the sensitivity of PIG to the sliding law with different beds where the range in SLE contribution doubles for Bedmap2-rC compared with Bedmap2-W but increases by 10 % for Bmach-rC compared with Bmach-W suggesting that the representation of basal drag has a greater influence on the predictive uncertainty with a Bedmap2 topography. This contrasts with the behaviour of TG, where there is a greater dependence of mass loss on the sliding law for BedMachine than Bedmap2, as is shown by the difference in range of mass contribution. Therefore there is both an ice stream and a bed topography dependence of the response to alternative sliding laws.

5.5.4 Limitations and Future Work

An additional component of the influence of topography on ice dynamics occurs in the solid-earth feedbacks which are not modelled here. Studies have shown that visco-elastic vertical rebound of the earth in response to grounding line retreat and mass loss in areas of West Antarctica can result in an uplift rate of up to 45 mm yr^{-1} (Adhikari et al., 2014). This process has been shown to act as a negative feedback, limiting further grounding line retreat and ice flow (Whitehouse et al., 2019). Bedrock of a higher elevation in the ASE, which would occur in response to such a rebound, could limit mass loss from the region by up to 6.6 cm over 150 years (Castleman et al., 2021). This effect may reduce the differences between bed topographies, where increased mass loss from BedMachine would mean more uplift and stability.

Although the resolution of BedMachine is superior to Bedmap2, newer, higher resolution geometry products should also be investigated. This investigation could be further improved by using DeepBedMap (Leong and Horgan, 2020), a 250 m resolution topography product created using a trained super resolution deep neural network model. The adaptive mesh refinement of BISICLES ensures the detail of the 250 m topography and thickness data will be retained, whereas models with alternative mesh resolution can result in a smoothing of detail through interpolation due to the mesh refinement

methods. Therefore, this ice sheet model is best suited to such investigations and will be explored in future investigations.

In this investigation the modelled response of ice streams to future climate in the ASE are shown to have a bedrock dependence. While this key finding would suggest comparability between the projections of studies using either Bedmap2 and BedMachine datasets, the use of a modified Bedmap2 here means the details of the findings here cannot be used to directly infer differences between the two exact geometry products stated. As the Bedmap2 product used here incorporates some mass conservation in its modification, it is expected that the initial ice stream behaviour is more consistent with the BedMachine simulations than the original Bedmap2 dataset (Nias et al., 2016). Repetition of these simulations with the original Bedmap2 could provide additional context for model comparisons and is the aim of future work.

5.6 Conclusion

Here, a series of ice sheet model experiments were performed to explore the impact of an alternative bedrock topography datasets on modelled ice flow in two of the ASE's largest glaciers, PIG and TG. For both ice streams there is greater grounding line retreat and mass loss in response to both present day melt rates and elevated melt rates for BedMachine, a high resolution dataset produced using mass conservation methods. BedMachine results in greater extents of grounding line retreat and mass loss than Bedmap2 for both ice streams due to grounding line retreat over deeper bed, where ice flux is greater and the forces driving retreat are higher. Furthermore, the BedMachine product better captures high frequency but low amplitude bed features that provide only limited stabilising potential during retreat of the grounding line. Bedmap2 contains a number of high amplitude bed features where the grounding line is pinned which limits grounding line retreat and overall mass loss.

There is interplay between the magnitude of ice shelf basal melting and the difference in mass loss from the Embayment when using different bed topographies, where greater basal melting diverges and amplifies the difference in response from the two beds. Furthermore, the dependence of the ice stream response to the sliding law differs for both the ice streams and the bed topographies meaning the sensitivity to the sliding law is not universal for ice streams or topography datasets. Though in response to high

melting, overall the regularized Coulomb sliding law results in increased mass loss for both PIG and TG.

The nature of the basal melt forcing applied demonstrates that both bed topographies act to stabilise the grounding line in PIG and TG once the melt anomaly has been removed and basal melting overall reduces. This reduction in the rate of grounding line retreat following the removal of forcing occurs with the reduction in the rate of mass loss from PIG to present day levels. In contrast, the curbed grounding line retreat does little to mitigate high rates of mass loss from TG in the BedMachine simulation. As the ice stream is wider and the ice shelf is unconfined, the acceleration of the ice stream while the basal melting is elevated acts to commit future mass loss. Therefore, the use of the updated bed topography in ice sheet model simulations will contribute to the projected retreat of TG in simulations.

PIG and TG glaciers are among the most studied glaciers in the world, and demonstrating that the response of PIG and TG to varied melt forcing has a clear bedrock dependence is important for providing consistency between ice sheet modelling studies. Here it is shown that the bedrock dependent uncertainty in projections of future sea level rise are amplified for increasing sub-ice shelf melt anomalies. While modelling investigations begin to incorporate the newer bed topography BedMachine in simulations, there will therefore be inconsistency with existing modelling investigations using Bedmap2, particularly for simulations with more extreme forcings and direct comparison between these simulations should consider this dependence.

Chapter 6

Understanding the contribution of ice flow representation and melt rate parameterizations to uncertainty in future simulations of the Amundsen Sea Embayment

6.1 Introduction

Ice sheet modelling investigations show that the representation of processes controlling ice flow is responsible for much of the uncertainty in future sea level rise projections (Seroussi et al., 2020, 2019; Lowry et al., 2021). As policy is informed by projections of sea level change produced by ice sheet models, it is important that uncertainty can be quantified, understood and, ideally, constrained. In recent decades, the capabilities of ice sheet models have advanced substantially, with increased availability of observational data and improvements in the representation of the ice sheet system (Joughin et al., 2019; De Rydt et al., 2021). Despite these improvements, there remain stark differences between model projections of future ice sheet evolution, largely existing due to differences in model initialisation and the application of climate forcing (Seroussi et al., 2020, 2019).

Continental ice sheet models have existed since the 1990s (Blatter et al., 2010) and

have since increased in number and in complexity. The first generation of ice sheet model intercomparison studies focused on the ability of models to meet benchmarks, by assessing their ability to simulate theorised glaciological processes over idealised domains (Pattyn et al., 2008, 2013; Cornford et al., 2020). The Ice Sheet Model Intercomparison Project 6 (ISMIP6) (Seroussi et al., 2020) was the first study to explore the inter-model variability of continental ice sheet response to a range of future climate scenarios. For the investigation, 13 international ice sheet modelling groups performed simulations with prescribed ocean and atmospheric forcing for both continental Greenland and Antarctica. Under a high emissions (RCP8.5) scenario the projected AIS contribution to sea level ranges from -7.8 to 30.0 cm total by 2100 relative to a control simulation (Seroussi et al., 2020). This wide range demonstrates that the choice of ice sheet model plays an important role in the modelled response to forcing. However, part of this disagreement arises due to the flexibility in the experimental design which resulted in diversity in the application of external climate forcing (Seroussi et al., 2020).

Uncertainty in projection of ice sheet simulations has spatial variability, where the ASE has been widely shown to have the greatest intramodel parameter dependent uncertainty (Schlegel et al., 2018; Lowry et al., 2021; Nias et al., 2019). ASE ice streams are the biggest contributors to present day mass loss from Antarctica (Shepherd et al., 2018; Bamber et al., 2018) and have the greatest potential of sea level contribution over this century (Schlegel et al., 2018). Due to their grounding on retrograde bedrock below sea level (Morlighem et al., 2020) and exposure to warm water (Jenkins et al., 2016; Schmidtko et al., 2014; Nakayama et al., 2018), the ice streams could become unstable (Schlegel et al., 2018; Seroussi et al., 2017; Wild et al., 2021; Favier et al., 2014; Joughin et al., 2014) resulting in runaway mass loss from the region which could undermine other more stable basins in Antarctica (Martin et al., 2019). Representing present day ice flow in the region has been a focus for researchers (De Rydt et al., 2021; Joughin et al., 2019) to provide the most appropriate model configuration for performing future simulations.

Warm ocean water currently responsible for high observed ice shelf melting in the Amundsen Sea originates at depth off the continental shelf of Antarctica (Schmidtko et al., 2014). Modelling efforts and observations have indicated an increase in the heat content of the Amundsen Sea due to increased delivery and upwelling of warm water onto the shelf in deep bathymetric troughs (Naughten et al., 2022) linked to a southward

migration of westerly winds. This trend is projected to increase in the future, with a more positive phase of the Southern Annular Mode (see Chapter 2).

Here, a comparison of two high resolution ice sheet models, BISICLES (Cornford et al., 2013) and ISSM (Larour et al., 2012) is performed in order to investigate the model dependence of the simulated response of the ASE to future climate. The two models incorporate different approximations of the stress balance equations and therefore the uncertainty in the numerical representation of ice flow are captured. A series of experiments are performed to explore the response of each model to both projected and idealised basal melt forcings. The application of basal melt forcing is controlled, promoting a more direct understanding of the relative influence of the magnitude of basal melting on the response of ice streams for each model. This regional model comparison builds on the work of ISMIP6, utilising full model capability of resolving dynamic ice streams to a fine spatial resolution and examining the differences between models in more detail, given the regional focus.

6.2 Methods

Both BISICLES and ISSM are ‘data assimilation’ models and use observations to create a modelled representation of present-day (see Chapter 2 for more detail). Models are initialised by performing an inversion to match modelled velocity to observations by tuning two unobservable parameter fields, a traction and ice rheology (or rigidity) coefficient. To maintain consistency with existing literature, the BISICLES rigidity and basal traction parameters will use symbols ϕ and C and ISSM parameters for rigidity and basal traction will use B and β^2 .

6.2.1 Input Datasets

Both BISICLES and ISSM domains are initialised with the same data-sets. BedMachine Antarctica v1 from Morlighem et al. (2020) provides thickness and topography data, with surface elevation for the product from the Reference Elevation Model of Antarctica (Howat et al., 2019). Surface mass balance is taken from Arthern et al. (2006) and held constant through time. For both models an initial temperature field from Pattyn (2010) Higher Order model is used. The velocity from Mouginot et al. (2017) is used to tune the two models. This velocity product was used in the mass conservation method of

Morlighem et al. (2020) in creating the bed topography and therefore should be most consistent for running ice sheet model simulations.

6.2.2 BISICLES

BISICLES is finite difference L1L2 model with a rectangular domain with an irregular square mesh (for more detail see Chapter 2). The number of mesh elements change throughout the simulation with the adaptive mesh refinement (AMR). In these simulations, the rectangular mesh resolution varies between 0.25 km and 4 km in this domain and it evolves with the velocity.

The model is initialised for two different flow laws, Weertman sliding (Weertman, 1957, eq. 6.1) and regularized Coulomb sliding (Eq. 4.2; Joughin et al., 2019). For Weertman sliding, basal shear stress τ_b has a nonlinear dependence on the basal velocity u . The exponent $m = 3$ is used to model a hard viscous bed as has been proposed to best represent flow of ASE ice streams.

$$\tau_b = C|u_b|^{(\frac{1}{m}-1)}u_b \quad (6.1)$$

The regularized Coulomb sliding law (Joughin et al., 2019) based on Schoof (2005) incorporates the effect of cavitation of the bed on till deformation and subsequent basal slip (Eq. 6.2). For the greatest velocities of an ice stream, upstream of the grounding line, the till is considered saturated by water resulting in increased water pressure and slip at the bed. As such, there becomes a limit to the dependence of basal shear stress on velocity. For the regularized Coulomb simulations, a value of $m = 3$ and a transition velocity of $u_0 = 300 \text{ m yr}^{-1}$ is used to maintain consistency with Joughin et al. (2019).

$$\tau_b = C \left(\frac{|\mathbf{u}|}{|\mathbf{u}| + u_0} \right)^{\frac{1}{m}} \frac{u}{|u|} \quad (6.2)$$

In all BISICLES simulations, the initial calving front is fixed and a minimum thickness condition is set to a value of 10 m.

6.2.2.1 Inversion

In BISICLES, parameters $C(x, y)$ and ice rigidity $\phi(x, y)$ or the stiffening coefficient are tuned for simultaneously. The model uses a nonlinear conjugate gradient method

(Cornford et al., 2015) to minimize the objective cost function which incorporates both a misfit function J_m

$$J_m = \frac{1}{2} \int_{\Omega_v} \alpha_n^2(x, y) (|\mathbf{u}| - |\mathbf{u}_o|)^2 d\Omega \quad (6.3)$$

and a Tikhonov penalty function J_p

$$J_p = \frac{\alpha_C^2}{2} \int_{\Omega_v} |\nabla C|^2 d\Omega + \frac{\alpha_\phi^2}{2} \int_{\Omega_v} |\nabla \phi|^2 d\Omega \quad (6.4)$$

So

$$J = J_m + J_p \quad (6.5)$$

The coefficient $\alpha_u^2(x, y)$ relates to error estimates of velocity which is set to 0 where velocity data is not available and 1 where it is.

6.2.3 ISSM

ISSM is a finite element model (Larour et al., 2012) with an unstructured anisotropic mesh that has been constructed based on the spatial pattern of surface velocity, with the finest mesh resolution in the fastest flowing regions around the grounding line and coarser mesh in slower flowing areas. For this domain, the finest resolution element is 0.25 km with the coarsest element is 4 km. The triangular mesh was generated with a Bidimensional Anisotropic Mesh Generator (BAMG) (Hecht, 1998) and remains fixed through time. ISSM uses a Dirichlet boundary condition with the velocity in the grounded part of the boundary set according to velocity measurements.

Here, the SSA of Stokes flow (Chapter 2; MacAyeal, 1989; Hindmarsh, 2004) is used for the ISSM model initialisation and forward (time dependent) simulations. The SSA has been shown to capture fast flowing ice streams and shelves (see Section 2.3.3.3) such as those in the ASE and is less computationally expensive than the alternatives of Higher Order and Full Stokes in the ISSM framework (Larour et al., 2012). SSA models include horizontal normal and shear stresses for two dimensional, vertically integrated flow equations.

The inversion and forward simulations implement only Weertman (1957) sliding

over hard bed (Eq. 6.6).

$$\tau_b = \beta^2 |u_b|^{(\frac{1}{m}-1)} u_b \quad (6.6)$$

In all ISSM simulations, the initial calving front is fixed and a minimum thickness condition is set to a value of 10 m.

6.2.3.1 Inversion

In ISSM, the inversion solves for the depth averaged ice rigidity B first, which is included in the model as a parameter in Glen's flow law (Glen, 1955). Where here μ is the effective viscosity.

$$\mu = \frac{B}{2(\dot{\epsilon}_e^{1-\frac{1}{n}})} \quad (6.7)$$

The rigidity parameter B is calculated only over floating ice. Following inversion for B and with the inclusion of the B parameter in the model, the inversion is performed to produce a basal traction parameter β^2 over grounded ice. Using the Weertman sliding law, basal drag relates to the basal velocity by an exponent $m = 3$.

In ISSM the inversion is performed to tune modelled velocity to observations, however, within the ISSM framework there is also an option to adjust the cost function to account for minimising the misfit of thickness also. There is flexibility within the inversion procedure to incorporate different attributes into the cost function, the absolute misfit, relative misfit, logarithmic misfit, thickness misfit, drag gradient and thickness gradient. Here, the absolute misfit is included

$$J(abs) = \int_S \frac{1}{2} ((v_x - v_x^{obs})^2 + (v_y - v_y^{obs})^2) dS \quad (6.8)$$

in addition to the logarithmic misfit

$$J(log) = \int_S \left(\log \left(\frac{(\|v\| + \epsilon)}{(\|v^{obs}\| + \epsilon)} \right) \right)^2 dS. \quad (6.9)$$

The full cost function for the inversion of both parameters in turn, where $PAR = B$ and $PAR = \beta$, is

$$\begin{aligned}
J(v) = \int_S w_1 \frac{1}{2} ((v_x - v_x^{obs})^2) + (v_y - v_y^{obs})^2 dS + \int_S w_2 \left(\log \left(\frac{(\|v\| + \epsilon)}{(\|v^{obs}\| + \epsilon)} \right) \right)^2 dS \\
+ \int_b w_3 \frac{1}{2} \|\nabla PAR\|^2 dB.
\end{aligned}
\tag{6.10}$$

The final term is the Tikhonov regularization term which penalises strong gradients in the β^2 and B coefficient fields. Here, coefficients w_{1-3} are weighting terms that are assigned to each of the components of the cost function. The value of w_3 can be found using an l-curve method though for the purpose of this investigation values were assigned manually with $w_3 = 1 \times 10^{-8}$ for the B inversion and $w_3 = 1 \times 10^{-18}$ for β^2 .

6.2.4 Experiments

A total of 21 experiments are performed, comprising seven different basal forcings for the two ice sheet models. To provide some continuity with previous chapters, two different sliding laws are used for the BISICLES simulations and one sliding law is used for the ISSM simulations. The basal melt forcings have been selected due to their use in literature and therefore comparability with existing work. Simulations are performed from the year 2008 to 2100 and basal melt forcings using ocean or climate model output are taken from these years.

NEMO and FESOM For two of the forcings, basal melt rate anomalies are provided from the cavity resolving ocean models NEMO (Donat-Magnin et al., 2021) provided by Nicholas Jourdain and FESOM (Naughten et al., 2018b; Golledge et al., 2019) provided by Kaitlin Naughten. Basal melt rates are direct output from model simulations with fixed ice shelf geometry. NEMO and FESOM simulations use a RCP8.5 scenario as a boundary condition. The NEMO experiment has been performed for two periods, a historical period from 1989-2005 and a future simulation using RCP8.5 for 2085-2100 in order to save computational expense (Donat-Magnin et al., 2021). To obtain a continuous projection field, a two dimensional nonlinear interpolation is performed between the two periods to produce annual average melt rates from 2008 to 2100. To account for the ASE cold bias in FESOM (Naughten et al., 2018b), both FESOM and NEMO melt rates are applied as anomalies onto a present day melt field produced by Cornford

et al. (2015), which is used in earlier chapters. The forcing is applied annually using a grounding line localized function in the BISICLES code which allows the melt rates to follow the grounding line as it migrates (see Chapter 2). As no such function is inbuilt in ISSM, the BISICLES melt rate field is applied directly to ISSM. To account for any disparity in the grounding line position and therefore area exposed to melting, the melt rates within 10 km of the grounding line are extracted and averaged for each year. This average grounding line melt rate is then applied over the rest of the grounded domain in the input to the ISSM simulations so that any floating ice in ISSM that is grounded for the equivalent time in the BISICLES simulation will continue to experience basal melting. In both ISSM and BISICLES, only fully floating cells experience basal melting which has been shown to better represent the response to forcing (Seroussi and Morlighem, 2018).

NEMO-GL and FESOM-GL Two further melt rate fields are applied using the output from NEMO and FESOM but with greater magnitude melt rates at the grounding line of ASE ice streams (NEMO-GL and FESOM-GL) to compensate for the stretching of melting with grounding line retreat described in previous experiments. Melt rate anomalies within 10 km from the initial grounding line position are extracted annually and averaged. This grounding line melt rate anomaly time-series is then applied as an anomaly at the grounding line, in addition to the application of the melt rate field from both NEMO and FESOM described above. The grounding line anomaly is applied to decay with distance from the grounding line (as discussed in previous chapters). These simulations are performed with BISICLES first and the output forcing is used to force ISSM, as described above.

LINEAR A piecewise linear forcing with a depth dependence is used without an externally prescribed temporal evolution. While several values for this exist in literature, the depth and melt rate values from Barnes et al. (2020) are used for comparability with their work. Their study used three ice sheet models, one of which is ISSM, to compare the model initialisation procedure and therefore new results from BISICLES can be compared. The melt rate field m_b is generated based on the depth of the ice shelf z , where the greatest melt rates occur over the deepest parts of the shelf, here exceeding 500 m below sea level (Eq. 6.11).

$$M_b = \begin{cases} 0 & \text{if } z \geq 0 \\ -\frac{75}{500}z & \text{if } 0 > z > -500 \\ 75 & \text{if } z \leq -500, \end{cases} \quad (6.11)$$

CTRL A control simulation is performed where the present day melt field from Cornford et al. (2015) is applied over the 93 year simulation. The melt field is applied so that it is stretched over the ice shelf as the grounding line retreats. Though the magnitude of the melt rate decreases as the grounding line retreats, the total melting from each ice shelf remains constant.

ISMIP6 To provide comparability with international modelling investigations, the ISMIP6 protocol for applying basal melt forcings to both ice sheet models is used. The protocol is discussed in more depth in Chapter 4, and the full method is described in Jourdain et al. (2020). The inbuilt functions in both ice sheet models are used to apply basal melting as generated from the NorESM1-M RCP8.5 thermal forcing. The non-local melt rate is used given that it was the compulsory model experiment. Values for the velocity exchange coefficient γ_0 and temperature correction δT are used for the ASE sector exclusively. Although the PIGL forcing is shown to provide basal melt values that are most consistent with observations in the region, the MeanAnt γ_0 and δT are used to maintain consistency with the standard, compulsory simulations described in Seroussi et al. (2020).

Simulation Names Simulations will be referred to with the ice sheet model (ISSM or BISICLES) and sliding laws W for Weertman sliding (Weertman, 1957) and rC for regularized Coulomb sliding used only for BISICLES simulations (Joughin et al., 2019). The melt forcings are NEMO, FESOM, NEMO-GL, FESOM-GL, LINEAR, CTRL and ISMIP6, as presented in the same order described above.

6.3 Description of Melt Rate Inputs

The highest observed ice shelf basal melting occurs at the grounding line of PIG (fig. 6.1) which reaches up to 120 m yr^{-1} in the Rignot et al. (2013a) observations compared with 80 m yr^{-1} in Adusumilli et al. (2020). High melt rates occur over the western ice

tongue of TG in both sets of observations though the magnitude of melting is lower than that at the grounding line of PIG, reaching up to 70 m yr^{-1} . This pattern of melting is replicated in the ocean model NEMO but with a lower magnitude of melting beneath TG. NEMO models a high area of melting 30 km downstream of the PIG grounding line at the central trunk. The melt rates over Crosson and Dotson ice shelves are higher in NEMO than observed. The magnitude of basal melting in FESOM is on average 5 m yr^{-1} which is lower than observed. The BISICLES melt rate field produced to match modelled ice shelf thinning rates and ice flux is the highest overall, with melt rates exceeding 200 m yr^{-1} around the grounding line of PIG and beneath the TG western ice tongue.

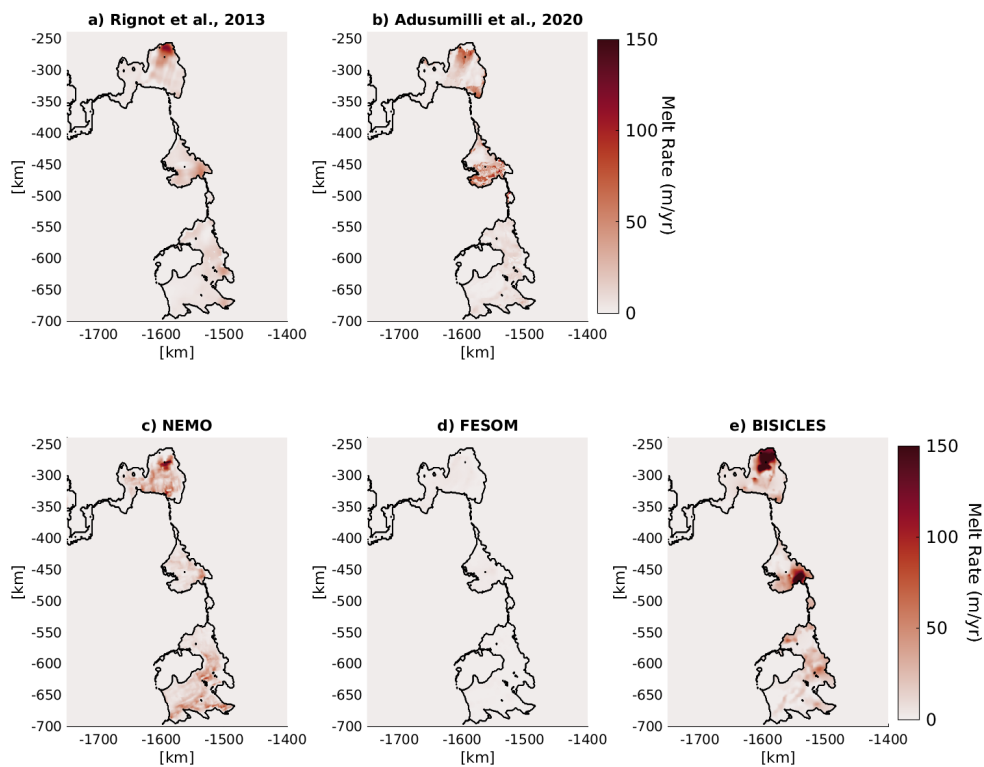


Figure 6.1: Melt rate fields from observations by a) Rignot et al. (2013a) b) Adusumilli et al. (2020) and ocean models c) NEMO and d) FESOM and melt rate field produced to reproduce observed thinning rates for e) BISICLES simulations (Cornford et al., 2015). Melt rate fields are averaged over 2000-2010, (2003 to 2008 for Rignot et al. (2013a)) and black contours define BedMachine (Morlighem et al., 2020) ice shelf extent for approximately 2007.

There is an increase in ice shelf melting over time for both the extrapolated Adusumilli et al. (2020) observations and ocean models NEMO and FESOM (fig. 6.2). The

Adusumilli et al. (2020) observational trend when extrapolated shows a linear increase of 175 Gt yr^{-1} over the century. Adusumilli et al. (2020) observations show high frequency variability with a standard deviation of 47 Gt yr^{-1} from 1992 to 2018. Rignot et al. (2013a) observations produced to match observed thinning rates over the ice shelf when accounting for ice velocity (and therefore mass conservation) are 282 Gt yr^{-1} over the period 2003 to 2008 which is 160 Gt yr^{-1} greater than the averaged Adusumilli et al. (2020) estimates over the same period.

Over the observational period, NEMO meltwater production values lie within the range of Rignot et al. (2013a) observations but vastly overestimate melt rates produced by Adusumilli et al. (2020) (fig. 6.2). The NEMO simulation exhibits the greatest increase in ice shelf melt, increasing from 275 Gt yr^{-1} in 2000 to over 400 Gt yr^{-1} in 2080. The smoothing of meltwater production is a product of the interpolation performed between the two time periods in order to get an annual melt rate over the century.

FESOM underestimates both Rignot et al. (2013a) and Adusumilli et al. (2020) melt rate observations in the ASE (fig. 6.2) which is explained by Naughten et al. (2018a) to be due to a deeper modelled mixed layer in the region resulting in a destratified water column with cold water on the shelf that prevents development of a warm bottom CDW layer (Nakayama et al., 2014). There is some inter-annual variability throughout the projection period though this has a detrended standard deviation of 3 Gt yr^{-1} . FESOM projects an increase in meltwater production over the century, from 20 Gt yr^{-1} in 2000 to 75 Gt yr^{-1} in 2100.

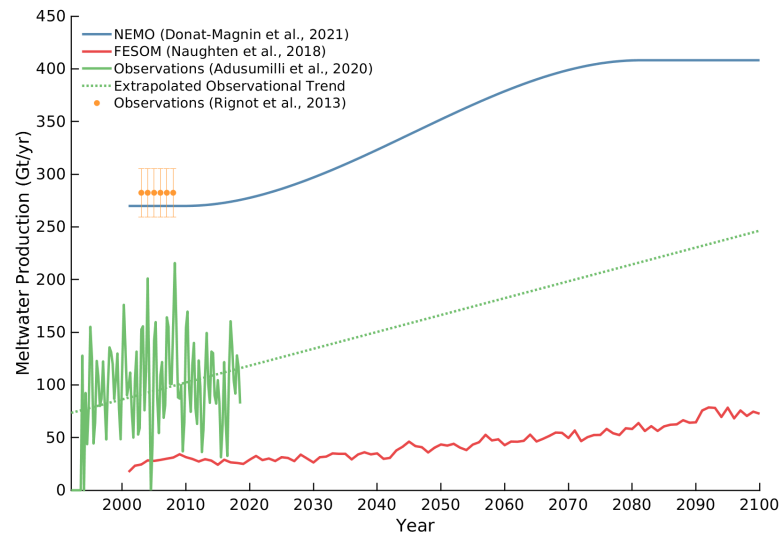


Figure 6.2: Time-series of meltwater production (Gt/yr) from 1994 to 2100 from ASE ice shelves. Observations from Adusumilli et al. (2020) are from 1992 to 2018 and values are quarter annually estimated. The Adusumilli et al. (2020) observational trend from 1992 to 2018 is linearly extrapolated to 2100. Annual values are presented from model simulations NEMO (Donat-Magnin et al., 2021) and FESOM (Naughten et al., 2018b) forced with RCP8.5 are from 2000 to 2100. Observations from Rignot et al. (2013a) from 2003 to 2008 are included with error bars based on values quoted in their study.

The modelled melt rate anomalies from NEMO and FESOM show an increase in basal melting over the century (fig. 6.2 & 6.2). Accounting for the cold bias of FESOM in the ASE, the anomaly results in a magnitude of basal melting that is closer to NEMO melt rate values. The maximum melt rate anomaly in NEMO reaches 60 m yr^{-1} approximately 10 km downstream of the 2008 grounding line of PIG (fig. 6.3). This area of high melting around the PIG grounding line is not captured in the FESOM melt rate data, instead the melt rate anomalies remain around 10 m yr^{-1} over PIG and TG, with 5 m yr^{-1} anomaly over the Dotson ice shelf.

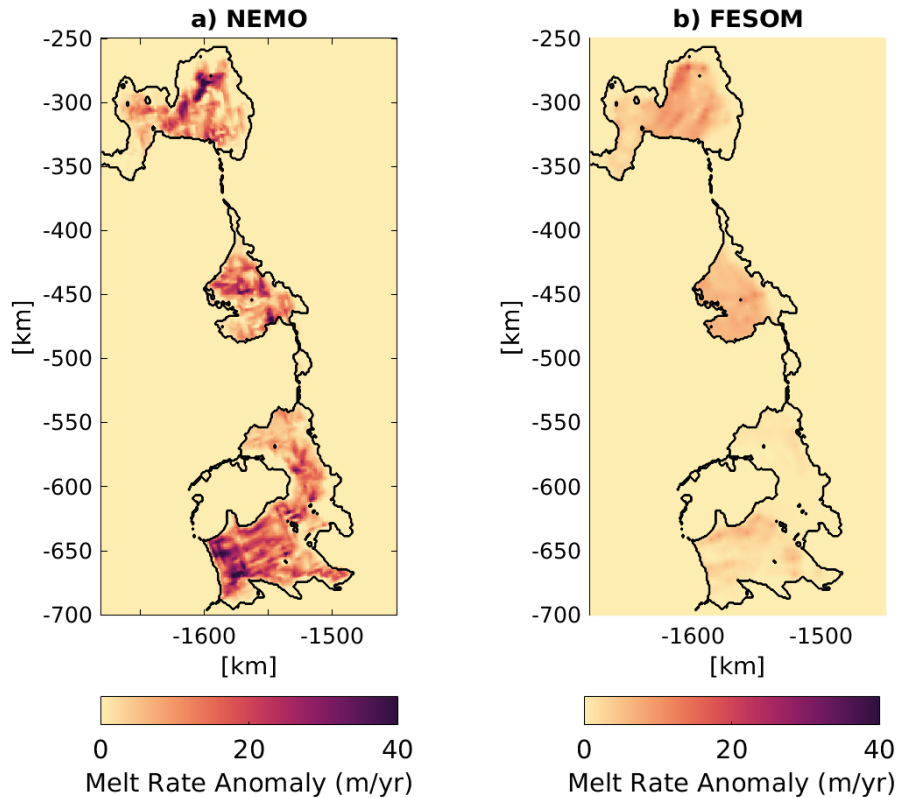


Figure 6.3: Melt rate anomalies projected over ASE ice shelves for a) NEMO (Donat-Magnin et al., 2021) and b) FESOM (Naughten et al., 2018b) averaged over 2090-2100 relative to the 2000-2010 average. Projections for both simulations are forced with RCP8.5 boundary conditions.

6.4 Initialized Models

Generally, the initialised model of BISICLES better matches observations than ISSM, although the pattern of difference is spatially variable (fig. 6.4). While BISICLES overestimates ice flow of the central trunk of PIG Ice Shelf by $\sim 800 \text{ m yr}^{-1}$, and the central trunk 20 km upstream of the grounding line by 200 m yr^{-1} , ISSM underestimates the ice shelf velocity by $\sim 700 \text{ m yr}^{-1}$ and 100 km upstream from the grounding line by $\sim 300 \text{ m yr}^{-1}$. BISICLES overestimates a wider area of the trunk of TG by up to 150 m yr^{-1} but better captures the velocity of the ice shelf and grounding line than ISSM. ISSM overestimates the velocity of the eastern ice shelf of TG and underestimates the western ice tongue. Both BISICLES and ISSM underestimate the velocity of Crosson though this is greater for ISSM. The velocity of Dotson is underestimated by approx-

imately 100 m yr^{-1} by BISICLES and overestimated by the equivalent magnitude in ISSM.

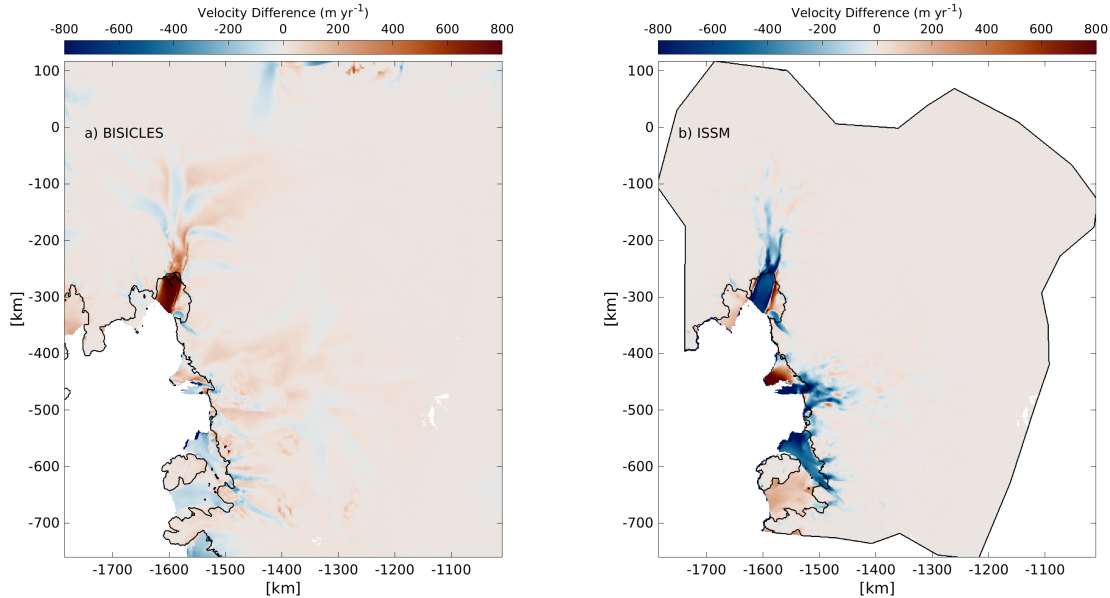


Figure 6.4: Initial velocity difference between a) BISICLES and b) ISSM simulations and Mouginot et al. (2017) velocity observations used for the model inversions. Black contours represent the modelled initial grounding line position

6.5 Results

6.5.1 Sea Level Contribution

Over the modelled 93 years, all simulations result in a positive contribution to global sea level by 2100 (fig. 6.5ac) as a result of increasing mass loss in response to elevated basal melt rates. There is a quasilinear increase in SLE contribution over time for all simulations excluding BISICLES-LINEAR-* and BISICLES-NEMO-GL-* which exhibit a nonlinear positive increase in SLE over time. For each respective melt forcing, BISICLES simulations result in greater SLE than ISSM over the 21st century.

Overall, the greatest end of century SLE contribution is the BISICLES-LINEAR-rC simulation, contributing 79 mm over the simulation and the lowest SLE contribution of 23 mm from ISSM-CTRL-W. ISSM simulations show the lowest range of the three sets of experiments of 10 mm, with BISICLES-*-rC having the greatest range of 47.8 mm. There is a clustering of simulations at the lower end of the SLE contribution range shown by the positive skew in the distribution of simulations in response to melting

(fig. 6.6) which is also replicated in the distribution of annual ice shelf melt rates (fig. 6.5bd). In each of the sets of simulations, the LINEAR melt forcing SLE contributions exceed the upper quartile of the respective distributions.

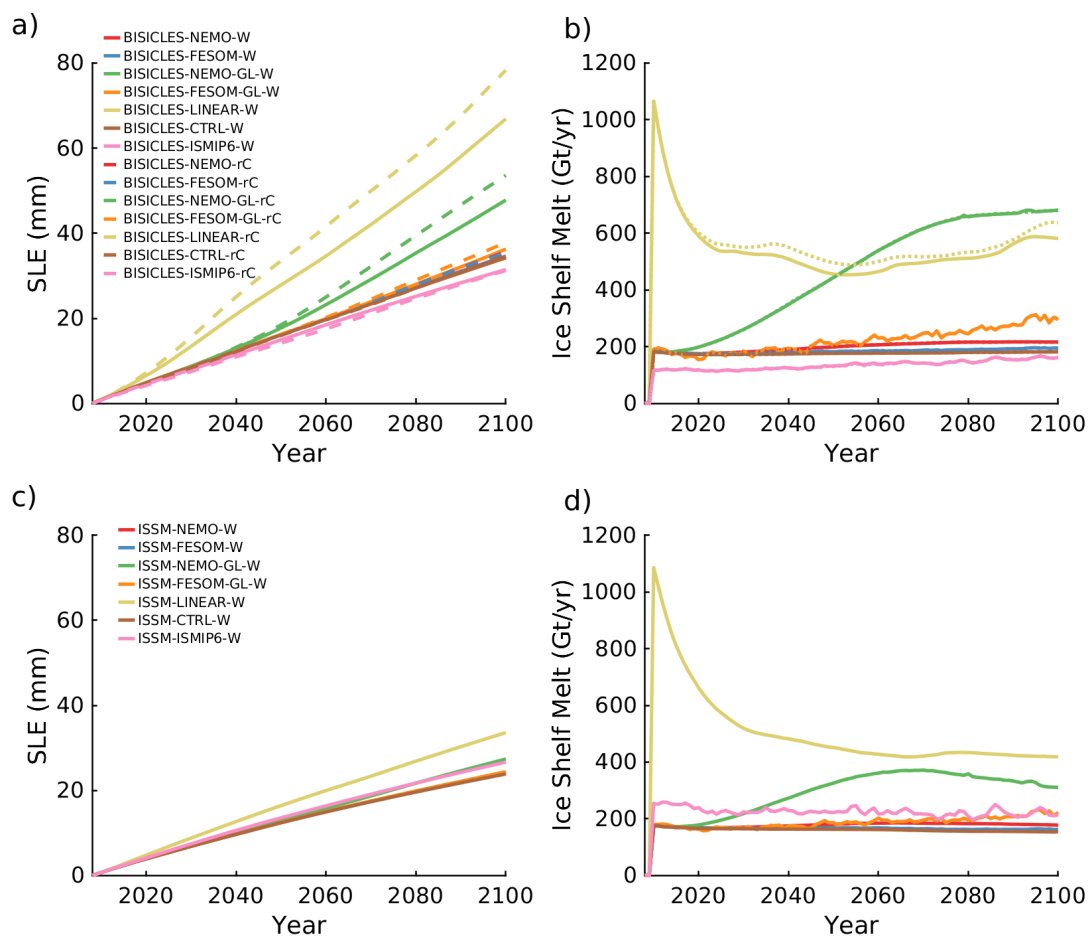


Figure 6.5: Sea level equivalent contributions from a) BISICLES and c) ISSM simulations. Annual ice shelf total melt in gigatonnes for b) BISICLES and d) ISSM simulations.

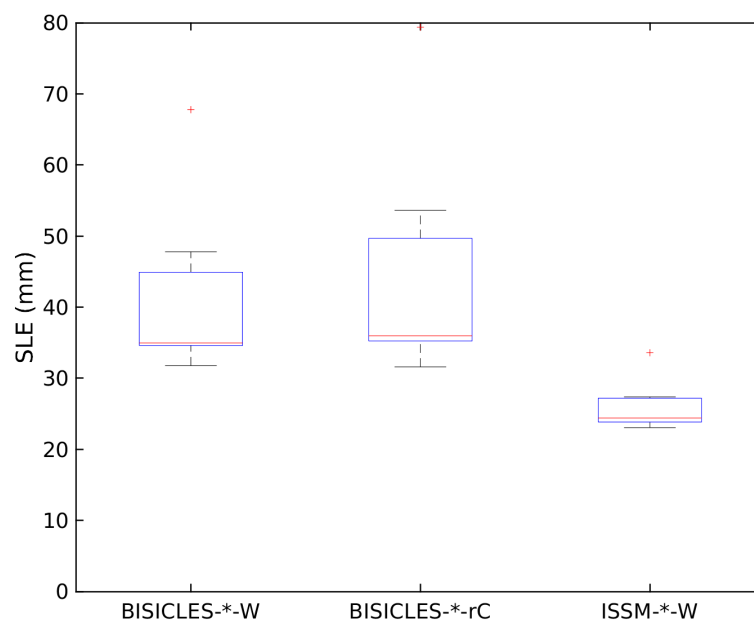


Figure 6.6: Box-plot of end of century sea level equivalent for all melt forced simulations with BISICLES-*-W, BISICLES-*-rC and ISSM-*-W respectively.

For all simulations there is a positive relationship between the cumulative melt and the SLE contribution (fig. 6.5). The gradient of the relationship varies according to the simulation, the melting and the sliding law. ISSM simulations generally have a flatter gradient than BISICLES, where there is a more gradual increase in SLE for increasing cumulative melt.

The difference between BISICLES-*-W and BISICLES-*-rC simulations increases for simulations with increased cumulative melting (fig. 6.5). This is most clear for NEMO-GL and LINEAR simulations which have the greatest cumulative melting and a greater divergence in the mass loss response to ice shelf melting.

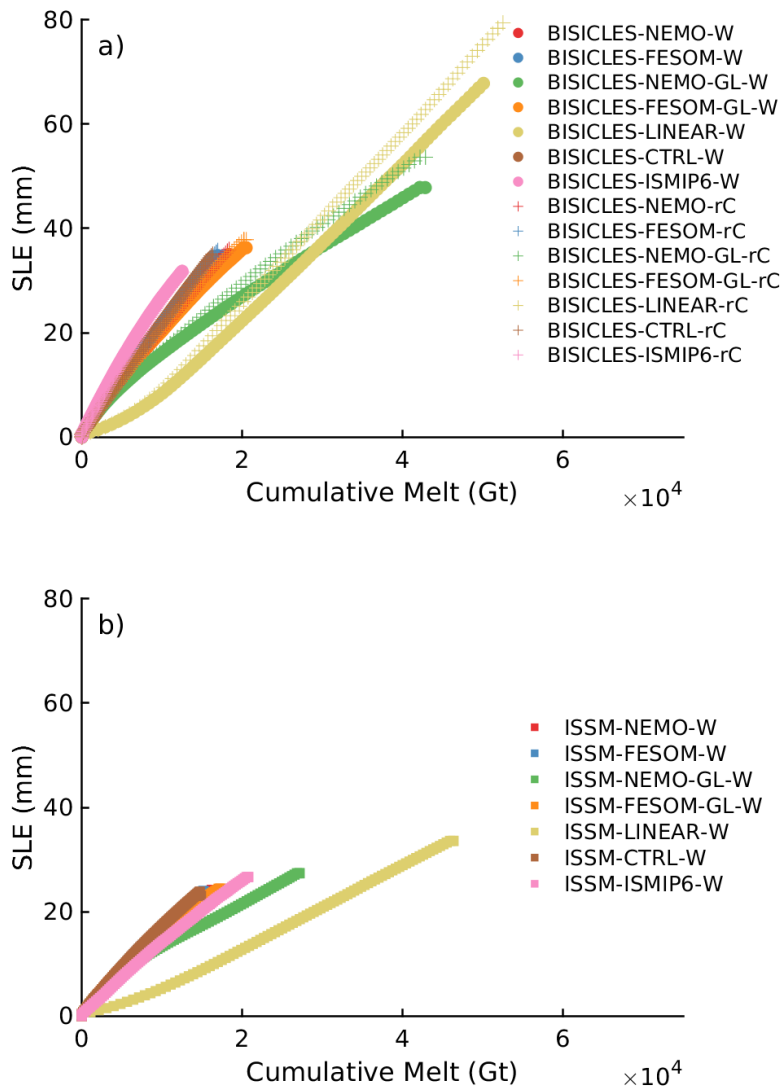


Figure 6.7: Relationship between the sea level contribution and the cumulative ice shelf melt of ASE ice shelves plotted every year over the century scale simulations for a) BISICLES and b) ISSM simulations.

6.5.2 Change in Grounded Area

With the exception of the ISMIP6 simulations, there is grounding line retreat in the BISICLES simulations compared with ISSM for equivalent melt forcing (fig. 6.8). Further, the range in grounding line retreat between melt simulations is greater for BISICLES simulations than ISSM (fig. 6.9). For the first 20 years in the simulation, the grounding lines retreat quicker in ISSM than BISICLES simulations for both sliding

laws, where net grounding line retreat only occurs in simulations after 2020, with the exception of the BISICLES-LINEAR-* simulations. From 2050 onward the rate of grounding line retreat decreases in ISSM NEMO, FESOM, FESOM-GL and CTRL simulations.

For the ISSM simulations only the grounding line of PSK shows a melt forcing dependence, where there is minimal difference in the grounding line position for different simulations over PIG and TG (fig. 6.8). In no ISSM simulations does the grounding line of PIG retreat more than 5 km upstream along the main trunk, although the ice shelf does widen through southward retreat and retreat of the Southwestern Tributary. The greatest extent of retreat occurs over TG with ~ 50 km of retreat southward over the eastern trunk. There is a ~ 40 km difference in end of simulation grounding lines over PSK.

In contrast, BISICLES simulations exhibit a greater dependence of the grounding line position on the magnitude of melt forcing (fig. 6.8). However, there remain some similarities with equivalent ISSM simulations. For all simulations excluding LINEAR, the grounding line of TG retreats ~ 40 km upstream. While there is less retreat over the eastern trunk than the ISSM simulations, there is more retreat over the western trunk. NEMO-GL and LINEAR simulations show the greatest difference in extent of grounding line retreat.

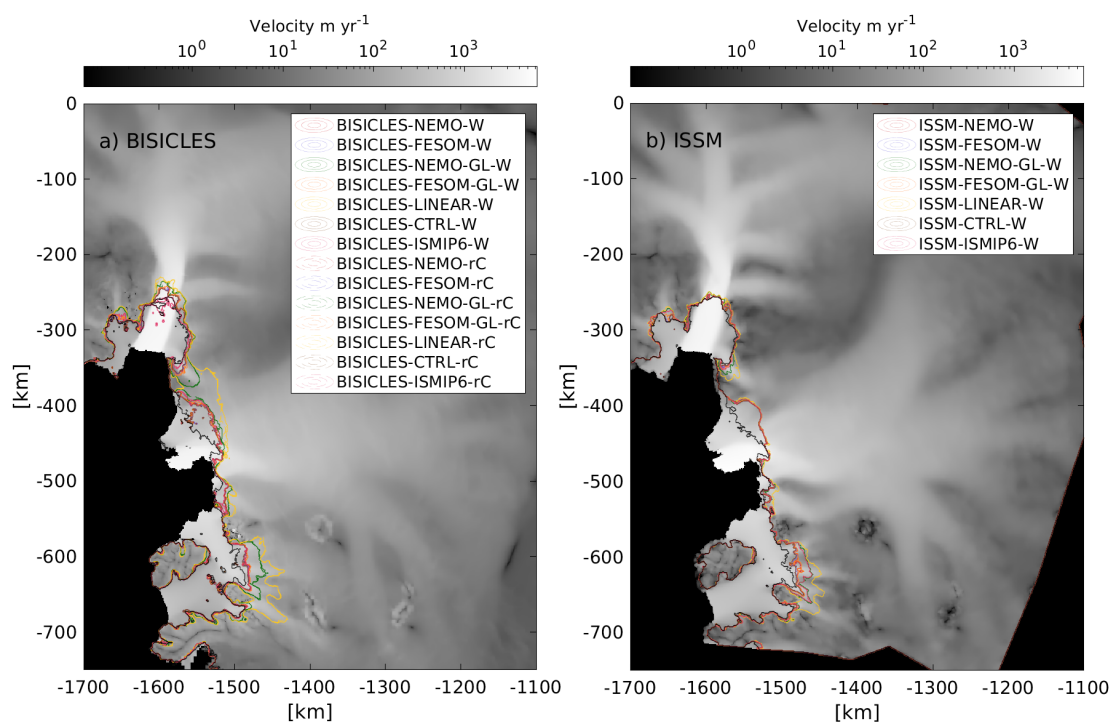


Figure 6.8: End of century grounding line positions for a) BISICLES and b) ISSM simulations. Dashed grounding lines in a) block lines represent BISICLES-*-rC sliding simulations. Background field is the initial modelled velocity in the year 2008 for respective simulations and the black grounding line marks the 2008 grounding line position.

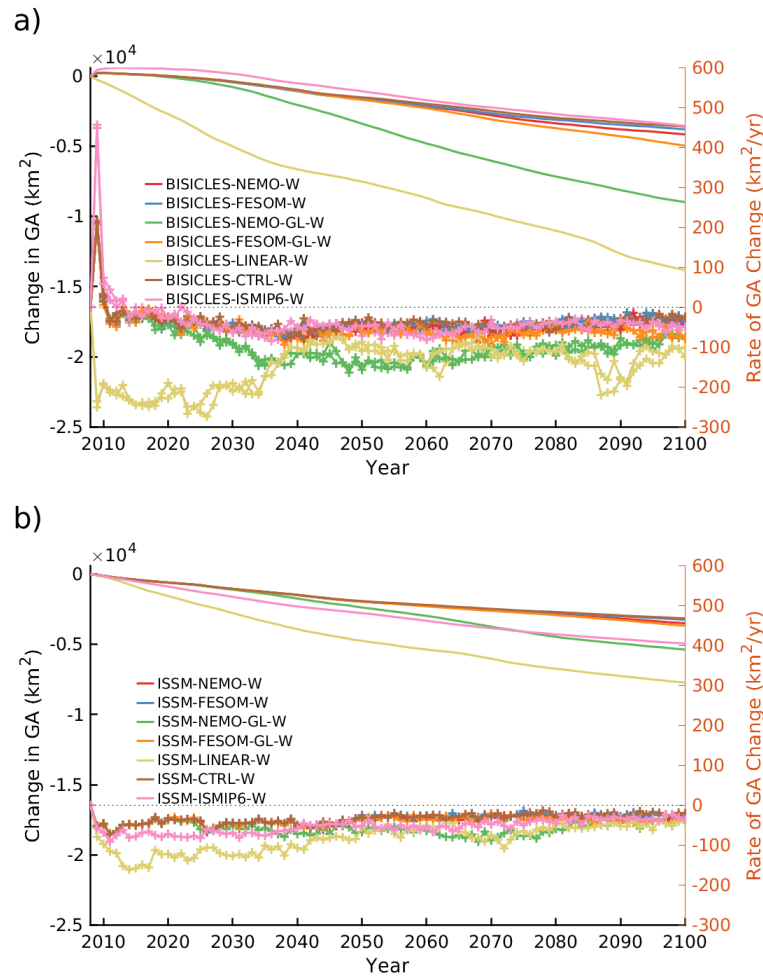


Figure 6.9: Change in grounded area over time (-, left axis) and rate of change in grounded area (+, right axis) from 2008 to 2100 for a) BISICLES-W simulations b) ISSM-W simulations.

6.5.3 Individual Simulations

6.5.3.1 CTRL-W

The CTRL-W simulations result in the lowest SLE contribution for each set of melt forced experiments. Initially at $t = 0$ modelled for 2008 the velocity difference between BISICLES and ISSM is spatially heterogeneous (fig. 6.10a). PIG and Crosson ice shelves are initially over 800 m yr^{-1} faster than ISSM. In PIG this velocity difference extends 20 km upstream from the grounding line through the trunk upstream, and in the ice stream tributaries the velocity for ISSM exceeds that modelled by BISICLES. The

eastern ice tongue of TG flows over 800 m yr^{-1} faster in ISSM relative to BISICLES. There is more similarity between the two models in representing the velocity of the grounded trunk of TG, where neither model is consistently representing faster ice flow.

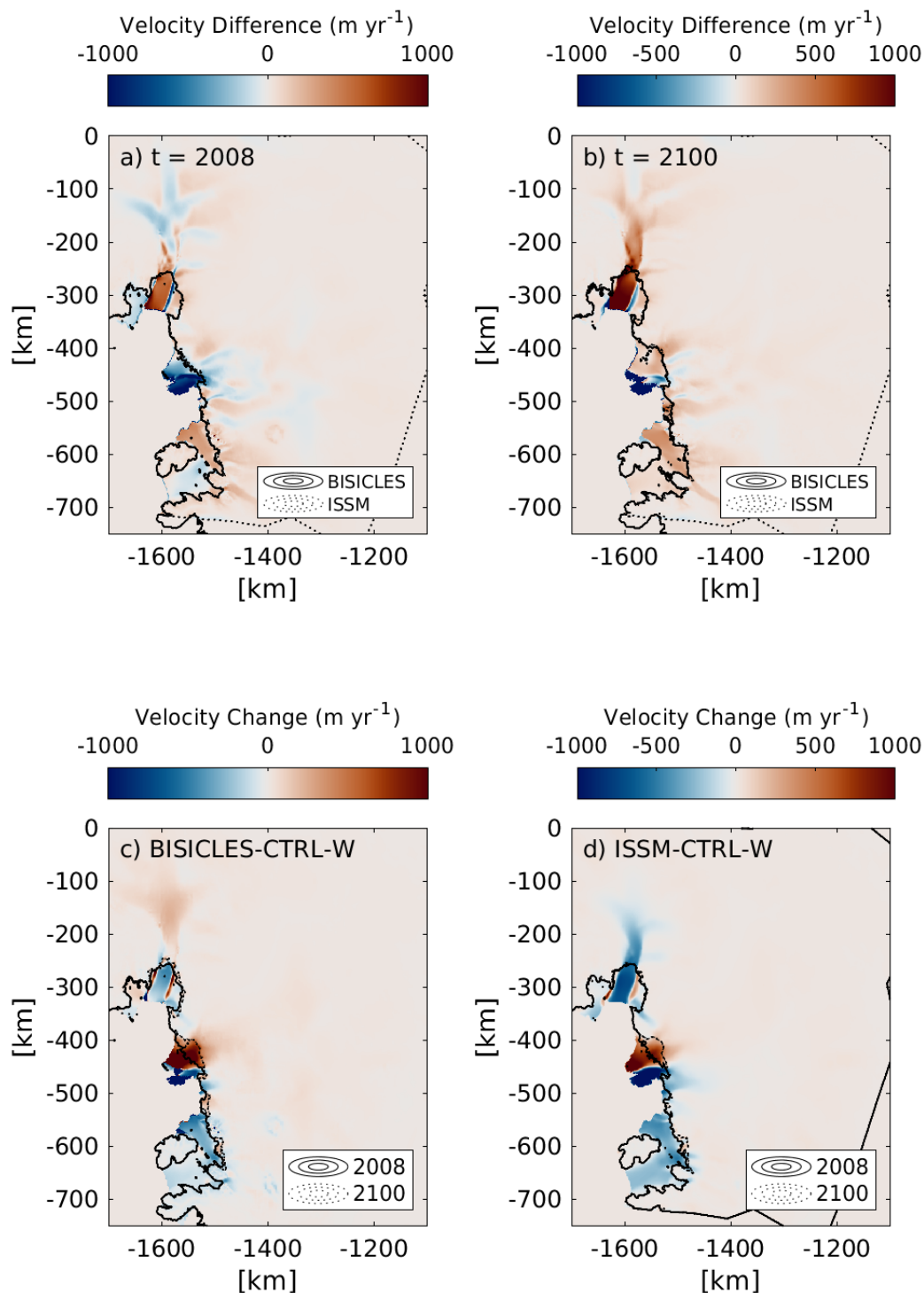


Figure 6.10: Velocity difference between BISICLES-CTRL-W and ISSM-CTRL-W simulations for the year a) 2008 and b) 2100. Positive (negative) where BISICLES velocity is higher (lower) than the ISSM CTRL simulation for the equivalent year. Blocked and dotted black lines represent the grounding line positions in each year for BISICLES and ISSM respectively. Velocity change in 2100 relative to 2008 for c) BISICLES-CTRL-W and d) ISSM-CTRL-W simulations. Blocked and dotted black lines represent the grounding line positions in each year for the year 2008 and 2100 respectively for each model simulation.

Although the grounding line retreats to almost the same position in BISICLES and ISSM CTRL simulations (fig. 6.10b), the velocity difference between the simulations is amplified. Both BISICLES and ISSM simulations show a decrease in velocity over PIG Ice Shelf (fig. 6.10). Whereas BISICLES results in a $\sim 100 \text{ m yr}^{-1}$ increase in velocity over the main trunk extending 100 km upstream, ISSM shows a decrease in velocity that extends upstream along the main trunk of PIG, the magnitude on average 400 m yr^{-1} lower than the initial velocity.

Both ISSM and BISICLES simulations show a speed up of the TG eastern ice shelf (fig. 6.10) and a decrease in velocity over the western ice tongue. The speed up extends over a greater horizontal extent for the BISICLES simulation which coincides with a wider area of grounding line retreat. The eastern grounding line of TG retreats further in ISSM than BISICLES, despite BISICLES showing a greater increase in velocity.

Both simulations show a decrease in the velocity of Dotson and Crosson ice shelves and PSK glaciers. Along with the 200 m yr^{-1} increase in velocity of PIG in the BISICLES simulation, much of the central and western trunk of TG also accelerates, by up to 500 m yr^{-1} .

In response to the CTRL melt forcing simulations there is thinning of PIG, TG and PSK grounded ice with an average of $\sim 150 \text{ m}$. In all simulations there is $\sim 100 \text{ m}$ of ice shelf thickening occurring in the central ice shelf of PIG and over TG, though thickening of TG ice shelf is greater for BISICLES simulations. BISICLES-CTRL-W, ISSM-CTRL-W and BISICLES-CTRL-rC experience grounding line retreat, the majority of which occur in TG. ISSM-CTRL-W experiences the lowest thinning over the domain with minimal grounding line retreat. ISSM-CTRL-W shows greater thinning to occur over Crosson than the BISICLES simulations, in addition to more grounding line retreat of Pope and Smith glaciers.

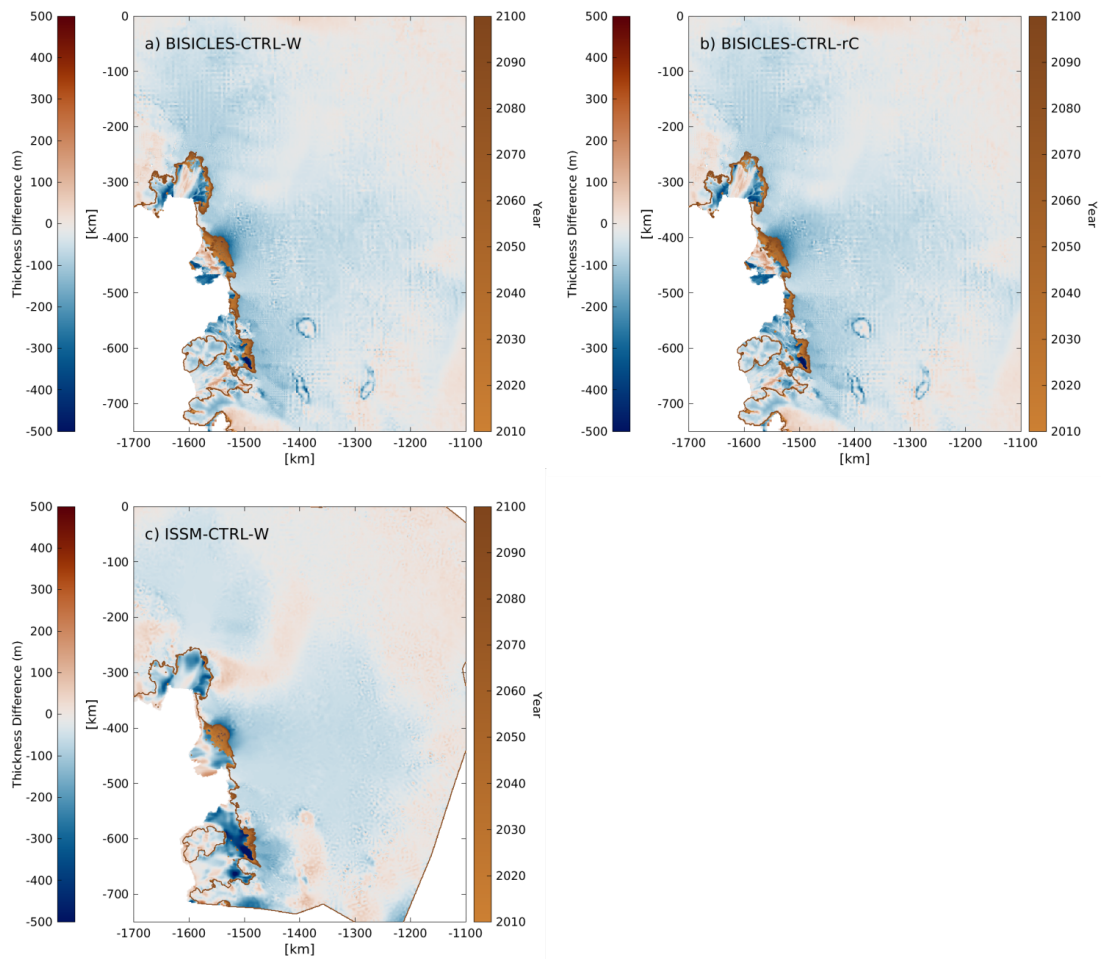


Figure 6.11: Thickness change (m) from 2008 to 2100 for a) BISICLES-CTRL-W b) BISICLES-CTRL-rC and c) ISSM-CTRL-W. For each simulation the grounding line position is plotted every year according to the colour gradient.

6.5.3.2 LINEAR-W

The LINEAR-W simulations have the highest SLE contribution and grounding line retreat of all the basal melt forcings (fig. 6.5 & 6.8). The grounding line retreats in response to the LINEAR forcing in both ISSM and BISICLES simulations, though to a greater extent in the latter (fig. 6.12). While both simulations show increased velocity in response to forcing, by the end of the century the velocity of the ASE in the BISICLES-LINEAR-W simulation increases to a greater extent over a larger area of the domain than ISSM. The BISICLES simulation experiences an increase in velocity of almost 2000 m yr^{-1} over the northern and southern ice shelves of PIG and 80 km upstream over the main trunk (fig. 6.12c). The grounding line of PIG and TG merge in

the BISICLES simulation, with almost 80 km of grounding line retreat over the eastern trunk. Further, PSK speed up by over 1000 m yr^{-1} , though Crosson and Dotson show a slight decrease in velocity.

In the ISSM simulation there is an increase in velocity in the shear margin of the central PIG ice shelf (fig. 6.12) and the northern and southern ice shelves which likely occurs due to a widening of the faster flowing central ice shelf. The eastern TG ice shelf increases in velocity by up to 2000 m yr^{-1} at the calving front. There is an increase in velocity of $\sim 500 \text{ m yr}^{-1}$ of newly floating ice over TG and PSK. Similarly to the equivalent BISICLES simulation, Dotson and Crosson show a decrease in velocity.

All simulations show net thinning over ice streams and ice shelves by the end of the century (fig. 6.13). BISICLES simulations show a greater magnitude of thinning over grounded ice whereas ISSM shows a greater magnitude of thinning over the floating ice in the domain. The greatest thinning in each of the simulations exceeds 500 m over ice shelves and the grounded ice of PSK.

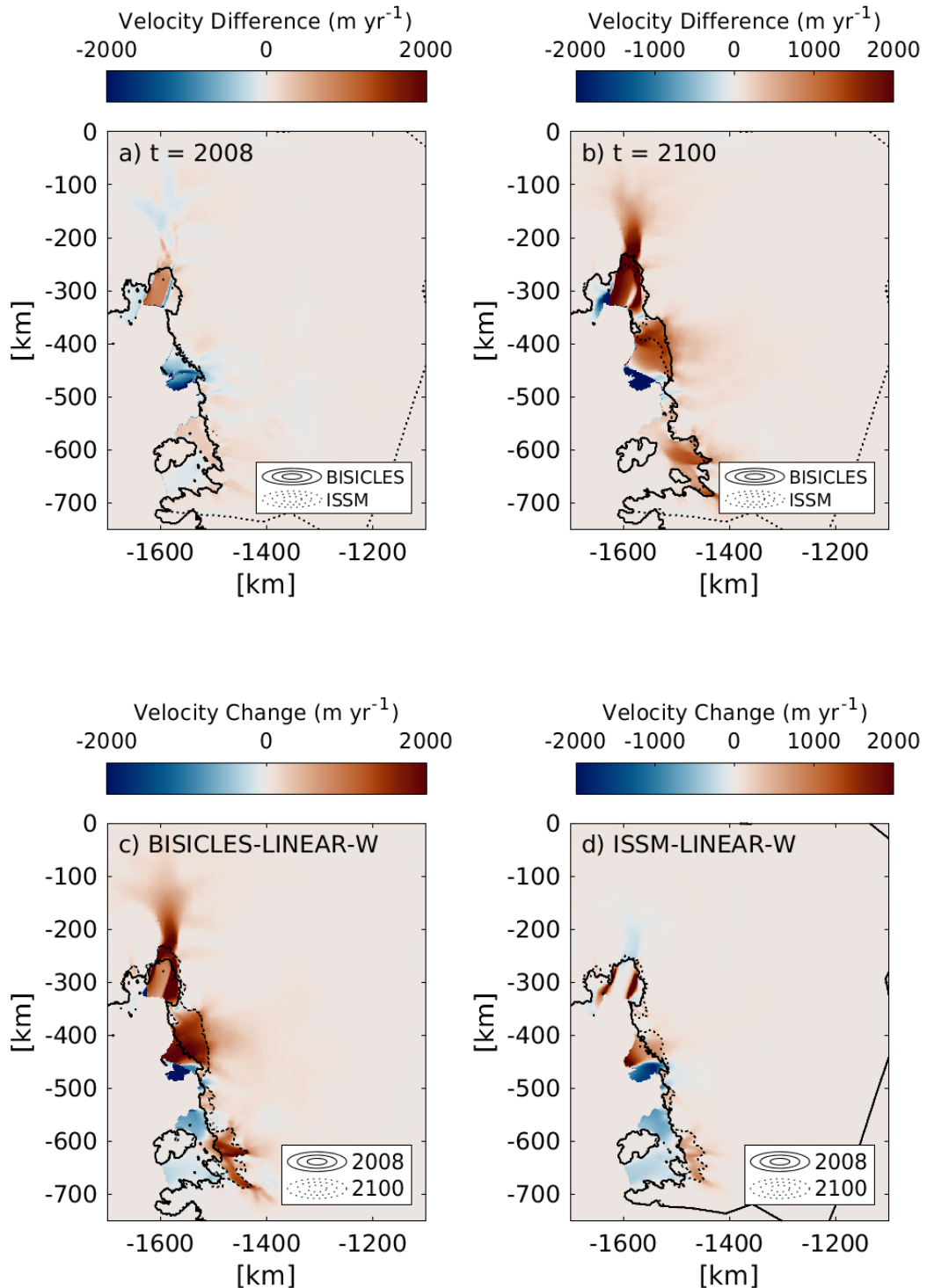


Figure 6.12: Velocity difference between BISICLES and ISSM LINEAR simulations for the year a) 2008 and b) 2100. Positive (negative) where BISICLES velocity is higher (lower) than the ISSM LINEAR simulation for the equivalent year. Blocked and dotted black lines represent the grounding line positions in each year for BISICLES and ISSM respectively. Velocity change in 2100 relative to 2008 for c) BISICLES-LINEAR-W and d) ISSM-LINEAR-W simulations. Blocked and dotted black lines represent the grounding line positions in each year for the year 2008 and 2100 respectively for each model simulation.

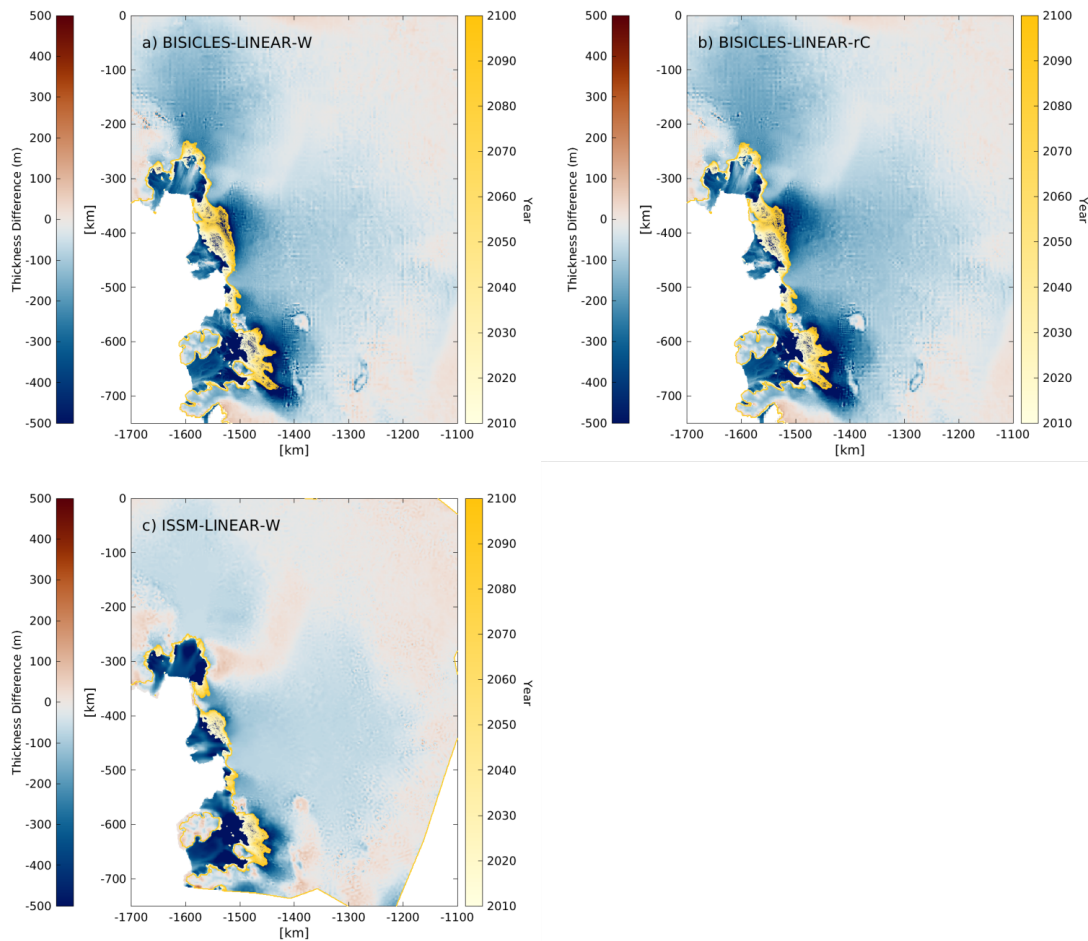


Figure 6.13: Thickness change (m) from 2008 to 2100 for a) BISICLES-LINEAR-W b) BISICLES-LINEAR-rC and c) ISSM-LINEAR-W. For each simulation the grounding line position is plotted every year according to the colour gradient.

6.6 Discussion

Here, a comparison of 21st century simulations of the ASE using two different high resolution ice sheet models is presented. Estimates of sea level contribution using two ice sheet models, two sliding laws and seven applications of basal mass balance perturbations result in a total range in sea level contribution of 23 to 79 mm (fig. 6.5). When considering simulations based on an RCP8.5 emissions pathway this range is reduced to 24 to 54 mm for 93 years. The projected mass loss from the RCP8.5 forced simulations compare well with those of Alevropoulos-Borrill et al. (2020) who found a 20 to 45 mm range with a Bedmap2 topography. Given that the ASE has been identified to have the greatest sensitivity to model parameters (Lowry et al., 2021) and high sensitivity

to perturbed basal melting (Alevropoulos-Borrill et al., 2020), the range of uncertainty from this investigation is relatively low.

The results here show a model dependent sensitivity of the ice stream response to varying magnitudes of basal melting. There is a larger range in mass loss in response to varied forcing for both sets of BISICLES simulations, 48 mm and 36 mm for *rC and *W respectively, compared with 10 mm for ISSM (fig. 6.6). Although there is overlap between the end of century SLE distributions for each of the model sets of experiments, this only occurs with the LINEAR simulation for ISSM exceeding the lower end BISICLES simulations. For each equivalent melt forcing, BISICLES consistently projects greater mass loss than ISSM. For an idealised marine ice stream domain, Pattyn and Durand (2013) show that SSA models respond more quickly to external perturbation than L1Lx models due to the neglect of vertical shear. Subsequently, ISSM would be expected to exhibit more mass loss and grounding line retreat than BISICLES, which does not occur here. It is therefore expected that there is an alternative cause of differences in model sensitivity to perturbation Cornford et al. (2020).

The primary explanation for the differences between BISICLES and ISSM simulations is the difference in model initialisation. ISSM underestimates the observed velocity of floating ice shelves (fig. 6.4) in addition to the PIG trunk up to 100 km upstream from the initial grounding line and 40 km upstream of the western TG grounding line. This is exacerbated by the areas of velocity that BISICLES overestimates, such as the ice shelf of PIG. Subsequently, the rate of mass loss as a result of the initialisation differs, where BISICLES simulations will experience more dynamic mass loss given its faster velocity over the domain. Comparing the perturbed SLE by subtracting the CTRL simulations from each set of model simulations (fig. 6.14), for all but NEMO-GL and LINEAR, there is a far more consistent magnitude of mass loss between BISICLES and ISSM. This is consistent with existing studies including Cornford et al. (2020) and Seroussi et al. (2019) which show disagreement in model projections are a product of differences in the initial state of the models.

Despite accounting for differences in the model initialisation by subtracting the CTRL simulation (fig. 6.14), there remain stark differences in the model sensitivity to simulations with the greatest cumulative basal melting, specifically in the NEMO-GL and LINEAR simulations. Here, BISICLES is more sensitive to greater perturbations of basal melting than ISSM. This result is somewhat a product of differences

in model initialisation that are not accounted for by subtracting the CTRL simulation. For NEMO-GL and LINEAR simulations, BISICLES experiences a greater magnitude of cumulative melting (fig. 6.5) compared with ISSM. Melting drives grounding line retreat resulting in a greater area of ice shelf available for melting meaning the cumulative melting is greater, which is a positive feedback. With a greater initial velocity of floating ice in BISICLES, there is increased thinning around the grounding line contributing to retreat that is then exacerbated by the positive feedback through increased melting. This finding is supported by the greater magnitude of thinning of floating ice in ISSM-LINEAR (fig. 6.13), where ice discharge is lower due to slower velocity so the ice shelves thin more from basal melting and are not thickened dynamically by the outflow of upstream ice. Furthermore, with slower flow and reduced dynamic thinning of grounded ice there is less ice flux and thinning of grounded ice in ISSM-LINEAR compared with BISICLES-LINEAR-*, again supporting reduced ice flux across the grounding line. This finding highlights that subtracting a control simulation does not fully account for differences in model initialisation as a result of feedbacks within the ice sheet system. This consideration should therefore be taken in the interpretation of Seroussi et al. (2020) results.

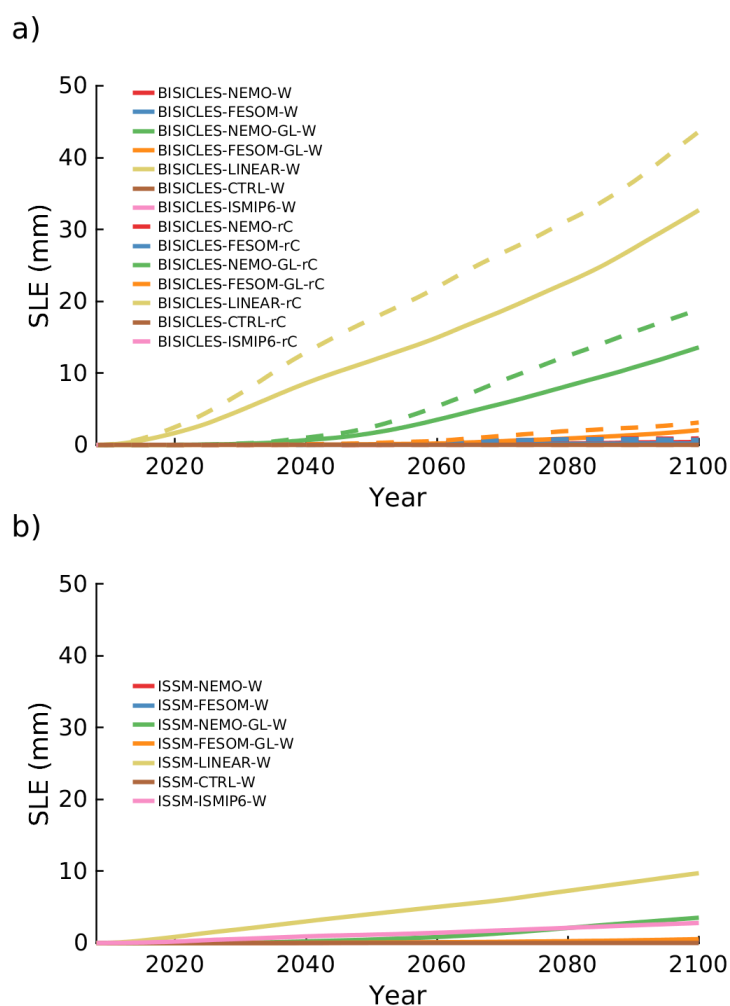


Figure 6.14: Sea level equivalent from 2008 to 2100 for a) BISICLES and b) ISSM simulations subtracting the respective CTRL simulations.

The method of parameterization of projected melt rates results in divergence in the modelled ice response. In response to direct RCP8.5 forced melt rates from NEMO, FESOM and NorESM1-ME (through the ISMIP6 forcing) the mass loss from the ASE is relatively modest (fig. 6.5) considering continued present day mass loss would result in 31 mm by 2100 (based on the 0.33 mm yr^{-1} ASE mass loss estimate from McMillan et al. (2014)). For NEMO and FESOM simulations, the stretching of the melt rates with the retreating grounding line results in a reduction in the magnitude of melting, causing a similar response to the CTRL forcing. As the anomalies for NEMO and FESOM are small compared with the magnitude of the background melt field (fig. 6.1), it is insufficient to drive much additional retreat (fig. 6.14). While the NEMO-GL and

FESOM-GL simulations account for this somewhat, the application of the -GL parameterization results in homogenising of the melt rate anomaly, which in reality is spatially variable. In averaging the melt anomalies within 10 km of the ASE grounding line, the high melt anomalies projected beneath PIG and western TG are lowered through the incorporation of the relatively low anomalies projected beneath Dotson and Crosson. Although increased CDW to the ASE will impact ocean temperature over much of the region (Donat-Magnin et al., 2017), there remains large spatial variability resulting in a wide range of melt rates for each ice shelf in the region. It is challenging to account for this variability when applying a parameterization scheme that does not account for differences between ice shelves (Burgard et al., 2022).

The ISMIP6 simulations lie at the lower end of the end of century SLE distribution (fig. 6.5). Burgard et al. (2022) found that the melt rates produced from the ISMIP6 ‘MeanAnt’ parameterizations showed good agreement with those produced by the ocean model NEMO. However, the cumulative melting is lower than that of the CTRL simulation, which does not include future increases in basal melting that are projected by ocean models (fig. 6.2). Furthermore, the mean annual total melting for ISSM-ISMIP6-W is 220 Gt yr^{-1} (fig. 6.5) which lies below the observations of near present day melting of Rignot et al. (2013a), which is consistent with present day modelled melt rates produced by NEMO but not future (fig. 6.2). Therefore, it is suggested that the ISMIP6 basal melt forcing does not replicate the projected warming from an RCP8.5 scenario in the ASE.

The ISMIP6 simulation is the only modelled simulation where the cumulative basal melt is greater in ISSM than BISICLES, although the end-of-simulation SLE contribution is greater for the latter by 4 mm. The nature of the forcing accounts for ice shelf depth which differs over the two simulations as a result of the different dynamic responses to forcing. The ISSM-ISMIP6-W simulation experiences more grounding line retreat in the first 35 years of the simulation than BISICLES-ISMIP6-W (fig. 6.9), which exhibits immediate grounding line advance as it equilibrates to the forcing. Following the year 2040 the rate of grounding line retreat decreases for ISSM but increases for BISICLES, but with a greater ice shelf area there is more cumulative melting in ISSM (fig. 6.15). Subsequently, as BISICLES ice flow is more sensitive to perturbations in melting, as a product of the initialisation, cumulative melting drives increased grounding line retreat and mass loss from years 2040 to 2100.

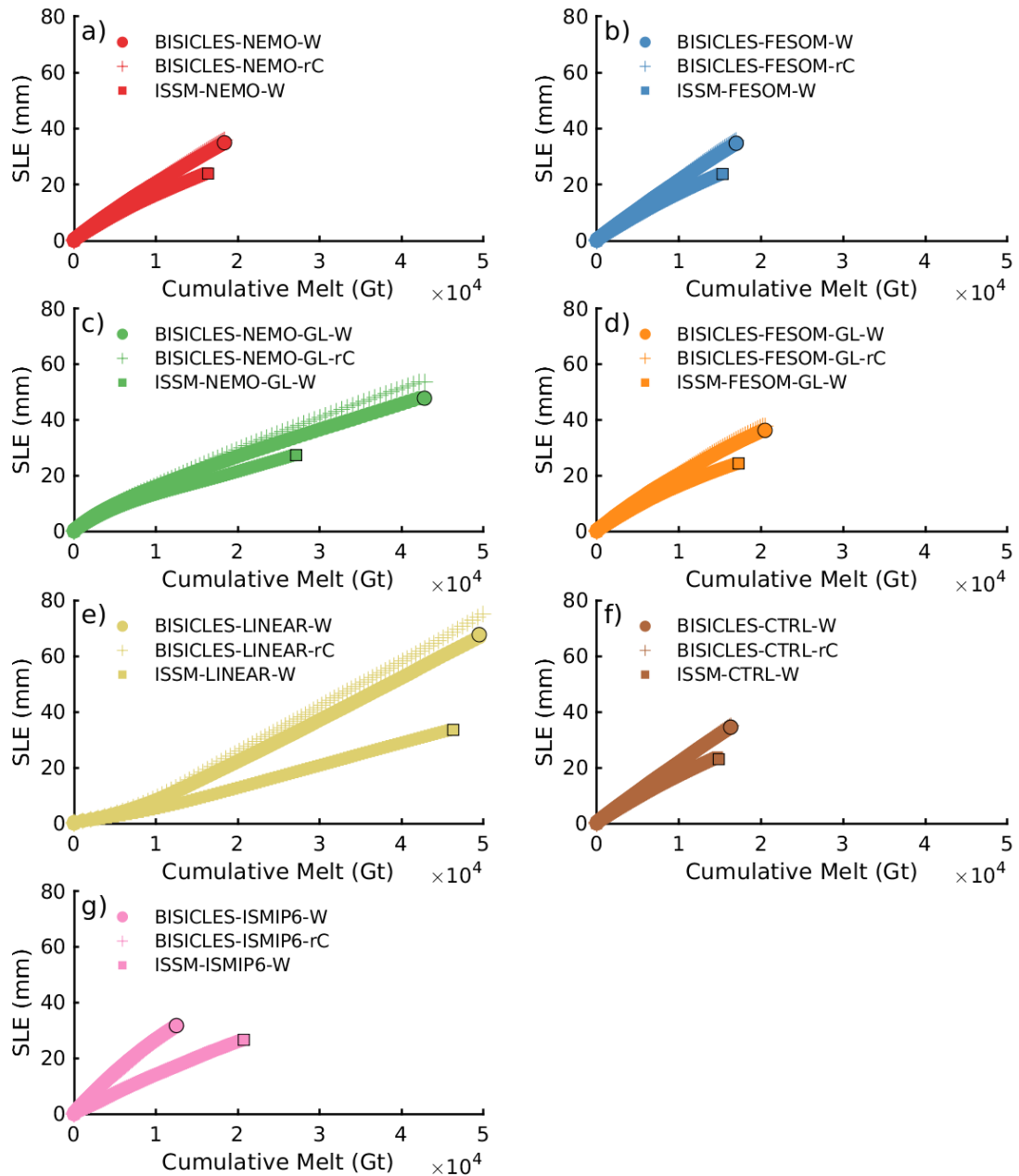


Figure 6.15: a-g) Relationship between cumulative melting and sea level equivalent each year for each melt forced simulation.

The LINEAR simulations do not have a prescribed temporal variation in the magnitude of melting, the cumulative melting changes as a product of the evolution of the ice shelf geometry. The initial spike in melt rate that occurs in the first 2 years of the simulation is a result of a greater portion of the ice shelves having a depth below 500 m and therefore the highest magnitude melting of 75 m yr^{-1} . This high cumulative melt rate then reduces, where both direct melt induced thinning and dynamic thinning as a

result of ice shelf and stream acceleration causes a reduction in the depth of the base of the shelf and therefore the magnitude of the applied melt rate. Following this the cumulative melt rate stabilises somewhat from the year 2020 onward, averaging 600 m yr^{-1} . The initial spike in melting coincides with a rapid retreat of the grounding lines of ASE ice streams (fig. 6.9) of $200 \text{ km}^2 \text{ yr}^{-1}$ over the first 30 years of the simulation in BISICLES simulations. Although the melt forcing applied is idealised, it simulates the role of ice shelf geometry in determining melt rates beneath ice shelves where melting increases with depth. This highlights the importance of modelling a fully coupled system where ice shelf depth and gradient can impact melt rates of ice shelves.

Limitations and Future Work The differences between ice sheet model projections here are attributed to disagreement in the model initialisation. This emphasises the importance in reducing the misfit between observations and the initialised model. That being said, the inverse problem is ill-posed and therefore there will always remain uncertainty in projections of future evolution of the ASE associated with the tuned parameter fields. To better constrain the uncertainty associated with the large misfit in the ISSM initialised model here, it could be beneficial to produce additional initialised domains and repeat the experiments.

The equivalent fine resolution mesh in these simulations is in part responsible for the similarity in model performance. In MISMIP3D+ (Cornford et al., 2020), found that mesh resolutions below 1 km promoted more similar model responses and removed the necessity for forms of sub-grid friction schemes that were required for coarser resolution simulations. With an adaptive mesh scheme employed here, BISICLES would continue to retain fine resolution representation of the grounded-floating ice interface for longer timescales and greater grounding line retreat. The fixed unstructured mesh employed in these simulations in ISSM is suitable to represent the grounding line over this timescale due to the relatively limited grounding line retreat occurring in the simulations but could become more problematic as the grounding line retreats away from the zone of 0.25 km grid resolution and over coarser areas of the domain.

6.7 Conclusion

In this chapter, 21st century simulations of the ASE were performed by two high resolution ice sheet models and the results were compared. Simulations were forced by

seven melt rate parameterizations for both ice sheet models, with an additional simulation performed by BISICLES with an alternative sliding law to explore the sensitivity of both ice sheet model and sliding law to perturbed basal melting. Projections of 21st century mass loss from the ASE under an RCP8.5 scenario are relatively modest, ranging from 24 to 54 mm for both ice sheet models and sliding laws, which is consistent with current mass loss trends but slightly exceeds estimates from recent investigations.

Differences in the initialised velocity of the two models is responsible for much of the model disagreement, as opposed to the approximation of englacial stress used by the models. While subtracting a control simulation from the perturbed simulations accounts for the differences in the initial dynamic mass loss from the region, it does little to account for the role of positive feedbacks in amplifying the initial differences in between the models when perturbed by the upper end of the range of basal melt projections. Therefore, investigations presenting results that account for initial model disagreement by subtracting control simulations may not be well suited for ice sheet modelling practices.

Challenges remain in projecting the response of the ASE to a changing climate when performing offline simulations with a parameterized external forcing. Existing parameterizations that relate the depth of the ice shelf to an extrapolated thermal forcing field, such as ISMIP6, results in a total melting from the region equivalent to present day, despite being forced with a high emissions climate scenario. While direct melt rates from cavity resolving ocean models may better reproduce the magnitude of melt rate anomalies that are better in line with projections of future climatology in the ASE, additional methods must be used to account for an evolving cavity which can add to the uncertainty in the projected ice response.

Chapter 7

Synthesis

The research presented in this thesis uses numerical ice sheet modelling to explore the evolution of the Amundsen Sea Embayment ice streams in response to future ocean forcing. The sensitivity of the region's ice streams to increases in sub-ice shelf melting is investigated, with further consideration of how representation of the bedrock, subglacial rheology, calving front position, englacial stress approximations and model initialisation control the modelled response to melting. In exploring the interplay between the dynamic ice stream response to ocean forcing and numerical representation of ice flow in the ice sheet models, a broader consideration of the uncertainties associated with future projections of the region are presented. These findings provide continuity between existing ice sheet modelling studies of the region by giving additional context for the interpretation of ice sheet model projections particularly with respect to the dependence of results on model set up. This chapter discusses key themes that extend throughout the research presented here. The aim of this chapter is to highlight the significance of the findings within this thesis.

7.1 The Response of the ASE Ice Streams to Sub-ice Shelf Melting

The future health of the ASE ice streams is somewhat at the mercy of future changes in sub-ice shelf melting. ASE ice shelves, particularly the confined ice shelves of PIG, Crosson and Dotson, regulate the discharge of ice across the grounding line and stabilise retreat (Fürst et al., 2016; Gudmundsson, 2013; Gudmundsson et al., 2019). However,

increased ice shelf thinning, damage (often exacerbated by melting) and calving front retreat will lead to acceleration of ice streams (Payne et al., 2007; Lhermitte et al., 2020; Fürst et al., 2016; De Rydt et al., 2021; Gudmundsson et al., 2019). The ASE ice shelf melt rates are some of the highest around Antarctica (Dutrieux et al., 2014b; Adusumilli et al., 2020; Shean et al., 2019) due to the presence of a warm CDW layer on the shelf which is driven toward the grounding lines of ice streams causing high melting at depth (Pritchard et al., 2012; Naughten et al., 2022). While there is large variability in the heat available for ice shelf melting in the ASE due to interannual and decadal trends in the atmospheric conditions that lead to increased CDW delivery in the region (Jenkins et al., 2016), there is a clear long-term trend of increasing CDW delivery (Naughten et al., 2022) which is expected to continue in the future (Bintanja et al., 2015b; Naughten et al., 2018b), driving increased ice shelf melting (Donat-Magnin et al., 2017). Subsequently, projected increases in sub-ice shelf basal melting are expected to drive future grounding line retreat and mass loss in the ASE (Donat-Magnin et al., 2017; Scheuchl et al., 2016; Alevropoulos-Borrill et al., 2020).

The ice sheet model simulations performed in this thesis support the existing evidence that ASE ice streams are highly sensitive to perturbations in sub-ice shelf basal melting (Pritchard et al., 2012; Payne et al., 2007; Nias et al., 2016; Joughin et al., 2014). Even relatively small increases in the magnitude of basal melting over decadal periods results in increased mass loss from ASE ice streams, where simulations forced with melt rate anomalies up to 5 m yr^{-1} over 20 years result in an additional SLE contribution of 4 mm relative to a control simulation. Furthermore, simulations show that the sensitivity to melting is ice stream dependent, whereby ice streams feeding confined ice shelves (PSK and PIG) are the most sensitive to perturbations in ice shelf melting due to reduced the buttressing which permits ice stream acceleration (Gudmundsson, 2013) and increased mass loss while melting is elevated.

Following a period of retreat, reducing the magnitude of basal melting relative to present-day limits the total SLE contribution from the ASE, promoting grounding line stability. Experiments here show ASE ice streams are sensitive to reductions in melting and refreezing, whereby negative melt anomalies allow ice shelves to thicken, slowing the rate of discharge across the grounding line. Future climate scenarios such as RCP2.6 that involve the implementation of carbon sequestration or other geo-engineering technologies, could mitigate mass loss from the ASE (Moore et al., 2018). However, since

even the lower overall warming of RCP2.6 could continue to produce warming in the ASE (Alevropoulos-Borrill et al., 2020; Wernecke et al., 2022), limiting mass loss will require a reduced volume of CDW accessing the shelf. Therefore, for direct reductions in basal melting of ASE ice shelves, more localised implementations of geoengineering may be required (Moore et al., 2018).

There is a positive relationship between cumulative melting and sea level contribution shown in all simulations throughout this thesis, however, the linearity and magnitude of the relationship varies. The sensitivity of the ASE ice streams to melting is dependent on the topography, ice shelf geometry, representation of sliding and initialisation of an ice sheet model. These findings add to those of Alevropoulos-Borrill et al. (2020) who found an interplay between the magnitude of melting and the mass loss response when ice sheet model parameters were perturbed. As numerical representation of ASE ice streams influences the modelled sensitivity to future melting, uncertainty in future evolution of the region in response to sub-ice shelf melting can be amplified.

7.2 Uncertainties in Ice Sheet Model Practices

In this thesis, ice sheet model simulations are performed with perturbed ice shelf melting as the primary external forcing and the sensitivity of ice streams to melting is considered through changing ice sheet model parameters, representation of processes and the ASE domain. The results demonstrate that altering the model configuration can amplify the sensitivity to ice shelf melting and expand the uncertainty in projections in response to a single ocean forcing, making it more challenging to determine the relationship between the future ocean forcing in response to climate change and the ice sheet response.

Representation of Calving and the Calving Front Position Ice shelves in the ASE play an important role in stabilising the flow of upstream ice and therefore regulating discharge from ice streams (Fürst et al., 2016; Reese et al., 2018b; Gudmundsson, 2013). Areas of the ice shelf shown to provide the greatest buttressing force are those in closer proximity to grounding lines and in shear margins (Fürst et al., 2016; Goldberg et al., 2019). Although calving front positions are sometimes fixed in ice sheet modelling investigations (e.g. Barnes et al., 2020; Favier et al., 2014), in reality, the horizontal extent of ASE ice shelves is constantly evolving (Turner et al., 2017). Large

calving events cause retreat and reduced contact with surrounding topography (Arndt et al., 2018) while unconfined ice tongues can form and advance a calving front. Over the last 20 years in the ASE, ice front retreat has been shown to drive grounding line retreat and acceleration of PIG (Joughin et al., 2021; Lhermitte et al., 2020) and PIG (Milillo et al., 2019; Yu et al., 2019). As an important physical process, misrepresenting ice shelf calving and damage in ice sheet modelling investigations promotes uncertainty in model projections.

Ice sheet modelling experiments that neglect calving and subsequent calving front migration could underestimate the future acceleration of marine terminating ice streams, particularly for those with confined ice shelves that provide strong buttressing forces (Fürst et al., 2016). The observed calving front retreat of PIG from 2014 to 2020 has increased the modelled sensitivity of the ice stream to melting through reduced lateral and basal drag (Chapter 4; Joughin et al., 2021). In simulations performed here, calving front retreat has an instantaneous impact on ice shelf acceleration which propagates up to 80 km upstream over grounded ice (Gudmundsson et al., 2019). The experiments show that the reduced ice shelf buttressing is most important for the ice stream while sub-ice shelf melting is increased, where the rate of grounding line retreat is increased relative to simulations with a fixed extent. The inclusion of freely evolving calving fronts, while numerically challenging, is important for projecting the evolving behaviour of PIG in response to a changing climate and evolving sub-shelf melt rates (Benn et al., 2007).

A fixed calving front promotes ice stream stability in model simulations that could be unrealistic. The implementation of a fixed calving front in the re-growth experiments (see Chapter 3) permits ice shelves to dynamically thicken over their entire initial spatial extent following multi-decadal periods of forcing. Without a migrating calving front, ice shelves help to re-stabilise ice streams and limit mass loss from the modelled ASE ice streams. This effect will be most important for initially confined ice shelves, where dynamic thickening in relation to the initial geometry of ice shelves will increase the buttressing from these ice shelves by allowing increased contact with lateral and basal topography. While a fixed calving front is an appropriate solution for simulations forced with continuously increasing sub-ice shelf melting, it may be less appropriate for experiments exploring ice stream stability through negative forcing. Therefore the condition of a fixed calving front may in part be promoting the stability shown in the re-advance

experiments presented in this thesis.

Representation of Basal Friction Basal slip or sliding at the ice-bed interface is a mechanism responsible for fast ice flow in Antarctic ice streams (Cuffey and Paterson, 2010). The properties and behaviour of subglacial sediments impacts the drag experienced at the base of ice streams and therefore the sliding at the bed. In ice sheet models, basal drag is often parameterized as a function of basal velocity in the form of a sliding or friction law (Brondex et al., 2019). Many models incorporate a non-linear relation with a variable exponent that often provides no upper limit on the basal resistance for increasing velocity (Weertman, 1957; Joughin et al., 2019; Nias et al., 2019). While such non-linear viscous sliding laws were initially shown to best represent sliding over hard bedrock (Nias et al., 2016), more recent investigations show ice flow in the ASE is better represented by a Coulomb-plastic type sliding law where there is an upper limit to the dependence of basal drag on velocity, representative of sliding over weak sediment (Joughin et al., 2019; De Rydt et al., 2021; Schoof, 2010). However, as properties at the bed are challenging to measure, there remain large uncertainties in the understanding of basal processes and their influence on ice dynamics.

The choice of friction law for ice sheet model simulations is responsible for model disagreement in simulations of ice stream evolution (Brondex et al., 2019; Nias et al., 2018; Schlegel et al., 2018; Wernecke et al., 2022; Cornford et al., 2020). In this thesis, simulations performed with a non-linear viscous (Weertman; Weertman, 1957) type sliding law representing sliding over a hard bed and a regularized Coulomb (Joughin et al., 2019) sliding law representing sliding over deformable sediment, are compared. The sensitivity of the ASE to increases in sub-ice shelf melting is amplified when including regularized Coulomb sliding, which is most notable for PIG. With a low magnitude melt forcing, regularized Coulomb sliding limits grounding line retreat and mass loss from the ice stream, whereas in response to high magnitude melt forcing, the ice stream accelerates over a wider area than the equivalent Weertman sliding law and subsequently loses more mass. In contrast, the regularized Coulomb sliding results in increased mass loss in response to any perturbation in melting for TG. Moreover, the modelled ice stream response to choice of sliding law is shown to have a bedrock dependence, where Bedmap2 amplifies the effects of regularized Coulomb sliding over PIG to a greater extent than BedMachine. Therefore, the results presented here show an ice stream and bedrock dependent sensitivity to the representation of sliding which

drives the predictive uncertainty of future projections.

While temporally constant friction or basal traction coefficients are widely used in ice sheet modelling practices, such parameterizations of basal drag neglect the evolution of subglacial hydrology and water pressure at the bed which in reality influences ice stream flow. Hydrological models can be used to provide effective pressure estimates (Schoof and Hindmarsh, 2010) and coupled subglacial hydrology - ice sheet models can be used to better capture the evolution of the subglacial system (Le Brocq et al., 2009; Fricker and Scambos, 2009; Fricker et al., 2007), though assumptions must be made regarding the method of water flow (e.g. as a thin film rather than series of channels; Arnold and Sharp, 2002). A more simplistic approach to represent evolution of subglacial hydrology can be incorporated with a gradual increase of effective pressure (or decrease in the friction coefficient) toward the grounding line which represents connectivity with the ocean and saltwater incursion in sediment (Vielı and Payne, 2003). Methods of incorporating this transition zone include a transition thickness above floatation incorporated in Joughin et al. (2019) which provides some temporal evolution of subglacial hydrology with grounding line retreat. Without such a scheme in these investigations, the migration of a water saturated till with grounding line retreat will not be represented and therefore the basal velocity around a migrating grounding line may be underestimated. That being said, Gillet-Chaulet et al. (2016) found century scale simulations, such as those performed here, are sufficiently short for the uncertainty associated with a constant C to be equivalent to the uncertainty that may be associated by incorporating a model that evolves water pressure.

Bed Topography Bed topography is an important control on mass loss from Antarctica, firstly, in the grounding of ice below sea level and the presence of glacial basins with a bed that deepens toward the interior which precondition instability of ice sheets (Schoof, 2012; Feldmann and Levermann, 2015). At finer spatial scales, bedrock features and consequent roughness can provide temporary stability of grounding line positions and provide resistance to the outward flow of ice shelves (Still et al., 2019; Castleman et al., 2021). Ice sheet geometry product comparisons have widely been performed (Schlegel et al., 2018; Nias et al., 2018, 2016; Wernecke et al., 2022) and it has generally been shown that finer resolution products result in increased mass loss from Antarctica or regions of Antarctica (Wernecke et al., 2022; Schlegel et al., 2018). Here, mass loss from PIG and TG doubles when BedMachine (Morlighem et al., 2020),

an improved, high resolution mass conserving bedrock is used in the model domain, compared with its predecessor Bedmap2 (Fretwell et al., 2013). Simulations performed with Bedmap2 exhibit more limited grounding line retreat, where high amplitude low frequency bed features pin the grounding line (Wernecke et al., 2022). Furthermore, the grounding lines of PIG and TG retreat over deeper bed in BedMachine simulations. Subsequently, existing modelling investigations will likely underestimate future mass loss from the region when using Bedmap2.

Neglecting vertical land movement ice sheet model projections could lead to an overestimation of mass loss from the ASE. Studies presenting measurements of vertical land movement over Antarctica show that West Antarctica experiences uplift on short timescales due to low mantle viscosity (Gomez et al., 2015). While simulations performed in these investigations are up to two centuries long, in response to the mass loss simulated, uplift of the bed could act to stabilise the ice streams in response to enhanced melting as a negative feedback (Barletta et al., 2018; Gomez et al., 2015). Barletta et al. (2018) suggest the PIG basin could uplift by 8 m by 2100 which could stabilise the ice stream and promote re-advance. Coupled ice sheet-earth models will therefore help to eliminate the uncertainty produced from neglecting these negative feedbacks in model simulations (Whitehouse et al., 2019).

Present and Future Ice Shelf Melt Rates Experiments in this thesis demonstrate that the ASE ice streams are sensitive to low magnitude and brief increases in ice shelf melting. However, the future evolution of ice shelf melt rates in the ASE is uncertain. Modelled projections vary in both the global climate response to emissions which influences the evolution of ocean properties in the ASE (Naughten et al., 2018a; Alevropoulos-Borrill et al., 2020) and through uncertainty in ice-ocean processes (Malyarenko et al., 2020). While the role of uncertainty in the future emissions scenarios and the climate and ocean response can be considered by performing ice sheet model simulations in response to a range of future forcings (Seroussi et al., 2020), this does little to constrain the uncertainty in future sea level rise projections.

Differences in the application of melt rates in models through parameterization can lead to model disagreement in the response to the same external climate forcing, as is shown by the ISMIP6 experiments (Seroussi et al., 2020). The results from the model comparison in Chapter 6 supports this, where the upper end of 21st century sea level contribution forced with an RCP8.5 scenario is double that of the lower end. Stretching

of melt rate anomalies through a grounding line proximity function results in a mass loss equivalent to a control simulation with constant present day melt rates. Furthermore, the compulsory ISMIP6 RCP8.5 forced basal melt parameterization also results in a total ice shelf melt equivalent to the control experiment in simulations presented in Chapter 6. Therefore, either the present-day melt rate field in these simulations overestimates the mass loss from the region, which is unlikely given that the total melt is consistent with observations, or the ISMIP6 parameterization results in underestimated melt rates in the ASE which was alluded to by Jourdain et al. (2020). Either way, differences in melt parameterization for the same future warming scenario can lead to uncertainty in future projections.

Some ice sheet model melt rate parameterizations attempt to incorporate the impacts of ice-ocean feedbacks. The quadratic dependence of ice shelf melting on thermal forcing, dictated by salinity and potential temperature, amplifies melt rates by representing the role of meltwater pumping (Holland et al., 2008), where increased melting results in acceleration of meltwater plumes and increased intrusion of warm water deep within an ice shelf cavity. This parameterization is incorporated in the ISMIP6 forcing (Jourdain et al., 2020) and has been shown to best represent coupled ice-ocean projected melt rates (Favier et al., 2019; Burgard et al., 2022). However, this parameterization neglects other feedbacks that occur in response to increased ice shelf melting such as warming of the subsurface due to increased stratification (Golledge et al., 2019) and the role of an evolving cavity geometry (Donat-Magnin et al., 2017). Such feedbacks are more realistically incorporated through coupled ice-ocean modelling (see Chapter 2).

Coupling ice sheet models to cavity resolving ocean models is the future progression of ice sheet modelling (Pattyn, 2018). While coupling ensures more physically based processes are represented (Jordan et al., 2018), uncertainty still remains. Although cavity resolving ocean models directly calculate ice shelf melting in coupled ice-ocean models, tuning parameters such as the heat transfer coefficient, γ_T vary widely in literature (Malyarenko et al., 2020) and can result in vast differences in calculated melt rates (Malyarenko, 2020). Furthermore, biases generated in the initialisation of ocean model domains can lead to underestimation of melt rates (Naughten et al., 2018a). Therefore, whilst fully coupled ice-ocean models may improve the representation of melt rates and ice shelf cavity evolution, uncertainties will remain.

Surface Mass Balance In the simulations performed throughout this thesis, a surface mass balance field from Arthern et al. (2006) is applied over the domain and held constant through time. While such practices are reasonable for century scale simulations (Nias et al., 2016), simulations representing an evolving climate may be neglecting important changes that may impact the dynamics of the region. While future warming scenarios are shown to result in increased ice sheet accumulation (Agosta et al., 2013; Palerme et al., 2017), warmer climates are also shown to lead to exponential increases in surface melt in relation to surface air temperature change which could lead to increased mass loss through ice shelf collapse (Munneke et al., 2014; Trusel et al., 2015). In the ASE, the ratio between melt and precipitation is projected to increase in response to increased warming and PIG is expected to experience significant surface melt in the 21st century although TG, Dotson and Crosson ice shelves surface melting will not exceed precipitation until the latter half of the 22nd century (Donat-Magnin et al., 2021). Therefore, while neglecting a temporally evolving SMB field from simulations will alter the projected rate of mass loss, where accumulation will offset dynamic mass loss, surface melting is unlikely to trigger ice shelf collapse over the duration of these simulations. Furthermore, even with increased surface melting occurring, implementing hydrofracturing in these model simulations would be numerically challenging and likely present large uncertainties (Pattyn et al., 2017).

Model Initialisation In Chapter 6, the results show that the ice sheet model initial state is of greater importance for predictive uncertainty than the choice of ice sheet model and its englacial stress approximations. This was alluded to in the idealised investigation by Cornford et al. (2020) and the real world model intercomparison in Seroussi et al. (2019). Furthermore, investigations such as Lowry et al. (2021), Nias et al. (2019) and Schlegel et al. (2018) show that the ASE ice streams are particularly sensitive to variations in initialisation parameters, where the effects are exacerbated by increased external forcing (Alevropoulos-Borrill et al., 2020). Given feedbacks in the ice sheet system, a simple subtraction of control simulations will not fully account for differences in the modelled initial state. While a standardised maximum misfit between an initialised model and observations could be required for future modelling investigations, the ill-posed nature of the inverse problem for data-assimilation models will remain a source of some uncertainty.

7.3 The Stability of the ASE Ice Streams

The present and future stability of the ice streams in the ASE has been a focus of international research for the last two decades (Scambos et al., 2017; Turner et al., 2017). As the observational record increases with extensive satellite datasets (Rignot et al., 2019; IMBIE, 2018; Mouginot et al., 2019) supported with direct measurements (Mouginot et al., 2012; Fretwell et al., 2013), and ice sheet modelling capabilities advance (Patyn, 2018), the dynamics of the ice streams can be better understood (De Rydt et al., 2021; Milillo et al., 2019). Favier et al. (2014) modelled the future evolution of PIG and proposed that the grounding line was undergoing unstable retreat which could reach 40 km. However, more recent observations suggest, given the current thinning trend over the trunk, that the ice stream is currently experiencing a period of stability (Bamber and Dawson, 2020). Joughin et al. (2014) also suggested that TG was experiencing unstable retreat but mass loss would accelerate from 2200 onward. More recent observational work indicates that the present behavior of ASE ice streams may not be indicative of instability (Bamber and Dawson, 2020; Milillo et al., 2019) but that is not to say the ice streams are not currently evolving toward a point of instability (Wild et al., 2021; Lhermitte et al., 2020).

Simulations performed in Chapter 3 show that grounding line retreat in the ASE can be limited through the prolonged reduction of basal melt rates, combined with re-freezing over the domain associated with a blocking of CDW from the continental shelf (Gürses et al., 2019). However, grounding line advance does not universally coincide with a negative SLE contribution in the ASE where TG shows continued positive mass loss despite grounding line advance and ice shelf thickening. Furthermore, negative melt rate anomalies may limit the upper end contribution to mass loss from the ice streams but are unable to offset the committed contribution from these ice streams of 28 mm over 200 years with Bedmap2 topography. While grounding line retreat and advance in addition to a reduction in the rate of mass loss can occur with reduced melting and refreezing, the physical occurrence of this is questionable given the present trends in increased CDW delivery in the ASE (Naughten et al., 2022). Thus, the stabilisation observed is largely a product of the idealised forcing applied and may be influenced further by model conditions.

Experiments here show temporarily stable grounding line positions can be reached following the removal of a positive melt anomaly for PIG and TG (see Chapter 3) as

dictated by the bed topography. Despite the difference in sliding law employed, the grounding lines of PIG and TG retreat up to 30 and 55 km using BedMachine geometry (see Chapter 5). Stable grounding line positions coincide with locations of topographic maxima and while the rate of grounding line retreat is slowed by topography following reduced melting, that is not to say these end of simulation stable positions are permanent. Furthermore, Castleman et al. (2021) show the reported uncertainty associated with Morlighem et al. (2020)'s BedMachine Antarctica leads to a range in SLE contribution over 200 years of 21.9 cm meaning the modelled grounding line stability is dependent on the accuracy of the bed topography product.

Alevropoulos-Borrill et al. (2020) explored the future evolution of the ASE in response to ocean forcing with earth system model simulations for an RCP8.5 scenario and found a range of 20 to 45 mm by 2100 for an optimised model set up with a Weertman sliding law (Weertman, 1957). This compares well with the range of 24 to 54 mm found here in Chapter 6, which incorporates simulations using two ice sheet models, two sliding laws and a variety of melt parameterizations under an RCP8.5 pathway. The experiments performed in Chapter 6 incorporate both a finer resolution BedMachine topography and more recent velocity (Mouginot et al., 2017) which would be expected to promote far greater mass loss compared with the model set-up of Alevropoulos-Borrill et al. (2020). The similarity in the modelled response of the ASE in Chapter 6 and Alevropoulos-Borrill et al. (2020) shows that the projected uncertainty from the ASE when forced with different CMIP5 AOGCMs matches the uncertainty associated with a different ice sheet model, bed topography and melt rate parameterizations of RCP8.5 forcings. It may be that longer duration simulations are required to see a divergence in the response to forcing associated with differences in model configuration, which supports the findings of Lowry et al. (2021).

Ultimately, the stability of the ice streams in these experiments is debatable. The term stability could have a variety of meanings, be it a stable grounding line position in reference to the MISI hypothesis (Weertman, 1974; Schoof, 2007), or a constant rate of mass loss, or a reduction in the rate of mass loss and retreat in response to the removal of a forcing. In the simulations explored throughout this thesis, melt anomalies are applied and removed over different durations to explore the dynamic response to forcing. In all simulations, the rate of mass loss of ASE ice streams decreases following the removal of the melt anomaly which implies that the ice streams are able to stabilise following

forcing of up to 100 years. Despite this stability, the most extreme mass loss from the region occurs with the BedMachine topography and regularized Coulomb sliding law which results in 125 mm of SLE contribution from PIG and TG over 200 years, 10 % of the total mass of the ASE. While the rate of mass loss is reduced following the removal of forcing, the dynamic annual mass loss of $\sim 0.2 \text{ mm yr}^{-1}$ from wide, fast, TG occurs as a product of the fast initialised velocity of the ice stream. Therefore, while grounding lines can stabilise and the rate of mass loss be lowered upon removal of forcing, the ongoing mass loss from the ASE is high and will be amplified should basal melt rates continue to rise.

7.4 Future Investigations

As is the case with all research, the findings presented in this thesis can be used to inform future research to further improve the understanding of modelled ice stream dynamics in the ASE. Here a number of these areas of further research are briefly introduced and described.

In Chapter 3 a series of idealised melt rate anomalies are applied to model domains of the ASE to explore the regrowth of the region's ice streams in response to negative basal melt anomalies. As is discussed in the Chapter, the application of the negative anomalies, while physically realistic for areas in close proximity to the grounding line that are forced with high positive melt rates in the background melt rate field, areas in close proximity to grounding lines with low initial melt rates are subsequently forced with high magnitudes of refreezing. In warm cavity ice streams, the highest melt rates are found at the grounding line and decrease toward the calving front where the gradient and depth of the ice shelf base decreases, leading to lower melt rates and refreezing (Lazeroms et al., 2018). Therefore, should CDW be blocked from the ASE ice shelf cavities, the distribution of melting in relation to the grounding line proximity may in fact be the reverse, where there are smaller negative anomalies around the grounding line and larger with increasing distance. In order to explore the effects of the spatial application of these idealised melt rates, end member simulations within the ensemble could be repeated with a calving front proximity function as opposed to grounding line proximity. This would provide some indication of the uncertainty in the ice stream response that arises as a result of the distribution of applied melt anomalies.

In Chapter 5, the acceleration of TG between the periods 2007-2009 (Rignot et al., 2011) and 2013-2018 (Mouginot et al., 2017) is attempted to be accounted for through calving of the TG western ice tongue and extreme thinning of the entire ice shelf. This, however, is found to be insufficient to elicit the observed acceleration between these periods due to differences in the bed topography and tuning of ice sheet model parameters. De Rydt et al. (2021) attributed the causes of the observed velocity evolution of PIG from 1996 to 2016 by externally forcing calving and geometry change based on observations. A similar investigation could be performed for TG. Repeating this investigation with the use of both topography products explored in this thesis would also provide further insight of the role of topography in determining the modelled response of the ice stream to forcing.

In Chapter 6, seven parameterizations of melting are applied beneath ASE ice streams. While offline forcing with melt parameterizations are widely performed in ice sheet modelling investigations, there remain large uncertainties associated with the methods employed (Burgard et al., 2022). Two parameterizations of cavity resolving ocean model projections are applied, one method which applies the ocean model melt rate anomalies directly and the second with an additional anomaly concentrated at the grounding line and the differences in cumulative melting as a result are stark. As melt rates evolve as the cavity evolves and grounded ice migrates, the best method of forcing an ice sheet model remains through ice-ocean model coupling (Jordan et al., 2020; Favier et al., 2019). Improving the uncertainty associated with sub-ice shelf melt rate projections by performing coupled ice-ocean model simulations will help to constrain projections of mass loss.

Chapter 8

Conclusions

8.1 Chapter Summaries

8.1.1 Re-growth of the ASE Ice Streams

1. Reducing melt rate values to below present day following a period of retreat encourages the grounding lines of ice streams in the Amundsen Sea Embayment to advance, limiting the sea level contribution from the region.
2. Two-hundred year long simulations forced with 180 years of refreezing over the ASE domain, combined with reduced melting at the grounding lines of PIG and TG, result in a committed sea level contribution of 28 mm.
3. PIG is most sensitive to changes in basal melting of the ice streams in the catchment, largely due to the topographically confined ice shelf and ability of the Southern and Northern ice shelves to thicken and reground.
4. TG is least sensitive to periods of increased basal melting and has the largest committed sea level contribution due to its present day disequilibrium. Reductions in melting do little to offset the overall mass loss from the ice stream despite grounding line advance.

8.1.2 The Sensitivity of PIG to Ice Shelf Melting

1. Simulations with the same magnitude of cumulative ice shelf melt over PIG can have different overall sea level contributions depending on the duration and magnitude of the

forcing.

2. PIG experiences 24 km of grounding line retreat along the main trunk over 200 years, regardless of the differences in basal melt anomalies, although the timing of the retreat is dependent on the duration and magnitude of elevated basal melting.
3. Incorporating a friction law that represents sliding with cavitation at the bed and a retreated ice front results in increased sensitivity to positive basal melting anomalies, though the sliding law has a greater control on the ice stream response by widening the range in SLE contribution in response to forcing.
4. A six year period of ice front retreat when sustained can result in a 9-11 % increase in mass loss from PIG over 200 years, where reduced buttressing increases the sensitivity of the ice stream to melting through accelerated grounding line retreat.

8.1.3 The Role of Bedrock Topography in Influencing Ice Stream Behaviour

1. The BedMachine Antarctica version 1 ice and bed geometry results in a greater extent of mass loss from PIG and TG than a modified Bedmap2 due to an increased sensitivity of the ice streams to melting and grounding line retreat over deeper bed with fewer high amplitude pinning points.
2. TG ice shelf calving and thinning over 10 years is insufficient to cause the acceleration required for the 2007-2009 velocity to increase to match 2013-2017 observations when using a Bedmap2 topography. This occurs due to limited grounding line retreat in Bedmap2 due to high amplitude topographic features and the initial model parameters, resulting in disparity in the modelled response to future melting with the two topographies.
3. There is a bedrock dependence of the ice stream sensitivity to melting when alternative friction laws are implemented in model simulations. Regularized Coulomb sliding doubles the sensitivity to ice shelf melting with Bedmap2 geometry, but only modestly increases sensitivity to melting with BedMachine.

8.1.4 Comparing Future Simulations from High Resolution Ice Sheet Models

1. Over 93 year simulations, the differences in the initialised ISSM and BISICLES domains is responsible for the altered modelled sensitivity to sub-ice shelf melting, which outweighs the effects of differences in stress balance approximations.
2. Accounting for differences in model initialisation in future simulations requires greater consideration than subtraction of the control run due to feedbacks that occur within the ice sheet system that acts to amplify the initial differences.
3. The ISMIP6 standard MeanAnt simulations forced with an RCP8.5 emissions scenario result in a cumulative ice shelf melting equivalent to a control simulation, underestimating the projected evolution of melt rates in the ASE that are projected by cavity resolving ocean models.

8.2 Key Conclusions

According to the simulations presented here, the ASE ice streams can stabilise over the next two centuries but this is dependent on century scale reductions in ice shelf melting occurring with the addition of refreezing over the domain. Furthermore, while grounding lines advance, the rate of mass loss will not become negative for TG due to its wide trunk and large discharge. The ice stream response to both positive and negative forcing varies, with the ice streams with confined ice shelves (PIG and PSK) tending to be more sensitive to melting than TG with an unconfined ice shelf. Stability is introduced through ice shelf thickening and re-grounding on pinning points, resulting in increased lateral and basal drag and subsequent increased buttressing. This response is somewhat dependent on the fixed calving front within the model allowing ice shelves to thicken over their initial extent.

The sensitivity of the ASE ice streams to perturbed ice shelf melting over 100 years is amplified by differences in the representation of geometry in the domain and parameter representation in models. With its confined ice shelf providing stability for the ice stream, PIG is highly sensitive to perturbations in melting due to the changes in the amount to which the ice shelf buttresses upstream flow. PIG's sensitivity to melting, however, is amplified by parameter representation. The results presented in this the-

sis show that a migrated calving front and plastic-type sliding law most influence the behaviour of the ice stream while positive melt anomalies are applied beneath the ice shelf, where the latter has the greatest influence on total mass loss. For both a modified Bedmap2 and BedMachine geometry product, the grounding line position stabilises at a position ~ 30 km upstream from the present day position after 200 modelled years, following the removal of a positive melt rate anomaly, challenging previous claims that the ice stream would recede near entirely over the next 100 years.

The behaviour of TG, the ‘doomsday’ glacier, however, exhibits behaviour more prone to increasing mass loss. With reduced ice shelf melting and refreezing, TG remains out of balance despite grounding line advance highlighting that the current state of disequilibrium is causing a positive commitment to future mass loss which will only be amplified with future positive forcing. With an updated geometry product used for model initialisation, mass loss from TG, in response to a century of increased melting up to 20 m yr^{-1} , doubles. Here, the removal of a positive melt anomaly does little to slow the retreat of the ice stream in the western trunk, with the rate of mass loss remaining at over 0.2 mm yr^{-1} . Although the rate of grounding line retreat slows and temporarily stabilises on topographic features, the long term stability of the ice stream remains unclear.

The results from the ice sheet model comparison here show that ice sheet model initialisation exerts greater control on the projected response to sub-ice shelf melt forcing than the stress balance approximation of the model over century-scale simulations. Model initialisation alters the sensitivity of an ice stream to melting, where positive feedbacks within the ice sheet system act to amplify simulated differences in ice flow representation. Greater efforts to constrain differences in initialised model states will be important for future ice sheet model intercomparisons.

While the uncertainty in future sub-ice shelf melting in the ASE is responsible for much of the uncertainty in future projections of the region’s evolution, this uncertainty is amplified by the numerical representation of ice flow in models. Accounting for representation of basal sliding, calving front position, ice and bed geometry, melt rate parameterization and tuning parameters can amplify the sensitivity to ice-shelf melting and therefore amplify the range in projected future sea level from the region. As these datasets and processes exert substantial control over future projections, continued improvements in observational and modelling efforts will help to provide clarity for the

future of the ASE ice streams.

Bibliography

- Adhikari, S., Ivins, E. R., Larour, E., Seroussi, H., Morlighem, M., and Nowicki, S. (2014). Future Antarctic bed topography and its implications for ice sheet dynamics. *Solid Earth*, 5(1):569–584.
- Adusumilli, S., Fricker, H. A., Medley, B., Padman, L., and Siegfried, M. R. (2020). Interannual variations in meltwater input to the Southern Ocean from Antarctic ice shelves. *Nature geoscience*, 13(9):616–620.
- Agosta, C., Favier, V., Krinner, G., Gallée, H., Fettweis, X., and Genthon, C. (2013). High-resolution modelling of the Antarctic surface mass balance, application for the twentieth, twenty first and twenty second centuries. *Climate Dynamics*, 41(11):3247–3260.
- Alevropoulos-Borrill, A., Nias, I., Payne, A. J., Golledge, N. R., and Bingham, R. J. (2020). Ocean Forced Evolution of the Amundsen Sea catchment, West Antarctica, by 2100. *The Cryosphere*, 14(4):1245–1258.
- Alley, K. E., Scambos, T. A., Alley, R. B., and Holschuh, N. (2019). Troughs developed in ice-stream shear margins precondition ice shelves for ocean-driven breakup. *Science Advances*, 5(10):eaax2215.
- Alley, K. E., Wild, C. T., Luckman, A., Scambos, T. A., Truffer, M., Pettit, E. C., Muto, A., Wallin, B., Klinger, M., Sutterley, T., et al. (2021). Two decades of dynamic change and progressive destabilization on the Thwaites Eastern Ice Shelf. *The Cryosphere Discussions*, pages 1–31.
- Alley, R. B., Anandakrishnan, S., Dupont, T. K., Parizek, B. R., and Pollard, D. (2007). Effect of sedimentation on ice-sheet grounding-line stability. *Science*, 315(5820):1838–1841.
- Anandakrishnan, S., Blankenship, D., Alley, R., and Stoffa, P. (1998). Influence of subglacial geology on the position of a West Antarctic ice stream from seismic observations. *Nature*, 394(6688):62–65.
- Anandakrishnan, S., Catania, G. A., Alley, R. B., and Horgan, H. J. (2007). Discovery of till deposition at the grounding line of Whillans Ice Stream. *Science*, 315(5820):1835–1838.

- Arblaster, J. M. and Meehl, G. A. (2006). Contributions of external forcings to southern annular mode trends. *Journal of Climate*, 19(12):2896–2905.
- Arblaster, J. M., Meehl, G. A., and Karoly, D. J. (2011). Future climate change in the Southern Hemisphere: Competing effects of ozone and greenhouse gases. *Geophysical Research Letters*, 38(2).
- Arndt, J. E., Larter, R. D., Friedl, P., Gohl, K., Höppner, K., et al. (2018). Bathymetric controls on calving processes at Pine Island Glacier. *The Cryosphere*, 12(6):2039–2050.
- Arneborg, L., Wåhlin, A., Björk, G., Liljebladh, B., and Orsi, A. (2012). Persistent inflow of warm water onto the central Amundsen shelf. *Nature Geoscience*, 5(12):876–880.
- Arnold, N. and Sharp, M. (2002). Flow variability in the Scandinavian ice sheet: modelling the coupling between ice sheet flow and hydrology. *Quaternary Science Reviews*, 21(4-6):485–502.
- Arthern, R. J., Winebrenner, D. P., and Vaughan, D. G. (2006). Antarctic snow accumulation mapped using polarization of 4.3-cm wavelength microwave emission. *Journal of Geophysical Research: Atmospheres*, 111(D6).
- Asay-Davis, X. S., Jourdain, N. C., and Nakayama, Y. (2017). Developments in simulating and parameterizing interactions between the Southern Ocean and the Antarctic ice sheet. *Current Climate Change Reports*, 3(4):316–329.
- Assmann, K., Jenkins, A., Shoosmith, D., Walker, D., Jacobs, S., and Nicholls, K. (2013). Variability of Circumpolar Deep Water transport onto the Amundsen Sea Continental shelf through a shelf break trough. *Journal of Geophysical Research: Oceans*, 118(12):6603–6620.
- Bamber, J. L. and Dawson, G. J. (2020). Complex evolving patterns of mass loss from Antarctica’s largest glacier. *Nature Geoscience*, 13(2):127–131.
- Bamber, J. L., Riva, R. E., Vermeersen, B. L., and LeBrocq, A. M. (2009). Reassessment of the potential sea-level rise from a collapse of the West Antarctic Ice Sheet. *Science*, 324(5929):901–903.
- Bamber, J. L., Vaughan, D. G., and Joughin, I. (2000). Widespread complex flow in the interior of the Antarctic ice sheet. *Science*, 287(5456):1248–1250.
- Bamber, J. L., Westaway, R. M., Marzeion, B., and Wouters, B. (2018). The land ice contribution to sea level during the satellite era. *Environmental Research Letters*, 13(6):063008.
- Barletta, V. R., Bevis, M., Smith, B. E., Wilson, T., Brown, A., Bordoni, A., Willis, M., Khan, S. A., Rovira-Navarro, M., Dalziel, I., and others (2018). Observed rapid bedrock uplift in Amundsen Sea Embayment promotes ice-sheet stability. *Science*,

- 360(6395):1335–1339. Publisher: American Association for the Advancement of Science.
- Barnes, J. M., dos Santos, T. D., Goldberg, D., Gudmundsson, G. H., Morlighem, M., and De Rydt, J. (2020). The transferability of adjoint inversion products between different ice flow models. *The Cryosphere Discussions*, pages 1–32.
- Barthel, A., Agosta, C., Little, C. M., Hattermann, T., Jourdain, N. C., Goelzer, H., Nowicki, S., Seroussi, H., Straneo, F., and Bracegirdle, T. J. (2020). CMIP5 model selection for ISMIP6 ice sheet model forcing: Greenland and Antarctica. *The Cryosphere*, 14(3):855–879.
- Bell, R. E., Chu, W., Kingslake, J., Das, I., Tedesco, M., Tinto, K. J., Zappa, C. J., Frezzotti, M., Boghosian, A., and Lee, W. S. (2017). Antarctic ice shelf potentially stabilized by export of meltwater in surface river. *Nature*, 544:344–348.
- Benn, D. and Evans, D. J. (2014). *Glaciers and Glaciation*. Routledge.
- Benn, D. I., Warren, C. R., and Mottram, R. H. (2007). Calving processes and the dynamics of calving glaciers. *Earth-Science Reviews*, 82(3-4):143–179.
- Berdahl, M., Leguy, G., Lipscomb, W. H., and Urban, N. M. (2020). Statistical emulation of a perturbed basal melt ensemble of an ice sheet model to better quantify Antarctic sea level rise uncertainties. *The Cryosphere Discussions*, pages 1–28.
- Bernales, J., Rogozhina, I., and Thomas, M. (2017). Melting and freezing under Antarctic ice shelves from a combination of ice-sheet modelling and observations. *Journal of Glaciology*, 63:731–744.
- Bevan, S. L., Luckman, A. J., Benn, D. I., Adusumilli, S., and Crawford, A. (2021). Brief Communication: Thwaites Glacier cavity evolution. *The Cryosphere Discussions*, pages 1–12.
- Bintanja, R., Van Oldenborgh, G., and Katsman, C. (2015a). The effect of increased fresh water from Antarctic ice shelves on future trends in Antarctic sea ice. *Annals of Glaciology*, 56(69):120–126.
- Bintanja, R., van Oldenborgh, G. J., and Katsman, C. A. (2015b). The effect of increased fresh water from Antarctic ice shelves on future trends in Antarctic sea ice. *Annals of Glaciology*, 56:120–126.
- Blatter, H. (1995). Velocity and stress fields in grounded glaciers: a simple algorithm for including deviatoric stress gradients. *Journal of Glaciology*, 41(138):333–344.
- Blatter, H., Greve, R., and Abe-Ouchi, A. (2010). A short history of the thermomechanical theory and modeling of glaciers and ice sheets. *Journal of Glaciology*, 56(200):1087–1094.

- Bougamont, M., Christoffersen, P., Hubbard, A., Fitzpatrick, A., Doyle, S., and Carter, S. (2014). Sensitive response of the Greenland Ice Sheet to surface melt drainage over a soft bed. *Nature Communications*, 5(1):1–9.
- Box, J., Fettweis, X., Stroeve, J., Tedesco, M., Hall, D., and Steffen, K. (2012). Greenland ice sheet albedo feedback: thermodynamics and atmospheric drivers. *The Cryosphere*, 6(4):821–839.
- Bracegirdle, T. J., Connolley, W. M., and Turner, J. (2008). Antarctic climate change over the twenty first century. *Journal of Geophysical Research: Atmospheres*, 113(D3).
- Bracegirdle, T. J., Shuckburgh, E., Sallée, J.-B., Wang, Z., Meijers, A. J. S., Bruneau, N., Phillips, T., and Wilcox, L. J. (2013). Assessment of surface winds over the Atlantic, Indian, and Pacific Ocean sectors of the Southern Ocean in CMIP5 models: Historical bias, forcing response, and state dependence. *Journal of Geophysical Research*, 118:547–562.
- Brisbourne, A. M., Smith, A. M., Vaughan, D. G., King, E. C., Davies, D., Bingham, R., Smith, E., Nias, I., and Rosier, S. H. (2017). Bed conditions of Pine Island Glacier, West Antarctica. *Journal of Geophysical Research: Earth Surface*, 122(1):419–433.
- Brondex, J., Gagliardini, O., Gillet-Chaulet, F., and Durand, G. (2017). Sensitivity of grounding line dynamics to the choice of the friction law. *Journal of Glaciology*, 63(241):854–866.
- Brondex, J., Gillet-Chaulet, F., and Gagliardini, O. (2019). Sensitivity of centennial mass loss projections of the Amundsen basin to the friction law. *The Cryosphere*, 13(1):177–195.
- Bronselaer, B., Winton, M., Griffies, S. M., Hurlin, W. J., Rodgers, K. B., Sergienko, O. V., Stouffer, R. J., and Russell, J. L. (2018). Change in future climate due to Antarctic meltwater. *Nature*, 564:53–58.
- Budd, W., Keage, P., and Blundy, N. (1979a). Empirical studies of ice sliding. *Journal of glaciology*, 23(89):157–170.
- Budd, W. F., Keage, P. L., and Blundy, N. A. (1979b). Empirical studies of ice sliding. *Journal of Glaciology*, 23:157–170.
- Bueler, E. and Brown, J. (2009). Shallow shelf approximation as a “sliding law” in a thermomechanically coupled ice sheet model. *Journal of Geophysical Research: Earth Surface*, 114(F3).
- Bulthuis, K., Arnst, M., Sun, S., and Pattyn, F. (2019). Uncertainty quantification of the multi-centennial response of the Antarctic ice sheet to climate change. *The Cryosphere*, 13(4):1349–1380.

- Burgard, C., Jourdain, N. C., Reese, R., Jenkins, A., and Mathiot, P. (2022). An assessment of basal melt parameterisations for Antarctic ice shelves. *The Cryosphere Discussions*, pages 1–56.
- Campbell, W. J. and Rasmussen, L. A. (1970). A heuristic numerical model for three-dimensional time-dependent glacier flow. *IASH Publ*, 86:177–190.
- Castleman, B. A., Schlegel, N.-J., Caron, L., Larour, E., and Khazendar, A. (2021). Derivation of bedrock topography measurement requirements for the reduction of uncertainty in ice sheet model projections of Thwaites Glacier. *The Cryosphere Discussions*, pages 1–33.
- Cheng, L., Abraham, J., Hausfather, Z., and Trenberth, K. E. (2019). How fast are the oceans warming? *Science*, 363(6423):128–129. Publisher: American Association for the Advancement of Science.
- Church, J., Clark, P. U., Cazenave, A., Gregory, J. M., Jevrejeva, S., Levermann, A., Merrifield, M. A., Milne, G. A., Nerem, R. S., Nunn, P. D., Payne, A. J., Pfeffer, W. T., Stammer, D., and Unnikrishnan, A. S. (2013). Sea level change. In Stocker, T., Qin, D., Plattner, G.-K., Tignor, M., Allen, S. K., Boschung, J., Nauels, A., Xia, Y., Bex, V., and Midgley, P. M., editors, *Climate Change 2013: The Physical Science Basis. Contribution of Working Group I to the Fifth Assessment Report of the Intergovernmental Panel on Climate Change*, pages 1137–1216. Cambridge University Press, Cambridge, United Kingdom and New York, NY, USA.
- Cornford, S., Martin, D., Payne, A., Ng, E., Le Brocq, A., Gladstone, R., Edwards, T., Shannon, S., Agosta, C., van den Broeke, M., and others (2015). Century-scale simulations of the response of the West Antarctic Ice Sheet to a warming climate. *The Cryosphere*, 9:1579–1600.
- Cornford, S. L., Martin, D. F., Graves, D. T., Ranken, D. F., Le Brocq, A. M., Gladstone, R. M., Payne, A. J., Ng, E. G., and Lipscomb, W. H. (2013). Adaptive mesh, finite volume modeling of marine ice sheets. *Journal of Computational Physics*, 232(1):529–549.
- Cornford, S. L., Seroussi, H., Asay-Davis, X. S., Gudmundsson, G. H., Arthern, R., Borstad, C., Christmann, J., Dias dos Santos, T., Feldmann, J., Goldberg, D., et al. (2020). Results of the third Marine Ice Sheet Model Intercomparison Project (MISMIP+). *The Cryosphere*, 14(7):2283–2301.
- Cuffey, K. M. and Paterson, W. S. B. (2010). *The Physics of Glaciers*. Academic Press.
- Das, I., Padman, L., Bell, R. E., Fricker, H. A., Tinto, K. J., Hulbe, C. L., Siddoway, C. S., Dhakal, T., Frearson, N. P., Mosbeux, C., et al. (2020). Multidecadal basal melt rates and structure of the Ross Ice Shelf, Antarctica, using airborne ice penetrating radar. *Journal of Geophysical Research: Earth Surface*, 125(3):e2019JF005241.

- Davies, D., Bingham, R. G., Graham, A. G., Spagnolo, M., Dutrieux, P., Vaughan, D. G., Jenkins, A., and Nitsche, F. (2017). High-resolution sub-ice-shelf seafloor records of twentieth century ungrounding and retreat of Pine Island Glacier, West Antarctica. *Journal of Geophysical Research: Earth Surface*, 122(9):1698–1714.
- Davis, P. E., Jenkins, A., Nicholls, K. W., Brennan, P. V., Abrahamsen, E. P., Heywood, K. J., Dutrieux, P., Cho, K.-H., and Kim, T.-W. (2018). Variability in basal melting beneath Pine Island Ice Shelf on weekly to monthly timescales. *Journal of Geophysical Research: Oceans*, 123(11):8655–8669.
- De Rydt, J. and Gudmundsson, G. H. (2016). Coupled ice shelf-ocean modeling and complex grounding line retreat from a seabed ridge. *Journal of Geophysical Research: Earth Surface*, 121(5):865–880.
- De Rydt, J., Holland, P. R., Dutrieux, P., and Jenkins, A. (2014). Geometric and oceanographic controls on melting beneath Pine Island Glacier. *Journal of Geophysical Research: Oceans*, 119(4):2420–2438.
- De Rydt, J., Reese, R., Paolo, F. S., and Gudmundsson, G. H. (2021). Drivers of Pine Island Glacier speed-up between 1996 and 2016. *The Cryosphere*, 15(1):113–132.
- Deb, P., Orr, A., Bromwich, D. H., Nicolas, J. P., Turner, J., and Hosking, J. S. (2018). Summer drivers of atmospheric variability affecting ice shelf thinning in the Amundsen Sea Embayment, West Antarctica. *Geophysical Research Letters*, 45(9):4124–4133.
- Depoorter, M. A., Bamber, J. L., Griggs, J. A., Lenaerts, J. T. M., Ligtenberg, S. R. M., Broeke, M. R. v. d., and Moholdt, G. (2013). Calving fluxes and basal melt rates of Antarctic ice shelves. *Nature*, 502:89–92.
- Dinniman, M. S., Asay-Davis, X. S., Galton-Fenzi, B. K., Holland, P. R., Jenkins, A., and Timmermann, R. (2016). Modeling ice shelf/ocean interaction in Antarctica: A review. *Oceanography*, 29(4):144–153.
- Dinniman, M. S., Klinck, J. M., Bai, L.-S., Bromwich, D. H., Hines, K. M., and Holland, D. M. (2015). The effect of atmospheric forcing resolution on delivery of ocean heat to the Antarctic floating ice shelves. *Journal of Climate*, 28(15):6067–6085.
- Donat-Magnin, M., Jourdain, N. C., Gallée, H., Amory, C., Kittel, C., Fettweis, X., Wille, J. D., Favier, V., Drira, A., and Agosta, C. (2020). Interannual variability of summer surface mass balance and surface melting in the Amundsen sector, West Antarctica. *The Cryosphere*, 14(1):229–249.
- Donat-Magnin, M., Jourdain, N. C., Kittel, C., Agosta, C., Amory, C., Gallée, H., Krinner, G., and Chekki, M. (2021). Future surface mass balance and surface melt in the Amundsen sector of the West Antarctic Ice Sheet. *Cryosphere*, 15:571–593.

- Donat-Magnin, M., Jourdain, N. C., Spence, P., Le Sommer, J., Gallée, H., and Durand, G. (2017). Ice-Shelf Melt Response to Changing Winds and Glacier Dynamics in the Amundsen Sea Sector, Antarctica. *Journal of Geophysical Research: Oceans*, 122(12):10206–10224.
- Dotto, T. S., Naveira Garabato, A. C., Wåhlin, A. K., Bacon, S., Holland, P. R., Kimura, S., Tsamados, M., Herraiz-Borreguero, L., Kalén, O., and Jenkins, A. (2020). Control of the oceanic heat content of the Getz-Dotson Trough, Antarctica, by the Amundsen Sea Low. *Journal of Geophysical Research: Oceans*, 125(8):e2020JC016113.
- Dupont, T. and Alley, R. (2005). Assessment of the importance of ice-shelf buttressing to ice-sheet flow. *Geophysical Research Letters*, 32(4).
- Durand, G., Gagliardini, O., Zwinger, T., Le Meur, E., and Hindmarsh, R. C. (2009). Full Stokes modeling of marine ice sheets: influence of the grid size. *Annals of Glaciology*, 50(52):109–114.
- Dutrieux, P., De Rydt, J., Jenkins, A., Holland, P. R., Ha, H. K., Lee, S. H., Steig, E. J., Ding, Q., Abrahamsen, E. P., and Schröder, M. (2014a). Strong sensitivity of Pine Island ice-shelf melting to climatic variability. *Science*, 343(6167):174–178.
- Dutrieux, P., De Rydt, J., Jenkins, A., Holland, P. R., Ha, H. K., Lee, S. H., Steig, E. J., Ding, Q., Abrahamsen, E. P., and Schröder, M. (2014b). Strong sensitivity of Pine Island ice-shelf melting to climatic variability. *Science*, 343(6167):174–178.
- Dutrieux, P., Vaughan, D. G., Corr, H. F. J., Jenkins, A., Holland, P. R., Joughin, I., and Fleming, A. (2013). Pine Island glacier ice shelf melt distributed at kilometre scales. *The Cryosphere*, 7:1543–1555.
- Dutton, A., Carlson, A., Long, A., Milne, G., Clark, P., DeConto, R., Horton, B., Rahmstorf, S., and Raymo, M. (2015). Sea-level rise due to polar ice-sheet mass loss during past warm periods. *Science*, 349:aaa4019.
- Edwards, T. L., Brandon, M., Durand, G., Edwards, N. R., Golledge, N. R., Holden, P. B., Nias, I., Payne, A., Ritz, C., and Wernecke, A. (2019). Revisiting Antarctic ice loss due to marine ice cliff instability. *Nature*, 566:58–64.
- Edwards, T. L., Nowicki, S., Marzeion, B., Hock, R., Goelzer, H., Seroussi, H., Jourdain, N. C., Slater, D. A., Turner, F. E., Smith, C. J., et al. (2021). Projected land ice contributions to twenty-first-century sea level rise. *Nature*, 593(7857):74–82.
- Eyring, V., Bony, S., Meehl, G. A., Senior, C. A., Stevens, B., Stouffer, R. J., and Taylor, K. E. (2016). Overview of the Coupled Model Intercomparison Project Phase 6 (CMIP6) experimental design and organization. *Geoscientific Model Development*, 9(5):1937–1958.
- Favier, L., Durand, G., Cornford, S., Gudmundsson, G., Gagliardini, O., Gillet-Chaulet, F., Zwinger, T., Payne, A., and Le Brocq, A. (2014). Retreat of Pine Island Glacier controlled by marine ice-sheet instability. *Nature Climate Change*, 4:117–121.

- Favier, L., Jourdain, N. C., Jenkins, A., Merino, N., Durand, G., Gagliardini, O., Gillet-Chaulet, F., and Mathiot, P. (2019). Assessment of sub-shelf melting parameterisations using the ocean–ice-sheet coupled model NEMO (v3. 6)–Elmer/Ice (v8. 3). *Geoscientific Model Development*, 12(6):2255–2283.
- Feldmann, J., Albrecht, T., Khroulev, C., Pattyn, F., and Levermann, A. (2014). Resolution-dependent performance of grounding line motion in a shallow model compared to a full-Stokes model according to the MISMIP3d intercomparison. *J. Glaciol.*, 60:353–360.
- Feldmann, J. and Levermann, A. (2015). Collapse of the West Antarctic Ice Sheet after local destabilization of the Amundsen Basin. *Proceedings of the National Academy of Sciences*, 112(46):14191–14196. Publisher: National Academy of Sciences.
- Fretwell, P., Pritchard, H. D., Vaughan, D. G., Bamber, J. L., Barrand, N. E., Bell, R., Bianchi, C., Bingham, R. G., Blankenship, D. D., Casassa, G., and others (2013). Bedmap2: improved ice bed, surface and thickness datasets for Antarctica. *The Cryosphere*, 7(1):375–393.
- Fricker, H. A. and Scambos, T. (2009). Connected subglacial lake activity on lower Mercer and Whillans ice streams, West Antarctica, 2003–2008. *Journal of Glaciology*, 55(190):303–315.
- Fricker, H. A., Scambos, T., Bindschadler, R., and Padman, L. (2007). An active subglacial water system in West Antarctica mapped from space. *Science*, 315(5818):1544–1548.
- Fürst, J. J., Durand, G., Gillet-Chaulet, F., Tavard, L., Rankl, M., Braun, M., and Gagliardini, O. (2016). The safety band of Antarctic ice shelves. *Nature Climate Change*, 6(5):479–482.
- Fürst, J. J., Goelzer, H., and Huybrechts, P. (2015). Ice-dynamic projections of the Greenland ice sheet in response to atmospheric and oceanic warming. *The Cryosphere*, 9(3):1039–1062.
- Gardner, A. S., Moholdt, G., Scambos, T., Fahnestock, M., Ligtenberg, S., van den Broeke, M., and Nilsson, J. (2018). Increased West Antarctic and unchanged East Antarctic ice discharge over the last 7 years. *The Cryosphere*, 12(2):521–547.
- Gillet-Chaulet, F., Durand, G., Gagliardini, O., Mosbeux, C., Mouginot, J., Rémy, F., and Ritz, C. (2016). Assimilation of surface velocities acquired between 1996 and 2010 to constrain the form of the basal friction law under Pine Island Glacier. *Geophysical Research Letters*, 43(19):10–311.
- Gillett, N. P., Fyfe, J. C., and Parker, D. E. (2013). Attribution of observed sea level pressure trends to greenhouse gas, aerosol, and ozone changes. *Geophysical Research Letters*, 40(10):2302–2306.

- Gladstone, R. M., Lee, V., Rougier, J., Payne, A. J., Hellmer, H., LeBrocq, A., Shepherd, A., L. Edwards, T., Gregory, J., and L. Cornford, S. (2012). Calibrated prediction of Pine Island Glacier retreat during the 21st and 22nd centuries with a coupled flow-line model. *Earth and Planetary Science Letters*, 333-334:191–199.
- Glen, J. (1952). Experiments on the deformation of ice. *Journal of Glaciology*, 2(12):111–114.
- Glen, J. W. (1955). The creep of polycrystalline ice. *Proceedings of the Royal Society of London. Series A. Mathematical and Physical Sciences*, 228(1175):519–538.
- Goelzer, H., Nowicki, S., Edwards, T., Beckley, M., Abe-Ouchi, A., Aschwanden, A., Calov, R., Gagliardini, O., Gillet-Chaulet, F., Golledge, N. R., and others (2018). Design and results of the ice sheet model initialisation initMIP-Greenland: an IS-MIP6 intercomparison. *The Cryosphere*, 12(4):1433–1460. Publisher: European Geosciences Union.
- Goldberg, D., Gourmelen, N., Kimura, S., Millan, R., and Snow, K. (2019). How accurately should we model ice shelf melt rates? *Geophysical Research Letters*, 46(1):189–199.
- Goldberg, D., Heimbach, P., Joughin, I., and Smith, B. (2015). Committed retreat of Smith, Pope, and Kohler Glaciers over the next 30 years inferred by transient model calibration. *The Cryosphere*, 9(6):2429–2446.
- Goldberg, D., Snow, K., Holland, P., Jordan, J., Campin, J.-M., Heimbach, P., Arthern, R., and Jenkins, A. (2018). Representing grounding line migration in synchronous coupling between a marine ice sheet model and a z-coordinate ocean model. *Ocean Modelling*, 125:45–60.
- Golledge, N. R., Keller, E. D., Gomez, N., Naughten, K. A., Bernales, J., Trusel, L. D., and Edwards, T. L. (2019). Global environmental consequences of twenty-first-century ice-sheet melt. *Nature*, 566:65–72.
- Golledge, N. R., Kowalewski, D., Naish, T., Levy, R., Fogwill, C., and Gasson, E. (2015). The multi-millennial Antarctic commitment to future sea-level rise. *Nature*, 526:421–425.
- Gomez, N., Pollard, D., and Holland, D. (2015). Sea-level feedback lowers projections of future Antarctic Ice-Sheet mass loss. *Nature Communications*, 6:8798. Publisher: Nature Publishing Group.
- Gong, Y., Zwinger, T., Cornford, S., Gladstone, R., Schäfer, M., and Moore, J. C. (2017). Importance of basal boundary conditions in transient simulations: case study of a surging marine-terminating glacier on Austfonna, Svalbard. *Journal of Glaciology*, 63(237):106–117.

- Gourmelen, N., Goldberg, D. N., Snow, K., Henley, S. F., Bingham, R. G., Kimura, S., Hogg, A. E., Shepherd, A., Mouginot, J., Lenaerts, J. T., et al. (2017). Channelized melting drives thinning under a rapidly melting Antarctic ice shelf. *Geophysical Research Letters*, 44(19):9796–9804.
- Goyal, R., Jucker, M., Sen Gupta, A., and England, M. H. (2021). Generation of the Amundsen Sea low by Antarctic orography. *Geophysical Research Letters*, 48(4):e2020GL091487.
- Greene, C. A., Gwyther, D. E., and Blankenship, D. D. (2017). Antarctic mapping tools for MATLAB. *Computers & Geosciences*, 104:151–157.
- Greve, R. and Blatter, H. (2009). *Dynamics of Ice Sheets and Glaciers*. Springer Science & Business Media.
- Greve, R. and Blatter, H. (2016). Comparison of thermodynamics solvers in the polythermal ice sheet model SICOPOLIS. *Polar Science*, 10(1):11–23.
- Gudmundsson, G. H. (1999). A three-dimensional numerical model of the confluence area of Unteraargletscher, Bernese Alps, Switzerland. *Journal of Glaciology*, 45(150):219–230.
- Gudmundsson, G. H. (2013). Ice-shelf buttressing and the stability of marine ice sheets. *The Cryosphere*, 7:647–655.
- Gudmundsson, G. H., Paolo, F. S., Adusumilli, S., and Fricker, H. A. (2019). Instantaneous Antarctic ice sheet mass loss driven by thinning ice shelves. *Geophysical Research Letters*, 46(23):13903–13909.
- Gürses, O., Kolatschek, V., Wang, Q., and Rodehacke, C. B. (2019). Brief communication: A submarine wall protecting the Amundsen Sea intensifies melting of neighboring ice shelves. *The Cryosphere*, 13(9):2317–2324.
- Hansen, P. C. (1992). Analysis of discrete ill-posed problems by means of the L-curve. *SIAM review*, 34(4):561–580.
- Haseloff, M. and Sergienko, O. V. (2018). The effect of buttressing on grounding line dynamics. *Journal of Glaciology*, 64(245):417–431.
- Hecht, F. (1998). BAMG: bidimensional anisotropic mesh generator. *User Guide. INRIA, Rocquencourt*, 17.
- Hellmer, H., Kauker, F., Timmermann, R., Determann, J., and Rae, J. (2012). Twenty-first-century warming of a large Antarctic ice-shelf cavity by a redirected coastal current. *Nature*, 485:225–228.
- Hellmer, H. H. and Olbers, D. J. (1989). A two-dimensional model for the thermohaline circulation under an ice shelf. *Antarctic Science*, 1:325–336.

- Herterich, K. (1988). A three-dimensional model of the Antarctic ice sheet. *Annals of Glaciology*, 11:32–35.
- Hindmarsh, R. (2004). A numerical comparison of approximations to the Stokes equations used in ice sheet and glacier modeling. *Journal of Geophysical Research: Earth Surface*, 109(F1).
- Hindmarsh, R. C. (1993). Qualitative dynamics of marine ice sheets. In *Ice in the climate system*, pages 67–99. Springer.
- Hindmarsh, R. C. (2006). Stress gradient damping of thermoviscous ice flow instabilities. *Journal of Geophysical Research: Solid Earth*, 111(B12).
- Hirano, D., Tamura, T., Kusahara, K., Ohshima, K. I., Nicholls, K. W., Ushio, S., Simizu, D., Ono, K., Fujii, M., Nogi, Y., et al. (2020). Strong ice-ocean interaction beneath Shirase Glacier Tongue in East Antarctica. *Nature Communications*, 11(1):1–12.
- Holland, D. M., Nicholls, K. W., and Basinski, A. (2020). The southern ocean and its interaction with the Antarctic ice sheet. *Science*, 367(6484):1326–1330.
- Holland, P. R., Bracegirdle, T. J., Dutrieux, P., Jenkins, A., and Steig, E. J. (2019). West Antarctic ice loss influenced by internal climate variability and anthropogenic forcing. *Nature Geoscience*, 12(9):718–724.
- Holland, P. R., Corr, H. F., Vaughan, D. G., Jenkins, A., and Skvarca, P. (2009). Marine ice in Larsen ice shelf. *Geophysical Research Letters*, 36(11).
- Holland, P. R., Jenkins, A., and Holland, D. M. (2008). The response of ice shelf basal melting to variations in ocean temperature. *Journal of Climate*, 21(11):2558–2572.
- Holland, P. R., Jenkins, A., and Holland, D. M. (2010). Ice and ocean processes in the Bellingshausen Sea, Antarctica. *Journal of Geophysical Research: Oceans*, 115(C5).
- Hosking, J. S., Orr, A., Bracegirdle, T. J., and Turner, J. (2016). Future circulation changes off West Antarctica: Sensitivity of the Amundsen Sea Low to projected anthropogenic forcing. *Geophysical Research Letters*, 43(1):367–376.
- Howat, I. M., Porter, C., Smith, B. E., Noh, M.-J., and Morin, P. (2019). The reference elevation model of Antarctica. *The Cryosphere*, 13(2):665–674.
- Hughes, T. J. (1981). The weak underbelly of the West Antarctic ice sheet. *Journal of Glaciology*, 27(97):518–525.
- Hutter, K. (2017). *Theoretical glaciology: material science of ice and the mechanics of glaciers and ice sheets*, volume 1. Springer.
- Huybrechts, P. (1990). A 3-D model for the Antarctic ice sheet: a sensitivity study on the glacial-interglacial contrast. *Climate Dynamics*, 5(2):79–92.

- Huybrechts, P. and Oerlemans, J. (1988). Evolution of the East Antarctic Ice Sheet: a numerical study of thermo-mechanical response patterns with changing climate. *Annals of Glaciology*, 11:52–59.
- Huybrechts, P., Payne, T., et al. (1996). The EISMINT benchmarks for testing ice-sheet models. *Annals of Glaciology*, 23:1–12.
- IMBIE (2018). Mass balance of the Antarctic Ice Sheet from 1992 to 2017. *Nature*, 558:219–222.
- Iverson, N. R. and Zoet, L. K. (2015). Experiments on the dynamics and sedimentary products of glacier slip. *Geomorphology*, 244:121–134.
- Jacobs, S., Jenkins, A., Hellmee, H., Giulivi, C., Nitsche, F., Huber, B., and Guerro, R. (2012). The Amundsen Sea and the Antarctic Ice Sheet. *Oceanography*, 25(3):154–163.
- Jacobs, S. S., Hellmer, H. H., and Jenkins, A. (1996). Antarctic ice sheet melting in the Southeast Pacific. *Geophysical Research Letters*, 23(9):957–960.
- Jacobs, S. S., Jenkins, A., Giulivi, C. F., and Dutrieux, P. (2011). Stronger ocean circulation and increased melting under Pine Island Glacier ice shelf. *Nature Geoscience*, 4(8):519–523.
- Jenkins, A., Dutrieux, P., Jacobs, S., Steig, E. J., Gudmundsson, G. H., Smith, J., and Heywood, K. J. (2016). Decadal ocean forcing and Antarctic ice sheet response: Lessons from the Amundsen Sea. *Oceanography*, 29(4):106–117.
- Jenkins, A., Shoosmith, D., Dutrieux, P., Jacobs, S., Kim, T. W., Lee, S. H., Ha, H. K., and Stammerjohn, S. (2018). West Antarctic Ice Sheet retreat in the Amundsen Sea driven by decadal oceanic variability. *Nature Geoscience*, 11(10):733–738.
- Jenssen, D. (1977). A three-dimensional polar ice-sheet model. *Journal of Glaciology*, 18(80):373–389.
- Jordan, J. R., Holland, P. R., Goldberg, D., Snow, K., Arthern, R., Campin, J.-M., Heimbach, P., and Jenkins, A. (2018). Ocean-forced ice-shelf thinning in a synchronously coupled ice-ocean model. *Journal of Geophysical Research: Oceans*, 123(2):864–882.
- Jordan, T. A., Porter, D., Tinto, K., Millan, R., Muto, A., Hogan, K., Larter, R. D., Graham, A. G., and Paden, J. D. (2020). New gravity-derived bathymetry for the Thwaites, Crosson, and Dotson ice shelves revealing two ice shelf populations. *The Cryosphere*, 14(9):2869–2882.
- Joughin, I. and Alley, R. B. (2011). Stability of the West Antarctic ice sheet in a warming world. *Nature Geoscience*, 4(8):506–513.
- Joughin, I., Shapero, D., Smith, B., Dutrieux, P., and Barham, M. (2021). Ice-shelf retreat drives recent Pine Island Glacier speedup. *Science Advances*, 7(24):eabg3080.

- Joughin, I., Smith, B. E., and Holland, D. M. (2010). Sensitivity of 21st century sea level to ocean-induced thinning of Pine Island Glacier, Antarctica. *Geophysical Research Letters*, 37(20).
- Joughin, I., Smith, B. E., and Medley, B. (2014). Marine Ice Sheet Collapse Potentially Under Way for the Thwaites Glacier Basin, West Antarctica. *Science*, 344:735–738.
- Joughin, I., Smith, B. E., and Schoof, C. G. (2019). Regularized Coulomb friction laws for ice sheet sliding: application to Pine Island Glacier, Antarctica. *Geophysical Research Letters*, 46(9):4764–4771.
- Jourdain, N. C., Asay-Davis, X., Hattermann, T., Straneo, F., Seroussi, H., Little, C. M., and Nowicki, S. (2020). A protocol for calculating basal melt rates in the ISMIP6 Antarctic ice sheet projections. *The Cryosphere*, 14(9):3111–3134.
- Jourdain, N. C., Mathiot, P., Merino, N., Durand, G., Le Sommer, J., Spence, P., Dutrieux, P., and Madec, G. (2017). Ocean circulation and sea-ice thinning induced by melting ice shelves in the Amundsen Sea. *Journal of Geophysical Research: Oceans*, 122(3):2550–2573.
- Khazendar, A., Rignot, E., Schroeder, D. M., Seroussi, H., Schodlok, M. P., Scheuchl, B., Mouginot, J., Sutterley, T. C., and Velicogna, I. (2016). Rapid submarine ice melting in the grounding zones of ice shelves in West Antarctica. *Nature Communications*, 7(1):1–8.
- Kim, T.-W., Ha, H. K., Wåhlin, A., Lee, S., Kim, C.-S., Lee, J. H., and Cho, Y.-K. (2017). Is Ekman pumping responsible for the seasonal variation of warm circumpolar deep water in the Amundsen Sea? *Continental Shelf Research*, 132:38–48.
- Klages, J. P., Kuhn, G., Graham, A. G., Hillenbrand, C.-D., Smith, J., Nitsche, F. O., Larter, R. D., and Gohl, K. (2015). Palaeo-ice stream pathways and retreat style in the easternmost Amundsen Sea Embayment, West Antarctica, revealed by combined multibeam bathymetric and seismic data. *Geomorphology*, 245:207–222.
- Konrad, H., Shepherd, A., Gilbert, L., Hogg, A., McMillan, M., Muir, A., and Slater, T. (2018). Net retreat of Antarctic glacier grounding lines. *Nature Geosciences*, 11:258–262.
- Kyrke-Smith, T. M., Gudmundsson, G. H., and Farrell, P. E. (2018). Relevance of detail in basal topography for basal slipperiness inversions: a case study on Pine Island Glacier, Antarctica. *Frontiers in Earth Science*, 6:33.
- Larour, E., Seroussi, H., Morlighem, M., and Rignot, E. (2012). Continental scale, high order, high spatial resolution, ice sheet modeling using the Ice Sheet System Model (ISSM). *Journal of Geophysical Research*, 117:F01022.
- Larour, E., Utke, J., Csatho, B., Schenk, A., Seroussi, H., Morlighem, M., Rignot, E., Schlegel, N., and Khazendar, A. (2014). Inferred basal friction and surface mass balance of the Northeast Greenland Ice Stream using data assimilation of ICESat (Ice

- Cloud and land Elevation Satellite) surface altimetry and ISSM (Ice Sheet System Model). *The Cryosphere*, 8(6):2335–2351.
- Lazeroms, W. M., Jenkins, A., Gudmundsson, G. H., and Van De Wal, R. S. (2018). Modelling present-day basal melt rates for Antarctic ice shelves using a parametrization of buoyant meltwater plumes. *The Cryosphere*, 12(1):49–70.
- Le Brocq, A. M., Payne, A., Siegert, M., and Alley, R. (2009). A subglacial water-flow model for West Antarctica. *Journal of Glaciology*, 55(193):879–888.
- Lenaerts, J., Vizcaino, M., Fyke, J., Van Kampenhout, L., and van den Broeke, M. R. (2016). Present-day and future Antarctic ice sheet climate and surface mass balance in the Community Earth System Model. *Climate Dynamics*, 47(5):1367–1381.
- Leong, W. J. and Horgan, H. J. (2020). DeepBedMap: a deep neural network for resolving the bed topography of Antarctica. *The Cryosphere*, 14(11):3687–3705.
- Leuliette, E. W. and Nerem, R. S. (2016). Contributions of Greenland and Antarctica to global and regional sea level change. *Oceanography*, 29(4):154–159.
- Levermann, A., Winkelmann, R., Albrecht, T., Goelzer, H., Golledge, N. R., Greve, R., Huybrechts, P., Jordan, J., Leguy, G., Martin, D., Morlighem, M., Pattyn, F., Pollard, D., Quiquet, A., Rodehacke, C., Seroussi, H., Sutter, J., Zhang, T., Van Breedam, J., DeConto, R., Dumas, C., Garbe, J., Gudmundsson, G. H., Hoffman, M. J., Humbert, A., Kleiner, T., Lipscomb, W., Meinshausen, M., Ng, E., Perego, M., Price, S. F., Saito, F., Schlegel, N.-J., Sun, S., and van de Wal, R. S. W. (2019). Projecting Antarctica’s contribution to future sea level rise from basal ice-shelf melt using linear response functions of 16 ice sheet models (LARMIP-2). *Earth System Dynamics Discussions*, 2019:1–63.
- Lhermitte, S., Sun, S., Shuman, C., Wouters, B., Pattyn, F., Wuite, J., Berthier, E., and Nagler, T. (2020). Damage accelerates ice shelf instability and mass loss in Amundsen Sea Embayment. *Proceedings of the National Academy of Sciences*, 117(40):24735–24741.
- Lilien, D. A., Joughin, I., Smith, B., and Gourmelen, N. (2019). Melt at grounding line controls observed and future retreat of Smith, Pope, and Kohler glaciers. *The Cryosphere*, 13(11):2817–2834.
- Liu, Y., Moore, J. C., Cheng, X., Gladstone, R. M., Bassis, J. N., Liu, H., Wen, J., and Hui, F. (2015). Ocean-driven thinning enhances iceberg calving and retreat of Antarctic ice shelves. *Proceedings of the National Academy of Sciences*, 112:3263–3268.
- Lowry, D. P., Golledge, N. R., Bertler, N. A., Jones, R. S., and McKay, R. (2019). Deglacial grounding-line retreat in the Ross Embayment, Antarctica, controlled by ocean and atmosphere forcing. *Science Advances*, 5(8):eaav8754.

- Lowry, D. P., Krapp, M., Golledge, N. R., and Alevropoulos-Borrill, A. (2021). The influence of emissions scenarios on future Antarctic ice loss is unlikely to emerge this century. *Communications Earth & Environment*, 2(1):1–14.
- Lythe, M. B. and Vaughan, D. G. (2001). BEDMAP: A new ice thickness and subglacial topographic model of Antarctica. *Journal of Geophysical Research: Solid Earth*, 106(B6):11335–11351.
- MacAyeal, D. R. (1989). Large-scale ice flow over a viscous basal sediment: Theory and application to ice stream B, Antarctica. *Journal of Geophysical Research: Solid Earth*, 94(B4):4071–4087.
- MacAyeal, D. R. (1992). The basal stress distribution of Ice Stream E, Antarctica, inferred by control methods. *Journal of Geophysical Research: Solid Earth*, 97(B1):595–603.
- MacGregor, J. A., Catania, G. A., Markowski, M. S., and Andrews, A. G. (2012). Widespread rifting and retreat of ice-shelf margins in the eastern Amundsen Sea Embayment between 1972 and 2011. *Journal of Glaciology*, 58(209):458–466.
- Mackie, S., Smith, I. J., Ridley, J. K., Stevens, D. P., and Langhorne, P. J. (2020). Climate response to increasing Antarctic iceberg and ice shelf melt. *Journal of Climate*, 33(20):8917–8938.
- Mahaffy, M. (1976). A three-dimensional numerical model of ice sheets: Tests on the Barnes Ice Cap, Northwest Territories. *Journal of Geophysical Research*, 81(6):1059–1066.
- Mallett, H. K., Boehme, L., Fedak, M., Heywood, K. J., Stevens, D. P., and Roquet, F. (2018). Variation in the distribution and properties of Circumpolar Deep Water in the eastern Amundsen Sea, on seasonal timescales, using seal-borne tags. *Geophysical Research Letters*, 45(10):4982–4990.
- Malyarenko, A., Wells, A. J., Langhorne, P. J., Robinson, N. J., Williams, M. J., and Nicholls, K. W. (2020). A synthesis of thermodynamic ablation at ice-ocean interfaces from theory, observations and models. *Ocean Modelling*, page 101692.
- Malyarenko, E. (2020). *Ice shelf - ocean boundary interaction*. PhD thesis, University of Otago.
- Martin, D. F., Cornford, S. L., and Payne, A. J. (2019). Millennial-scale Vulnerability of the Antarctic Ice Sheet to Regional Ice Shelf Collapse. *Geophysical Research Letters*, 46:1467–1475.
- Martin, M., Winkelmann, R., Haseloff, M., Albrecht, T., Bueler, E., Khroulev, C., and Levermann, A. (2011). The potsdam parallel ice sheet model (PISM-PIK)–Part 2: dynamic equilibrium simulation of the antarctic ice sheet. *The Cryosphere*, 5(3):727–740.

- Massom, R. A., Scambos, T. A., Bennetts, L. G., Reid, P., Squire, V. A., and Stammerjohn, S. E. (2018). Antarctic ice shelf disintegration triggered by sea ice loss and ocean swell. *Nature*, 558:383–389. Publisher: Nature Publishing Group.
- McCormack, F., Warner, R., Seroussi, H., Dow, C., Roberts, J., and Treverrow, A. (2022). Modeling the Deformation Regime of Thwaites Glacier, West Antarctica, Using a Simple Flow Relation for Ice Anisotropy (ESTAR). *Journal of Geophysical Research: Earth Surface*, 127(3):e2021JF006332.
- McGrath, D., Steffen, K., Rajaram, H., Scambos, T., Abdalati, W., and Rignot, E. (2012). Basal crevasses on the Larsen C Ice Shelf, Antarctica: Implications for melt-water ponding and hydrofracture. *Geophysical Research Letters*, 39(16).
- McMichael, C., Dasgupta, S., Ayeb-Karlsson, S., and Kelman, I. (2020). A review of estimating population exposure to sea-level rise and the relevance for migration. *Environmental Research Letters*, 15(12):123005.
- McMillan, M., Shepherd, A., Sundal, A., Briggs, K., Muir, A., Ridout, A., Hogg, A., and Wingham, D. (2014). Increased ice losses from Antarctica detected by CryoSat-2. *Geophysical Research Letters*, 41(11):3899–3905.
- Medley, B., Joughin, I. R., Smith, B., Das, S. B., Steig, E. J., Conway, H., Gogineni, S., Lewis, C. S., Criscitiello, A. S., McConnell, J. R., et al. (2014). Constraining the recent mass balance of Pine Island and Thwaites glaciers, West Antarctica, with airborne observations of snow accumulation. *The Cryosphere*, 8:1375—1392.
- Medley, B., McConnell, J. R., Neumann, T. A., Reijmer, C. H., Chellman, N., Sigl, M., and Kipfstuhl, S. (2018). Temperature and snowfall in western Queen Maud Land increasing faster than climate model projections. *Geophysical Research Letters*, 45:1472–1480.
- Medley, B. and Thomas, E. (2019). Increased snowfall over the Antarctic Ice Sheet mitigated twentieth-century sea-level rise. *Nature Climate Change*, 9(1):34–39.
- Mercer, J. H. (1978). West Antarctic ice sheet and CO₂ greenhouse effect: a threat of disaster. *Nature*, 271(5643):321–325.
- Miles, B., Stokes, C., Jenkins, A., Jordan, J., Jamieson, S., and Gudmundsson, G. (2020). Intermittent structural weakening and acceleration of the Thwaites Glacier Tongue between 2000 and 2018. *Journal of Glaciology*, 66(257):485–495.
- Milillo, P., Rignot, E., Rizzoli, P., Scheuchl, B., Mouginot, J., Bueso-Bello, J., and Prats-Iraola, P. (2019). Heterogeneous retreat and ice melt of Thwaites Glacier, West Antarctica. *Science Advances*, 5(1):eaau3433.
- Millan, R., Rignot, E., Bernier, V., Morlighem, M., and Dutrieux, P. (2017). Bathymetry of the Amundsen Sea Embayment sector of West Antarctica from Operation Ice-Bridge gravity and other data. *Geophysical Research Letters*, 44(3):1360–1368.

- Millstein, J. D., Minchew, B. M., and Pegler, S. S. (2022). Ice viscosity is more sensitive to stress than commonly assumed. *Communications Earth & Environment*, 3(1):1–7.
- Moore, J. C., Gladstone, R., Zwinger, T., and Wolovick, M. (2018). Geoengineer polar glaciers to slow sea-level rise. *Nature*, 555:303–305.
- Moore, J. C., Jevrejeva, S., and Grinsted, A. (2010). Efficacy of geoengineering to limit 21st century sea-level rise. *Proceedings of the National Academy of Sciences*, 107(36):15699–15703.
- Morland, L. (1987). Unconfined ice-shelf flow. In *Dynamics of the West Antarctic Ice Sheet*, pages 99–116. Springer.
- Morlighem, M., Rignot, E., Binder, T., Blankenship, D., Drews, R., Eagles, G., Eisen, O., Ferraccioli, F., Forsberg, R., Fretwell, P., et al. (2020). Deep glacial troughs and stabilizing ridges unveiled beneath the margins of the Antarctic ice sheet. *Nature Geoscience*, 13(2):132–137.
- Morlighem, M., Rignot, E., Seroussi, H., Larour, E., Ben Dhia, H., and Aubry, D. (2010). Spatial patterns of basal drag inferred using control methods from a full-Stokes and simpler models for Pine Island Glacier, West Antarctica. *Geophysical Research Letters*, 37(14).
- Morlighem, M., Rignot, E., Seroussi, H., Larour, E., Ben Dhia, H., and Aubry, D. (2011). A mass conservation approach for mapping glacier ice thickness. *Geophysical Research Letters*, 38(19).
- Morlighem, M., Williams, C. N., Rignot, E., An, L., Arndt, J. E., Bamber, J. L., Catania, G., Chauché, N., Dowdeswell, J. A., Dorschel, B., and others (2017). BedMachine v3: Complete bed topography and ocean bathymetry mapping of Greenland from multibeam echo sounding combined with mass conservation. *Geophysical Research Letters*, 44(21).
- Mouginot, J., Rignot, E., and Scheuchl, B. (2014). Sustained increase in ice discharge from the Amundsen Sea Embayment, West Antarctica, from 1973 to 2013. *Geophysical Research Letters*, 41(5):1576–1584.
- Mouginot, J., Rignot, E., and Scheuchl, B. (2019). Continent-wide, interferometric SAR phase, mapping of Antarctic ice velocity. *Geophysical Research Letters*, 46(16):9710–9718.
- Mouginot, J., Rignot, E., Scheuchl, B., and Millan, R. (2017). Comprehensive annual ice sheet velocity mapping using Landsat-8, Sentinel-1, and RADARSAT-2 data. *Remote Sensing*, 9(4):364.
- Mouginot, J., Scheuchl, B., and Rignot, E. (2012). Mapping of ice motion in Antarctica using synthetic-aperture radar data. *Remote Sensing*, 4(9):2753–2767.

- Mueller, R. D., Hattermann, T., Howard, S. L., and Padman, L. (2018). Tidal influences on a future evolution of the Filchner–Ronne Ice Shelf cavity in the Weddell Sea, Antarctica. *The Cryosphere*, 12(2):453–476.
- Munneke, P. K., Ligtenberg, S. R., Van Den Broeke, M. R., and Vaughan, D. G. (2014). Firn air depletion as a precursor of Antarctic ice-shelf collapse. *Journal of Glaciology*, 60(220):205–214.
- Nakayama, Y., Menemenlis, D., Zhang, H., Schodlok, M., and Rignot, E. (2018). Origin of Circumpolar Deep Water intruding onto the Amundsen and Bellingshausen Sea continental shelves. *Nature Communications*, 9(1):1–9.
- Nakayama, Y., Timmermann, R., Rodehacke, C. B., Schröder, M., and Hellmer, H. H. (2014). Modeling the spreading of glacial meltwater from the Amundsen and Bellingshausen Seas. *Geophysical Research Letters*, 41(22):7942–7949.
- Naughten, K. A., Holland, P. R., Dutrieux, P., Kimura, S., Bett, D. T., and Jenkins, A. (2022). Simulated twentieth-century ocean warming in the Amundsen Sea, West Antarctica. *Geophysical Research Letters*, page e2021GL094566.
- Naughten, K. A., Meissner, K. J., Galton-Fenzi, B. K., England, M. H., Timmermann, R., Hellmer, H. H., Hattermann, T., and Debernard, J. B. (2018a). Intercomparison of Antarctic ice-shelf, ocean, and sea-ice interactions simulated by MetROMS-iceshelf and FESOM 1.4. *Geoscientific Model Development*, 11:1257–1292.
- Naughten, K. A., Meissner, K. J., Galton-Fenzi, B. K., England, M. H., Timmermann, R., and Hellmer, H. H. (2018b). Future Projections of Antarctic Ice Shelf Melting Based on CMIP5 Scenarios. *Journal of Climate*, 31:5243–5261.
- Nias, I. (2017). *Modelling the Amundsen Sea ice streams, West Antarctica*. PhD thesis, University of Bristol.
- Nias, I., Cornford, S., and Payne, A. (2018). New mass-conserving bedrock topography for Pine Island Glacier impacts simulated decadal rates of mass loss. *Geophysical Research Letters*, 45(7):3173–3181.
- Nias, I. J., Cornford, S. L., Edwards, T. L., Gourmelen, N., and Payne, A. J. (2019). Assessing uncertainty in the dynamical ice response to ocean warming in the Amundsen Sea Embayment, West Antarctica. *Geophysical Research Letters*, 46(20):11253–11260.
- Nias, I. J., Cornford, S. L., and Payne, A. J. (2016). Contrasting the modelled sensitivity of the Amundsen Sea Embayment ice streams. *Journal of Glaciology*, 62(233):552–562.
- Nitsche, F., Jacobs, S., Larter, R., and Gohl, K. (2007). Bathymetry of the Amundsen Sea continental shelf: Implications for geology, oceanography, and glaciology. *Geochemistry, Geophysics, Geosystems*, 8(10).

- Nowicki, S., Goelzer, H., Seroussi, H., Payne, A. J., Lipscomb, W. H., Abe-Ouchi, A., Agosta, C., Alexander, P., Asay-Davis, X. S., Barthel, A., et al. (2020). Experimental protocol for sea level projections from ISMIP6 stand-alone ice sheet models. *The Cryosphere*, 14(7):2331–2368.
- Nowicki, S. and Seroussi, H. (2018). Projections of future sea level contributions from the Greenland and Antarctic Ice Sheets: Challenges beyond dynamical ice sheet modeling. *Oceanography*, 31(2):109–117.
- Nowicki, S. M., Payne, A., Larour, E., Seroussi, H., Goelzer, H., Lipscomb, W., Gregory, J., Abe-Ouchi, A., and Shepherd, A. (2016). Ice sheet model intercomparison project (ISMIP6) contribution to CMIP6. *Geoscientific Model Development*, 9(12):4521–4545.
- Oerlemans, J. (1983). A numerical study on cyclic behaviour of polar ice sheets. *Tellus A*, 35(2):81–87.
- Oppenheimer, M. and Hinkel, J. (2019). Sea Level Rise and Implications for Low Lying Islands, Coasts and Communities Supplementary Material. *IPCC special report on the ocean and cryosphere in a changing climate*.
- Palermo, C., Genthon, C., Claud, C., Kay, J. E., Wood, N. B., and L'Ecuyer, T. (2017). Evaluation of current and projected Antarctic precipitation in CMIP5 models. *Climate Dynamics*, 48(1):225–239.
- Paolo, F., Padman, L., Fricker, H., Adusumilli, S., Howard, S., and Siegfried, M. (2018). Response of Pacific-sector Antarctic ice shelves to the El Niño/Southern oscillation. *Nature Geoscience*, 11(2):121–126.
- Parizek, B., Christianson, K., Anandakrishnan, S., Alley, R., Walker, R., Edwards, R., Wolfe, D., Bertini, G., Rinehart, S., Bindschadler, R., et al. (2013). Dynamic (in) stability of Thwaites Glacier, West Antarctica. *Journal of Geophysical Research: Earth Surface*, 118(2):638–655.
- Paterson, W. S. B. (1994). *Physics of Glaciers*. Butterworth-Heinemann.
- Pattyn, F. (2003). A new three-dimensional higher-order thermomechanical ice sheet model: Basic sensitivity, ice stream development, and ice flow across subglacial lakes. *Journal of Geophysical Research: Solid Earth*, 108(B8).
- Pattyn, F. (2008). Investigating the stability of subglacial lakes with a full Stokes ice-sheet model. *Journal of Glaciology*, 54(185):353–361.
- Pattyn, F. (2010). Antarctic subglacial conditions inferred from a hybrid ice sheet/ice stream model. *Earth and Planetary Science Letters*, 295(3-4):451–461.
- Pattyn, F. (2018). The paradigm shift in Antarctic ice sheet modelling. *Nature Communications*, 9(1):1–3.

- Pattyn, F. and Durand, G. (2013). Why marine ice sheet model predictions may diverge in estimating future sea level rise. *Geophysical Research Letters*, 40(16):4316–4320.
- Pattyn, F., Favier, L., Sun, S., and Durand, G. (2017). Progress in numerical modeling of Antarctic ice-sheet dynamics. *Current Climate Change Reports*, 3(3):174–184.
- Pattyn, F., Huyghe, A., De Brabander, S., and De Smedt, B. (2006). Role of transition zones in marine ice sheet dynamics. *Journal of Geophysical Research: Earth Surface*, 111(F2).
- Pattyn, F., Perichon, L., Aschwanden, A., Breuer, B., De Smedt, B., Gagliardini, O., Gudmundsson, G. H., Hindmarsh, R. C., Hubbard, A., Johnson, J. V., et al. (2008). Benchmark experiments for higher-order and full-Stokes ice sheet models (ISMIP–HOM). *The Cryosphere*, 2(2):95–108.
- Pattyn, F., Perichon, L., Durand, G., Favier, L., Gagliardini, O., Hindmarsh, R. C., Zwinger, T., Albrecht, T., Cornford, S., Docquier, D., et al. (2013). Grounding-line migration in plan-view marine ice-sheet models: results of the ice2sea MISMP3d intercomparison. *Journal of Glaciology*, 59(215):410–422.
- Pattyn, F., Schoof, C., Perichon, L., Hindmarsh, R. C. A., Bueler, E., de Fleurian, B., Durand, G., Gagliardini, O., Gladstone, R., Goldberg, D., Gudmundsson, G. H., Huybrechts, P., Lee, V., Nick, F. M., Payne, A. J., Pollard, D., Rybak, O., Saito, F., and Vieli, A. (2012). Results of the Marine Ice Sheet Model Intercomparison Project, MISMP. *The Cryosphere*, 6:573–588.
- Pattyn, F., Sun, S., and Golledge, N. (2017-04). Model intercomparison of sea-level response to sudden Antarctic ice-shelf collapse. In *EGU General Assembly Conference Abstracts*, volume 19 of *EGU General Assembly Conference Abstracts*, page 12838.
- Payne, A. J., Holland, P. R., Shepherd, A. P., Rutt, I. C., Jenkins, A., and Joughin, I. (2007). Numerical modeling of ocean-ice interactions under Pine Island Bay’s ice shelf. *Journal of Geophysical Research: Oceans*, 112(C10).
- Payne, A. J., Vieli, A., Shepherd, A. P., Wingham, D. J., and Rignot, E. (2004). Recent dramatic thinning of largest West Antarctic ice stream triggered by oceans. *Geophysical Research Letters*, 31(23).
- Pegler, S. S. (2018a). Marine ice sheet dynamics: the impacts of ice-shelf buttressing. *Journal of Fluid Mechanics*, 857:605–647.
- Pegler, S. S. (2018b). Suppression of marine ice sheet instability. *Journal of Fluid Mechanics*, 857:648–680.
- Pelle, T., Morlighem, M., and Bondzio, J. H. (2019). Brief communication: PICOP, a new ocean melt parameterization under ice shelves combining PICO and a plume model. *The Cryosphere*, 13(3):1043–1049.

- Pimentel, S., Flowers, G., and Schoof, C. (2010). A hydrologically coupled higher-order flow-band model of ice dynamics with a Coulomb friction sliding law. *Journal of Geophysical Research: Earth Surface*, 115(F4).
- Pollard, D. and DeConto, R. M. (2012). A simple inverse method for the distribution of basal sliding coefficients under ice sheets, applied to Antarctica. *The Cryosphere*, 6:953–971.
- Previdi, M. and Polvani, L. M. (2016). Anthropogenic impact on antarctic surface mass balance, currently masked by natural variability, to emerge by mid-century. *Environmental Research Letters*, 11(9):094001.
- Pritchard, H. D., Arthern, R. J., Vaughan, D. G., and Edwards, L. A. (2009). Extensive dynamic thinning on the margins of the Greenland and Antarctic ice sheets. *Nature*, 461(7266):971–975.
- Pritchard, H. D., Ligtenberg, S. R. M., Fricker, H. A., Vaughan, D. G., van den Broeke, M. R., and Padman, L. (2012). Antarctic ice-sheet loss driven by basal melting of ice shelves. *Nature*, 484:502–505.
- Raphael, M. N., Marshall, G., Turner, J., Fogt, R., Schneider, D., Dixon, D., Hosking, J., Jones, J., and Hobbs, W. R. (2016). The Amundsen sea low: variability, change, and impact on Antarctic climate. *Bulletin of the American Meteorological Society*, 97(1):111–121.
- Rasmussen, L. and Campbell, W. (1973). Comparison of three contemporary flow laws in a three-dimensional, time-dependent glacier model. *Journal of Glaciology*, 12(66):361–373.
- Reese, R., Albrecht, T., Mengel, M., Asay-Davis, X., and Winkelmann, R. (2018a). Antarctic sub-shelf melt rates via PICO. *The Cryosphere*, 12(6):1969–1985.
- Reese, R., Gudmundsson, G. H., Levermann, A., and Winkelmann, R. (2018b). The far reach of ice-shelf thinning in Antarctica. *Nature Climate Change*, 8(1):53–57.
- Ridley, J. K., Huybrechts, P., Gregory, J. u., and Lowe, J. (2005). Elimination of the Greenland ice sheet in a high CO₂ climate. *Journal of Climate*, 18(17):3409–3427.
- Rignot, E. (2008). Changes in West Antarctic ice stream dynamics observed with ALOS PALSAR data. *Geophysical Research Letters*, 35(12).
- Rignot, E., Jacobs, S., Mouginot, J., and Scheuchl, B. (2013a). Ice-shelf melting around Antarctica. *Science*, 341:266–270.
- Rignot, E., Jacobs, S., Mouginot, J., and Scheuchl, B. (2013b). Ice-shelf melting around Antarctica. *Science*, 341(6143):266–270.
- Rignot, E. and Jacobs, S. S. (2002). Rapid bottom melting widespread near Antarctic ice sheet grounding lines. *Science*, 296(5575):2020–2023.

- Rignot, E., Mouginot, J., Morlighem, M., Seroussi, H., and Scheuchl, B. (2014). Widespread, rapid grounding line retreat of Pine Island, Thwaites, Smith, and Kohler glaciers, West Antarctica, from 1992 to 2011. *Geophysical Research Letters*, 41:3502–3509.
- Rignot, E., Mouginot, J., and Scheuchl, B. (2011). Antarctic grounding line mapping from differential satellite radar interferometry. *Geophysical Research Letters*, 38.
- Rignot, E., Mouginot, J., Scheuchl, B., van den Broeke, M., van Wessem, M. J., and Morlighem, M. (2019). Four decades of Antarctic Ice Sheet mass balance from 1979–2017. *Proceedings of the National Academy of Sciences*, 116(4):1095–1103. Publisher: National Acad Sciences.
- Ritz, C., Edwards, T. L., Durand, G., Payne, A. J., Peyaud, V., and Hindmarsh, R. C. (2015). Potential sea-level rise from Antarctic ice-sheet instability constrained by observations. *Nature*, 528:115–118.
- Robel, A. A. and Banwell, A. F. (2019). A Speed Limit on Ice Shelf Collapse through Hydrofracture. *Geophysical Research Letters*. Publisher: Wiley Online Library.
- Robel, A. A., Seroussi, H., and Roe, G. H. (2019). Marine ice sheet instability amplifies and skews uncertainty in projections of future sea-level rise. *Proceedings of the National Academy of Sciences*, 116(30):14887–14892.
- Robel, A. A. and Tziperman, E. (2016). The role of ice stream dynamics in deglaciation. *Journal of Geophysical Research*, 121:1540–1554.
- Scambos, T., Fricker, H. A., Liu, C.-C., Bohlander, J., Fastook, J., Sargent, A., Massom, R., and Wu, A.-M. (2009). Ice shelf disintegration by plate bending and hydrofracture: Satellite observations and model results of the 2008 Wilkins ice shelf break-ups. *Earth and Planetary Science Letters*, 280(1-4):51–60.
- Scambos, T. A., Bell, R. E., Alley, R. B., Anandakrishnan, S., Bromwich, D., Brunt, K., Christianson, K., Creyts, T., Das, S., DeConto, R., et al. (2017). How much, how fast?: A science review and outlook for research on the instability of Antarctica's Thwaites Glacier in the 21st century. *Global and Planetary Change*, 153:16–34.
- Scheuchl, B., Mouginot, J., Rignot, E., Morlighem, M., and Khazendar, A. (2016). Grounding line retreat of Pope, Smith, and Kohler Glaciers, West Antarctica, measured with Sentinel-1a radar interferometry data. *Geophysical Research Letters*, 43(16):8572–8579.
- Schlegel, N.-J., Seroussi, H., Schodlok, M. P., Larour, E. Y., Boening, C., Limonadi, D., Watkins, M. M., Morlighem, M., and Broeke, M. R. (2018). Exploration of Antarctic Ice Sheet 100-year contribution to sea level rise and associated model uncertainties using the ISSM framework. *The Cryosphere*, 12(11):3511–3534.
- Schmidtko, S., Heywood, K. J., Thompson, A. F., and Aoki, S. (2014). Multidecadal warming of Antarctic waters. *Science*, 346(6214):1227–1231.

- Schodlok, M. P., Menemenlis, D., Rignot, E., and Studinger, M. (2012). Sensitivity of the ice-shelf/ocean system to the sub-ice-shelf cavity shape measured by NASA IceBridge in Pine Island Glacier, West Antarctica. *Annals of Glaciology*, 53(60):156–162.
- Schoof, C. (2005). The effect of cavitation on glacier sliding. *Proceedings of the Royal Society A: Mathematical, Physical and Engineering Sciences*, 461(2055):609–627.
- Schoof, C. (2006). Variational methods for glacier flow over plastic till. *Journal of Fluid Mechanics*, 555:299–320.
- Schoof, C. (2007). Ice sheet grounding line dynamics: Steady states, stability, and hysteresis. *Journal of Geophysical Research: Earth Surface*, 112(F3).
- Schoof, C. (2010). Coulomb friction and other sliding laws in a higher-order glacier flow model. *Mathematical Models and Methods in Applied Sciences*, 20(01):157–189.
- Schoof, C. (2012). Marine ice sheet stability. *Journal of Fluid Mechanics*, 698:62–72.
- Schoof, C. and Hindmarsh, R. C. (2010). Thin-film flows with wall slip: an asymptotic analysis of higher order glacier flow models. *Quarterly Journal of Mechanics and Applied Mathematics*, 63(1):73–114.
- Schroeder, D. M., Dowdeswell, J. A., Siegert, M. J., Bingham, R. G., Chu, W., MacKie, E. J., Siegfried, M. R., Vega, K. I., Emmons, J. R., and Winstein, K. (2019). Multidecadal observations of the Antarctic ice sheet from restored analog radar records. *Proceedings of the National Academy of Sciences*, 116(38):18867–18873.
- Sergienko, O. V. and Wingham, D. J. (2021). Bed topography and marine ice-sheet stability. *Journal of Glaciology*, pages 1–15.
- Seroussi, H. and Morlighem, M. (2018). Representation of basal melting at the grounding line in ice flow models. *The Cryosphere Discussions*, pages <https://doi.org/10.5194/tc-2018-117>.
- Seroussi, H., Morlighem, M., Rignot, E., Mougintot, J., Larour, E., Schodlok, M., and Khazendar, A. (2014). Sensitivity of the dynamics of Pine Island Glacier, West Antarctica, to climate forcing for the next 50 years. *The Cryosphere*, 8(5):1699–1710.
- Seroussi, H., Nakayama, Y., Larour, E., Menemenlis, D., Morlighem, M., Rignot, E., and Khazendar, A. (2017). Continued retreat of Thwaites Glacier, West Antarctica, controlled by bed topography and ocean circulation. *Geophysical Research Letters*, 44(12):6191–6199.
- Seroussi, H., Nowicki, S., Payne, A. J., Goelzer, H., Lipscomb, W. H., Abe-Ouchi, A., Agosta, C., Albrecht, T., Asay-Davis, X., Barthel, A., et al. (2020). ISMIP6 Antarctica: a multi-model ensemble of the Antarctic ice sheet evolution over the 21st century. *The Cryosphere*, 14(9):3033–3070.

- Seroussi, H., Nowicki, S., Simon, E., Abe-Ouchi, A., Albrecht, T., Brondex, J., Cornford, S., Dumas, C., Gillet-Chaulet, F., Goelzer, H., and others (2019). initMIP-antarctica: an ice sheet model initialization experiment of ISMIP6. *The Cryosphere*, 13(5):1441–1471.
- Shean, D. (2016). *Quantifying ice-shelf basal melt and ice-stream dynamics using high-resolution DEM and GPS time series*. PhD thesis, University of Washington.
- Shean, D. E., Joughin, I. R., Dutrieux, P., Smith, B. E., and Berthier, E. (2019). Ice shelf basal melt rates from a high-resolution digital elevation model (DEM) record for Pine Island Glacier, Antarctica. *The Cryosphere*, 13(10):2633–2656.
- Shepherd, A., Ivins, E., Rignot, E., Smith, B., Van Den Broeke, M., Velicogna, I., Whitehouse, P., Briggs, K., Joughin, I., Krinner, G., et al. (2018). Mass balance of the Antarctic Ice Sheet from 1992 to 2017. *Nature*, 558:219–222.
- Smith, J. A., Andersen, T., Shortt, M., Gaffney, A., Truffer, M., Stanton, T. P., Bindshadler, R., Dutrieux, P., Jenkins, A., Hillenbrand, C.-D., et al. (2017). Sub-ice-shelf sediments record history of twentieth-century retreat of Pine Island Glacier. *Nature*, 541(7635):77–80.
- Smith, R. S., Mathiot, P., Siahayan, A., Lee, V., Cornford, S. L., Gregory, J. M., Payne, A. J., Jenkins, A., Holland, P. R., Ridley, J. K., et al. (2021). Coupling the UK Earth System Model to dynamic models of the Greenland and Antarctic ice sheets. *Journal of Advances in Modeling Earth Systems*, 13(10):e2021MS002520.
- Smith-Johnsen, S., de Fleurian, B., and Nisancioglu, K. H. (2020). The role of subglacial hydrology in ice streams with elevated geothermal heat flux. *Journal of Glaciology*, 66(256):303–312.
- Stearns, L. A., Smith, B. E., and Hamilton, G. S. (2008). Increased flow speed on a large East Antarctic outlet glacier caused by subglacial floods. *Nature Geoscience*, 1(12):827–831.
- Steig, E. J., Ding, Q., Battisti, D., and Jenkins, A. (2012). Tropical forcing of Circumpolar Deep Water inflow and outlet glacier thinning in the Amundsen Sea Embayment, West Antarctica. *Annals of Glaciology*, 53(60):19–28.
- Steig, E. J., Huybers, K., Singh, H. A., Steiger, N. J., Ding, Q., Frierson, D. M., Popp, T., and White, J. W. (2015). Influence of West Antarctic ice sheet collapse on Antarctic surface climate. *Geophysical Research Letters*, 42(12):4862–4868.
- Stewart, C., Christofferson, P., Nicholls, K., Williams, M., and Dowdeswell, J. (2019). Basal melting of Ross Ice Shelf from solar heat absorption in an ice-front polynya. *Nature Geoscience*, pages <https://doi.org/10.1038/s41561-019-0356-0>.
- Still, H., Campbell, A., and Hulbe, C. (2019). Mechanical analysis of pinning points in the Ross Ice Shelf, Antarctica. *Annals of Glaciology*, 60(78):32–41.

- Stokes, C. R. and Clark, C. D. (1999). Geomorphological criteria for identifying Pleistocene ice streams. *Annals of Glaciology*, 28:67–74.
- Sun, S., Cornford, S. L., Liu, Y., and Moore, J. C. (2014). Dynamic response of Antarctic ice shelves to bedrock uncertainty. *The Cryosphere*, 8(4):1561–1576.
- Sun, S., Cornford, S. L., Moore, J. C., Gladstone, R., and Zhao, L. (2017). Ice shelf fracture parameterization in an ice sheet model. *The Cryosphere*, 11(6).
- Taylor, K. E., Stouffer, R. J., and Meehl, G. A. (2012). An overview of CMIP5 and the experiment design. *Bulletin of the American meteorological Society*, 93(4):485–498.
- Tewari, K., Mishra, S. K., Dewan, A., and Ozawa, H. (2021). Effects of the Antarctic elevation on the atmospheric circulation. *Theoretical and Applied Climatology*, 143(3):1487–1499.
- Thoma, M., Jenkins, A., Holland, D., and Jacobs, S. (2008). Modelling circumpolar deep water intrusions on the Amundsen Sea continental shelf, Antarctica. *Geophysical Research Letters*, 35(18).
- Thomas, R. H. (1979). The dynamics of marine ice sheets. *Journal of Glaciology*, 24(90):167–177.
- Thomas, R. H. and Bentley, C. R. (1978). A model for Holocene retreat of the West Antarctic ice sheet. *Quaternary Research*, 10(2):150–170.
- Thompson, D. W. and Solomon, S. (2002). Interpretation of recent Southern Hemisphere climate change. *Science*, 296(5569):895–899.
- Tinto, K. and Bell, R. E. (2011). Progressive unpinning of Thwaites Glacier from newly identified offshore ridge: Constraints from aerogravity. *Geophysical Research Letters*, 38(20).
- Trusel, L. D., Frey, K. E., Das, S. B., Karnauskas, K. B., Kuipers Munneke, P., van Meijgaard, E., and van den Broeke, M. (2015). Divergent trajectories of Antarctic surface melt under two twenty-first-century climate scenarios. *Nature Geoscience*, 8:927–932.
- Trusel, L. D., Frey, K. E., Das, S. B., Munneke, P. K., and Van Den Broeke, M. R. (2013). Satellite-based estimates of Antarctic surface meltwater fluxes. *Geophysical Research Letters*, 40(23):6148–6153.
- Tsai, V. C., Stewart, A. L., and Thompson, A. F. (2015). Marine ice-sheet profiles and stability under Coulomb basal conditions. *Journal of Glaciology*, 61:205–215.
- Tulaczyk, S., Kamb, W. B., and Engelhardt, H. F. (2000). Basal mechanics of Ice Stream B, west Antarctica: 2. Undrained plastic bed model. *Journal of Geophysical Research: Solid Earth*, 105(B1):483–494.

- Turner, J., Orr, A., Gudmundsson, G. H., Jenkins, A., Bingham, R. G., Hillenbrand, C.-D., and Bracegirdle, T. J. (2017). Atmosphere-ocean-ice interactions in the Amundsen Sea embayment, West Antarctica. *Reviews of Geophysics*, 55(1):235–276.
- Van Vuuren, D. P., Stehfest, E., den Elzen, M. G., Kram, T., van Vliet, J., Deetman, S., Isaac, M., Goldewijk, K. K., Hof, A., Beltran, A. M., et al. (2011). RCP2.6: exploring the possibility to keep global mean temperature increase below 2°C. *Climatic change*, 109(1):95–116.
- Vieli, A. and Payne, A. J. (2003). Application of control methods for modelling the flow of Pine Island Glacier, West Antarctica. *Annals of Glaciology*, 36:197–204.
- Vieli, A. and Payne, A. J. (2005). Assessing the ability of numerical ice sheet models to simulate grounding line migration. *Journal of Geophysical Research: Earth Surface*, 110(F1).
- Vizcaino, M. (2014). Ice sheets as interactive components of Earth System Models: progress and challenges. *Wiley Interdisciplinary Reviews: Climate Change*, 5(4):557–568.
- Wåhlin, A., Kalén, O., Arneborg, L., Björk, G., Carvajal, G., Ha, H. K., Kim, T., Lee, S. H., Lee, J., and Stranne, C. (2013). Variability of warm deep water inflow in a submarine trough on the Amundsen Sea shelf. *Journal of Physical Oceanography*, 43(10):2054–2070.
- Wåhlin, A. K., Steiger, N., Darelius, E., Assmann, K. M., Glessmer, M. S., Ha, H. K., Herraiz-Borreguero, L., Heuzé, C., Jenkins, A., Kim, T.-W., et al. (2020). Ice front blocking of ocean heat transport to an Antarctic ice shelf. *Nature*, 578(7796):568–571.
- Waibel, M., Hulbe, C., Jackson, C., and Martin, D. (2018). Rate of mass loss across the instability threshold for Thwaites Glacier determines rate of mass loss for entire basin. *Geophysical Research Letters*, 45(2):809–816.
- Walker, D. P., Brandon, M. A., Jenkins, A., Allen, J. T., Dowdeswell, J. A., and Evans, J. (2007). Oceanic heat transport onto the Amundsen Sea shelf through a submarine glacial trough. *Geophysical Research Letters*, 34(2).
- Walker, D. P., Jenkins, A., Assmann, K. M., Shoosmith, D. R., and Brandon, M. A. (2013). Oceanographic observations at the shelf break of the Amundsen Sea, Antarctica. *Journal of Geophysical Research: Oceans*, 118(6):2906–2918.
- Wearing, M. G., Kingslake, J., and Worster, M. G. (2020). Can unconfined ice shelves provide buttressing via hoop stresses? *Journal of Glaciology*, 66(257):349–361.
- Webber, B. G., Heywood, K. J., Stevens, D. P., Dutrieux, P., Abrahamsen, E. P., Jenkins, A., Jacobs, S. S., Ha, H. K., Lee, S. H., and Kim, T. W. (2017). Mechanisms driving variability in the ocean forcing of Pine Island Glacier. *Nature Communications*, 8:14507.

- Weertman, J. (1957). On the sliding of glaciers. *Journal of glaciology*, 3(21):33–38.
- Weertman, J. (1974). Stability of the junction of an ice sheet and an ice shelf. *Journal of Glaciology*, 13(67):3–11.
- Wernecke, A., Edwards, T. L., Holden, P. B., Edwards, N. R., and Cornford, S. L. (2022). Quantifying the impact of bedrock topography uncertainty in Pine Island Glacier projections for this century. *Geophysical Research Letters*, 49(6):e2021GL096589.
- Wessem, J. M. v., Berg, W. J. v. d., Noël, B. P., Meijgaard, E. v., Amory, C., Birnbaum, G., Jakobs, C. L., Krüger, K., Lenaerts, J., Lhermitte, S., et al. (2018). Modelling the climate and surface mass balance of polar ice sheets using RACMO2–Part 2: Antarctica (1979–2016). *The Cryosphere*, 12(4):1479–1498.
- Whitehouse, P. L., Gomez, N., King, M. A., and Wiens, D. A. (2019). Solid earth change and the evolution of the antarctic ice sheet. *Nature communications*, 10(1):1–14.
- Wild, C. T., Alley, K. E., Muto, A., Truffer, M., Scambos, T. A., and Pettit, E. C. (2021). Weakening of the pinning point buttressing Thwaites Glacier, West Antarctica. *The Cryosphere Discussions*, pages 1–28.
- Winkelmann, R., Martin, M. A., Haseloff, M., Albrecht, T., Bueller, E., Khroulev, C., and Levermann, A. (2011). The Potsdam parallel ice sheet model (PISM-PIK)–Part 1: Model description. *The Cryosphere*, 5(3):715–726.
- Yu, H., Rignot, E., Seroussi, H., and Morlighem, M. (2018). Retreat of Thwaites Glacier, West Antarctica, over the next 100 years using various ice flow models, ice shelf melt scenarios and basal friction laws. *The Cryosphere*, 12(12):3861–3876.
- Yu, H., Rignot, E., Seroussi, H., Morlighem, M., and Choi, Y. (2019). Impact of iceberg calving on the retreat of Thwaites Glacier, West Antarctica over the next century with different calving laws and ocean thermal forcing. *Geophysical Research Letters*, 46(24):14539–14547.
- Zhang, T., Price, S. F., Hoffman, M. J., Perego, M., and Asay-Davis, X. (2020). Diagnosing the sensitivity of grounding-line flux to changes in sub-ice-shelf melting. *The Cryosphere*, 14(10):3407–3424.
- Zheng, F., Li, J., Clark, R. T., and Nnamchi, H. C. (2013). Simulation and projection of the Southern Hemisphere annular mode in CMIP5 models. *Journal of Climate*, 26(24):9860–9879.
- Zoet, L. K. and Iverson, N. R. (2020). A slip law for glaciers on deformable beds. *Science*, 368(6486):76–78.